Structural characterisation of nonsubstituted and Mo- or Re-substituted proton-conducting $La_{6-x}WO_{12-\delta}$ by diffraction of X-rays and neutrons

vorgelegt von

Diplom-Physiker

Andrea Fantin

geb. in Treviso

von der Fakultät III – Prozesswissenschaften
der Technischen Universität Berlin
zur Erlangung des akademischen Grades

Doktor der Naturwissenschaften
- Dr. rer. nat. -

genehmigte Dissertation

Promotionsausschuss:

Vorsitzender: Prof. Dr. Felix Ziegler
Gutachter: Prof. Dr. John Banhart
Gutachter: Prof. Dr. Lorenz Singheiser

Tag der wissenschaftlichen Aussprache: 27. Mai 2016

Berlin 2016

Abstract

In this work a detailed characterisation of proton-conducting materials, $La_{6-x}WO_{12-\delta}$ ($0.4 \leq x \leq 0.8$; LWO) and $La_{5.4}W_{1-y}M_yO_{12-\delta}$ (*M* = Mo, Re; $0 \leq y \leq 0.2$; LW*M*O), is carried out. These systems belong to the family of mixed ionic-electronic conductors, which can be employed as solid electrolytes in fuel cells or as gas-separation membranes. The motivation of this study lies in the improvement of hydrogen permeation achieved with Mo- and Re-substitution on the parent compound LWO, making LW*M*O (*M* = Mo, Re) compounds suitable for hydrogen-related technologies. These technologies are the basis for clean energy production and can either replace the existing engines running on fossil fuel, or reduce and control carbon emissions within the carbon capture and storage processes.

The main focus of this work is the determination of the crystal structure of these novel materials by means of neutron and X-ray diffraction. In addition, systematic studies on composition and water uptake were performed. The specimen compositions were investigated by electron probe micro-analysis, while the water uptake was determined by thermogravimetry. The thermogravimetry technique is fundamental to establish the ion conduction-related properties, mainly driven by the oxygen vacancy concentration in the unit cell. As will be shown, the oxygen vacancy concentration is correlated to the cation concentration. Such correlation provides the reason for performing detailed composition studies.

Despite many studies on the LWO system during the recent years claim that this system is well-understood, this work presents different inconsistencies reported in the recent literature and re-opens questions that seemed to have been already answered. As a starting point, the two most recent crystal structure models available for LWO are compared to each other by analysis of the atomic vibrations as well as of nuclear and electron density maps. In literature, LWO is proven to crystallise in the fluorite structure ($Fm\bar{3}m$ space group) with a doubled unit cell to account for La and W cation ordering. Even if the best model approximates well the crystal structure of LWO and is directly comparable to the electron density maps drawn in the present work, some details are not accounted for. For instance, anion anharmonic vibrations such as in the YSZ structure have been identified in this work, in addition to the existence of not negligible anion librations, visible by means of nuclear density maps. Both of these features are at present not modelled, and contribute the most to the remaining static disorder in the unit cell. As side effects, an unexpected bond length shortening with increasing temperature and the underestimation of the Debye temperatures by means of atomic vibration studies were observed. Nevertheless, the feasibility of the implementation of anharmonic vibrations and libration movements in the crystal structure model for LWO is still unclear and needs to be tested in the most recent software. The not optimized LWO crystal structure is not the major question raised by this work: the charge compensation model for LWO currently used in the literature yields a substantial deviation of the vacancy concentration prediction of about 35 % from the experimental data obtained with thermogravimetry. The rationalisation of this deviation is unclear at present and instils also doubts on the validity of the LWO chemical formulation.

With these bases, the composition, water uptake and crystallographic studies on LW*M*O (*M* = Mo, Re) were carried out, where the series of specimens with less than 20 mol % substitution of W by *M* were synthesized by a citrate complexation route based on the Pechini procedure. In the investigated systems, for substitution of W by *M* < 20 mol %, no change in crystal structure compared with the mother compound is observed for any of the substituted specimens. It will be proven that the Mo and Re atoms statistically occupy the W Wyckoff sites within the $Fm\bar{3}m$ space group. This has been inferred through the average neutron scattering length and average X-ray scattering power methods.

Therefore, the conclusions drawn above for the LWO crystal structure are applicable also to the LW*M*O (*M* = Mo, Re) systems. It will be shown that the oxygen vacancies in LW*M*O (*M* = Mo, Re) occupy the same Wyckoff site (32*f*, $Fm\bar{3}m$) and that their concentration depends on the La/W ratio, comparably to LWO. However, the vacancy concentration depends also on the oxidation state of the W or *M* donors bonded to the vacancy (48*h*, $Fm\bar{3}m$). This allows to conclude that Re-substitution on 48*h* site is the responsible for a decrease in the vacancy concentration in LW(Re)O system compared to LWO. It will also be shown that the oxidation states of the substituent atoms *M* = Mo, Re strongly depend on the specimen preparation conditions, such as reducing/oxidizing and wet/dry conditions used. These findings will be thoroughly discussed in the final comparison between the three system investigated (LWO, LW*M*O). Here, in addition to the discussion between the oxidation states of W and the substituent atoms *M* = Mo, Re in LWO and LW*M*O, the temperature dependence of the thermal expansion, the bond lengths, the unit cell average disorder and the anionic anharmonic vibrations will be described.

Contents

1 Introduction

United Nations, Framework Convention on Climate Change, COP* 21st (30 Nov – 11 Dec 2015, Paris[1]), Paris Agreement:

Article 2

1. This Agreement, in enhancing the implementation of the Convention, including its objective, aims to strengthen the global response to the threat of climate change, in the context of sustainable development and efforts to eradicate poverty, including by:
   a. Holding the increase in the global average temperature to well below 2 °C above pre-industrial levels and to pursue efforts to limit the temperature increase to 1.5 °C above pre-industrial levels, recognizing that this would significantly reduce the risks and impacts of climate change;

The COP 21st session took place 18 years after the Kyoto Protocol was signed. Despite the Kyoto Protocol and many subsequent meetings (e.g. COP 15th, 2009), the United Nations (UN) failed to reduce carbon emissions due to the lack of a common commitment of the States[2-4]. Nevertheless, the argument presented at the COP 16th (2010), stating: "we must limit the global temperature rise to 2 °C above pre-industrial levels to avoid dangerous interference with the climate system", has been in the focus of the UN climate conventions ever since 2010 (see Article 2.1 comma *a*). In order to achieve a 2 °C scenario (66 % likelihood), less than 1000 additional Gt CO_2 after 2011 can be emitted by the entire world, according to IPCC†,[5]. However, according to the synthesis report by the UN itself, if all the 2015 State pledges were respected, about 723 Gt would be emitted up to 2030[6]. This leaves about 7 years at a rate of 40 Gt CO_2 per year (IEA‡ estimations[7,8]) to cease CO_2 emissions completely. Despite such very demanding and alarming previsions, the CO_2 emission problem derives mainly from fuel combustion (68 %, IEA[9]), which oxidizes e.g. carbon ($C + O_2 \rightarrow CO_2$) or methane ($CH_4 + 2O_2 \rightarrow CO_2 + 2H_2O$). In this scenario, carbon capture and storage (CCS) processes may reduce the world CO_2 emissions up to 20 %[10]. Different approaches can be used for the capture CO_2 released by coal-derived power generation, such as post-combustion, pre-combustion and oxy-combustion capture[11,12]. In pre-combustion capture a promising approach is the integrated gasification combine cycle (IGCC), which yields CO_2 and H_2 as products through the water gas shift reaction. For this purpose, solid CO_2 capture sorbents (metal-organic frameworks[12], zeolites[13]), enzyme-based systems, ionic liquids and many other materials and technologies are investigated. If CO_2 is efficiently captured by one of these technologies, by controlling CO_2 emissions it is possible to focus at the same time on the production of hydrogen gas. Hydrogen-related technologies could replace existing power generators running on fossil fuels. Instead of CO_2, the sole emission products of H_2-based engines would be water and heat, thus zero-emissions. The IGCC in pre-combustion capture is just an example of how CCS and H_2 production are strongly related in order to

* COP: Conference of Parties
† IPCC: Intergovernmental Panel on Climate Change
‡ IEA: International Energy Agency

overcome global pollution. In addition to the fact that H_2 is a zero-emission fuel, hydrogen has the highest energy density amongst all fuels and is, therefore, suggested to be used as primary energy carrier, e.g., in cars[14,15], buses[16], submarines[17] and power plants[18,19]. A further advantage is that hydrogen gas can be produced from clean and renewable energy sources such as solar, wind and hydroelectric power through water electrolysis. Despite the fact that water electrolysis is the cleanest source for hydrogen production, natural gas reforming and coal gasification are still economically more favourable. However, hydrogen production from fossil fuels leads to different gas impurities such as H_2O, CO_x, NO_x, SO_x, which restrict its use as a fuel of high purity. Therefore, it is desirable to develop efficient technologies suitable for delivering highly pure H_2 out of a mixture of different gases and at the same time enabling to control, collect and store the other gas components such as CO_2 separated during the process (CCS). Here lies the focus of this work, where the characterisation of new materials able to act as gas-separators for H_2 (CO_2) is carried out: specifically, dense ceramic materials for membrane production. Such materials are presented in this work focusing on the crystal structure. Determination of the crystal structure is the basis for a better understanding of macroscopic properties such as permeation and conductivity across the membrane. Specifically, the ceramic materials investigated in this work are referred to as mixed ionic-electronic conducting materials, for reasons explained in the following sections.

2 Mixed ionic-electronic conducting materials

New technologies to obtain pure hydrogen through gas separation are applicable using ceramic membranes as solid separators, which must have enough proton and electron bulk conductivity (good mixed conductors) allowing for net H_2 flux across the membrane. Moreover, materials for hydrogen separation membranes should be chemically stable in acidic gas atmospheres (e.g. CO_x,NO_x, SO_x), exhibit high H_2 selectivity and activity at their surfaces and be mechanically and thermally stable for long–term operation and elevated temperatures. While for most of the materials a choice between either good conductivity (perovskites with alkaline earth metal[20-22]) or stability (Rare-earth sesquioxides[23], pyrochlores[24], acceptor-doped niobates[25-28]) had to be made, rare-earth tungstates (LnWO) have been identified as appropriate candidates exhibiting both properties. One of the latest reviews on many of the above cited materials suitable for membrane hydrogen separation was published recently by Tao *et al.*[29]. As shown in recent studies, LnWO specimens with Ln = La (LWO), Nd show a conductivity comparable with the best perovskites[30-32] and excellent stability in acidic atmospheres[33-35]. Substitution of the W site with the more reducible Re[31] or Mo[31,36] increases the electronic conductivity and leads, in the case of Re, to the highest values of H_2 permeation flow in the bulk at intermediate temperatures reported to date[31]. These outstanding macroscopic properties of Mo- and Re-substituted LWO (LW*M*O, *M* = Mo, Re) are the motivation for structural studies on these materials. A short resume of the basics of conductivity and H_2-permeation theory is reported in the following sections along with the measurements of the LW*M*O (*M* = Mo, Re) conductivity and H_2 permeation reported in literature[37]. After this, more detailed motivations under a crystallographic point of view will be addressed.

2.1 Conductivity

The total conductivity in mixed ionic-electronic conductors, σ_{tot}, is given by the sum of the individual ionic, σ_{ion}, and electronic, σ_{e^-}, contributions[38]

$$\sigma_{tot} = \sigma_{ion} + \sigma_{e^-}. \tag{2.1}$$

In addition, the transport (transference) number, t_k, commonly used to describe the conductivity properties of mixed-conducting materials for any charge carrier *k*, is defined by[38]

$$t_k = \frac{\sigma_k}{\sigma_{tot}}, \tag{2.2}$$

which applied to Eq. (2.1) results in

$$\sigma_{tot} = \sigma_{ion} + \sigma_{e^-} = \sigma_{tot}(t_{ion} + t_{e^-}). \tag{2.3}$$

From Eq. (2.3), it follows that the sum of the transport numbers must be equal to 1 ($\sum_k t_k = 1$).
The general conductivity term σ_{ion} contains the proton (σ_{H^+}) and the oxygen ion ($\sigma_{O^{2-}}$)* conductivity contributions, mentioned explicitly in the following. Each one of the σ_{H^+}, σ_{e^-} and $\sigma_{O^{2-}}$ terms depends on the measurement configuration. Reducing and oxidizing atmospheres can be employed, as well as dry or wet conditions. For each atmosphere and condition, the conductivity is described by specific chemical equations. Such equations are not discussed in the present work, for which the reader is referred to the literature[39-42] for details. However, the Kröger-Vink (K-V) notation[43,44], commonly used to describe such chemical equations in mixed ionic-electronic conductors, will be employed throughout the whole work. The K-V notation is a useful nomenclature to account for the defect chemistry of ionic crystals such as point defects (vacancies, interstitials) and the carried excess charge relative to the neutral lattice. Some examples are reported in Table 2.1.

Table 2.1. Examples of the Kröger-Vink (K-V) notations. In general, K-V notations are expressed in the form M_B^A, where M is the species (atom/molecule, vacancy v, electron e, hole h), B the lattice site that the species occupies (atomic site M, interstitial site i for instance) and A the charge excess relative to the neutral lattice (x = 0, / = -1, ● = +1).

Symbol	Explanation	Charge
O_O^x	Oxygen at oxygen site	0
O_i''	Oxygen at interstitial site	-2
$v_O^{\bullet\bullet}$	Vacancy at oxygen site	+2
v_i^x	Vacancy at interstitial site	0
$OH_O^{\bullet}$	OH-group at oxygen site	+1
OH_i'	OH-group at interstitial site	-1
e'	electron	-1
$h^{\bullet}$	hole	+1

In Fig. 2.1, taken from Seeger[37], the latest results on conductivity measurements performed on non-substituted LWO and Re- (Fig. 2.1a) or Mo- (Fig. 2.1b) substituted lanthanum tungstates are reported as a function of temperature, for three different atmospheres, dry Ar, dry Ar/H_2 and wet Ar/H_2.
For the LW*M*O ceramic systems different temperature regions can be defined, where the contributions of each of the σ_{H^+}, σ_{e^-}, $\sigma_{O^{2-}}$ terms dominates the other two depending on the specimen environment. In the temperature region $T \lesssim 750$ °C, the conductivity of LWO is greater for wet(Ar/H_2) compared to the dry(Ar) and dry(Ar/H_2) atmospheres. In the temperature region $T \gtrsim 750$ °C, the conductivity is comparable for the three different atmospheres being slightly higher in the most reducing condition dry(Ar/H_2). This behaviour is rationalised as following. In the $T \lesssim 750$ °C region, the wet(Ar/H_2) atmosphere is responsible for the oxygen vacancy filling by OH groups ($OH_O^{\bullet}$ in K-V). These $OH_O^{\bullet}$ groups act as positive charges according to Table 2.1, thus in the $T \lesssim 750$ °C the proton conductivity (σ_{H^+}) dominates. In the temperature region $T \gtrsim 750$ °C, the material is mainly dehydrated due to the $OH_O^{\bullet}$ groups leaving the specimen, and the electron/oxygen ion contributions become larger than the proton contribution to conductivity.

* The oxygen ion contribution to conductivity, $\sigma_{O^{2-}}$, can equivalently be described in terms of oxygen vacancy ($v_O^{\bullet\bullet}$ in Kröger-Vink notation, see Table 2.1) contribution to conductivity.

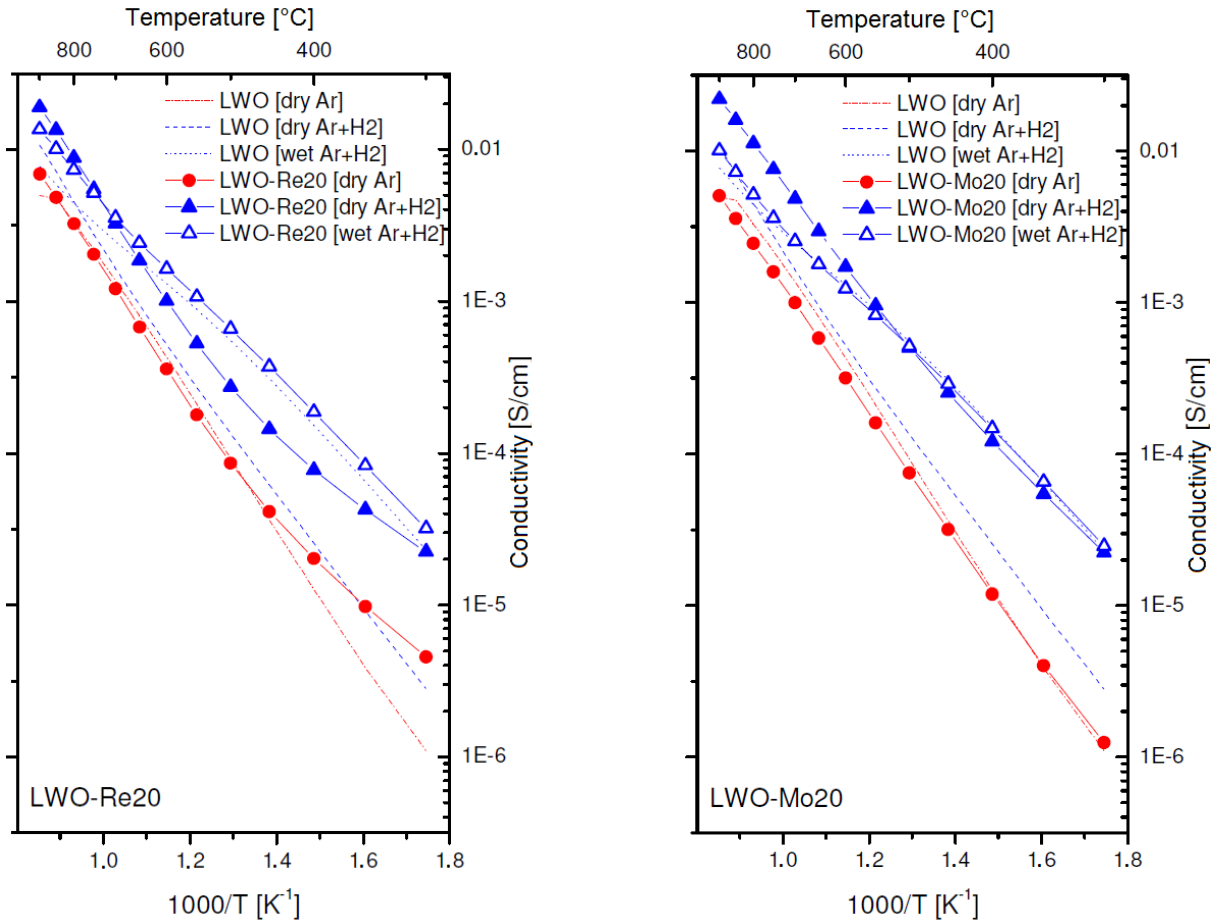

*Fig. 2.1. Conductivity measurements under different atmospheres of the LWO system with Re-substitution **a)** and Mo-substitution **b)**, readjusted from Seeger[37] with permission of the author.*

The effect of Re- and Mo-substitution on conductivity is evident from Fig. 2.1. From both Mo- and Re-substituted specimens the conductivity in the dry(Ar/H_2) atmosphere increases when substitution is performed in the whole temperature range compared to the parent compound due to the increase of the electron/oxygen ion contributions as expected from the higher reducibility of Mo/Re compared to W. Moreover, no substantial change is observed upon substitution on LWO in the T < 600 °C region in wet(Ar/H_2) atmosphere, where the proton conductivity dominates. Overall, according to Fig. 2.1, Mo/Re-substitution on LWO increases the electronic/ionic conductivity without substantially altering the proton conductivity.

2.2 H_2-permeation

The hydrogen flux for a mixed proton-electron-oxygen ion conductor is governed by[41,45]

$$j_{H^+} = \frac{-RT}{2F^2L}\int_I^{II} \sigma_{H^+}[t_{e^-} d\ln p_{H_2} + t_{O^{2-}} d\ln p_{H_2O}], \tag{2.4}$$

where R and F are gas and Faraday constants, T the absolute temperature, L the thickness of the membrane, *I* and *II* the regions separated by the membrane, σ_{H^+} the proton conductivity, t_{e^-} and $t_{O^{2-}}$ the electron and oxygen ion transference number and p_{H_2} and p_{H_2O} the hydrogen and water vapour

partial pressure at either side *I*, *II* of the membrane. The different hydrogen and water vapour partial pressures across the membrane give the driving force for electronic/ionic diffusion.

The hydrogen flux measurements on the Mo/Re-substituted LWO system and the parent compound, together with the configuration used for the measurements, are shown in Fig. 2.2 (data taken from Seeger[37] with permission of the author).

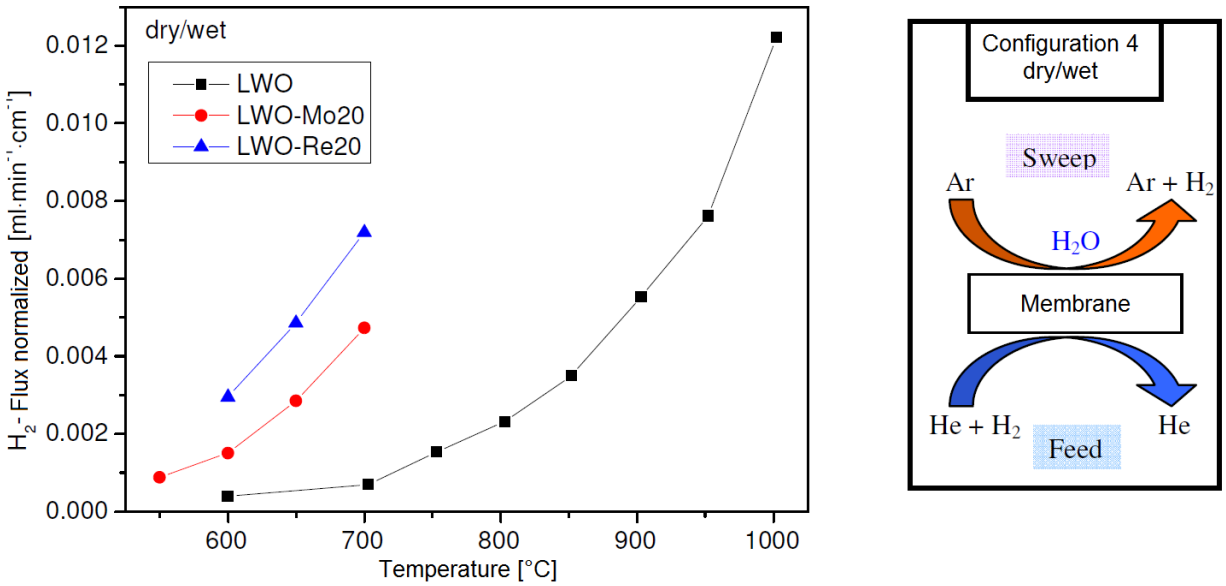

a) ***b)***

Fig. 2.2. ***a)*** *Normalized hydrogen flux measurements as a function of temperature on non-substituted and Mo/Re-substituted LWO, where Mo20 and Re20 denote the nominal amount in mol % of Mo- and Re-substitution on W site, respectively, and* ***b)*** *configuration used in a). Data in a) and b) were readjusted from Seeger[37] with permission of the author.*

The increase of hydrogen permeation with Mo/Re-substituted specimens is evident and agrees with the conductivity measurements reported in Fig. 2.1. The factor limiting the hydrogen flux in LWO is electronic conductivity (see Fig. 2.1), which, according to Eq. (2.4), decreases the overall hydrogen flux across the membrane. The configuration used for either side of the membranes (feed/sweep) also changes the hydrogen flux. Amongst the different possible configurations for the feed/sweep sides (dry/dry, wet/dry, dry/wet and wet/wet), the dry/wet configuration shown in Fig. 2.2b results in the highest observed flux of hydrogen for all compounds. This is the case because H_2 production is given by two different additive mechanisms, the H_2 permeation mechanism and H_2 generation due to the water splitting reaction coupled to oxygen ion diffusion. The H_2 permeation mechanism is governed by ambipolar proton-electron diffusion and the different hydrogen partial pressure between the feed and the sweep side, giving the term $\sigma_{H^+} t_e \, d \ln p_{H_2}$ in Eq. (2.4). Due to the different water vapour partial pressure across the membrane in the dry/wet configuration used (Fig. 2.2b), the oxygen ions produced by water splitting migrate in the opposite direction, i.e. from the sweep to the feed side, resulting in hydrogen formation on the sweep side. Due to electronic transport, hydrogen and oxygen ion transport are decoupled. The two opposite proton and oxygen ion fluxes rise to charge transport in the same direction and are compensated by a flux of electrons being the sum of the two[45]. A more detailed description of the fundamentals of H_2-permeation is given elsewhere[37,41,45].

3 Motivation

Besides the macroscopic material properties mentioned in the previous sections, the crystallographic structure of lanthanum tungstate LWO has frequently been investigated[46-52]. Subtle distortions in the LWO crystal lattice prevented a reliable determination of crystal structure until very recently. The main problem was the discrepancy between the refined and the nominal stoichiometry. Specifically, around 20 mol % of W in the composition of the refined crystal structure was missing[46]. The first attempt to account for the tungsten deficiency was by Magraso *et al.*[46] by placing tungsten onto interstitial positions. Later, a definite formula for the dissolution of tungsten in one of the two lanthanum positions was reported by Scherb[53] and later by Magraso *et al.*[48]. Subsequently, investigations on a local scale by density functional theory (DFT) calculations and pair distribution function (PDF) analysis were presented[51], while studies on the average crystal structure were carried out by means of neutron diffraction on Ca-doped LWO[50]. Those results confirmed that the 20 mol % of non-localized tungsten atoms occupy the lanthanum position, which exhibits a highly distorted environment and hence larger flexibility to substitution of the smaller tungsten atoms. Scherb *et al.*[54] identified the local crystal structure in the $Pa\bar{3}$ space group and quantitatively compared the crystal structure on an average (by diffraction), intermediate (by PDF) and local (by PDF and EXAFS[*]) scale. They suggested a model of local order where the $Pa\bar{3}$ space group describes the data up to about three unit cells (35 Å) very well. Above this value, modelling with an average crystal structure ($Fm\bar{3}m$ space group) yielded better fit residuals.

The aim of this work is to analyse in detail the structure of Mo/Re-substituted LWO. These compounds have been selected because of their high stability in acidic atmospheres and their high values of bulk-H_2 permeation flow (see Fig. 2.2). Mo/Re atoms enhance the overall conductivity due to the increase of electronic charge carriers, which make this compound more suitable for H_2-related technologies (Fig. 2.1 and literature[31,32]). Determination of the structure details of Mo/Re-substituted LWO lanthanum tungstates is carried out mainly by diffraction techniques. X-ray diffraction allows for establishing the position of the heavy cations in the structure, while neutron diffraction permits one to refine confidently the oxygen positions in the lattice and therefore establish the metal-oxygen bond lengths. Moreover, neutron diffraction allows for estimating more accurately the atomic displacement parameters than X-ray diffraction. However, before entering the structural details of Mo/Re-substituted LWO specimens, a thorough study on the parent compound LWO is carried out. The characterisation of the parent compound will cover the first results and discussion part of this work, followed by a chapter on the Re-substituted LWO system (LW(Re)O), one on the Mo-substituted LWO system (LW(Mo)O) and a final chapter where a comparison between the systems investigated is presented.

[*] EXAFS: extended X-ray absorption fine structure

4 Experimental

4.1 Samples

4.1.1 Synthesis

Powders of the sample series $La_{6-x}WO_{12-\delta}$ ($0.4 \leq x \leq 0.8$) were prepared via solid state reaction. In $La_{6-x}WO_{12-\delta}$, x and δ represent the deviations from the stoichiometry of the material family Ln_6WO_{12} (Ln = rare earth) reported in the 1960s and 1970s[55-57]. Although it is possible to produce a large amount of powder with the conventional solid state procedure, its drawback lies in the limited diffusion of the reactants. This is especially the case when samples containing a low concentration of one or more atomic species are produced as for the Mo/Re-substituted (< 3 wt. %) lanthanum tungstate. Therefore, the samples of the series $La_{5.4}W_{1-y}M_yO_{12-\delta}$ (M = Mo, Re; $0 \leq y \leq 0.2$) were prepared through the citrate-complexation route which is based on the Pechini reaction[58]. In $La_{5.4}W_{1-y}M_yO_{12-\delta}$, y represents the substitution of W by M = Mo, Re. The use of the solid state reaction process and the citrate-complexation route for the production of $La_{6-x}WO_{12-\delta}$ ($0.4 \leq x \leq 0.8$) and $La_{5.4}W_{1-y}M_yO_{12-\delta}$ (M = Mo, Re; $0 \leq y \leq 0.2$) is described in detail by Seeger *et al.*[32,37].

Concerning specimen production, the y values of M substitution on W sites have been chosen according to the literature, where a limit of Re solubility in lanthanum tungstate has been reported by Seeger *et al.*[32] and Escolastico *et al.*[31], and was estimated to be around 20 mol % (y = 0.2), corresponding to about 3 wt. %. Above this value, depending on the La/(W+Re) ratio, secondary phases form and a decrease in conductivity as well as a deterioration of mechanical and permeation properties were observed on the parent compound LWO[32,46,59]. Although a phase transition for Mo-substituted lanthanum tungstates from cubic to rhombohedral space group has recently been observed only above a ratio of Mo/(W+Mo) = 0.40, only LW(Mo)O specimens with $y \leq 0.2$ have been synthesized for comparison with the LW(Re)O system and for the use for conductivity/H_2 permeation measurements on similar specimens as reported by project partners (see Fig. 2.1, Fig. 2.2).

The main steps of the conventional solid state reaction and the citrate-complexation route (Pechini procedure) used are shortly recapitulated in the following.

4.1.1.1 Solid state reaction

The solid state reaction (SSR) was used to prepare the $La_{6-x}WO_{12-\delta}$ series ($0.4 \leq x \leq 0.8$). For the $La_{6-x}WO_{12-\delta}$ series ($0.4 \leq x \leq 0.8$) the oxide reactants La_2O_3 (Treibacher, 99.9 %) and WO_3 (Fluka, 99.9 %) were employed. The steps were the following:

1. Calcine La_2O_3 to evaporate the crystal water
    a. 7 K/min → 1000 °C, hold for 2 h
    b. -7 K/min → 200 °C, hold on temperature until weighing
2. Weighing WO_3 (no drying necessary)
3. Put powders with ethanol and milling balls in PET bottle (250 ml for 15 g powder)
    a. 3 mm diameter milling balls in proportion to the powder 5:1 (75 g for 15 g powder)

   b. Fill the PET bottle with ethanol until it is half full
4. Put the bottle for 24 h on a roller bench
5. Sieve milling balls and dry the powder
6. Press pellets and sinter them
   a. 2 K/min → 1500 °C, hold for 12 h
   b. -2 K/min → room temperature
7. Check pellet surfaces with conventional X-ray diffraction and polish ≈ 0.05 mm – 0.1 mm to remove eventual contamination during sintering until no change of the X-ray diffraction pattern is observed
8. Grind the pellets into powders

4.1.1.2 Pechini procedure

The Pechini procedure was employed to prepare the specimen series $La_{5.4}W_{1-y}M_yO_{12-\delta}$, with *M* = Mo, Re and $0 \leq y \leq 0.2$. This procedure is carried out in solution (see below), thus improving the diffusion of the small amounts of Mo/Re (< 3 wt. %) in the specimen compared to the standard solid state reaction. The Pechini procedure allows for the production of a maximum of 15 g powder per glass. Hydrates and nitrates were employed as precursors such as ammonium paratungstate tetrahydrate ($(NH_4)_{10}H_2(W_2O_7)_6$ x $4H_2O$, Sigma Aldrich 99.99 %) and lanthanum trinitrate hexahydrate ($La(NO_3)_3$ x $6H_2O$, Sigma Aldrich, 99.9 %). To provide Mo- and Re-substitution in LWO, ammonium heptamolybdate tetrahydrate ($(NH_4)_6Mo_7O_{24}$ x $4H_2O$, Sigma Aldrich, 99.95 %) and dirhenium heptaoxide dihydrate (Re_2O_7 x $2(H_2O)$, Alfa Aesar, 99.99 %) were employed, respectively. The procedure used was as following:

Steps done with the covered glass

1. Insert the ammonium paratungstate and the W-site doping in the Pechini glass,
   a. Dissolve in a little amount of water
   b. Stir (magnet) for 1 h at 80 °C
2. Add lanthanum trinitrate in the Pechini-glass
   a. Stir until the lanthanum trinitrate is dissolved
3. Add to the solution citric acid
   a. Stir for 1 h at 120 °C
4. Add ammonium hydroxide until the solution is transparent
5. Add ethylene glycol
   a. Stir for 1 h at 120 °C

Steps done after uncovering the glass (exposure to oxygen)

6. Stir at 180 °C until a gel is formed, then remove the magnet
7. Leave the solution on the heating plate at 180 °C overnight or longer until it goes to the furnace
8. Put the glass into the furnace, pre-heated at 180 °C
   a. 1.2 K/min → 600 °C, hold for 2 h
   b. -1.2 K/min → room temperature
9. Press pellets and sinter them
   a. 2 K/min → 1500 °C, hold for 12 h
   b. -2 K/min → room temperature
10. Check pellet surfaces with conventional X-ray diffraction and polish ≈ 0.05 mm – 0.1 mm to remove eventual contamination during sintering until no change of the X-ray diffraction pattern is observed
11. Grind the pellets into powders

4.1.2 Pre-treatment

Dry specimens. The samples were dried in a glass tube which was placed in a movable furnace. After evacuation of the glass tube and purging with argon gas twice, the samples were dried under a continuous stream of argon gas (Ar) or synthetic air (S.A.) in Al_2O_3 holders (50 x 20 x 20 mm^3) at 900 °C for 4 h.

Wet specimens. D_2O humidification (2.5 vol. %) was performed under a continuous flow of argon gas or synthetic air. After the dry samples had been cooled down to room temperature, two bubble bottles filled with D_2O were connected to the argon or synthetic air pipe supplying the atmosphere to the furnace. The furnace was kept at 350 °C for 5 h. Finally, the pre-treated powders were stored in glass holders filled with argon gas prior to the transfer to the experimental stations.

4.1.3 Notations used

In the present work, samples labelled dry(Ar) or dry(S.A.) refer to samples dried under argon or synthetic air atmospheres, respectively, as described in the 'Dry specimens' section. D_2O-humidification performed under a stream of argon gas and synthetic air are referred to as D_2O(Ar) and D_2O(S.A.), respectively, with details reported in the 'Wet specimens' section. 'Ex-situ' and 'In-situ' mean that the specimen treatments under reducing or oxidizing atmospheres were performed prior to or during the experiment, respectively.

The LWO specimen synthesized through the Pechini procedure (in $La_{5.4}W_{1-y}M_yO_{12-\delta}$, y = 0, M = Mo, Re) is labelled as LWO_**P**, while the specimens prepared by SSR are generally referred to as LWO series or specifically as LWO*k*, where *k* denotes the nominal La/W ratio multiplied by ten ($52 \leq k \leq 56$), as currently used in the literature. Since LWO_**P** and LWO*k* specimens yield comparable results, the label LWO is used as a general notation for LaWO and, in the present work, it refers to all the non-substituted LWO specimens investigated (LWO_**P** and LWO*k*), for the sake of simplicity. Mo-substituted LWO systems and Re-substituted LWO systems are denoted as LW(Mo)O and LW(Re)O, respectively, and labelled with Re*y* or Mo*y*, where *y* is the nominal substitution on W in mol %. The general Mo/Re-substitution in LWO is referred to as LW*M*O (*M* = Mo, Re).

4.2 Electron probe micro-analysis

The composition of the specimens was measured by electron probe micro-analysis (EPMA) in a JEOL JXA 8530F field emission microprobe. The oxides La_2O_3, WO_3, ReO_3 and Mo metal were used as reference materials. Samples and reference materials were embedded in epoxy-resin holders (2.5 cm diameter) after which the surface was covered with carbon by evaporation. For each specimen, 15 measurements were performed in different specimen regions and at different grains to enhance the precision of the analysis. The following measurement specifications were used, accelerating voltage: 20 kV; electron current: 50 nA, beam diameter Ø = 2 µm or Ø ≈ 500 nm (spot mode). Elemental maps were taken with 512 x 512 points in a 45 x 45 μm^2 region (step size: 0.0879 µm, time per point: 20 ms) in spot mode, at 20 kV and 50 nA. Images of the specimens were recorded in the back-scattered electron (BSE) mode prior to elemental maps acquisition.

In order to obtain reliable results, the analysed specimens have to exhibit the following features:

i. Grains of at least 5 µm in size

With EPMA, measurements within an area of a few μm^2 can be performed, with the probing depth depending on the accelerating voltage and mean atomic number of the sample. Defocused measurements have been carried out with a beam diameter of 2 µm while the focused measurements performed reach a beam diameter of Ø ≈ 500 nm (spot mode). The lateral resolution, as obtained from

beam simulations, is about ± 1.5 µm perpendicular to the beam direction. If a beam with diameter of Ø = 2 µm is employed, this value added to the estimated lateral resolution results in a 5 µm diameter along the specimen surface. For the 20 kV accelerating voltage used in the present analysis, an electron penetration depth of about 2 µm was calculated. Thus, the grain diameter must be above 5 µm in order to be appropriate for EPMA. If a grain is approximated by a sphere and supposed to be cut in half by polishing, the corresponding grain size below the surface would be 2.5 µm. This proves that a reliable measurement of the composition must be done on grains larger than 5 µm.

Beam penetration simulations were made according to a mean atomic number Z = 62.5, a valid approximation for most of the specimen characterised in this work.

ii. Compact samples

In order to have fewer pores, i.e. the highest density, parts of the sintered pellets were reserved for EPMA.

iii. Dry samples

Carbo-hydrates groups (glue + coating) can be cracked by the electron beam during the measurement giving rise to intense black rings around the point measured where the contamination is higher (see Fig. 4.1). Such contaminations may be also increased by eventual remnants of ethanol in pores, via interaction between ethanol and the electron beam. Therefore, it is preferable to use dry samples.

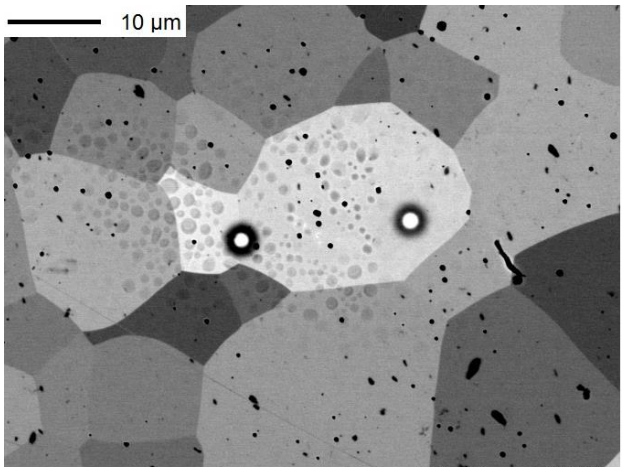

Fig. 4.1. Examples of EPMA test measurements (Ø = 2 µm) on an investigated specimen with some contamination. The build-up of cracked carbo-hydrate groups (dark zones around the measured point) is evident especially in the regions containing pores (presence of alcohol).

iv. Metal oxides as references (when possible)

During spectrometer calibration, the peak positions of the specific X-ray element line could be eventually shifted by the different oxidation states or bonding distances. Hence, it is preferred to use reference compounds similar to the investigated specimens. In the present case, it is preferable to use oxides, as every metal atom in the $La_{6-x}WO_{12-\delta}$ or $La_{5.4}W_{1-y}M_yO_{12-\delta}$ is bonded to an oxygen atom in the first shell. Amongst the reactant oxides employed, La_2O_3 has been the most difficult one to handle. As La_2O_3 is highly hygroscopic, it rapidly changes its volume in humid environments upon water absorption. Therefore, after embedding and polishing dried La_2O_3 pellet pieces without using water, the La_2O_3 reference was carried inside a plastic bottle filled with argon gas to the microprobe facility. The carbon coating and the specimen mounting in the sample holder were performed as fast as possible before the data were collected. Other references were also tried to account for La properly, but the discrepancy with the La values measured using the La_2O_3 reference was usually above 25 %.

4.3 Thermogravimetry

A Netzsch TG209F1 Iris micro-balance equipped with a mass-spectrometer (QMS 403 Aëolos) was used for thermogravimetric measurements (TG) to determine the mass loss of the specimens during heating. Al_2O_3 sample holders were used for the TG measurements. The sample mass varied between 150 mg and 300 mg. Prior to the measurements, the chamber was evacuated twice and then purged with a stream of 50 ml/min argon gas for one hour followed by heating at 10 K/min from room temperature up to 1000 °C. In order to analyse the TG curves in a unique way, definitions for the mass loss Δm, the initial temperature T_i and final temperature T_f are required:

Δm. The initial mass value m_i (wt. %) was established by averaging the mass values in the plateau at low T (30 °C ≤ T ≤ 200 °C in the present case). Similarly, the final mass value m_f (wt. %) was established by averaging the mass values in the plateau at high T (800 °C ≤ T ≤ 1000 °C in the present case). *The mass loss is therefore defined as* $\Delta m = m_i - m_f$ *(wt. %) and the cumulative mass difference is defined as* $\Delta m_i(T) = m_i - m(T)$ *or similarly* $\Delta m_f(T) = m(T) - m_f$ *where m(T) is the mass value (wt. %) at temperature T.*

T_i. T_i is the temperature at which the cumulative-mass change of the TG curve reaches a magnitude that the thermobalance can detect (onset temperature).

T_f. T_f is the temperature at which the cumulative-mass change of the TG curve reaches a maximum.

If σ *is the sensitivity of the thermobalance (*σ *= 0.005 wt. %),* T_i *is the temperature at which* $\Delta m_i(T_i) = 3\sigma = 0.015$ *wt. %.* T_f *is that temperature at which* $\Delta m_f(T_f) = 3\sigma = 0.015$ *wt.%.*

4.4 Diffraction and refinements

4.4.1 Basics of diffraction

The diffraction technique is based on the periodic arrangement of the atoms in a crystal lattice. The diffraction signal is given by the constructive and destructive interference of the plane waves scattered from the parallel planes building the lattice, as presented in Fig. 4.2. The diffraction phenomenon is described by the Bragg's law[60]:

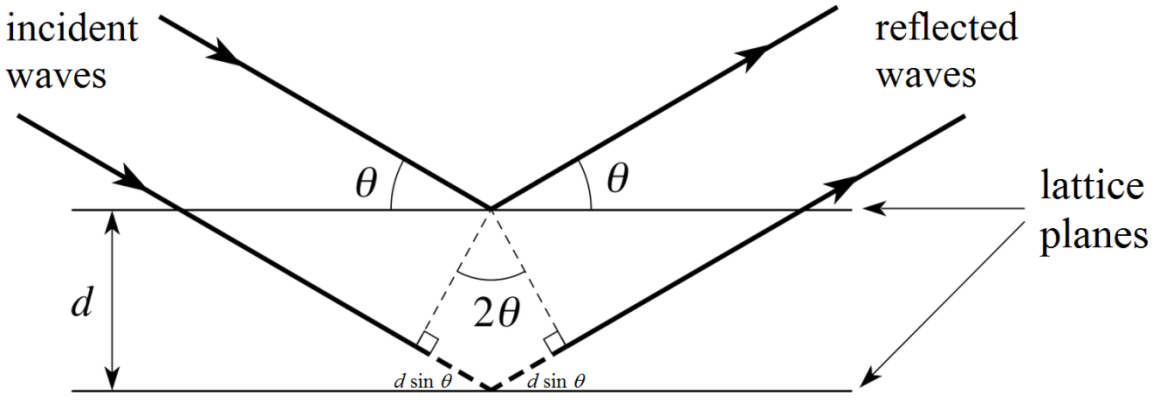

Fig. 4.2. Schematic representation of the interference of neutrons, X-rays or electrons. d is the distance between the parallel lattice planes which diffract the incident plane waves, θ is the Bragg angle and 2dsin θ is the path difference between the incoming and the outgoing plane waves. In order to give constructive interference the path difference should be equal to an integer number n of the wavelength λ (Bragg's law, Eq. (4.1)).

$$n\lambda = 2d \sin\theta \,. \tag{4.1}$$

n is an integer number, λ the wavelength of the incident plane wave, *d* the distance between the *hkl* lattice planes and θ is the Bragg angle. The indices *hkl* define a family of lattice planes, orthogonal to $b_1^*h+b_2^*k+b_3^*l$, where (b_1^*, b_2^*, b_3^*) are the reciprocal lattice basis vectors. *hkl* are also referred to as Miller indices.

Bragg's law expresses the condition for diffraction in real space. Similarly, Bragg's law can be obtained in reciprocal lattice. If $\vec{q}$ is the wave vector transfer between the incident plane wave with initial wave vector $\vec{k}_i$ and the outgoing wave with final wave vector $\vec{k}_f$, given that diffraction is an elastic process ($|\vec{k}_i|=|\vec{k}_f|=2\pi/\lambda$)*, it follows that

$$\vec{q} = \vec{k}_f - \vec{k}_i \rightarrow |\vec{q}| = |\vec{k}_f| \sin\theta + |\vec{k}_i| \sin\theta = \frac{4\pi}{\lambda} \sin\theta\,, \tag{4.2}$$

where θ is the Bragg angle.

Until Eq. (4.2), only the signal coming from the lattice periodicity has been evaluated. However, this signal is modulated by the atomic species present in the structure. The intensity I_{hkl} of the *hkl* reflections is proportional to the square of the corresponding structure factor F_{hkl} ($I_{hkl} \propto |F_{hkl}|^2$), which is defined by

$$F_{hkl} = \sum_j S_j e^{\left[2\pi i(hx_j+ky_j+lz_j)\right]}\,, \tag{4.3}$$

where the sum runs over the atoms $j = 1, \ldots, N$ in the unit cell; x_j, y_j, z_j are the fractional atomic coordinates in the unit cell of the *j*-th atom and *hkl* are the Miller indices. For X-rays, *S* denotes the atomic form factor *f*, while for neutrons, *S* corresponds to the coherent scattering length b_{coh}. X-rays interact mainly with the electrons of the atoms, while neutrons interact mainly with the atomic nuclei. Due to the size of the electron cloud, magnitudes larger than the atomic nuclei, X-ray scattering is predominantly in the forward direction, thus resulting in a scattering angle dependence of the f_j. Scattering angle dependence of f_j is generally expressed as a function of $\sin\theta/\lambda$. From Eq. (4.2), it follows that f_j can be equivalently defined as a function of *q*. This gives the more compact Eq. (4.4):

$$f_j{}^0(q) = 4\pi \int_0^\infty \frac{\rho(r)\sin(qr)r^2}{qr}\,dr, \tag{4.4}$$

where $\rho(r)$ is the electronic charge density at location *r*. The superscript in $f_j{}^0$ indicates that Eq. (4.4) is not the full expression of the atomic form factor, which contains additional contributions in the vicinity of the X-ray absorption edges. These contributions are referred to as anomalous or resonant dispersion effects. Such detailed features will be treated separately in section 4.4.3.3 (Method of the average X-ray scattering power).

Finally, for both neutron and X-ray diffraction there is an additional weakening of the scattering power, caused by the temperature factor $B(T) = 8\pi^2\langle u(T)^2\rangle$ (Debye-Waller factor). $U = \langle u(T)^2\rangle$ is the mean square atomic displacement of an atom from its equilibrium position. The atomic vibrations induced by the temperature give an angle dependence to the form factor, which is expressed as

* The wave vector transfer or scattering vector $\vec{q}$ and the wave vectors $\vec{k}_i$ and $\vec{k}_f$ are related to the momentum transfer and the plane wave initial and final momentum by $\hbar\vec{q}$, $\hbar\vec{k}_i$ and $\hbar\vec{k}_f$, respectively. $\hbar$ is the reduced Planck constant.

$$S_B\left(\frac{\sin\theta}{\lambda}\right) = Se^{-B\left(\frac{\sin\theta}{\lambda}\right)^2}, \tag{4.5}$$

where S_B is the form factor S modified by the temperature factor B.
If Eqs. (4.3) and (4.5) are merged, the equation for the structure factor becomes

$$F_{hkl} = \sum_j N_j S_j e^{[2\pi i(hx_j+ky_j+lz_j)]}\, e^{-B_j\left(\frac{\sin\theta}{\lambda}\right)^2}, \tag{4.6}$$

where N_j is the j-th site occupancy factor divided by the j-th site multiplicity[61].

4.4.2 Instruments for neutron and X-ray diffraction

After preparing the specimens as described in section 4.1.1 and pre-treating them as reported in section 4.1.2, pre-characterisation was carried out by conventional X-Ray diffraction (XRD). XRD was performed in Bragg-Brentano geometry with a Bruker D8 Advance instrument equipped with a LYNXEYE detector and a nickel filter (0.5 µm). The characteristic radiation lines used are CuKα_1 (1.5406 Å) and CuKα_2 (1.5444 Å). Phase identification was carried out with the ICDD PDF2 database in the EVA14 software.
After this, the specimens were pre-treated once more and were carried in sealed bottles to the experimental station where they were stored in gloveboxes under argon gas. The sample holders were filled inside the glovebox to prevent any contamination with oxygen or moisture. For neutron diffraction (ND) experiments and at every experimental station and for any temperature, a can with a diameter of Ø = 6 mm made of vanadium was used due to the low coherent (b_{coh}(V) = -0.44(1) fm) and high incoherent scattering of V. For high resolution X-ray diffraction (HRXRD) experiments, glass capillaries of diameter Ø = 0.2 mm were used when measuring in a cryostat. Glass capillaries of diameter Ø = 0.1 mm were used when measuring with a cryojet and without any sample environment. To reduce absorption effects, specimens filled in Ø = 0.2 mm capillaries were diluted with silicon powder (Si640d NIST) as too much X-ray absorption of the materials can compromise the data quality. The amount of dilution was calculated according to NIST[62] at the X-ray energy used at the experimental station. The details of the experiments performed are reported in Table 4.1.

Table 4.1. Institutes, experimental stations, wavelengths, temperature, specimens and literature for the experimental stations.

Institutes	Instrument	Wavelength (Å)	Temperature (K)	Specimens	Literature
ILL	D2B	1.594	5 – 298	LaW*M*O (*M* = Mo, Re)	([63,64])
PSI-SINQ	HRPT	1.494	1.5 – 295	LaW*M*O (*M* = Mo, Re)	([65,66])
PSI-SLS	MS	0.6231	10 – 295	LaW*M*O (*M* = Mo, Re)	([67-70])
HZB	FIREPOD	1.798	298 - 1173	LWO_**P**, Re20	([71,72])

Some specimens were re-measured at the MS beamline with HRXRD at a later stage (*T* = 295 K, Ø = 0.1 mm). The capillaries were filled at the PSI-SINQ with the same pre-treated powder used to fill the vanadium cans for the neutron diffraction at the HRPT station. The diffraction measurements at the neutron sources and at the synchrotron source were carried out in Debye-Scherrer geometry (transmission mode). As sample environment at D2B a closed-cycle cryo-cooler (*T* = 3.5 K – 320 K), at PSI-SINQ an orange cryostat (*T* = 1.5 K – 300 K) equipped with a sample changer for four specimens, at PSI-SLS a Janis cryostat (*T* = 4.5 K – 300 K), an OXFORD cryojet (*T* = 90 K – 500 K) and at HZB a high

temperature furnace (*T* = 400 K – 1800 K) were used. For further details the reader is referred to the references reported in Table 4.1.

4.4.3 Refinement procedure

The refinements performed on diffraction data aim to model the measured pattern in a way that the algorithm used optimizes the model function to minimize the weighed sum of squared differences between the observed ($y_i(obs)$) and computed ($y_i(calc)$) intensity values, i.e. to minimize the residual S_y[61,73]

$$S_y = \sum_{i=1}^{N} w_i \left(y_i(obs) - y_i(calc)\right)^2 , \tag{4.7}$$

where according to David[74] and Prince[75], the used weight $w_i = 1/\sigma^2[y_i(obs)]$ yields the smallest uncertainties in the fit parameters.. The residual factors (*R*-factors) reported in the discussion part along with the refinement results are defined as following[61,73].

R-expected
$$R_{exp} = \left[\frac{N - P + C}{\sum_{i=1}^{N} w_i y_i^2(obs)}\right]^{1/2} \tag{4.8}$$

R-pattern
$$R_p = \frac{\sum_{i=1}^{N} w_i \left(y_i(obs) - y_i(calc)\right)}{\sum_{i=1}^{N} y_i(obs)} \tag{4.9}$$

R-weighted pattern
$$R_{wp} = \left[\frac{\sum_{i=1}^{N} w_i \left(y_i(obs) - y_i(calc)\right)^2}{\sum_{i=1}^{N} w_i y_i^2(obs)}\right]^{1/2} \tag{4.10}$$

Chi-squared
$$\chi^2 = \left(\frac{R_{wp}}{R_{exp}}\right)^2 = \left[\frac{\sum_{i=1}^{N} w_i \left(y_i(obs) - y_i(calc)\right)^2}{\mathrm{N - P + C}}\right] \tag{4.11}$$

Goodness of fit
$$GOF = \frac{R_{wp}}{R_{exp}} = \chi \tag{4.12}$$

R-structure
$$R_{F^2} = \frac{\sum_{hkl}\left|F_{hkl}^2(obs) - F_{hkl}^2(calc)\right|}{\sum_{hkl}\left|F_{hkl}^2(obs)\right|} \tag{4.13}$$

R-Bragg
$$R_B = \frac{\sum_{hkl}|I_{hkl}(obs) - I_{hkl}(calc)|}{\sum_{hkl}|I_{hkl}(obs)|} \tag{4.14}$$

In the previous equations, *N* is the number of the measured data points, *P* the number of the varied parameters and *C* the number of constraints. $F_{hkl}(obs/calc)$ is the structure factor obtained from the measurement and calculated from the model for the *hkl* planes (defined in Eq. (4.6)) and I_{hkl}(obs/calc) is

the Bragg intensity obtained from the measurement and calculated from the model for the *hkl* planes. I_{hkl} is proportional to the square of the absolute value of the structure factor, $|F_{hkl}|^2$. GSAS[76,77], FULLPROF[78] and TOPAS[79] software were employed to refine the diffraction data. GSAS and TOPAS were used for full pattern refinements, while FULLPROF was employed for single-peak fitting. In order to evaluate how much the crystallographic model matches the measured diffraction patterns, GSAS gives the *R*-structure (R_F^2) while TOPAS and FULLPROF the R-Bragg (R_B) values. These values and the R_{exp}, R_{wp} and χ^2 values are reported in the refinement result tables throughout this work.

The three main algorithms or refinement procedures used in the community, named according to their authors, are the Rietveld[80], Pawley[81] or LeBail[82] refinements.

The Pawley or LeBail fits optimize the calculated intensities without the constraint of a structural model[81,82]. Rietveld includes in his algorithm an estimation of structure factor according to the ratio of the contributing reflections to the same diffraction peak[61,80], in dependence of the atomic form factor. In the following, the refinement sequences for the algorithms used, namely LeBail and Rietveld, are presented.

4.4.3.1 LeBail and Rietveld refinements

LeBail refinements

The LeBail refinement algorithm was first introduced by Le Bail *et al.*[82,83] using a modified Rietveld analysis working without structural model. This is the main advantage of the LeBail algorithm, thus allowing for getting information on the possible space groups, the lattice and profile parameters without knowing the structure details. LeBail refinement was carried out in the following way for neutron diffraction and laboratory X-ray diffraction:

1. Depending on the program used, the background was firstly interpolated manually (GSAS) or automatically (FULLPROF, TOPAS) and then kept fixed.
2. The cell parameter was then refined along with
    a. the zero correction (Debye-Scherrer geometry)
    b. the displacement parameter (Bragg-Brentano geometry).
3. The cell parameter and the zero correction / displacement parameter were fixed and the profile parameters were refined one by one until convergence with the general assumptions:
    a. For neutron diffraction, which gives mainly Gaussian profile peak shapes, the profile parameter responsible of the Lorentzian size broadening is kept zero.
    b. For laboratory X-ray diffraction, which gives mainly Lorentzian peak shapes, the Gaussian profile parameters not accounting for the slit size contribution were kept zero whenever possible.
4. All the profile parameters were refined together.
5. Finally, all the parameters were refined together.

LeBail refinements performed on patterns collected at the high-resolution X-ray diffraction beamline MS at SLS need a more extensive discussion, since the capillary position calibration on a reference sample has to be carried out before step 1 of the sequence reported above by means of an ‘ad hoc’ macro to be implemented in the refinement program. Such a macro can only be implemented in the software TOPAS. An example of the calibration procedure is described by Gozzo *et al.*[69]. For the specimens re-measured with HRXRD at T = 295 K at a later stage, the alignment of the capillary position (Ø = 0.1 mm) was not optimal and the calibration of the capillary position to the reference did not succeed, causing a slight shift of the refined cell parameter to higher values compared to ND and XRD data without, however, influencing the structural results. The refined results of these specimens can be found

throughout this work in Table 5.2 (LWO_**P**-dry(Ar)/D_2O(S.A.)), Table 5.8 (Re20-dry(Ar)), and Table 5.13 (Mo20(2)-dry(Ar)).

Rietveld refinements

The Rietveld refinement algorithm was developed in the 1960s[80,84]. Refinements performed with the Rietveld algorithm include in the calculations of the structure factor structural parameters such as atomic positions, site occupation factors (*SOF*s) and thermal vibrations. The refinement procedure can present systematic errors caused by the way the refinement is carried out or by the sequence of steps used to achieve convergence. Guidelines have been proposed on how to perform a Rietveld refinement and systematic errors in the refinement procedure are reported. The reader is referred to McCusker *et al.*[85] (general guidelines and references therein), Hill[86], Hill and Cranswick[87] (IUCR* surveys on $PbSO_4$ and ZrO_2). In the present work, reliable Rietveld refinements could not be carried out on laboratory X-ray data, possibly due to the $CuK\alpha_1/CuK\alpha_2$ doublet and the intermediate resolution. The steps used for a Rietveld refinement on neutron and synchrotron data are reported in the following

1. The values of the LeBail refinement were taken as a starting point (lattice parameter, zero correction, profile parameter, background)
2. Structural information such as space group, atomic positions, *SOF*s and isotropic displacement parameters were inserted into the refinement program used, uploading a CIF file from the database when available[88] and/or manually adding atoms.
3. An absorption correction was included in GSAS and TOPAS refinements and calculated according to the respective manuals for neutrons[89] and X-rays[62].
4. The scale factor was refined with all other parameters fixed.
5. The isotropic displacement parameters (IDPs), U_{iso}, were refined one by one, together with the scale factor. Constraints were applied to the U_{iso} to be the same for the same Wyckoff site. Then the U_{iso} were kept fixed.
6. The fractional atomic coordinates *x*, *y*, *z* of each Wyckoff site were refined independently, together with the lattice parameter and the zero correction. The lattice parameter and the zero correction were then fixed.
7. The fractional atomic coordinates *x*, *y*, *z* together with the U_{iso} of the same Wyckoff site were refined together until convergence was achieved. Then, the fractional atomic coordinates *x*, *y*, *z* and the U_{iso} of all the Wyckoff sites were refined together until convergence was achieved, after which they were kept fixed.
8. The *SOF* for each Wyckoff site was refined until convergence except for the case where three atoms occupy one Wyckoff site. In this case the *SOF*s of these three atoms were kept fixed according to the specimen composition established with EPMA (details in the discussion part).
9. The fractional atomic coordinates *x*, *y*, *z* and the *SOF*s of the same Wyckoff site were refined together until convergence. Then, the fractional atomic coordinates *x*, *y*, *z* and the *SOF*s of the all Wyckoff sites (except the site shared by three atoms) were refined together.
10. In a cyclic fashion, the *SOF*s were fixed and step 7 was repeated. Then, the U_{iso} were fixed and step 9 was repeated until convergence.
11. At this stage, refining the anisotropic displacement parameters (ADPs), U_{aniso}, was attempted, repeating step 7, 8, 9 and 10 with U_{aniso} instead of U_{iso}

Whenever it was not possible to perform refinements with ADPs, the following steps were performed with IDPs:

* IUCR: International Union of Crystallography.

12. Refinements of the Wyckoff position shared by three atoms was attempted, fixing the largest *SOF* and refining the other two *SOF*s repeating step 8, 9 and 10.
13. Fractional atomic coordinates *x*, *y*, *z*, displacement parameters and *SOF*s were tried to be refined together.

Due to the high correlation between the displacement parameters and the *SOF*s, step 13 could not be performed in many cases on substituted specimens, especially in dry(Ar) conditions, measured through neutron diffraction (see discussion). In this case, the final refinements values correspond to step 12, if a different procedure is not explicitly mentioned.

4.4.3.2 Method of the average neutron scattering length

The average scattering length method is described by Furrer *et al.*[90]. The neutrons scatter with the atomic nuclei proportionally to the coherent scattering length of the element ($S = b_{coh}$ in Eq. (4.6)). If more than one element occupies the same Wyckoff site *A*, the effective scattering length of that Wyckoff site *A* will be the weighted average of the coherent scattering length of all the elements occupying that particular site *A*. The weights are the *SOF*s.

If the elements *i* (*i* = 1,…, *N*) have a coherent scattering length b_i and a site occupancy factor SOF_i, the average scattering length of the Wyckoff site *A*, $\bar{b}_A^{exp}$, is defined as following:

$$\bar{b}_A^{exp} = \sum_{i=1}^{N} b_A^i \times SOF_A^i , \tag{4.15}$$

where it is assumed that no vacancies are present in *A*, so that $\sum_{i=1}^{N} SOF_A^i = 1$. However, assuming that the coherent scattering length of a vacant site is zero, this reasoning can be extended to vacancies (see literature[91]). In Table 4.2 the atomic species investigated in the present work are listed with the corresponding atomic numbers, atomic mass units, neutron coherent scattering length and cross sections.

Table 4.2. Atomic number Z, atomic mass unit (a.m.u.), coherent scattering length (b_{coh}) and coherent (σ_{coh}), incoherent (σ_{inc}) and absorption (σ_{abs}) cross section of the investigated elements in the present work[92].

Atom	Z	a.m.u.	b_{coh} (fm)	σ_{coh} (barn)	σ_{inc} (barn)	σ_{abs} (barn)
H	1	1.01	-3.741(2)	1.757(1)	80.26(6)	0.3326(7)
D	1	2.01	6.674(6)	5.592(7)	2.05(3)	0.00052(1)
O	8	16	5.805(4)	4.232(6)	0.000(8)	0.00019(2)
Mo	42	95.94	6.72(2)	5.67(3)	0.04(5)	2.48(4)
La	57	138.91	8.24(4)	8.53(8)	1.1(2)	8.97(2)
W	74	183.84	4.76(2)	2.97(2)	1.63(6)	18.3(2)
Re	75	186.21	9.2(2)	10.6(5)	0.9(6)	90(1)

4.4.3.3 Method of the average X-ray scattering power

The general expression for the atomic form factor at any energy *E* and for any exchanged momentum *q* is

$$f(q,E) = f^0(q) + f'(\mathrm{E}) + \mathrm{i}f''(\mathrm{E}) , \tag{4.16}$$

where $f^0(q)$ is given by Eq. (4.4) and $f'(E)$ and $f''(E)$ are the anomalous contributions to the atomic form factor $f(q,E)$. Eq. (4.16) can then be rewritten as[93]

$$f(q,E) = Re(f) + iIm(f)\,, \tag{4.17}$$

where $Re(f)$ is

$$Re(f(q,E)) = f^0(q) + f'(E) + f_{NT}\,. \tag{4.18}$$

$f^0(q)$ is the "normal" coherent scattering factor (Eq. (4.4)), f' is an anomalous scattering factor (depending on the X-ray energy E) and f_{NT} is a small nuclear Thomson term.
$f'(E)$ can also be expressed in terms of a small relativistic correction term f_{rel}, the atomic number Z and the function $f_1(E)$ often used to characterise these form factors:

$$f'(E) = f_1(E) + f_{rel} - Z. \tag{4.19}$$

When the approximation of forward scattering is made ($q \rightarrow 0$), $f^0(q \rightarrow 0)$ reduces to the number of electrons Z *(Eq.* (4.4)*)*. Therefore, from Eqs. (4.18) and (4.19),

$$Re(f(E)) = f_1(E) + f_{rel} + f_{NT}\,. \tag{4.20}$$

The imaginary part $Im(f)$ of the $f(q,E)$ expressed in Eq. (4.17) is related to the photoelectron absorption process with cross section σ_{PE}, becoming important at the absorption edges, and described by

$$Im(f) = f''(E) = f_2(E) = \frac{E\sigma_{PE}(E)}{2hcr_e}\,, \tag{4.21}$$

where h is the Planck constant, c the speed of light in vacuum, and r_e the Bohr electron radius.
Finally, as $f_1(E)$, $f_2(E)$, f_{rel} and f_{NT} are tabulated by Chantler[93], it is possible to use the $Re(f)$ as theoretical electron numbers for the atoms investigated as a starting point for the average X-ray scattering procedure. $f_1(E)$, $f_2(E)$, f_{rel} and f_{NT} are resumed for the samples of interests in the following table.

Table 4.3. Atoms, atomic numbers, $f_1(E)$, $f_2(E)$, f_{rel} and f_{NT} for the X-ray energy E = 19.9 keV (energy at which all patterns were collected), and effective Re(f(E)) after the corrections. The error associated to Re(f(E)) lies between 0.1 % (energy region far from any absorption edge) and 5 % (at the edge)[93,94]. Following the guidelines reported in the NIST documentation[94], an error of 1 % has been assumed for all the atoms.

Atom	Z	a.m.u.	f_1(19.9keV) e^-/atom	f_2(19.9keV) e^-/atom	$f_{rel}+f_{NT}$ e^-/atom	Re(f(19.9 keV)) e^-/atom
H	1	1.01	1	1.14E-7	-6.49E-4	1.00(1)
D	1	2.01	1	1.14E-7	-6.49E-4	1.00(1)
O	8	16	8.01	0.0044	-0.0064	8.00(8)
Mo	42	95.94	37.60	0.53	-0.225	37.4(4)
La	57	138.91	56.99	1.87	-0.465	56.5(5)
W	74	183.84	74.14	5.40	-0.876	73.3(7)
Re	75	186.21	75.07	5.68	-0.906	74.2(7)

In order to establish the effective scattering power of a Wyckoff site A, a similar way as described for neutrons can be applied to X-rays. It must be stated that this procedure is an approximation, described

as follows. In first approximation, *Im(f)* is neglected as the contribution of the *Im(f)* to the scattered intensities is negligible for all the atoms (see Table 4.3 and consider that $|f(q,E)| = \sqrt{Re(f)^2 + Im(f)^2}$. Hence, *f(q,E)* can be approximated with *Re(f)*. From Eq. (4.18) and Eq. (4.19), it follows that

$$\overline{Re(f)}_A = \sum_{i=1}^{N} \left[f_i^0(q)_A \times {SOF^i}_A + f_1(E)_i - Z_i + (f_{rel} + f_{NT})_i \right], \tag{4.22}$$

where $f_i^0(q)_A$ and ${SOF^i}_A$ are the parametrized atomic factor in the refinement programs and the site occupancy factor of the *i*-th atom of Wyckoff site *A,* respectively, obtained from X-ray refinements.
The software TOPAS uses the parametrization of the non-dispersive part of the atomic scattering factor ($f^0(q)$ in Eq. (4.16), (4.18)), as (see Prince and IUCR[95]) for the atomic form factor of an atom *j*

$$f_j{}^0\left(\frac{\sin\theta}{\lambda}\right) = \sum_{i=1}^{4} a_i \cdot e^{-b_i(\frac{\sin\theta}{\lambda})^2} + c\,, \tag{4.23}$$

where a_i, b_i and c are the 9 coefficients for the analytical approximation of the calculated atomic scattering curves[95]. The $f_j{}^0(\frac{\sin\theta}{\lambda} \to 0) \times {SOF^i}_A$ value is corrected according to Eq. (4.22) in order to consistently compare the theoretical and experimental values of *Re(f)*. The refinements were carried out using the parametrization of Eq. (4.23) for ions, as in the present work ionic compounds are investigated. This was possible only for the 'chemically significant ions', according to the literature[95], namely W (W^{6+}), La (La^{3+}), Mo (Mo^{6+}) and O (O^{2-}), but not for Re, whose oxidation states are not included in the tabulations after Chantler[93]. Re atoms, supposed to be also in the +6 oxidation state (Re^{6+}), were then approximated by W^{6+}, as W and Re are indistinguishable for X-rays. According to the experimental values for *Re(f)* (Eqs. (4.22) and (4.23) for ions) the theoretical values for *Re(f)* shown in Table 4.3 are modified including the presumed oxidation states.

4.4.3.4 Calculation of averages (statistics)

The averages were calculated weighing the values proportionally to the inverse of the associated error; if a refined value x_i had an associated uncertainty σ_i ($x_i \pm \sigma_i$), the average weighted value $\bar{x}_w$ and its error σ_w were calculated as follows

$$\bar{x}_w = \frac{\sum_{i=1}^{N} x_i/{\sigma_i}^2}{\sum_{i=1}^{N} 1/{\sigma_i}^2}, \tag{4.24}$$

$$\sigma_w = \sqrt{\frac{1}{\sum_{i=1}^{N} 1/{\sigma_i}^2}}, \tag{4.25}$$

where the index *i* runs between 1 and the number of values *N*. This calculation has been employed for instance in the average scattering length procedure described previously. In this case, x_i represents the refined average scattering length of a Wyckoff site of one single pattern, while $\bar{x}_w$ represents the average scattering length of that Wyckoff site averaged for all the *N* patterns available.

4.4.4 Fourier analysis

In Macchi *et al.*[96], the electron charge density in real space is defined by Fourier summation over all Bragg structure factors F_{hkl} measured in X-ray diffraction experiments:

$$\langle \rho(r) \rangle = \frac{1}{V} \sum_{hkl} F_{hkl} e^{\left[-2\pi i(hx_j + ky_j + lz_j)\right]} \ , \tag{4.26}$$

where the <> denotes the thermally averaged electron density [96], which is neglected in the following discussion. Eq. (4.26) is the Fourier transformation in q of Eq. (4.6) and can be extended to atomic nuclear densities, obtainable from neutron diffraction data. The first term of the sum operator in Eq. (4.26), F_{000}, calculated for hkl = 000, corresponds to the total sum of the electrons or the sum of the atomic scattering lengths in the unit cell for X-rays and neutrons, respectively. The densities $\rho(r)$ of Eq. (4.26) can be obtained from the observed ($\rho_{obs}(r)$) and calculated ($\rho_{calc}(r)$) structure factors and from their difference ($\rho_{diff}(r) = \rho_{obs}(r) - \rho_{calc}(r)$). $\rho_{diff}(r)$ is referred to as difference Fourier map and may give information on the atom positions in the unit cell not yet identified. However, as the structure factors F_{hkl} are inferred from the pattern intensities ($I_{hkl} \propto |F_{hkl}|^2$), the phase information is lost. This is commonly addressed to as phase problem and goes beyond the purpose of this work (see Taylor[97] and references therein for details).

5 Results and discussion

5.1 $La_{6-x}WO_{12-\delta}$ ($0.4 \leq x \leq 0.8$)

5.1.1 Composition studies

In this chapter, the specimen series $La_{6-x}WO_{12-\delta}$ ($0.4 \leq x \leq 0.8$) synthesized with the solid state reaction (SSR) procedure will be discussed. In addition, another LWO sample, synthesized with the Pechini procedure[58] with a nominal composition of $La_{5.4}WO_{12-\delta}$ (La/W = 5.4) is taken into consideration. For the specimen abbreviations used in the following, refer to Table 5.1 and section 4.1.3. Both SSR and Pechini preparation methods applied to LWO specimens are described in more detail by Seeger[37] and Seeger et al.[32], and are referred to in the experimental part. The final sintering temperature used for the samples prepared by SSR or Pechini method was the same (T = 1500 °C). As a first step of the analysis, the sample composition is determined. Strict correlations exist between composition, hydration properties (concentration of oxygen vacancies) and crystal structure (lattice parameter, atomic site occupancy factors). These properties have been investigated in all the above-mentioned specimens and the obtained results are presented in this chapter. In the first part of this chapter, LWO_**P** has been compared with the LWO series, as the former has been extensively investigated by means of different diffraction methods (neutron/X-rays) and under different conditions (dry, humidified, temperature-dependent studies), presented together at a later stage.

Table 5.1. Nominal composition, synthesis route and final sintering temperature for the specimen series $La_{6-x}WO_{12-\delta}$ ($0.4 \leq x \leq 0.8$) and for the reference sample $La_{5.4}WO_{12-\delta}$. Possible secondary phases, sample labelling used throughout this work, lattice parameters of samples in the dry(Ar) state and La/W ratio scaled to the reference ratio (in red) are also depicted.

Nominal composition Synthesis route Sintering temperature	***La/W nominal***	***Secondary phases***	***Label***	***Lattice parameter – dry(Ar) – (Å)***	***La/W measured, La/W scaled to the reference (XRD + EPMA)***
$La_{5.4}WO_{12-\delta}$ reference Pechini 1500°C	5.4	No	LWO_**P**	11.1733(1)	5.56(3)
$La_{6-x}WO_{12-\delta}$ Solid state reaction 1500°C	5.2 – 5.6		LWO series		5.4 – 5.8
$La_{5.2}WO_{12-\delta}$	5.2	$La_6W_2O_{15}$	LWO52	11.1687(1)	5.36(4)
$La_{5.3}WO_{12-\delta}$	5.3	No	LWO53	11.1713(1)	5.48(4)
$La_{5.4}WO_{12-\delta}$	5.4	No	LWO54	11.1740(1)	5.59(3)
$La_{5.45}WO_{12-\delta}$	5.45	No	LWO545	11.1747(1)	5.62(3)
$La_{5.5}WO_{12-\delta}$	5.5	No	LWO55	11.1763(1)	5.69(4)
$La_{5.6}WO_{12-\delta}$	5.6	La_2O_3	LWO56	11.1780(1)	5.76(4)

EPMA of LWO_**P** yielded a composition of $La_{5.56(3)}WO_{12-\delta}$ (La/W = 5.56(3)), which is clearly different from the nominal value of $La_{5.4}WO_{12-\delta}$ (La/W = 5.4). This shift towards higher values of La/W ratio might be

due to evaporation of W during sample synthesis or due to segregation/contamination of W rich phases at the surface of the specimen pellet which has been completely removed by polishing. A detailed insight is, therefore, required to quantify possible composition shifts of the LWO specimens.

The basic relation employed to estimate the composition of the LWO specimens relies on the atomic radius of the elements constituting the specimens. La and W have ionic radii (e.g. in 6-fold coordination and +6 oxidation state) of $R_i(La)_{3+}^{6fold}$ = 1.03 Å and $R_i(W)_{6+}^{6fold}$ = 0.60 Å, respectively[98]. One might expect that with increasing lanthanum content, i.e., with increasing La/W ratio, the lattice parameter increases. For site substituted binary alloys, Vegard[99] predicted a linear relation between the amount of substitution and the lattice parameter of the alloy. Making the following assumptions, Vegard's law can be applied to ceramic materials like LWO and used to estimate the composition of the LWO series:

i. In the La/W range considered (5.2 ≤ La/W ≤ 5.6) it can be inferred from structural studies[48,50,52,53] that LWO can be considered as a binary system: substitution of W occurs only at one particular La position, while all the other cations Wyckoff sites are completely occupied.
ii. W substitution on one La Wyckoff site is low and estimated to be in the ratio 1:24 (about 4% or one atom per unit cell). When the amount of such substitution is low enough[100], it is possible to neglect higher-order deviations of Vegard's law[101-105] from the expected linear behaviour of the lattice parameter with increasing substitution.

Other examples of applied Vegard's law to ceramic systems can be found elsewhere[106,107].

Nevertheless, this simplistic approach does not consider the amount of oxygen vacancies[108,109] varying with the La/W ratio and the presence of secondary phases[32,46,59]. Both of these features could lead to a deviation from the linear increase of the lattice parameter with increasing La/W ratio while the secondary phases modify the overall sample composition. However, in order to obtain a rough estimation of the composition of the LWO series, such effects may be neglected. Therefore, Vegard's law can be applied as shown in Eq. (5.1) (see below) and the corresponding results are summarized in the last column of Table 5.1.

Discussion: the linear fit of the lattice parameters of the LWO series listed in Table 5.1 as a function of the nominal La/W ratio follows a linear trend with R^2 = 0.993, thus complying with Vegard's law and the above-mentioned assumptions. Moreover, the satisfactory residual of R^2 = 0.993 suggests that the variation of the actual from the nominal La/W ratio might be assumed independent of La/W, i.e., the same for all the LWO*k* specimens. It is clear from the measured EPMA value of LWO_**P** (depicted in red colour in Table 5.1) and the corresponding lattice parameter that the actual compositions of the LWO*k* specimens are shifted to larger La/W ratios. In the last column of Table 5.1, the LWO*k* ratio scaled to the LWO_**P** reference sample is listed, where the following formula is used:

$$\frac{La^{scaled}}{W}_{LWOk} = \frac{La^{EPMA}}{W}_{LWO\_\boldsymbol{P}} + \frac{a_{LWOk} - a_{LWO\_\boldsymbol{P}}}{m}, \tag{5.1}$$

where $\frac{La^{scaled}}{W}_{LWOk}$ is the value reported in the last column of Table 5.1 for LWO*k* (52 ≤ *k* ≤ 56), $\frac{La^{EPMA}}{W}_{LWO\_\boldsymbol{P}}$ = 5.56(3), *a* is the refined lattice parameter of the LWO*k*-dry(Ar) specimen (a_{LWOk}) and of the LWO_**P** specimen ($a_{LWO\_\boldsymbol{P}}$ = 11.1733(1) Å). *m* = 0.0235(1) is the slope of the linear regression performed on the data set of lattice parameters of the LWO*k* specimens as a function of their nominal La/W ratio.

5.1.2 Phase analysis

The XRD patterns of the LWO-dry(Ar) specimens are shown in Fig. 5.1 as a function of the scattering angle *2Θ* (10° ≤ *2Θ* ≤ 138°). Magnifications of the low (10° ≤ *2Θ* ≤ 35°) and high (108.5° ≤ 2*Θ* ≤ 110.5°)

scattering angles are presented in Fig. 5.2a and Fig. 5.2b, respectively, with peak indexing according to a $Fm\bar{3}m$ space group (s.g.). From the peak indexing of Fig. 5.1 and Fig. 5.2 it can be recalled that

i. The indexed reflections allow Miller indices *hkl* to become all odd or all even (Fig. 5.1, Fig. 5.2)

ii. The low intensity reflections (e.g. for $2\Theta \leq 27°$, *hkl* = 111, 200, 220, 311, see Fig. 5.1, Fig. 5.2a) have been indexed according to the existence of a superstructure located at *q* = ½, ½, ½ of the substructure reciprocal lattice vectors. The substructure is a simple fluorite cell ($Fm\bar{3}m$ space group)

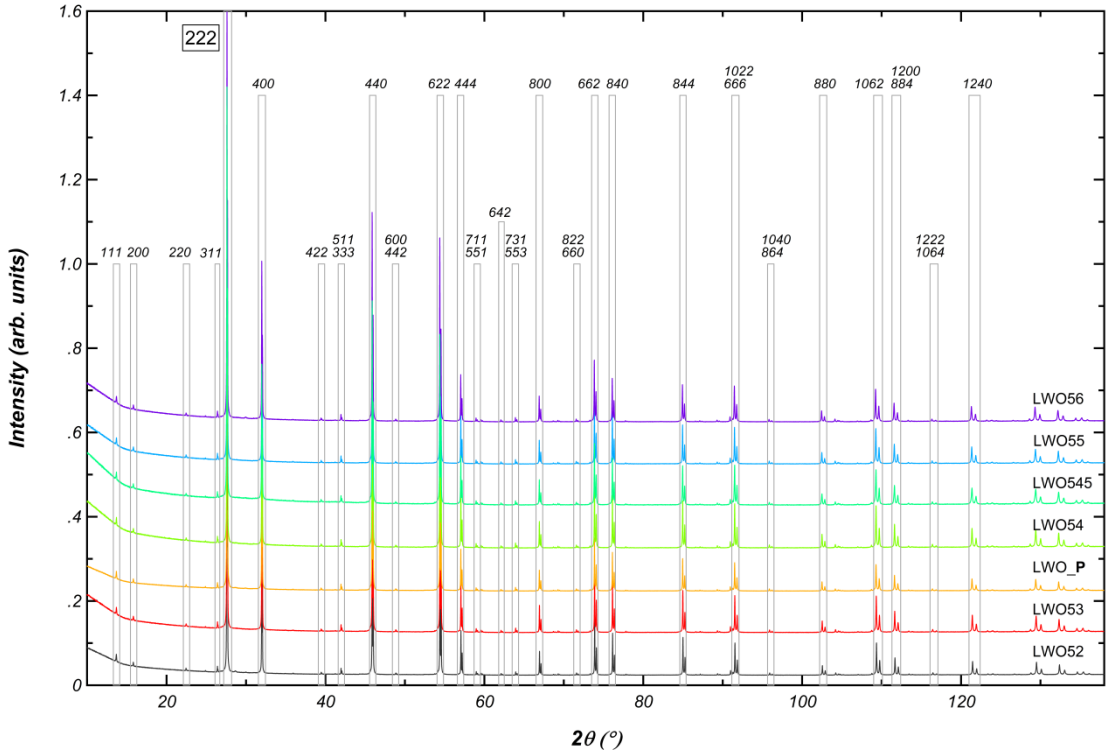

Fig. 5.1. XRD patterns of the LWO-dry(Ar) specimens as a function of the scattering angle 2Θ (10° ≤ 2Θ ≤ 138°). The patterns are presented from the lowest nominal La/W ratio (x = 0.8, in black colour) to the highest nominal La/W ratio (x = 0.4, in purple colour) from bottom to top, respectively. The hkl indices of the main reflections below 2Θ = 130° are also shown ($Fm\bar{3}m$ space group). The patterns are normalized to the peak of highest intensity (hkl = 222 reflection). Peak splitting is due to the CuKα$_1$/Kα$_2$ doublet.

Point i. justifies using the face-centred (*fcc*) unit cell due to the reflection conditions the *fcc* unit cell requires (*h*+*k*, *h*+*l*, *k*+*l* all even). Point ii. justifies the doubled lattice parameters to account for the broken symmetry: the superstructure is commensurate as all the low-intensity reflections are located at simple fractions (half) of the substructure reciprocal lattice vectors. Hence, the $Fm\bar{3}m$ space group with doubled lattice parameter as currently used for LWO in the literature is rationalised. Furthermore, from LeBail refinements it is obtained that

iii. The peaks at $2\Theta \approx 28.7°$ and $2\Theta \approx 30°$ (Fig. 5.2a, within black rectangles) are the reflections of highest intensity of the secondary phase $La_6W_2O_{15}$ (Crystallographic Information File -CIF- taken from Chambrier *et al.*[110]), indexed as the *hkl* = 221 and the *hkl* = 002 lattice planes, respectively.

iv. The peak at $2\Theta \approx 30°$ (Fig. 5.2a, within the purple rectangle) is the reflection of highest intensity (*hkl* = 101 and *hkl* = 011 lattice planes) of the secondary phase La_2O_3 (CIF taken from Schiller[111]). The two sets of *hkl* indices follow hexagonal symmetry.

v. The diffraction peak seen in all patterns at $2\Theta \approx 25°$ (Fig. 5.2a) is given by CuKβ radiation, largely but not entirely attenuated by the Ni filter employed. This peak corresponds to the *hkl* = 222 reflection.

Each diffractogram has been measured for 14 h in total in order to obtain a good signal-to-noise ratio, from which it can be inferred that the amount of secondary phases, indexed in points iii. and iv., is negligible. Single peak fitting and pattern simulations give an upper limit of 1 wt. % of $La_6W_2O_{15}$ for LWO52 and 1 wt. % of La_2O_3 for LWO56, respectively. Taking into account these contributions, the overall La/W ratio of LWO52 decreases from 5.36(4) (Table 5.1) to 5.34(4), while the overall La/W ratio of specimen LWO56 increases from 5.76(4) (Table 5.1) to 5.78(4).

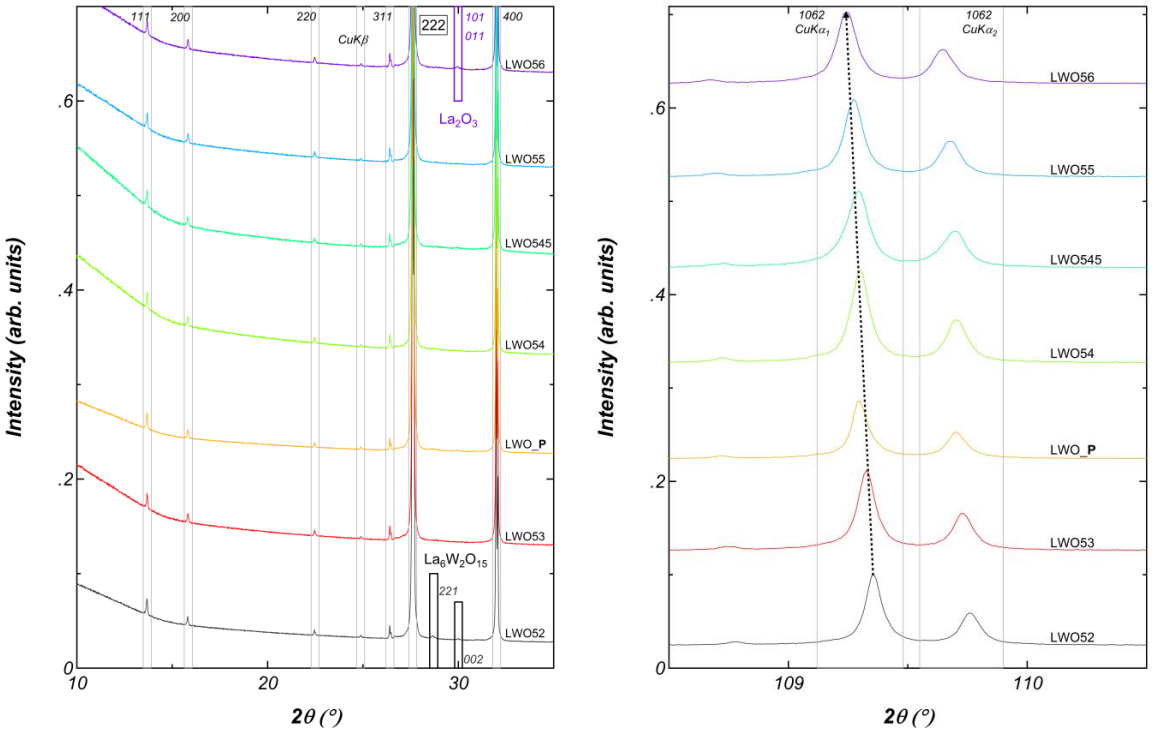

a) **b)**

Fig. 5.2. XRD patterns of the LWO-dry(Ar) specimens as a function of the scattering angle 2Θ. The patterns are presented from the lowest nominal La/W ratio (x = 0.8, in black colour) to the highest nominal La/W ratio (x = 0.4, in purple colour) from bottom to top, respectively. The hkl indices of the main reflections are also shown ($Fm\bar{3}m$ space group). The patterns are normalized to the peak of highest intensity at hkl = 222. Peak splitting is due to the CuKα$_1$/Kα$_2$ doublet. ***a)*** *Magnification of the XRD patterns in the low 2Θ region (10° ≤ 2Θ ≤ 35°). Amongst all the Bragg reflections, the superstructure reflections with all odd or all even hkl planes (hkl = 111, 200, 220 and 311) of the fluorite cell are indicated. Contributions of secondary phases $La_6W_2O_{15}$ and La_2O_3 are also labelled, with indexed peaks included in black and purple rectangles, respectively.* ***b)*** *Magnification of the XRD patterns in the high 2Θ region (108.5° ≤ 2Θ ≤ 110.5°). The Bragg reflection shown corresponds to the Miller indices hkl = 10, 6, 2, according to the $Fm\bar{3}m$ space group used. The dashed arrow is a guide to the eye indicating the increase of lattice parameter with increasing La/W ratio. The resolved peak splitting of the CuKα$_1$/Kα$_2$ doublet is also labelled.*

Discussion: the existence of secondary phases in LWO specimens occurring as La_2O_3 and $La_6W_2O_{15}$ was already reported in the literature[32,46,59]. For instance, Magraso *et al.*[46] and Seeger *et al.*[32] showed how secondary phases depend on the sintering temperature while the thermo-mechanical properties of $La_6W_2O_{15}$ and their influence on the main phase of LWO were investigated by Ivanova *et al.*[59]. The results of this work confirm the presence of three different regions, as shown in Fig. 5.2a. Amongst the LWO specimens investigated, the one with the lowest La/W ratio, LWO52, reveals a $La_6W_2O_{15}$ impurity of less than 1 wt. %, while that with the highest La/W ratio, LWO56, is composed of the main LWO phase and some (< 1 wt. %) unreacted La_2O_3 precursor. Between these two extremes, only the main LWO phase appears. Nevertheless, disagreement on the limits of the single-phase region exists in the

literature. In the latest review on LWO of Magraso and Haugsrud[52] the La/W ratio of LWO with a final sintering temperature of T = 1500 °C is reported to lie between 5.3 and 5.7. In contrast, the range of La/W ratio reported by Seeger *et al.*[32] is slightly narrower and was found to lie between 5.3 and 5.5 for the same sintering temperature. In Magraso and Haugsrud[52], a levelling-off of the LWO main phase lattice parameters at the single-phase region boundaries is reported. This means that the main LWO phase keeps a constant La/W ratio beyond its single-phase region. It follows that a further increase (decrease) of the overall composition results in the main LWO phase at the same La/W ratio with larger remainders of the secondary phases. Consequently, the combination of EPMA and XRD (Table 5.1, Fig. 5.2a) allows one to estimate the single phase region in the La/W range of 5.36(4) ≤ La/W ≤ 5.76(4). These results are more consistent with those of Magraso and Haugsrud[52] than with those of Seeger *et al.*[32].

5.1.3 Water uptake

In Fig. 5.3, the mass (wt. %) for LWO-D_2O(Ar) specimens as a function of temperature is depicted.

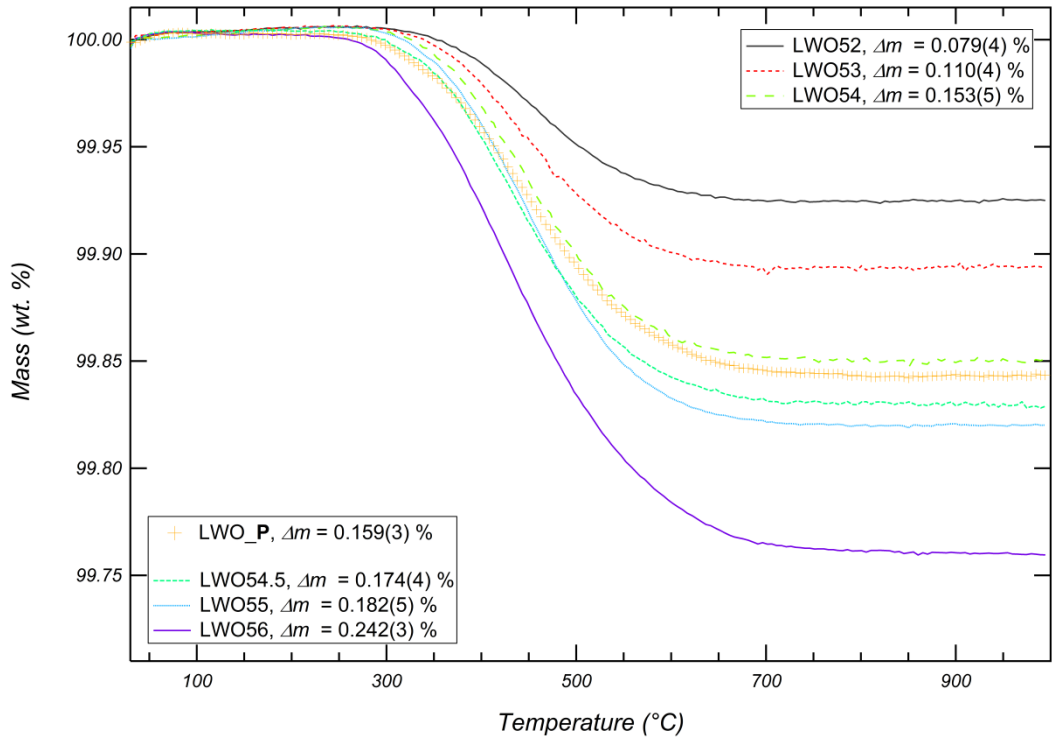

*Fig. 5.3. Thermogravimetric curves of LWO-D_2O(Ar) specimens measured under dry(Ar) gas, where the mass (wt. %) is shown as a function of temperature. Same colours as in Fig. 5.1 and Fig. 5.2 were used and the LWO_**P**-D_2O(Ar) specimen is the sole represented by individual symbols. Δm values are resumed in the legend with a 95 % confidence level (C.L.) uncertainty.*

In Fig. 5.3, two related features are visible:

1) the increase of total mass loss Δm with increasing La/W ratio
2) the decrease of the onset temperature of mass loss T_i with increasing La/W ratio

Point 1) reflects the increasing concentration of oxygen vacancies in the crystal structure with increasing La/W ratio. These vacancies had been filled with O atoms / OD groups during specimen pre-treatment. As the onset temperature T_i represents the thermal energy required for the first oxygen atoms and/or OD groups to leave the crystal structure, point 2) is related to the minimum energy required to create a vacancy. LWO52 shows the largest T_i (T_i^{LWO52} = 401(3) °C) value, which decreases with increasing La/W ratio, where for instance T_i^{LWO53} = 380(3) °C and T_i^{LWO55} = 355(3) °C (see Fig. 5.3). Due to the presence

of the secondary phase La_2O_3 in LWO56, its onset temperature (T_i^{LWO56} = 272(3) °C) is not representative, see discussion below. As T_i decreases with increasing La/W ratio, T_i decreases with increasing mass loss and thus with increasing vacancy concentration. Hence, a higher vacancy concentration in the specimen is related to a reduced stability of the crystal structure.

Particular attention is paid to the LWO56 specimen, where a separate reasoning must be addressed. In Fig. 5.4, the mass (wt. %) of LWO56-D_2O(Ar) (purple line) and La_2O_3-D_2O(Ar) ($La(OD)_3$, orange markers) along with the corresponding ion current signals (Fig. 5.4 inset) for *m* = 16 (O atoms) and *m* = 18 (OD groups), are shown as a function of temperature.

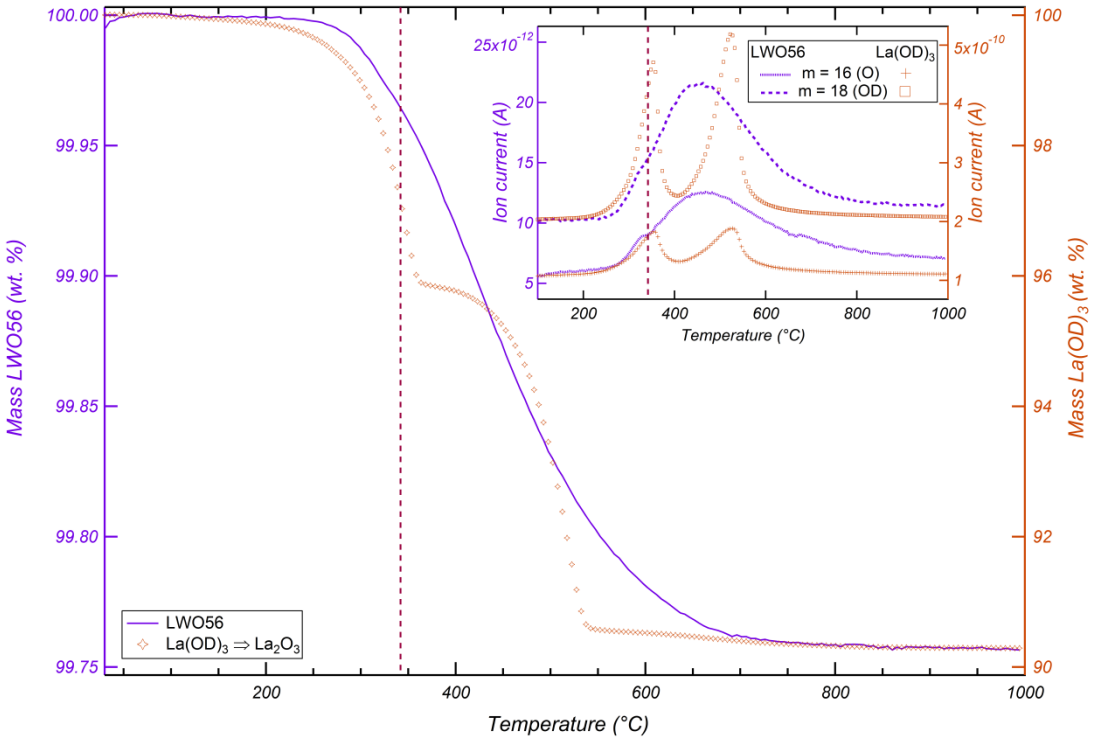

Fig. 5.4. Thermogravimetric curves of $La_{5.76(4)}WO_{12-\delta}$-$D_2O$(Ar) (LWO56, purple line) and $La(OD)_3$ (orange symbols) measured under dry(Ar) gas, where the mass (wt. %) is shown as a function of temperature. The left y-axis and the right y-axis are referred to the LWO56 and $La(OD)_3$ mass in wt. %, respectively. The scale of the y-axis on the right side is 40 times larger than that of the y-axis on the left side. In the inset, the mass spectrometer signals for m = 16 (O) and m = 18 (OD) of LWO56 (purple lines) and $La(OD)_3$ (orange markers) specimens, respectively, are reported as a function of temperature. Here, the scale of the right y-axis (ion current for $La(OD)_3$) is 500 times larger than the scale of the left y-axis (ion current for LWO56). The brown dashed vertical line corresponds to the temperature at which the first peak of the $La(OD)_3$ and the first shoulder of the LWO56 m = 16 and m = 18 ion currents appear (inset, T ≈ 342 °C).

The mass loss of LWO56 begins at T_i^{LWO56} = 272(3) °C, a temperature much lower than the onset temperature of LWO55 (T_i^{LWO55} = 355(3) °C), the specimen with closest composition to LWO56. LWO56 reveals also the highest recorded mass loss Δm of the whole LWO series (Δm^{LWO56} = 0.242(3) wt. %), being about 25 % higher than the mass loss of LWO55, Δm^{LWO55} = 0.182(5) wt. %. These discrepancies can be ascribed to the contribution Δm^{LWO56} by $La(OD)_3$, reflected by the first shoulder present in the LWO56 *m* = 16 and *m* = 18 ion currents, shown in the inset of Fig. 5.4. Such a shoulder can be directly compared with the TG and ion current measurements of $La(OD)_3$. Indeed, the $La(OD)_3$ ion current signals of oxygen atoms and OD groups correspond to the first shoulder in the ion current signals of LWO56, at about *T* ≈ 342 °C (brown dashed vertical line, see Fig. 5.4 inset). This suggests that in the TG curve of LWO56, T_i^{LWO56} is influenced by the $La(OD)_3$ phase. For $T > T_i^{LWO56}$, the contribution of $La(OD)_3$ to the mass loss of the main LWO phase starts to be notable. Amongst the two peaks of the ion current signals

of $La(OD)_3$, only the first one at $T \approx 342$ °C is visible, whilst the second one at $T \approx 522$ °C is hidden in the LWO56 mass spectrometer signals. Despite the very low amount (< 1 wt. %) of $La(OD)_3/La_2O_3$ phase inside LWO56, its relative mass loss is about 40 times higher than that of the main phase (9.72 wt. % compared to about 0.20 wt. %, see Fig. 5.4), making its contribution significant to the LWO56 mass loss and corresponding ion currents. For this reason, the left y-axis and the right y-axis of Fig. 5.4 and inset had to be represented on different scales.

Discussion: altogether, three steps are involved in the mass loss of LWO56, with different weights depending on the amount of the different phases in the specimen and their hygroscopicity. One step is due to the dehydration of the main LWO phase, observed for all specimens (see Fig. 5.3), while the other two steps are the consequence of the dehydration properties of $La(OD)_3$. Dehydration of $La(OD)_3$ is generally described by two main processes[112]:

$$La(OD)_3 \rightarrow LaOOD + D_2O \quad and \qquad (\approx 250\ °C < T < \approx 410\ °C) \qquad (5.2)$$

$$2LaOOD \rightarrow La_2O_3 + D_2O\,, \qquad (\approx 410\ °C < T < \approx 590\ °C) \qquad (5.3)$$

where the temperatures reported in reactions (5.2) and (5.3) are estimates derived from the ion current signals. However, in the TG curve of $La(OD)_3$ (see Fig. 5.4) a slight mass loss in the region $T < 250$ °C, in addition to another slight mass loss contribution for ≈550 °C < T < ≈750 °C can be noticed. DSC and TG measurements reported for $La(OH)_3$[113] and slightly Ln doped $La(OH)_3$:Ln (Ln = rare earth, < 8 at. % doping)[114] show four different dehydration stages, comparably to the present work. The weight losses reported in literature[114] are Δm = 1.8 wt. %, 9.7 wt. %, 4.3 wt. % and wt. 1.3 % for $T < 280$ °C, $T \approx 280$ °C – 430 °C, $T \approx 430$ °C – 560 °C and $T \approx 560$ °C – 800 °C, respectively. However, Yamamoto *et al.*[115] did not report a first stage comparable to the one observed in the present work while Rosynek and Magnuson[112] suggest that the last stage is due to a surface carbonate layer caused by the reaction of $La(OH)_3$ with CO_2 contained in air. As the detailed study of the reaction $La(OD)_3 \rightarrow La_2O_3$ is not the purpose of the present work, the discussion of this point is not further developed.

According to Fig. 5.4, the peak widths of the two maxima in the ion current curves (m = 16 and m = 18) for $La(OD)_3$ are much narrower than the corresponding peak widths of LWO56. The two phenomena involved might be different: the narrow $La(OD)_3$ peaks reflect a narrow distribution of activation energies induced by reaction (5.2) and reaction (5.3), contrarily to the ion current signal broadening of the main LWO phase, discussed in the following. Such signal broadening for all the LWO specimens is presented in Fig. 5.5 where the ion currents of m = 16 and m = 18 are depicted. The ion currents were scaled on the background signal measured before the peak. From Fig. 5.5 it is evident that the ion current signal of m = 16 (O) and m = 18 (OD) increases with increasing La/W ratio. Moreover, it is clear that LWO56 does not behave equally to the other LWO specimens as expressed by the shoulder observed at $T \approx 342$ °C (brown vertical dashed line), which is attributed to $La(OD)_3$. Hence, LWO56 is not considered when single-peak fitting is performed on the LWO ion current peaks shown in Fig. 5.5. Due to fact that the current signal of m = 16 is close to the sensitivity range of the mass spectrometer for most of the specimens ($I < 10^{-11}$ A), and that it is expected that most of the vacancies are occupied by OD groups, only the m = 18 signal is treated in the following. The Full Width at Half Maximum (*FWHM*) of the m = 18 ion current curves slightly decreases with increasing La/W ratio (16(6) °C between LWO52 and LWO55). However, the peak position of the m = 18 ion current seems to be independent of the La/W ratio. The temperatures corresponding to the ion current peaks can be related to the average

bond energy of the vacancies in the LWO crystal structure, while the *FWHM* corresponds to their bond energy distribution.

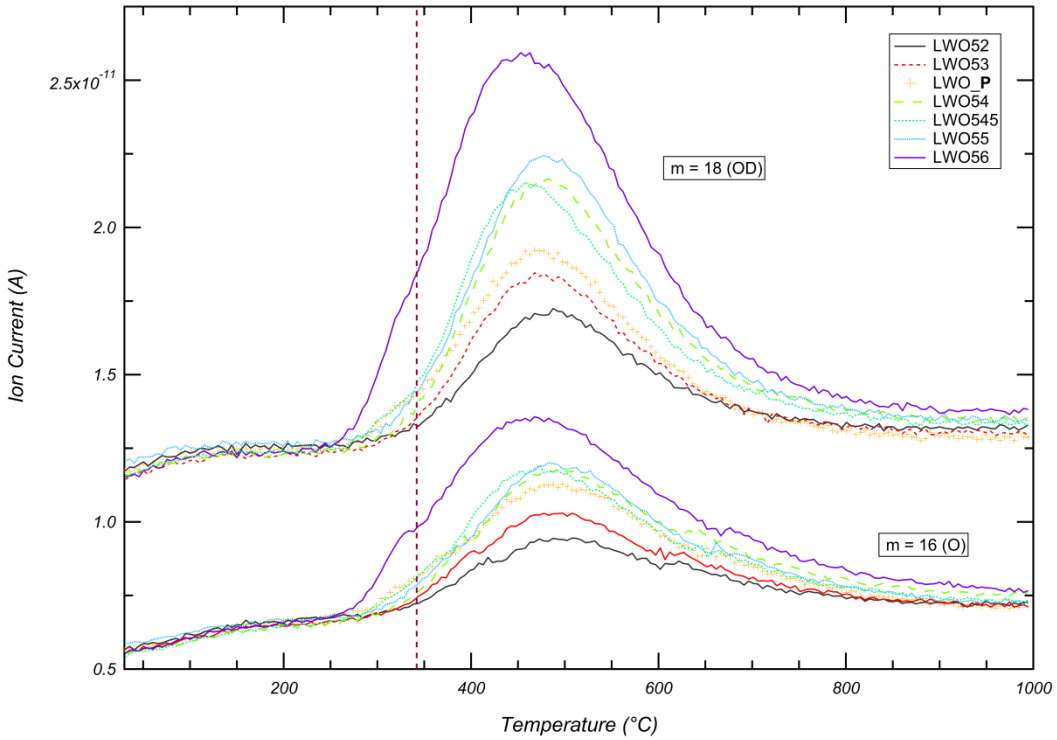

Fig. 5.5. Ion currents of the LWO-D_2O(Ar) specimens measured with the mass spectrometer, as a function of the temperature for m = 16 (O) and m = 18 (OD). The brown vertical dashed line represents the temperature T = 342 °C at which the ion current peak of $La(OD)_3$ was observed (see Fig. 5.4).

Even if these results suggest that the average bond energy of the vacancies in LWO and their energy distribution do not vary appreciably with composition, the broadened signal reflects a broad distribution of activation energies needed for vacancy creation in the lattice. As will be confirmed in the structural part of this work (see section 5.2.5), vacancies occupy the same site in the structure and only their number increases with increasing La/W ratio. Therefore, the broad activation energy distribution observed in Fig. 5.5 may be assigned to lattice distortions around the vacant site.

5.1.4 Crystal structure of LWO_P ($La_{5.56}WO_{12-\delta}$)

In the following paragraphs, a detailed crystallographic study on the LWO_**P** specimen used as a reference in the previous sections will be presented. A comparison between the existing structural models will be carried out through the analysis of the atomic displacement parameters on the basis of neutron diffraction (ND) measurements taken at D2B (ILL) as a function of temperature. Moreover, an estimation of the remaining static disorder in the unit cell at T = 5 K using the model of Housley and Hess[116] is also reported for the structural models employed. Once a model has been selected, the bond length of the first metal-oxygen shells is reported as a function of temperature (5 K ≤ T ≤ 1200 K), where the data sets were collected at D2B (ILL) and FIREPOD (BERII) for LWO_**P**-dry(Ar) specimens, below and above room temperature (T = 298 K), respectively. In the second part, high-resolution X-ray diffraction (HRXRD) studies on LWO_**P**-dry(Ar/S.A.) and LWO_**P**-D_2O(Ar/S.A.) specimens are presented, where Rietveld and LeBail refinements results on the LWO_**P**-dry(S.A.) specimen in dependence of the temperature are shown. Finally, the complementary information obtained by HRXRD and ND measurements are compared to each other and interpreted.

5.1.4.1 Neutron diffraction

The LWO_**P** sample has approximately the same composition as the $La_{5.65}WO_{12-\delta}$ specimen used by Magraso *et al.*[50] and was treated under similar conditions: the same sintering temperature (T = 1500 °C in air), comparable La/W ratio (5.56(3) vs 5.65(4)) and similar experimental conditions (dry(Ar)), ex-situ 900 °C for LWO_**P**, in-situ 800 °C to 150 °C for the specimen $La_{5.65}WO_{12-\delta}$ of Magraso *et al.*[50]). Scherb *et al.*[54] reported a similar ratio of La/W = 5.57(3) for a LWO specimen treated under the same dehumidifying conditions (dry(Ar), ex situ at 900 °C) but lower sintering temperature (1400 °C in air) than the present one. As shown in the literature,[32,46] the main structure-related effect of lower sintering temperature could be small remainders of secondary phases. Hence, it is assumed that the structure of the three specimens considered is equivalent.

The ND patterns taken on LWO_**P**-dry(Ar) were analysed in the following way: the final models of Magraso *et al.*[50] and Scherb *et al.*[54] were used to fit the data sets obtained in the present work as the two proposed models are similar but not identical. For instance, La_2 and W_2 atoms are reported to sit on the 24*d* Wyckoff site ($Fm\bar{3}m$ s.g., Magraso *et al.*[50]) or on the 48*h* Wyckoff site with half occupancies ($Fm\bar{3}m$ s.g., Scherb *et al.*[54]). Another unclear point is that Magraso *et al.*[50] report negative anisotropic displacement parameters (ADPs) for W_2 (ADPs not constrained with La_2) and for the oxygen atoms sitting on the 96*k* Wyckoff site, whose occupancy is the sole refined. In order to obtain the best structural model for the analysis of the Re- and Mo-substituted specimens and also to rule out structural inconsistencies in LWO specimens, a thorough study on the refined anisotropic displacement parameters as a function of temperature is presented. Refinements using both models have been performed constraining La_2 and W_2 coordinates and ADPs to be the same and constraining La_2 and W_2 site occupancies in a way that the 24*d* (Magraso *et al.*[50]) or 48*h* (Scherb *et al.*[54]) Wyckoff site show full or half site occupancy, respectively. At the final stage of the refinements, all the structural parameters were allowed to vary freely for the lowest temperature (T = 5 K) in both cases to minimize thermal vibrations and the correlation between ADPs and site occupancies. Subsequently, all the site occupancy values found at T = 5 K were fixed for all the other refined data sets collected at higher temperatures.

In Fig. 5.6, a comparison between the anisotropic displacement parameters obtained by applying the models of Magraso *et al.*[50] and Scherb *et al.*[54] to the data of the present work taken at $T \leq 298$ K is shown as a function of temperature. In addition, data points taken from Magraso *et al.*[50] above T = 298 K are added. As an indication of the region at overlap between the results of this work and the results of Magraso *et al.*[50], T = 298 K is represented by a brown vertical dashed line. In Fig. 5.6a, the diagonal terms of the ADP tensor of oxygen O_1 (96*k*) and O_2 (32*f*) atoms are depicted. The data for $T \leq$ 298 K fitted with the model of Magraso *et al.*[50] (open symbols) or the model of Scherb *et al.*[54] (full symbols) yield similar results with respect to oxygen ADP values. Good agreement is also achieved in the overlapping region of the two data sets at T = 298 K, irrespective of the model used. However, although the two models show similar oxygen ADP values (Fig. 5.6a), the ADP tensor orthogonalisation gives non-positive definite thermal ellipsoids of the O_1-96*k* Wyckoff site for all the refinements using the model of Magraso *et al.*[50], in accordance with the results of Magraso *et al.*[50]. On the other hand, considering the cation anisotropic displacements (Fig. 5.6b), the fits performed with the models of Magraso *et al.*[50] and Scherb *et al.*[54] yield different results in two cases: (i) La_1U_{xx} and (ii) $La_2/W_2U_{22/33}$ ADP terms, where U_{xx} (x = 1, 2, 3) are the diagonal elements of the symmetric anisotropic tensor matrix (values given in Å^2). U is related to the mean square atomic displacements via $U = \langle u^2 \rangle$.

Concerning the La_1 atom, there is a discontinuity of the U_{xx} values of the ADP term between the data set of LWO_**P** ($T \leq 298$ K) and the data set of Magraso *et al.*[50] ($T \geq 298$ K) in the region of overlap at T = 298 K, with a value reported by Magraso *et al.*[50] being about twice as big as the value of the present

work. This discrepancy in the values of La_1U_{xx} could be due to non-equivalent occupancies, which influence the displacement parameters, or due to different types of data acquisition (time of flight measurements in Magraso *et al.*[50] and measurements at constant wavelength in the present work). For a detailed comparison between different instruments and methods of data collection the reader is referred to Hill and Cranswick[87]. On the other hand, the difference in $U_{22/33}$ ADP values of La_2/W_2 is more relevant, being an order of magnitude higher and constant in the whole temperature range when the model of Magraso *et al.*[50] is used. This can be explained as follows: when the La_2/W_2 atom is located on a 24*d* Wyckoff site (0, 0.25, 0.25) the different orientations of the W_1–O_1 octahedra situated at (0, 0, 0 – *x*, *x*, *z*) and (0, 0.5, 0.5 – *x*, *x*, *z*) result in a net electrostatic force applied by the O_1 atoms on the La_2/W_2 atom (Scherb *et al.*[54]). This net electrostatic force is applied to a La_2/W_2 atom along the diagonal (yz direction) between the two octahedra, i.e. either towards the W_1–O_1 octahedron centred at (0, 0, 0) or towards the W_1–O_1 octahedron centred at (0, 0.5, 0.5). In turn, the La_2/W_2 atom is pulled either to (0, 0, 0) or to (0, 0.5, 0.5) and explains the splitting of the La_2/W_2 site which accounts for the high values of the $U_{22/33}$ terms in the model of Magraso *et al.*[50]. The two major inconsistencies reported above for the model of Magraso *et al.*[50], one for the anions (non-positive thermal ellipsoids for the 96*k* oxygen site) and one for the cations (high $U_{22/33}$ ADP term of La_2/W_2, see Fig. 5.6b) are related and express the same aspect. The $La_2/W_2U_{22/33}$ displacement parameter is elongated towards the 96*k*-O_1 sites and decreases the 96*k*-O_1 displacement parameters in a way that the 96*k*-O_1 orthogonalised ADP in the direction towards the 24*d* site ($U_{11/22}$) becomes negative.

As pointed out e.g. by Massa[117] the off-diagonal terms of the ADP tensor U_{xy} refer to the orientation of the thermal ellipsoid to that of the reciprocal cell axes. In non-orthogonal systems, they also have a component related to the lengths of the principal ellipsoid axes. For detailed information see Fischer and Tillmanns[118]. They state that the orthogonalisation of the ADPs tensor should give positive values in the diagonal to obtain a complete set of physically meaningful ADPs. In other words, before using any ADP value, the three eigenvalues of the anisotropic tensor (which correspond to the reciprocals of the squares of ellipsoid's semi-axes) have to be positive-definite. As the LWO_**P** structure is represented by a cubic ($Fm\bar{3}m$) space group, none of the off-diagonal terms referred to as La_2/W_2, O_1 and O_2 is shown in Fig. 5.6 but reported in the Appendix along with all the refinement results of the LWO_**P**-dry(Ar) specimen in the whole range of temperatures and for both structural models of Scherb *et al.*[54] and Magraso *et al.*[50]. In these tables (*LWO_**P** Tables*, Appendix), note whenever the condition of orthogonalisation into positive-definite eigenvalues of the ADPs tensor is not fulfilled (marked in red colour).

From Fig. 5.6, it can be noticed that the extrapolation of anisotropic displacement parameters to zero at T = 0 K does not appear to be satisfied for almost all ADPs for any of the models used.

Due to the Heisenberg uncertainty principle, the relationship between thermally induced mean-square atomic displacements and the temperature is not linear and vibrations persist even at T = 0 K (zero-point energy). Thus, for any chosen temperature, the displacement parameter is a combination of a static and a temperature-dependent term which reflects dynamic disorder:

$$B_k(T) = B_k^{thermal}(T) + B_k^{static}, \tag{5.4}$$

where B_k is the displacement parameter of atom *k* and B_k is proportional to the mean square atomic displacement $\langle u^2 \rangle$, with $B = 8\pi^2\langle u^2 \rangle$. T is the absolute temperature.

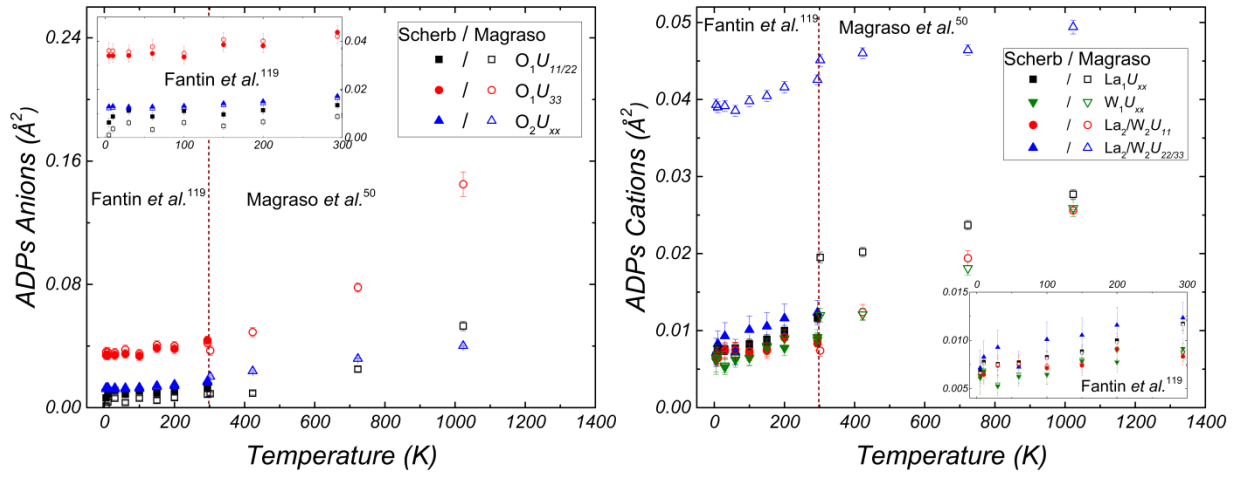

a) ***b)***

*Fig. 5.6. Temperature dependence of the anisotropic atomic displacement parameters of the LWO_**P**-dry(Ar) specimen, **a)** anions and **b)** cations. Measurements between T = 5 K and T = 298 K were performed at ILL (labelled as Fantin et al.[119]) and refined with the $Fm\bar{3}m$ space group, using Scherb's model (Scherb et al.[54], full symbols) and Magraso's model (Magraso et al.[50], open symbols). A magnification of the results between T = 5 K and T = 300 K is shown in the corresponding insets. Above T = 298 K, brown dashed line, the results taken from Magraso et al.[50] are added (open symbols, region labelled as Magraso et al.[50]). The data point at T = 298 K of Magraso et al.[50] is shifted to T = 302 K, while the data point of the present work at T = 298 K is shifted to T = 294 K for better visualization. U_{xy} (x, y = 1, 2, 3; x ≠ y) are not shown because they are rotations around xyz axes and in orthogonal systems they do not contribute to the length of the principal axes of the thermal ellipsoids (cf. text and literature[117,118]). In Fig. 5.6a, the values shown in open black squares (denoted as $O_1U_{11/22}$ Magraso in the figure) are not physical (cf. text). In Fig. 5.6b, W_2 diagonal ADP values at T = 423 K, T = 723 K, T = 1050 K taken from Magraso et al.[50] are not visible because they lie outside the range ($W_2U_{22/33}$) and are negative (W_2U_{11}).*

In order to estimate the maximum thermal contribution of the mean square atomic displacements at $T = 0$ K the approach from Housley and Hess[116] was adopted. With this approach, the minimum static component of the refined atomic displacements was determined. This procedure has also been used for the determination of static disorder in Cs hollandites[120] and ZrO_2[121]. Expressing B_k as a function of the normal mode frequencies, Housley and Hess[116] state the following upper limit of the temperature-dependent term:

$$\left(B_k^{thermal}(T = 0\ K)\right)_{max}^2 \leq \frac{h^2}{2m_k k_B T} B_k(T)\,, \tag{5.5}$$

where h and k_B are Planck's and Boltzmann's constants, respectively, and m_k is the mass of atom k. The equality in relation (5.5) holds for high temperatures.

The maximum thermal values of all anisotropic displacement parameters were calculated for both models according to Eq. (5.5) at the highest temperature data available measured with the same instrument and conditions, i.e., at $T = 298$ K.

Subtracting $B_k^{thermal}(T = 0\ \mathrm{K})_{max}$ from the refined ADP values at the lowest experimental temperature, $B_k(T = 5\ \mathrm{K})$, the minimum value of the static disorder contribution, B_k^{static}, was determined. The results obtained by the use of the approach of Housley and Hess[116] are plotted in Fig. 5.7.

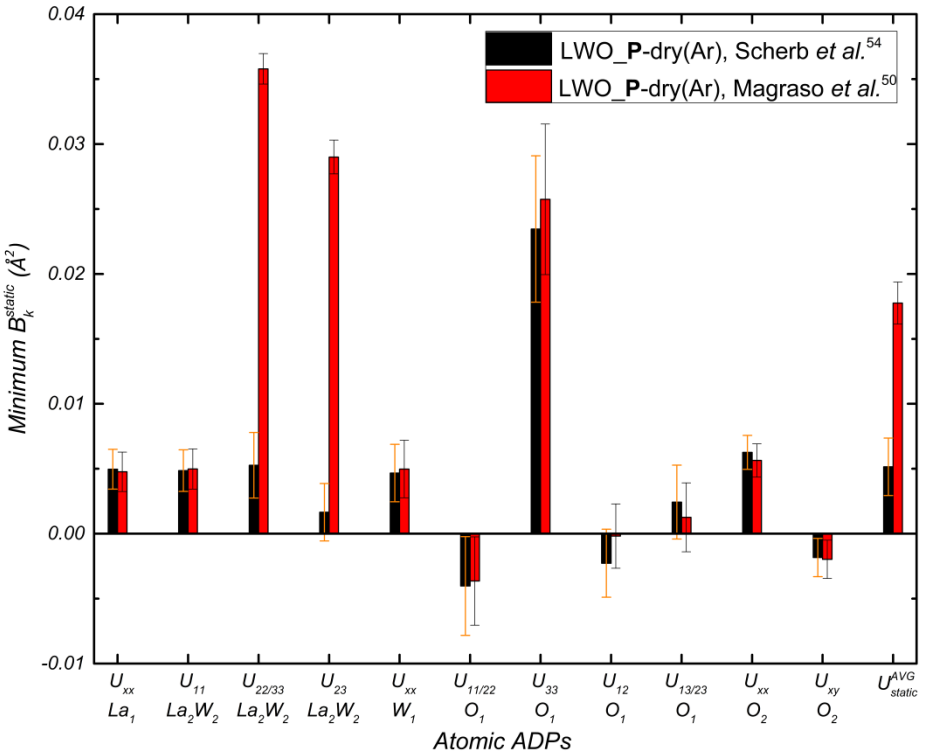

Fig. 5.7. Minimum static disorder according to the approach of Housley and Hess[116] for the models of Scherb et al.*[54] (black bars) and Magraso et al.[50] (red bars), applied to LWO_**P**-dry(Ar) and calculated at T = 5 K. Each atom and all of its anisotropic displacement parameters (ADPs) are included. The last column represents the weight-averaged minimum static disorder in the unit cell, i.e.,* $U^{AVG}_{static} = \frac{1}{8\pi^2 M}\sum_k^{cell} m_k B_k$*, where* $M = \sum_k^{cell} m_k$ *is the sum of the masses* m_k *of each of the atom k in the unit cell.*

As the Housley and Hess[116] approach calculates the minimum of B_k^{static}, the actual values of B_k^{static} could be higher than the ones shown in Fig. 5.7. Before drawing any conclusion on the negative minimum B_k^{static} shown in Fig. 5.7, e.g., for the O$_1$*U$_{11/22}$* ADP value, it has to be pointed out that only two values of $B_k(T)$ are considered in Eqs. (5.4) and (5.5) and that the ADP tensor is not orthogonalised. The two values used ($B_k(T$ = 298 K*)* and $B_k(T$ = 5 K*)*) induce uncertainties to the values shown in Fig. 5.7, while the non-orthogonalised ADP tensor could mislead the reader to think about actual negative displacement parameters.

The effect of constant and high ADP values in 24*d* Wyckoff sites in the model of Magraso *et al.*[50] is seen in Fig. 5.7, according to which the minimum static disorder of all positions with the exception of La$_2$/W$_2$ atoms in *U$_{22/33}$* (and rotation *U$_{23}$*) terms is the same for the models of Magraso *et al.*[50] and Scherb *et al.*[54]. The inequality of the La$_2$/W$_2$ ADP values leads to a higher average unit cell static displacement of 0.018(2) Å^2 for the model of Magraso *et al.*[50] compared to 0.005(2) Å^2 for the model of Scherb *et al.*[54]. The O$_1$*U$_{33}$* ADP term also reflects static disorder independently of the model used and is caused by the different orientations of distorted W$_1$–O$_1$ octahedra in the unit cell, averaged in time and space, in addition to a presumed O$_1$ libration around W$_1$ and to O$_1$ anharmonic vibrations, which the present models cannot parametrize accurately (see discussion in sections 5.1.5 and 5.4.3, respectively). All other diagonal *U$_{xx}$* ADPs have maximum values around 0.005 Å^2 (root mean square, r.m.s., displacement value of about 0.07 Å) and indicate a remaining static disorder in the sample. However, their corresponding r.m.s. values are too low to improve the model significantly. Refinements using La$_1$ on 48*i*, O$_2$ on 96*k* and O$_1$ on 192*l* Wyckoff sites of the $Fm\bar{3}m$ space group were performed. The $F4\bar{3}m$ space group was also employed but relevant differences compared to the model of Scherb *et al.*[54] were not observed. Finally,

the structure of LWO_**P**-dry(Ar) specimen is presented in Fig. 5.8 using the model of Scherb *et al.*[54] and refinements of ND data collected at ILL at T = 5 K.

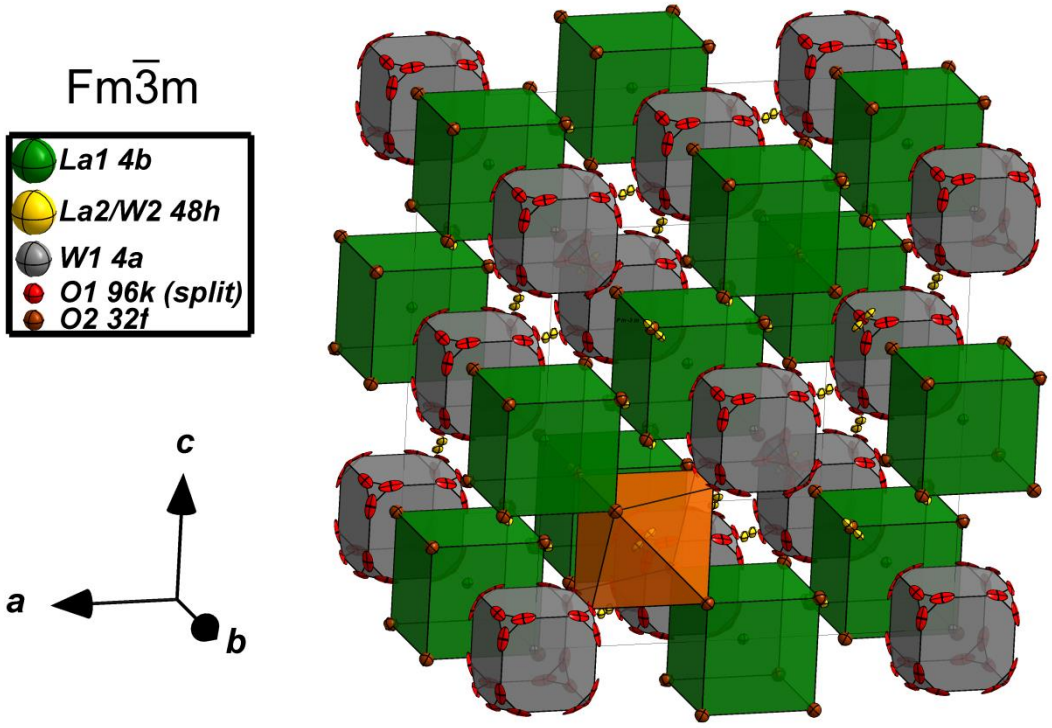

*Fig. 5.8. Average crystal structure of the LWO_**P**-dry(Ar) specimen with space group, atoms and Wyckoff sites as refined from the diffractogram collected at 5 K at the ILL. Grey and green cubes represent W (W_1, 4a site) and La (La_1, 4b site) polyhedra, respectively. W_1 is 6-fold coordinated by the O_1 oxygen atoms (96k site partially occupied, red atoms). La_1 is 8-fold coordinated by the O_2 oxygen atoms (32f site almost fully occupied, brown atoms). The orange polyhedron denotes the La_2/W_2 shared and split 48h site. Locally, the La_2/W_2 site is 7-fold (La_2) or 6-fold (W_2) coordinated by oxygen atoms due to the different orientation of the neighbouring W_1–O_1 octahedra. However, the diffraction techniques average out the W_1–O_1 octahedra in cubes with oxygen partial occupancies. The shown ADPs represent 50 % probability of finding an atom in the corresponding sphere/ellipsoid.*

Refinements on the LWO_**P**-D_2O(Ar/S.A.) specimens were performed in order to locate deuteron sites. However, due to the low amount of D (0.44 D_2O per unit cell) and the size of one unit cell ($a^3 \approx 1400$ Å^3), it was impossible to locate deuteron sites even for very low temperatures (T = 5 K (D2B), T = 1.5 K (HRPT)).

5.1.4.2 High-resolution X-ray diffraction

Sample $La_{5.56}WO_{12-\delta}$ (LWO_**P**) has been measured in its dry(Ar/S.A.)/D_2O(Ar/S.A.) conditions at the MS-beamline at the SLS synchrotron (PSI, Villigen). The observed electronic density map (ρ_{obs}) of LWO_**P**-dry(Ar) is shown in Fig. 5.9. The electron density map (ρ_{obs}) of the LWO_**P**-dry(Ar) specimen has been determined by Fourier transformation of the observed structure factor by HRXRD (see Eq. (4.26)). The atoms are represented as filled spheres where the coloured filling agrees to the refined occupancies of LWO_**P**-dry(Ar) (see Table 5.2 below). On the Wyckoff site 4*a* (cube corners and face centres) and 4*b* (cube edges and cube centre), the electronic density corresponds to W and La, respectively. That the Wyckoff site 4*a* is occupied by the larger scatterer tungsten (Z = 74) compared to lanthanum (Z = 57) can be inferred from Fig. 5.9 where around the 4*a* Wyckoff sites a larger cloud of observed electronic density is observed. This cloud belongs to the complete 4*f* shell (14 electrons) of tungsten ([Xe] $4f^{14}$ $5d^4$ $6s^2$), which lanthanum does not exhibit ([Xe] $5d^1$ $6s^2$). This statement derives from the fact that the

tungsten 4*f* electrons (i) do not participate in bonds as 4*f* orbitals are generally contracted and localized in space, (ii) are not present around the 4*b* site which, therefore, corresponds to La. The La and W outer orbitals $5d^1\ 6s^2$ and $5d^4\ 6s^2$, respectively, participate in bonding giving an oxidation state of +3 (La^{3+}) and +6 (W^{6+}), respectively. The electrons belonging to those orbitals cannot be distinguished in Fig. 5.9 as they are too few and too disperse. The tabulated distances for the 5*d* and 6*s* orbitals of La and W isolated atoms are 2.17 Å, 4.15 Å, and 1.47 Å, 3.12 Å, respectively.[122] These values are the radii at which the magnitude of the 5*d* / 6*s* wave functions is greatest (R_{max}). From Fig. 5.9, the cloud of the observed electronic density at the 4*a* Wyckoff site can be estimated to lie at about 0.5 Å distance from the nucleus. This value is comparable with the tabulated distance of the valence *f* shell of the isolated W atom (R_{max} = 0.424 Å).[122] In addition, the electron densities corresponding to the 48*h* split site can also be ascertained in Fig. 5.9. This structural detail has been controversial as it is reported that such a 48*h* site would lead to unstable structural refinements compared to a 24*d* site[50]. According to Scherb[53,54] and the present work (see Fig. 5.6 and Fig. 5.9), the determination of the 48*h* position as a split site for La_2/W_2 is an improvement of the former structural model.

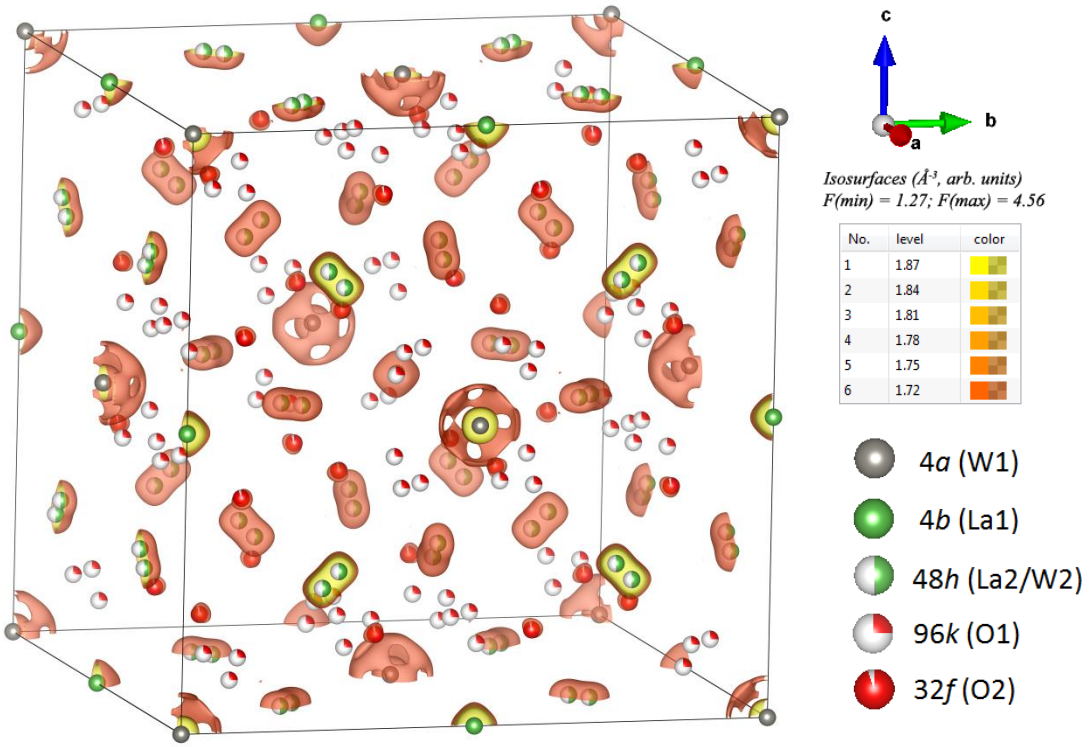

*Fig. 5.9. Electron density map (ρ_{obs}, in $Å^{-3}$) of LWO_**P**-dry(Ar) specimen, determined by Fourier transformation of HRXRD observed intensity at T = 295 K. Iso-surfaces towards yellow colour have higher observed electron density while iso-surfaces towards red colour represent lower observed electron density. The partial filling of the atoms (coloured) represent the site occupancy factors as refined (cf. text).*

As a first refinement, the average X-ray scattering power method has been applied to the data sets of LWO_**P**-dry(Ar)/D_2O(S.A.) specimens, collected at *T* = 295 K and the results are reported in Table 5.2. From Table 5.2, one can see that the W_1 and La_1 sites are fully occupied, La_2 split sites show about half occupancies, O_1 atoms have an occupancy of about 0.25, which agrees with the W_1 octahedral coordination, and O_2 sites slightly deviate from full occupancy due to the vacancy contribution.

*Table 5.2. Fractional atomic coordinates, x, y, z, site occupancy factors, SOFs, isotropic displacement parameters B_{iso} for LWO_**P**-dry(Ar)/D_2O(S.A.) ($La_{5.56}WO_{12-\delta}$) derived by high-resolution X-ray diffraction at T = 295 K refined with space group $Fm\bar{3}m$. The lattice parameters and the residuals are also reported. The parameters marked with an asterisk (*) could not be simultaneously refined with the others during the final cycles.*

Atom condition	Site	x	y	z	SOF	B_{iso} (Å^2)
W_1 Dry(Ar)	4*a*	0	0	0	1.023(9)	0.333(8)
D_2O(S.A.)					1.039(7)	0.270(5)
La_1 Dry(Ar)	4*b*	0.5	0.5	0.5	0.998(8)	0.736(11)
D_2O(S.A.)					1.002(6)	0.773(7)
La_2 Dry(Ar)	48*h*	0	0.23614(2)	0.23614(2)	0.5082(41)	0.385(5)
D_2O(S.A.)		0	0.23583(1)	0.23583(1)	0.5078(30)	0.412(4)
O_1 Dry(Ar)	96*k*	0.1122(4)	0.1122(4)	0.0682(6)	0.250(3)*	1.56 (13)
D_2O(S.A.)		0.1130(3)	0.1130(3)	0.0663(4)	0.256(2)*	1.47(10)
O_2 Dry(Ar)	32*f*	0.3666(1)	0.3666(1)	0.3666(1)	0.946(7)*	0.90(5)
D_2O(S.A.)		0.3663(1)	0.3663(1)	0.3663(1)	0.954(6)*	1.07(4)
	Lattice parameter (Å)	T (K)	R_{exp} (%)	R_{wp} (%)	χ^2	R_B (%)
Dry(Ar)	11.21710(1)	295	0.970	2.809	8.39	4.62
D_2O(S.A.)	11.22566(1)	295	0.861	2.761	10.28	2.72

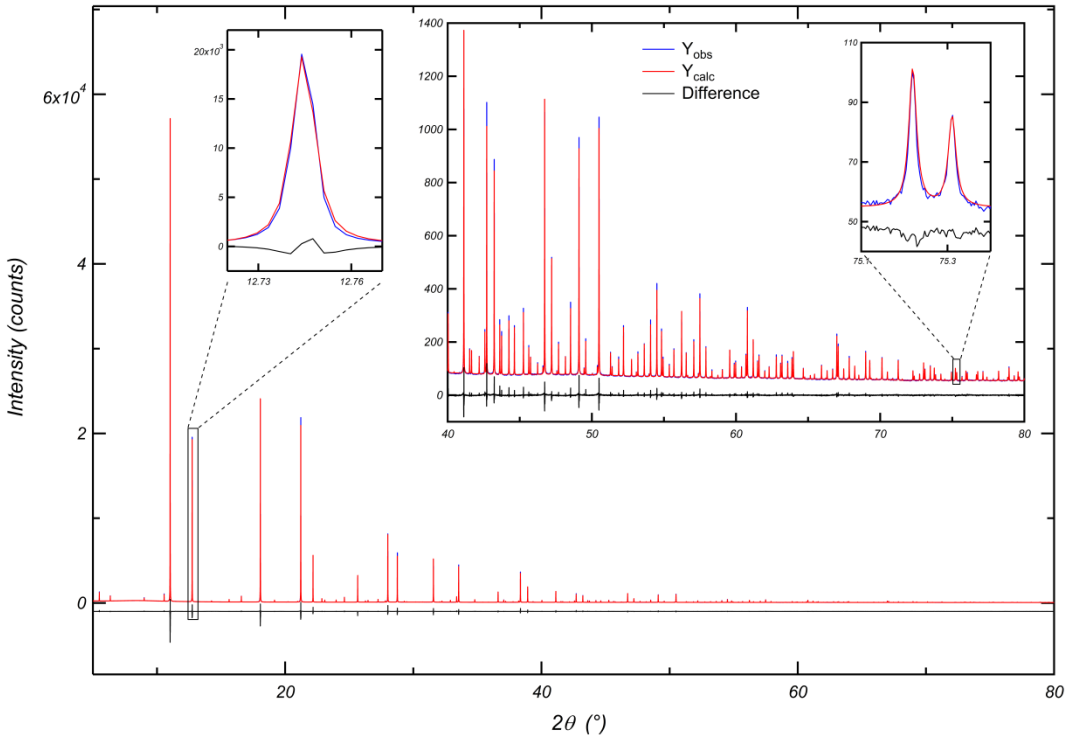

*Fig. 5.10. High-resolution X-ray diffraction intensity plots of LWO_**P**-dry(Ar) ($La_{5.56}WO_{12-\delta}$) data collected at T = 295 K at the MS beamline (SLS), as a function of the scattering angle 2Θ (blue line), calculated data (red line) and difference of the two (black line). In the inset, the high-angle data (40° ≤ 2Θ ≤ 80°) is magnified, as well as three chosen reflections, one at low scattering angles (2Θ ≈ 12.7°) and two at high scattering angles (2Θ ≈ 75.3°). In the insets, the difference line is shifted for better peak visualization.*

As reported in the literature[48-51,53], a tiny amount of W (W_2) occupies the La_2 site. This finding agrees with the La_2 occupancies reported in Table 5.2 for the 48*h* split site, larger than half site occupancy (*SOF* > 0.5) because of the larger atomic number of W (Z_W = 74) compared to La (Z_{La} = 57). Such amount of W_2 is needed to give the right stoichiometry to the compound. As the presence of W at the La_2 site is

already well investigated, this issue will not be further discussed. Instead, an estimation of the W_2 anti-site disorder on the La_2 site (W_{La2}) is reported. X-ray and neutron refinements on LWO_**P**-dry(Ar)/D_2O(Ar) give W_{La2}^{X-rays} = 6(4) at. % (from Table 5.2) and $W_{La2}^{Neutrons}$ = 6(3) at. %, respectively. In the calculation of these values, the uncertainties in the X-ray scattering power or the neutron scattering length were also considered. These values are in agreement to each other and within the error of the estimated amount reported in the literature ($W_{La2}^{Neutrons}$= 4(2) at. %, Scherb *et al.*[54]) and to the value determined by the chemical formulation currently used for LWO, applied to LWO_**P** (W_{La2}^{Calc} = 3.7(2) at. %). Finally, the refinement of the LWO_**P**-dry(Ar) pattern collected at *T* = 295 K, including the W_2 atom on the 48*h* site along with La_2, is presented in Fig. 5.10. In addition, the corresponding table of refined parameters is listed in Table 5.3.The last cycles of the structural refinement were performed with all atom coordinates, all the cation or anion occupancies, and all the ADPs left free to vary. Within the X-ray diffraction technique such refinements are normally not achievable. The refined composition is slightly different from that established with EPMA but within the error, being $La_{27.0(4)}W_{5.2(4)}O_{54.4(5)}$ (La/W = 5.2(6)). The refinement gives reasonable occupancies and displacement parameter values also for the oxygen atoms. Moreover, by comparison with the refinement on the LWO_**P**-dry(Ar) pattern performed with the average X-ray scattering power (see Table 5.2), the model with ADPs and W anti-site disorder gives a better R_B residual (≈ 17 % lower). Although Magraso *et al.*[48] shows that the LWO crystal structure presents a slight tetragonal distortion, the high-resolution measurements of LWO_**P**-dry(Ar) and LWO_**P**-D_2O(Ar) contradict this finding. Another proof comes from the refinement of the LWO54-dry(S.A.) pattern collected at the MS beamline (not shown here), which also does not present any distortion from the cubic structure.

*Table 5.3. Fractional atomic coordinates x, y, z, site occupancy factors, SOFs, equivalent displacement parameters, U_{eq}, for LWO_**P**-dry(Ar) specimen ($La_{5.56(3)}WO_{12-\delta}$) from high-resolution X-ray diffraction data collected at T = 295 K, refined with space group $Fm\bar{3}m$. All the displacement parameters (U_{eq}, U_{xx} and U_{xy}) are multiplied by a factor of 100. The lattice parameter and the residuals are also reported.*

Atom	Site	x	y	z	U_{eq}(Å^2)	SOF
La_1	4*b*	0.5	0.5	0.5	0.89(2)	1.000(6)
W_1	4*a*	0	0	0	0.46(1)	1.025(7)
La_2	48*h*	0	0.23632(2)	0.23632(2)	0.55(1)	0.478(8)
W_2	48*h*	0	0.23632(2)	0.23632(2)	0.55(1)	0.022(8)
O_1	96*k*	0.1127(3)	0.1127(3)	0.0673(6)	2.2(3)	0.250(3)*
O_2	32*f*	0.3664(2)	0.3664(2)	0.3664(2)	1.18(6)	0.951(8)*
	U_{11}(Å^2)	U_{22}(Å^2)	U_{33}(Å^2)	U_{12}(Å^2)	U_{13}(Å^2)	U_{23}(Å^2)
La_1	0.89(2)	0.89(2)	0.89(2)			
W_1	0.46(1)	0.46(1)	0.46(1)			
La_2	0.44(1)	0.61(1)	0.61(1)			0.25(1)
W_2	0.44(1)	0.61(1)	0.61(1)			0.25(1)
O_1	1.6(2)	1.6(2)	3.4(4)	-0.5(2)	-0.5(2)	-0.5(2)
O_2	1.18(6)	1.18(6)	1.18(6)	0.23(7)	0.23(7)	0.23(7)
Lattice parameter (Å)	T (K)	R_{exp} (%)	R_{wp} (%)	χ^2	R_B (%)	
11.21710(1)	295	0.970	2.74	7.98	3.82	

Moreover, the sample LWO_**P**-dry(S.A.) was studied through high-resolution X-ray diffraction at MS(SLS) as a function of temperature. In Fig. 5.11, one chosen diffraction peak of some of the LWO_**P**-dry(S.A.) patterns recorded during cooling is shown. Although the forty-one patterns collected during cooling were simultaneously refined with program TOPAS, for the sake of clarity only ten are reported in Fig. 5.11.

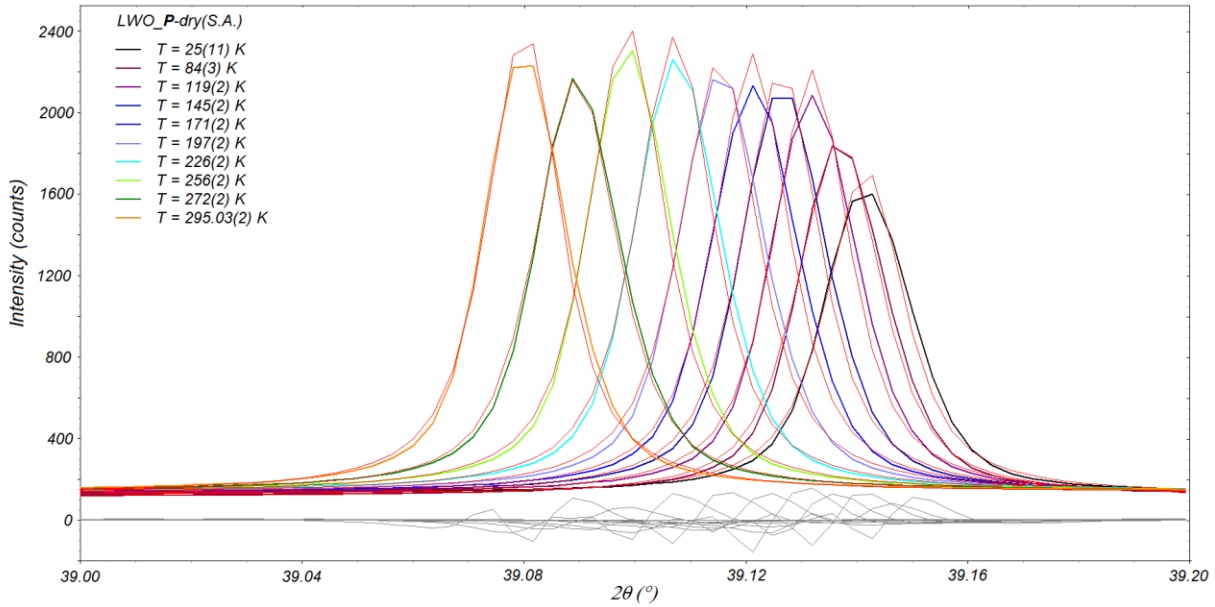

*Fig. 5.11. High-resolution X-ray diffraction intensity plots of LWO_**P**-dry(S.A.) ($La_{5.56(3)}WO_{12-\delta}$) data as a function of the scattering angle 2Θ and of the temperature (coloured lines, not red), calculated data (red lines) and difference of the two (grey line). The diffraction peak is shown for ten diffractograms for the sake of clarity. It corresponds to two superimposed reflections, hkl = 884/12, 0, 0. The intensity decrease and the increasing peak width with decreasing temperature is due to some increase of capillary wobbling (cf. detailed discussion in section 5.3.4.3) and also, especially at T = 25(11) K, due to the temperature variation during collection. In the legend, the mean temperature values and their uncertainties are reported.*

The coloured patterns (not red) correspond to the observed intensities in the temperature region 295 K ≥ T > 10 K (from left to right in Fig. 5.11). The LeBail-calculated and difference intensities are represented in red and grey colour, respectively. The first pattern on the left side of Fig. 5.11 was collected at T = 295.03(2) K, before initiating the cooling procedure, while the last pattern on the right side of Fig. 5.11 corresponds to T = 25(11) K before measurements at constant temperatures during re-heating were performed. In the refinement program, the same instrumental parameters obtained after capillary position calibration were used for all patterns. Calibration was performed fixing the lattice parameter of the diluent Si640d NIST to the tabulated value reported in the NIST certificate at T = 295 K[123] ($a_{T=295\ K}^{Si640d\ NIST}$ = 5.43123(2) Å). In the refinements, the profile parameters, zero offsets, lattice parameters and background for the Si640d NIST and the LWO_**P**-dry(S.A.) phases were left free to vary. Finally, the refinement was performed on forty-one patterns and ≈ 2500 free parameters simultaneously. The average residual values are R_{exp} = 0.54 % and R_{wp} = 1.89 %, respectively, which give *GOF* = 3.5 or equivalently χ^2 ≈ 12.3. The lattice parameters for the LWO_**P**-dry(S.A.) specimen and for the Si640d NIST reference obtained through LeBail refinements on the patterns collected during cooling are shown in Fig. 5.12 in black diamonds and squares, respectively. In addition, Rietveld refinements of patterns collected at constant temperatures (T = 10 K, 30 K, 60 K, 100 K, 150 K, 200 K, 240 K, 270 K) fixed during re-heating were performed. The T = 295 K pattern was collected before cooling in a steady state (T = 295.03(2) K) and was used for calibration according to the lattice parameter of the diluent Si640d NIST. Therefore, it was included in both cooling and re-heating (steady state) data sets. The lattice parameters obtained from patterns recorded in a steady state are reported in red diamonds and squares for LWO_**P**-dry(S.A.) and Si640d NIST, respectively. However, the capillary in the cryostat normally changed its position slightly during cooling due to glue instability. Therefore, the refinements on all the patterns collected during cooling were performed together with the pattern collected at

T = 10 K by fixing the computed capillary position at the calibrated values (T = 295 K). Then, the pattern collected at T = 10 K was refined alone, fixing the lattice parameter of the Si640d NIST at T = 10 K as found from the refinements during cooling and allowing a variation of the computed capillary position. After this, the capillary position was fixed for all the refinements of the patterns collected during re-heating. These patterns were then refined altogether. For this reason, the values recorded during the cooling and re-heating procedure must be compared separately. If the cooling values or the re-heating values are considered, some conclusions can be drawn from Fig. 5.12. For instance, the temperature variation acting during cooling on each of the patterns causes an apparent shift of the Si640d NIST negative thermal expansion region, known to exist at 18 K ≤ T ≤ 125 K[124]. When the temperature was kept constant, instead, the lattice parameter results on Si were in agreement with the literature. Also, the tiny positive thermal expansion of Si in the low temperature region as reported in the literature (T < 18 K[124]) was observed. This finding proves that the lattice parameter temperature dependence of the LWO_**P**-dry(S.A.) specimen is reliable. The LWO_**P**-dry(S.A.) lattice parameter decreases smoothly with decreasing temperature and seems to level off in the low-temperature region, hence giving a thermal expansion which decreases to 0 when T approaches 0 K. For low temperatures (T < 100 K), the LWO_**P**-dry(S.A.) lattice parameter temperature dependence $a(T)$ agrees with the Debye model, where $a(T)$ is found to be proportional to T^4 (R^2 = 0.989, not shown here). Details on the Debye model and the thermal expansion of LWO_**P** and substituted LWO will be discussed in the final part of this work.

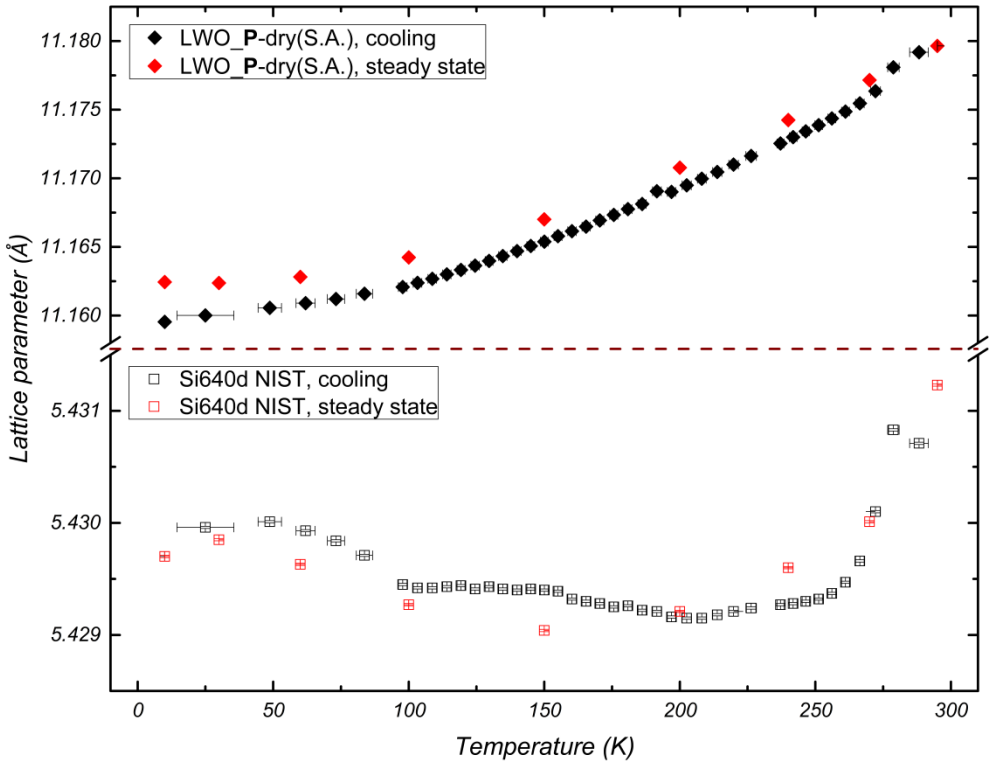

*Fig. 5.12. Lattice parameters of LWO_**P**-dry(S.A.) (above the break in brown dashed line) and of the diluted NIST Si640d reference (below the break) as a function of temperature. Lattice parameters were obtained through LeBail refinements on patterns collected during cooling (black symbols) and Rietveld refinements during re-heating at constant temperatures (red symbols). The T = 295 K pattern was collected in a steady state before cooling and used for calibration, thus it appears in both data sets. Diamonds and squares represent the lattice parameters of LWO_**P**-dry(S.A.) and Si640d NIST, respectively.*

5.1.5 Comparison and discussion

In Fig. 5.13 the scaled ratio of the LWO specimens (Eq. (5.1), Table 5.1), in dependence of their lattice parameter in dry(Ar) (Table 5.1, Fig. 5.1) and D_2O(Ar) conditions are shown. In order to understand the

increase in lattice parameter upon deuteration and the vacancy concentration in the unit cell, it is necessary to refer to the defect chemistry of LWO specimens according to the literature[48,49,108,109]. It is reported that for the non-substituted LWO an effective positive charge of +3 is carried by the tungsten donors substituted on lanthanum La_2 positions ($W_{La2}^{\bullet\bullet\bullet}$ in Kröger-Vink notation, see Table 2.1). The general chemical formulation for LWO is found to be

$$La_{28-x}W_{4+x}O_{54+\delta}v_{2-\delta}\,, \tag{5.6}$$

where $\delta = 3x/2$ and v denotes the number of vacancies per unit cell. According to Magraso *et al.*[48], δ defines the oxygen content which compensates the $W_{La2}^{\bullet\bullet\bullet}$ donors. Therefore, at a given x (or given La/W ratio), it is possible to estimate by charge compensation the amount of vacancies in the unit cell. For increasing La/W ratio, charge compensation predicts an increase of vacancy concentration. Subsequently, it is expected that the concentration of filled vacancies also increases with increasing La/W content, confirming the results presented earlier (see Fig. 5.3). When more vacancies are occupied by oxygen atoms or OD groups (see Fig. 5.5) the anion-anion repulsion becomes stronger and it is expected that structural rearrangements lead to an increase of the unit cell with increasing number of filled vacant oxygen sites.

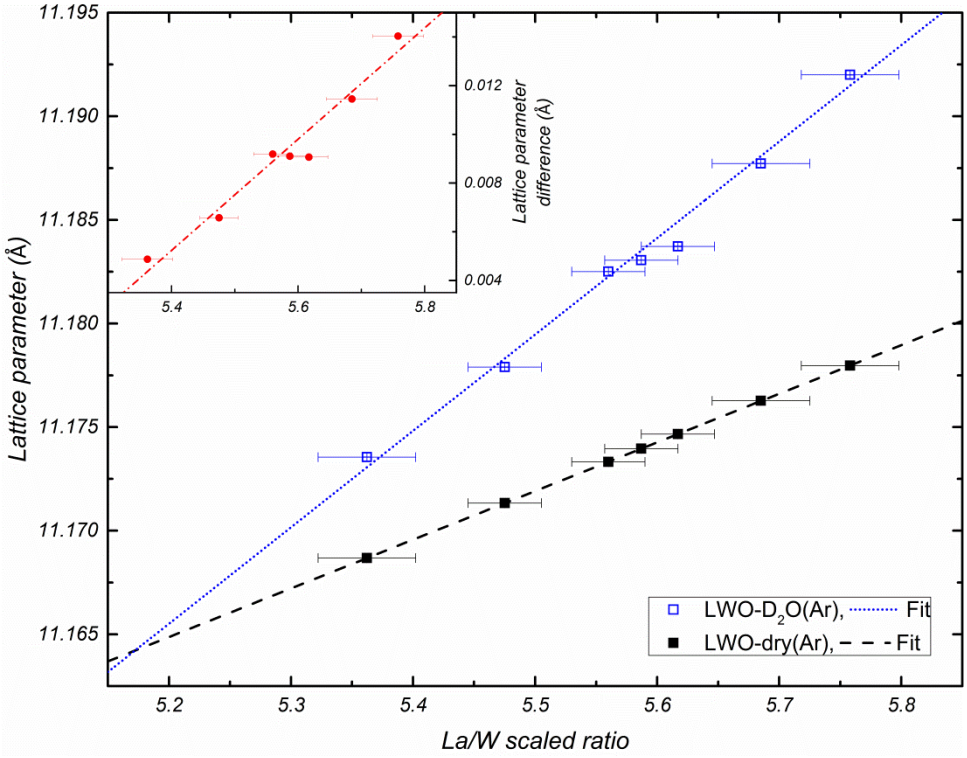

Fig. 5.13. Lattice parameters of the LWO specimens in dry(Ar) (full squares) and D_2O(Ar) (open squares) conditions as a function of the scaled La/W ratios (listed in Table 5.1). In the inset, the difference between the lattice parameters obtained for the LWO-dry(Ar)/D_2O(Ar) specimens is depicted. Fits are straight lines.

In Fig. 5.13, the linear increase of the lattice parameters in D_2O(Ar) conditions (R^2 = 0.99) confirms what has been shown in Fig. 5.3 and what is predicted by the theory. Another way to represent the linear increase of lattice parameters in D_2O(Ar) and dry(Ar) condition is to depict their difference for the same La/W ratio. As it can be seen in the inset, such difference increases with increasing La/W ratio (Fig. 5.13 inset), following also a linear trend (R^2 = 0.96). This fact suggests that the La/W ratios obtained through Eq. (5.1) are a good approximation of the actual values. However, the two linear regression fits in Fig.

5.13 intersect at La/W = 5.18(5), a value at which LWO should not contain vacancies (δ = 2 in formula (5.6)). If the value δ = 2 was substituted in (5.6), the corresponding theoretical ratio would be La/W = 5, which differs from the ratio La/W = 5.18(5) found experimentally. At present, the reason for the discrepancy between the experimental (La/W = 5.18(5)) and theoretical (La/W = 5) results seems to be the wrong chemical formulation for δ in Eq. (5.6), as a clear shift between the charge compensation predictions[48,109] and all the experimental values measured in the present work has been observed, as presented in the following. From the chemical formulation (5.6), the theoretical vacancy predictions can be related to the TG measurements. By TG, the amount of (heavy) water dissolved in the specimen can be measured according to the hydration reaction (in Kröger-Vink notation, see Table 2.1)

$$D_2O(g) + O_O^x + v_O^{\bullet\bullet} = 2OD_O^{\bullet} . \tag{5.7}$$

Applying Eq. (5.7) to LWO (formulation (5.6)) yields

$$La_{28-x}W_{4+x}O_{54+\delta}v_{2-\delta} + yD_2O \overset{water\ splitting}{\longleftrightarrow} (OD)_y + D_y + La_{28-x}W_{4+x}O_{54+\delta}v_{2-\delta} , \tag{5.8}$$

$$(OD)_y + D_y + La_{28-x}W_{4+x}O_{54+\delta}v_{2-\delta} \overset{OD,\ D\ taken\ up}{\longleftrightarrow} La_{28-x}W_{4+x}O_{54+\delta+y}D_{2y}v_{2-\delta-y} , \tag{5.9}$$

where *y,* the amount of dissolved water, is calculated from the mass loss according to Schober and Friedrich[125]. *y* corresponds to the number per unit cell of OD groups taken up during deuteration

$$y = c_{D_2O} = \frac{\Delta m\ (\%)}{100} \times \frac{M_{LWO}}{M_{D_2O}} , \tag{5.10}$$

where the D_2O number of molecules (c_{D_2O}) per unit cell is equal to the number of OD groups per unit cell. The results are reported in the following Table 5.4.

*Table 5.4. Sample labels (LWOk and LWO_**P**), La/W ratio according to Eq. (5.1), theoretical amount x of W occupying the La_2 positions ($W_{La2}^{\bullet\bullet\bullet}$), oxygen content δ which compensates the $W_{La2}^{\bullet\bullet\bullet}$ donors and calculated vacancies (v). Mass loss in wt. %, heavy water concentration according to Eq. (5.10) and ratio between the experimental amount of filled (c_{D2O}) to theoretical (v_{theory}) vacancies are also shown. For comparison, the results on two LWO specimens taken from Hancke et al.[109] are also reported. The asterisk (*) indicates that in the measured mass loss and the calculated c_{D_2O} there is a non-negligible $La(OD)_3$ contribution (see Fig. 5.4).*

Sample label	La/W ratio	x	δ	v	Δm (wt. %)	c_{D_2O} (Eq.(5.10))	v_{TG}/v_{theory}
LWO_P	5.560	0.878	1.317	0.683	0.159	0.441	0.646
LWO52	5.362	1.030	1.545	0.455	0.079	0.220	0.482
LWO53	5.475	0.942	1.413	0.587	0.110	0.305	0.520
LWO54	5.587	0.858	1.287	0.713	0.153	0.424	0.595
LWO545	5.617	0.836	1.254	0.746	0.174	0.483	0.646
LWO55	5.685	0.787	1.180	0.820	0.182	0.504	0.615
LWO56	5.758	0.735	1.103	0.897	0.242*	0.670*	0.747*
LWO53[109]	5.3(Nom)	1.079	1.619	0.381		0.38 [109]	1.00 [109]
LWO56[109]	5.6(Nom)	0.848	1.273	0.727		0.48 [109]	0.66 [109]

In Fig. 5.14 the theoretical amount of vacancies *v* (red dotted line) reported in Table 5.4 and of the vacancies obtained from TG measurements (Eq. (5.10), Table 5.4, full blue squares) as a function of the

scaled La/W ratio (Eq. (5.1),Table 5.4) are depicted. Also, in open black squares two values from Hancke *et al.*[109] are shown.

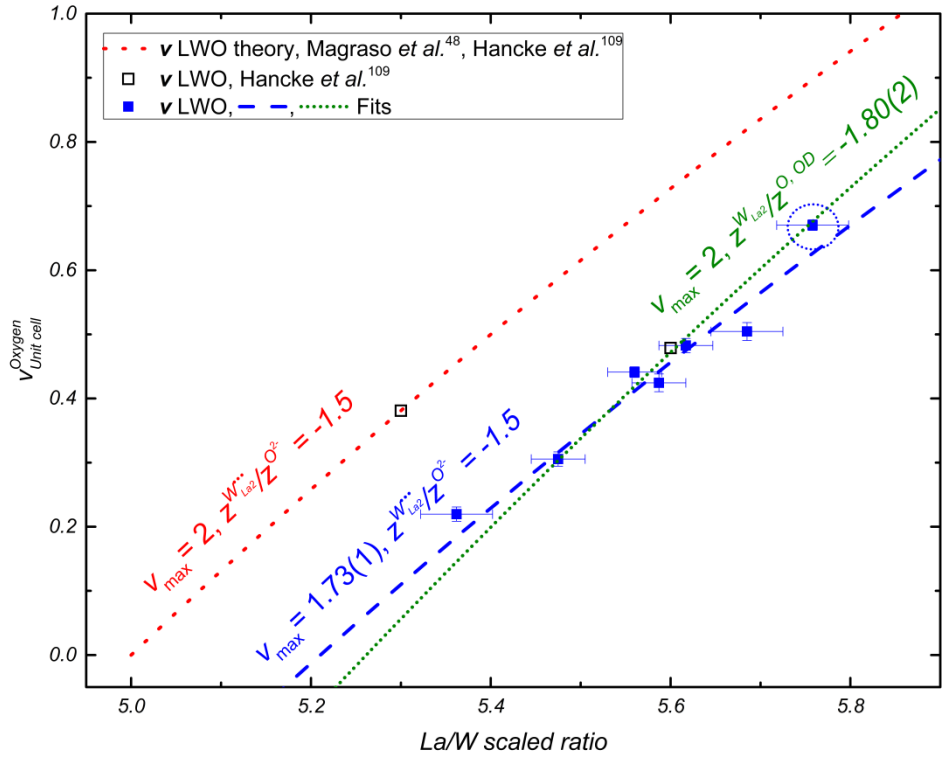

Fig. 5.14. Theoretical (red dotted line) and TG-measured (full blue squares) amount of oxygen vacancies as a function of the La/W ratio. The theoretical amount of oxygen vacancies in LWO was calculated according to the charge compensation equation derived from formulation (5.6) and reported in the literature[48,109]. In open black squares the two values from Hancke et al.[109] are shown, whereas the data point inside the blue circle denotes the LWO56 sample not included in the fit due to the not negligible contribution of its secondary phase $La(OD)_3$ to mass loss (see Fig. 5.4). Fits were performed with Eq. (5.12).

The red dotted line intercepts $v = 0$ at La/W = 5 (theoretical zero vacancy prediction, see formulation (5.6)). It is possible to induce from formula (5.6) a general equation for charge compensation in LWO, expressing v (theoretical vacancy number) as a function of x ($W_{La2}^{\bullet\bullet\bullet}$)

$$v(x) = v_{Unit\ cell}^{Oxygen}(x) = v_{max} + \frac{z^W}{z^v}x\,, \tag{5.11}$$

where v_{max} is the maximum theoretical amount of vacancies in the unit cell, z^W is the charge carried from the tungsten donor on La site, and z^v the charge at the filled vacancy position.
Developing x, $v(x)$ in Eq. (5.11) can be equivalently expressed as a function of the La/W ratio

$$v(La/W) = v_{Unit\ cell}^{Oxygen}(La/W) = v_{max} + \frac{z^W}{z^v}\left(\frac{28 - 4 \times La/W}{La/W + 1}\right). \tag{5.12}$$

Eq. (5.12) was used to fit the data in Fig. 5.14, where the theoretical fit was chosen according to the literature[48,49,109] and formulation (5.6), thus obtained with $v_{max} = 2$, $z^W = z(W_{La2}^{\bullet\bullet\bullet}) = +3$, $z^v = z^O = -2$. The resulting fit is shown in Fig. 5.14 as a red dotted line.
Firstly, in Fig. 5.14 it can be noticed that the experimentally determined water uptake follows a linear trend ($R^2 = 0.95$, not presented), as expected from the lattice parameters in the D_2O(Ar) condition. The

specimen with the highest La/W ratio (LWO56, inside the blue dotted circle) contains less than 1 wt. % La_2O_3. This deviates towards higher values from the calculated water uptake due to the high hygroscopicity of the secondary La_2O_3 phase. Therefore, it was not included in any of the fits presented in Fig. 5.14. The data point corresponding to specimen LWO52 was considered in the fitting procedure as the changes in mass loss induced even assuming zero vacancies in $La_6W_2O_{15}$ (< 1 wt. % in LWO52, see Fig. 5.2a) would be beyond the resolution of the instrument. Also, the two data points taken from the literature[109] were not considered in the interpolations performed due to the unknown composition. From those two data points at La/W = 5.3 and La/W = 5.6 (open black squares), the latter matches with the experimental values found in the present work. However, the former deviates from the latter one and from all data of the present work, being the sole agreeing with the theoretical predictions of formulation (5.6) and the corresponding Eq. (5.12). However, small shifts in La/W ratios due to possible systematic errors in the EPMA measurement calibrations on the LWO_**P** specimen cannot be entirely excluded (cf. section 4.2 Electron probe micro-analysis). Therefore, is reasonable to say that the data point from the literature[109] matching the theoretical prediction may correspond to a different composition. This statement cannot be proven as sample composition studies were not included in Hancke *et al.*[109]. In addition, Hancke *et al.*[109] claim that the data point at La/W = 5.6 (open black square, right of Fig. 5.14) does not match the theoretical calculations (red dotted line) because either some segregation of La_2O_3 could occur and lower the hydration of LWO, or a certain extent of vacancy ordering exists. The former statement is proven wrong by the properties of La_2O_3, as shown in Fig. 5.4. Concerning the latter, it is not expected that vacancy ordering could appear when one single unit cell is composed by about 86 atoms and 0.5 vacancies. However, that vacancy ordering does not subsist cannot be univocally excluded. Different possibilities could be ascribed to the discrepancies between the theoretical model used in Fig. 5.14 (red dotted line) and the experimental data (blue squares in Fig. 5.14), to which two interpolations have been applied as depicted in Fig. 5.14. If it is assumed that only charge compensation accounts for the vacancy concentration in LWO, only two parameters in Eq. (5.12) can be varied: v_{max} and the ratio $z^* = \frac{z^W}{z^v}$. z^* is the ratio between the effective charge of the tungsten donor and the charge at the filled vacancy position. The blue dashed line in Fig. 5.14 represents the situation where $z^* = -1.5$ or considering that the W donor gives a 3+ effective charge ($z^W = +3$) and the vacancies are filled only by oxygen ions ($z^v = z^O = -2$). The parameter v_{max} was left free to vary. On the other hand, a second fit fixing $v_{max} = 2$ and leaving the ratio $z^* = \frac{z^W}{z^v}$ free to vary was performed (green dotted line). This situation would allow for a certain reduction of W and / or an increase of the charge at the filled vacancy position. Such increase could, for instance, be due to OD or OH groups ($z_{OD/OH} = -1$). A proton contribution in the charge compensation equation for LWO is mentioned in Erdal *et al.*[49]. X-ray Photoelectron Spectroscopy (XPS)[49] and Temperature-Programmed Reduction (TPR)[31] studies on LWO, however, suggest no reduction of W, which seems to keep its +6 oxidation state (W^{6+}) even in very reducing atmospheres (dry 10 % H_2 in Ar)[31]. In one case, the interpolation yields $v_{max} = 1.73(1)$ with $z^* = -1.5$ ($R^2 = 0.92$), while in the other case the interpolation gives $z^* = -1.80(2)$ with $v_{max} = 2$ ($R^2 = 0.78$). Although the fit with less predicted vacancies gives better residuals, at present no exhaustive interpretation could be drawn. Nevertheless, it can be stated that the theoretical model for LWO vacancies and also the subsequent chemical formulation (5.6) currently used by the scientific community need to be reviewed, following these results.

A different approach to study the effect of the vacancy concentration and site substitution in LWO is to investigate the peak broadening of all the LWO-dry(Ar)/D_2O(Ar) XRD patterns in dependence of the La/W ratio. Single-peak fitting of the diffraction peaks is performed in the 2Θ range of $30° \leq 2\Theta \leq 80°$. Such interval has been chosen to avoid peak asymmetry ($2\Theta \leq 30°$) and instrumental peak broadening

due to the CuKα satellite radiation coming from the tube, which is relevant at high scattering angles ($2\Theta \geq 80°$). In order to establish the instrument contribution to peak width, a certified reference specimen ($LaB_6$660a NIST[123]) was measured with the same instrumental parameters as the LWO specimens. Then, peak fitting of the $CuK\alpha_1/K\alpha_2$ doublet was performed with a pseudo-Voigt (*pV(x)*) curve

$$pV(x) = \eta * L(x) + (1-\eta) * G(x)\,, \tag{5.13}$$

where η is the Lorentzian contribution (in %) to the pseudo-Voigt curve, and $L(x)$ and $G(x)$ are a Lorentzian and a Gaussian function, respectively. Intensity, Full Width at Half Maximum (*FWHM*), one asymmetry parameter and η are refined, together with the background (linear function). The $CuK\alpha_1/K\alpha_2$ ratio was fixed to the theoretical value of 0.5. Fits were made with WINPLOTR (FULLPROF). The peak widths, *FWHM*, obtained by single peak fitting, are plotted in Fig. 5.15 as a function of the scattering angle 2Θ, where the results on LWO-dry(Ar)/D_2O(Ar) specimens are shown in Fig. 5.15a and Fig. 5.15b, respectively. The angular dependence of the *FWHM* has been fitted by the second-order polynomial in tan Θ (Caglioti *et al.*[126])

$$FWHM^2 = U\tan(\theta)^2 + Vtan(\theta) + W\,, \tag{5.14}$$

where *U*, *V*, *W* are constants and Θ the Bragg angle measured in Bragg-Brentano geometry.
The literature on SEM and TEM investigations on LWO suggests that the grain size of LWO specimens with final sintering temperature of 1500 °C lies between 3 and 10 µm[46,52]. It is known that the contribution to the peak widths due to crystallite size starts to be relevant approximately below the µm region and increases with decreasing crystallite size. Therefore, by assuming that the crystallite sizes are similar to the grain sizes reported in the literature, the peak broadening is not expected to be influenced by the crystallite size above the lower limit of 3 µm. Furthermore, it is assumed that upon specimen deuteration, the average crystallite size does not change.

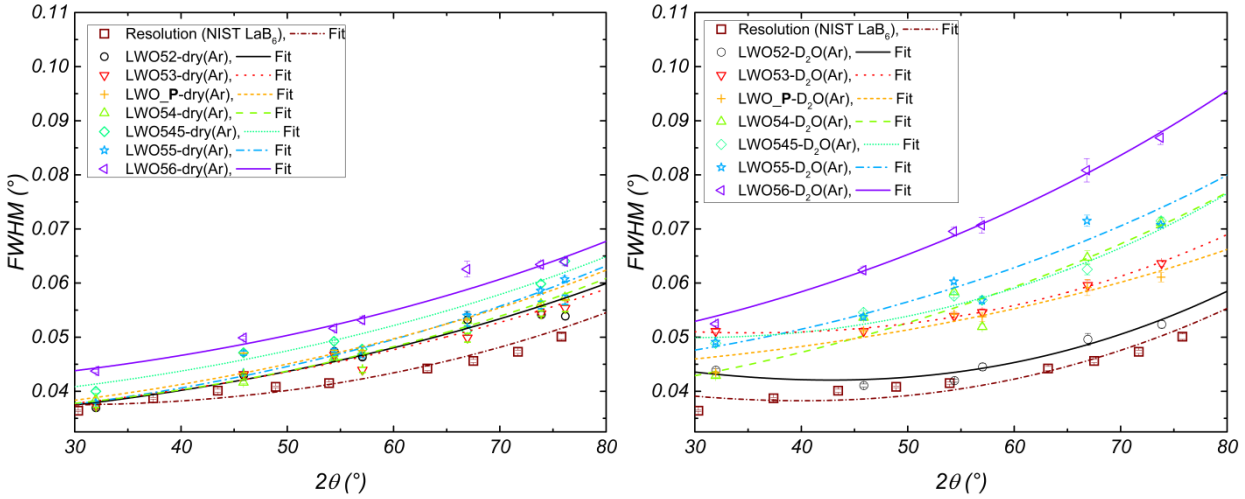

a) ***b)***

*Fig. 5.15. FWHM obtained by single-peak fitting of LWO XRD patterns, as a function of the scattering angle 2Θ ($30° \leq 2\Theta \leq 80°$) for **a)** dry(Ar) and **b)** D_2O(Ar) conditions. The FWHM of $LaB_6$660a NIST diffraction peaks in dependence of 2Θ are also shown (open brown squares). Fits according to Eq. (5.14) of the instrumental resolution (LaB_6) and of the LWO-dry(Ar)/D_2O(Ar) specimens are also reported.*

Finally, as these samples were ground from one single pressed pellet, concentration gradients can be excluded and therefore, if any effects are visible, these are due to the strain induced by the vacant sites, oxygen disorder, or lattice parameter gradients due to La_2 substitution by W_2. Effects are indeed visible

in both dry(Ar) and D_2O(Ar) pre-treated specimens, but more evident in the latter. In Fig. 5.15a, most of the *FWHM* curves obtained with Eq. (5.14) are close to the instrumental resolution. Despite the small differences between the resolution and LWO *FWHM* curves, broadening seems to increase with increasing La/W ratio, being largest for the LWO545, LWO55 and LWO56 specimens. The reason might be the lattice parameter gradient induced by La_2 substitution by W_2 and the increasing amount of oxygen vacancies with increasing concentration. However, as the peak width values do not separate much from those of the LaB_6 specimen (≈ 20 % for LWO56), it is difficult to prove this univocally. The behaviour seen for the dry(Ar) pre-treated LWO specimens is similar to that of the D_2O(Ar) treated ones, whose peak width results are presented in Fig. 5.15b. The *FWHM* value corresponding to $2\Theta \approx 32°$ in Fig. 5.15b is in many cases inaccurate due to appreciable peak asymmetry (e.g. LWO53-D_2O(Ar)). In Fig. 5.15b, the increasing *FWHM* in the LWO-D_2O(Ar) specimens upon deuteration and with increasing La/W ratios is ascribed to oxygen atoms / OD groups filling the vacant oxygen sites in the unit cell. This may be explained considering either that the filled oxygen sites are different in number for different unit cells, or that the lattice is more distorted when the vacancies are filled. Both these interpretations would rationalise the peak broadening as induced by lattice parameter variation amongst different unit cells. These interpretations would also agree with the peak broadening of the ion currents presented in Fig. 5.5. That each unit cell presents slightly different structures is also supported by the chemical formulation (5.6), from which follows that the amount of vacant sites in the unit cell depends on La_2 substitution by W_2, inducing local distortions around the substituted site. Thus, as some unit cells may not present any vacant site or empty(dry(Ar)) / filled(D_2O(Ar)) vacant sites, possibly with distorted surroundings, the lattice parameter variation may be ascribed to the disordered LWO structure in the first place. The disorder in LWO may be related to inhomogeneous La_2 substitution by W_2 and subsequent inhomogeneous surroundings of the vacant sites in different unit cells.

As mentioned in the first part of this chapter, neutron diffraction data of LWO_**P**-dry(Ar) have been collected in the low-temperature range ($5\ K \leq T \leq 298\ K$) at the D2B experimental station and in the high temperature range ($298\ K \leq T \leq 1200\ K$) at the FIREPOD experimental station. The lower resolution of the data acquired at FIREPOD compared to D2B did not allow for refining consistently all the anisotropic displacement parameters, which is the reason why the comparison in Fig. 5.6 takes into account the data of Magraso *et al.*[50] for $T \geq 298\ K$. However, the FIREPOD data could be refined including only the single anisotropic vibrations of the O_1 atom, whose anisotropic motion is the most relevant in the unit cell (see Fig. 5.6, Fig. 5.7). Despite the not completely identical refinements, such modelling of O_1 vibrations allows for a better comparison between the metal-oxygen bond lengths obtained from D2B data and FIREPOD data, presented in Fig. 5.16. In Fig. 5.16, the refinements on D2B data performed with ADPs (shown in Fig. 5.6) for $5\ K \leq T \leq 298\ K$, in addition to those on FIREPOD data allowing O_1 to vibrate anisotropically, are depicted in full symbols. In empty symbols, instead, the results taken from refinements performed allowing only for isotropic motion for all atoms are added. Straight fits for the anisotropic and isotropic models are also shown in solid and dash-dotted lines, respectively. These fits are a guide to the eye, as at low temperatures ($T \lesssim 150\ K$) the bond lengths remain approximately constant. In Fig. 5.16, no relevant differences for the La_1–O_2 and 48*h*–O_2 presented bonds between the anisotropic and the isotropic model are observed in dependence of temperature: the absolute values are slightly larger for the anisotropic model and the bond lengths increase with increasing temperature, as expected for a positive thermal expansion (see section 5.4.2 for details). However, allowing anisotropic vibrations of O_1 atoms results in an unexpected bond length shortening with increasing temperature. The isotropic model gives physically meaningful results on the W_1–O_1 octahedra, where the W_1–O_1 bond lengths increase with increasing temperature.

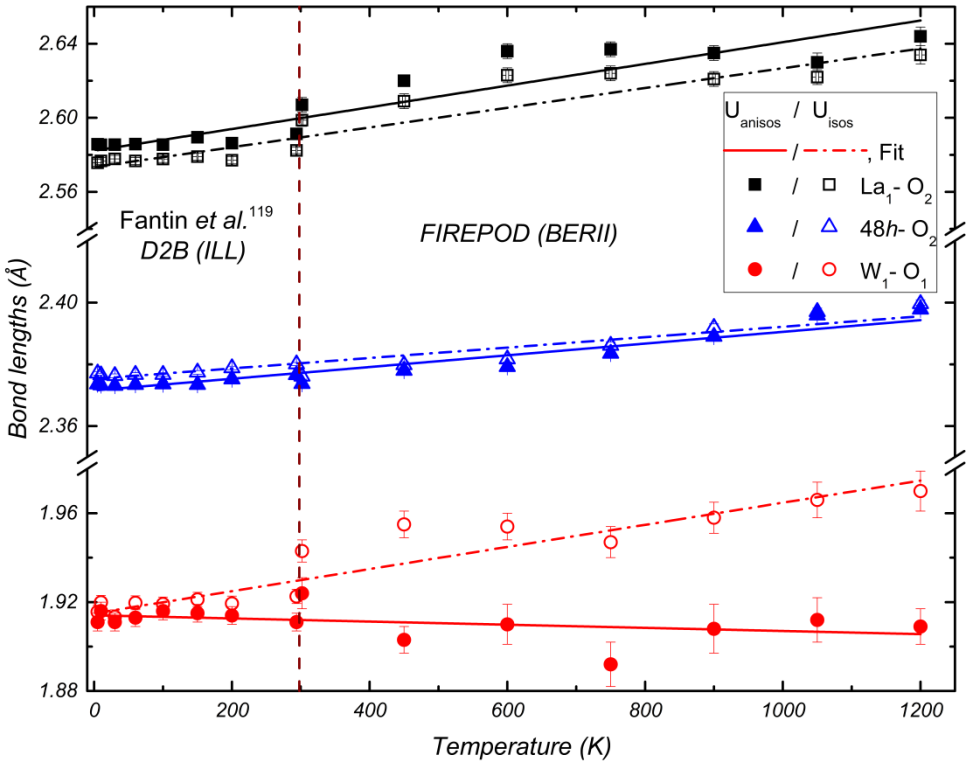

*Fig. 5.16. Selected metal-oxygen bond lengths as a function of temperature of LWO_**P**-dry(Ar), obtained from ND data collected at D2B (Fantin et al.[119], $T \leq 298$ K) and FIREPOD ($T \geq 298$ K). The bond lengths obtained allowing only for isotropic vibrations are shown in open symbols. Refined bond lengths allowing for complete anisotropic vibration (D2B data, $T \leq 298$ K) or the most intense anisotropic vibration (O_1 atoms, FIREPOD data, $T \geq 298$ K) are presented in full symbols. The two data sets are separated by a brown dashed line ($T = 298$ K) and the data points at room temperature shifted from $T = 298$ K to $T = 294$ K (D2B) or to $T = 302$ K (FIREPOD) for better visualization. Fits are straight lines.*

Refinements with anisotropic displacement parameters found in the literature for LWO also showed W–O bond length shortening with increasing temperature[50], where a mathematical rigid-body correction to the W–O shortened bonds was applied according to Downs *et al.*[127]. However, the magnitude of W–O bond shortening with increasing temperature reported in Magraso *et al.*[50] is much larger to that shown in Fig. 5.16. For instance, they report for T = 473 K a $d_{W1–O1} \approx 1.89$ Å and at T = 1073 K a $d_{W1–O1} \approx 1.86$ Å. From the fit (solid red line) of Fig. 5.16, the bond lengths $d_{W1–O1} \approx 1.911$ Å and $d_{W1–O1} \approx 1.906$ Å for the same temperatures were extrapolated, which yields a bond length decrease in the present work of a factor six smaller than in Magraso *et al.*[50]. This discrepancy is ascribed to the large vibrations of the 24*d* Wyckoff site for La_2/W_2 employed in the model used in Magraso *et al.*[50]. It is mentioned in Magraso *et al.*[50] that the apparent W–O apparent bond shortening is caused by circular oscillating movements (libration) of oxygen atoms around W, which make the interatomic distances appear shorter on average. Becka and Cruickshank[128] state that if a molecule is undergoing angular oscillations, in the simplest case the atomic distances will appear too close to the axis of angular oscillations by roughly $1/2rH^2$, where r is their distance from the axis and H^2 the mean square amplitude of angular oscillation (see literature[127] for a detailed derivation). This effect is reported to be generally appreciable above room temperature, as it could be seen for the present W–O bonds in Fig. 5.16 and in Magraso *et al.*[50]. Limiting the oxygen positions along the cubic edge (96*k* - *x*, *x*, *z*) and constraining the vibrations to be perpendicular to the bond seem to also create anharmonic vibrations, as discussed separately in section 5.4.3. As the refinement algorithms try to account for the libration movements projecting such circular trajectories onto a plane, this may result in an off-centred equilibrium position of O_1 atoms. Indeed, structure modelling in common refinement programs allows for only linear anisotropic displacement and thus

cannot model accurately angular oscillations[128]. Although splitting the O_1 site from the 32*f* Wyckoff site (cube corners as for O_2) into the 96*k* Wyckoff site yields better fit residuals, the O_1 atoms in the structure could be better modelled. As it is presented in Fig. 5.17a, the angular oscillations or circular trajectories of O_1 around W_1 might be deduced from the observed neutron scattering densities (ρ_{obs}, in fm x Å^{-3}). The scale is arbitrary and the dots tending towards yellow colour denote higher observed densities. The clouds of the observed densities at the corners of Fig. 5.17a belong to the O_2 atoms situated in the planes perpendicular to the viewing direction [100] and behind the represented W_1–O_1. The structural model used for fitting is shown in Fig. 5.17b, where the O_1 split site (96*k*) and the O_2 site (32*f*) are clearly shown for comparison with Fig. 5.17a. In addition, in Fig. 5.17b one iso-surface (yellow colour) of the nuclear densities calculated from the structural model (ρ_{calc}) used is also presented. By comparing Fig. 5.17a with Fig. 5.17b, it can be ascertained that the model used does not provide an accurate description of the observed scattering densities. This comes clear especially in between the O_1-96*k* split sites, where the observed scattering density is ascribed to the O_1 libration movements around W, averaged in time and space by the diffraction technique.

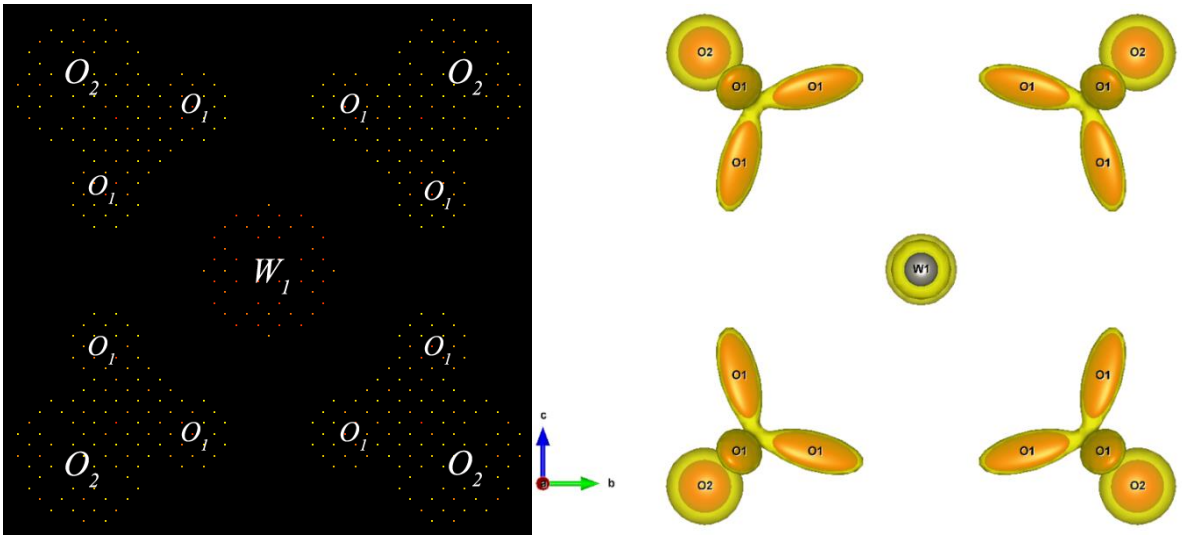

a) ***b)***

Fig. 5.17. ***a)*** *Neutron density map (ρ_{obs}, in fm x Å^{-3}) of LWO_**P**-dry(Ar) specimen, determined by Fourier transformation of observed ND intensity at T = 5 K, where the W_1–O_1 detail is presented. Dots tending towards yellow and red colours denote higher and lower observed scattering densities, respectively. At the corners of the figure the scattering densities of the O_2 atoms from the lattice planes behind O_1 are also visible. The reader is referred to Fig. 5.17b for comparison.* ***b)*** *W_1–O_1 cube as refined for T = 5 K, where the red ellipsoids represent 50 % probability. The iso-surfaces in yellow are the modelled nuclear densities (VESTA program). Both a) and b) figures are shown along the [100] direction.*

Finally, it is suggested that rigid body refinements as performed, e.g., in macromolecular crystallography with translation-libration-screw (TLS) motion[129] could describe more accurately the W_1–O_1 octahedron and decrease even further the O_1 associated static disorder found with the present model. TLS studies were for instance carried out on silicates and reported by Downs *et al.*[127]. Rigid body refinements and TLS studies are, at present, beyond the scope of this work.

In Fig. 5.18 some selected bond lengths as a function of temperature, obtained from ND and HRXRD data refinements on LWO_**P**-dry patterns collected at D2B (dry(Ar)) and MS (dry(S.A.)) experimental stations, respectively, are compared. The metal-oxygen (La_1–O_2, W_1–O_1, 48*h*–O_2) distances and the apparent *48*h*–48*h* distance (*La_2/W_2–La_2/W_2, where the asterisk means that is not a real bond) are represented, along with linear fits in dotted (HRXRD) and dash-dotted (ND) lines. ND data refinements were performed with the isotropic model (see Fig. 5.16), in order to give physical W_1–O_1 bond-length

temperature dependence and to compare consistently the results with the HRXRD data refinements, also performed with isotropic displacement parameters. The 48*h* site distances to the many different O_1 atom equivalent positions (real and apparent) are not considered here due to the large disorder of the W_1–O_1 octahedra and the split 48*h* site. The different (real and apparent) bond lengths are a consequence of the diffraction technique itself, which is averaging in time and space all the unit cells participating to scattering (see Fig. 5.8). Therefore, some of the bond lengths obtained from the Rietveld refinements are not real. To clarify this point, studies on a local scale with techniques such as pair distribution function (PDF) or X-ray absorption spectroscopy (XAS) studies on LWO have been carried out elsewhere[51,54].

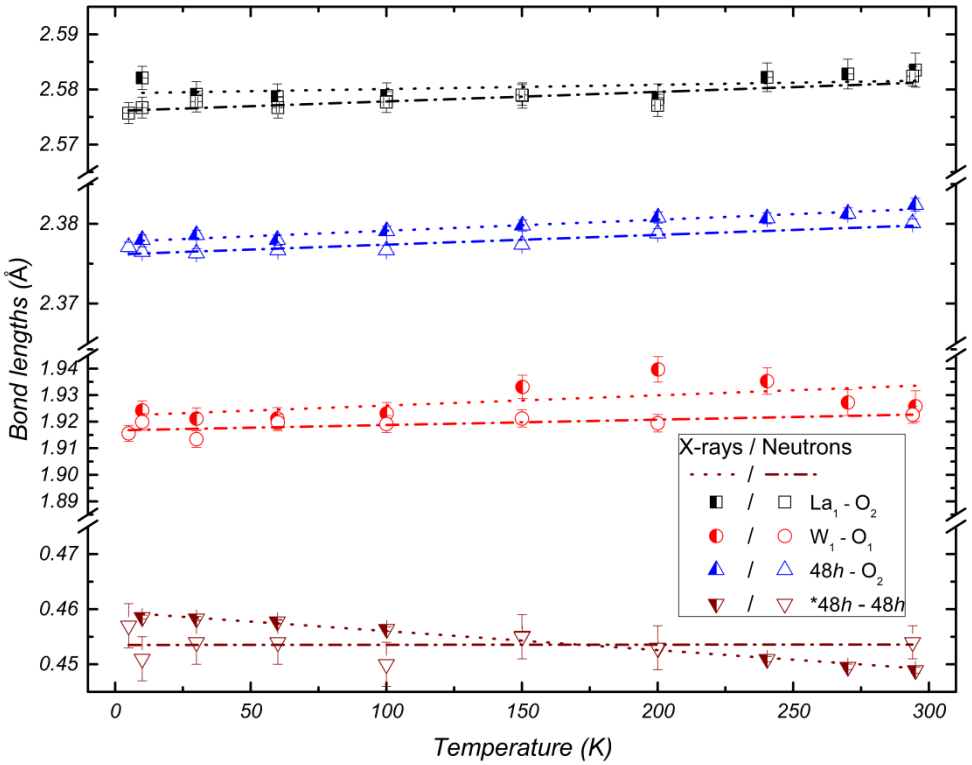

*Fig. 5.18. Selected bond lengths as a function of temperature, obtained from ND data and HRXRD data refinements of LWO_**P**-dry specimen at D2B, dry(Ar), and MS, dry(S.A.), experimental stations, respectively. Some of the first metal-oxygen shells and the apparent *48h–48h distance (*La_2/W_2-La_2/W_2) are represented, along with linear fits in dotted (HRXRD) and dash-dotted (ND) lines. ND data are refined with the isotropic model (see Fig. 5.16).The asterisk refers to an apparent bond length.*

Notice how in Fig. 5.18 the different diffraction techniques give complementary information. Neutrons are more reliable than X-rays in establishing positions of nuclei and light elements, in addition to the parameters accounting for their atomic vibrations. Due to the high-resolution achievable with synchrotron X-ray diffraction and the proportionality of the scattering power of X-rays to the atomic electron density, X-ray diffraction is more powerful to establish the position of heavy metals in the structure. These different characteristics of X-ray diffraction and neutron diffraction are evident from Fig. 5.18: the metal-oxygen distances obtained from ND data as a function of temperature (open symbols) are generally better interpolated due to the lower uncertainties (factor of two for *48*h*–48*h* and W_1–O_1) than those obtained from HRXRD data (half-filled symbols). Moreover, the refined W_1–O_1 bond distances in the HRXRD patterns (half-filled circles) collected at T = 150 K, T = 200 K and T = 240 K separate significantly from the W_1–O_1 bond lengths obtained with ND data (open circles). On the other hand, the apparent *48*h*–48*h* bond length (reversed triangles) could be fitted by a horizontal line when the ND data is considered. The resulting fit is very poor (brown dash dotted line, R^2 = 0.66). HRXRD

yields, instead, precise *48*h*–48*h* distances (the errors are within the symbols) and the linear fit performed gives a satisfactory R^2 = 0.98 and a decreasing *48*h*–48*h* distance with increasing temperature. This finding is represented in Fig. 5.19, where the meaning of real and apparent bond is stressed emphasizing the local structure of LWO according to Scherb *et al.*[54] from the refined average structure obtained through diffraction.

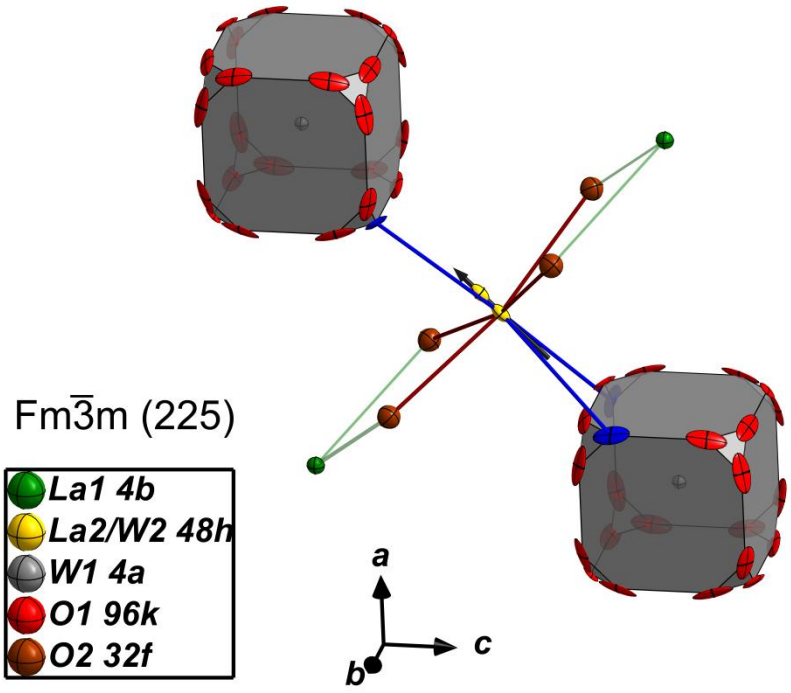

*Fig. 5.19. Average surroundings of the La_2/W_2 atoms (yellow ellipsoids) occupying the 48h 'split' position. If only the La_2 atom occupies the 48h Wyckoff site its average coordination is seven, where 4 oxygen atoms occupy the 32f position (brown spheres and bonding) bonded to the La_1 in the 4b position (green spheres), and the remaining 3 oxygen atom positions (blue ellipsoids and bonding) are shared with the two closest W (grey spheres). The La_2 atoms are closer to the octahedron with which they share two oxygen atoms. The black arrow represents the direction into which one single La_2 atom moves more and more with increasing temperature (cf. *48h–48h bond lengths in Fig. 5.18). The description is reversed (cf. text) for the 48h equivalent position (yellow ellipsoid represented without bonds).*

The La_2/W_2 atoms are represented by yellow ellipsoids and occupy the 48*h* Wyckoff sites according to the average structure shown in Fig. 5.8. Locally, one W_2 occupies the 48*h* Wyckoff site replacing La_2 in a 1:24 ratio. The coordination shown in Fig. 5.19 for one 48*h* site considers that only La_2 occupies that 48*h* site. Thus, the 7-fold coordination to oxygen atoms of La_2 is presented[51,54]. The following reasoning is therefore valid for La_2 atoms. In case of a vacancy-free structure, a La_2 atom shares 4 oxygen atoms (brown spheres) with a La_1 atom (green spheres) and the other 3 oxygen atoms (blue ellipsoids) with W_1 atoms of the two closest octahedra. La_2 atoms are bonded more strongly to the octahedron with which they share two oxygen atoms. The situation is reversed for the other La_2 atom (in yellow, without bonds), occupying the symmetric equivalent position, for which the same reasoning applies. As a general rule, when the temperature increases the bond lengths increases, provided that thermal expansion is positive in the temperature range studied (see Fig. 5.12). In the present case, the W_1–O_1 (Fig. 5.18 or Fig. 5.16) or the two closest La_2–O_1 bond distances (in blue) should increase with increasing temperature. In turn, the apparent distance between the *48*h*–48*h* Wyckoff sites decreases. Finally, one could speculate whether and at which temperature the split 48*h* position may be reasonably

represented by a 'un-split' 24*d* Wyckoff site. However, if the linear trend for the *48*h*–48*h* distance with increasing temperature of Fig. 5.19 is considered (brown dotted line), this temperature is by far beyond the melting point of LWO.

5.2 $La_{5.4}W_{1-y}Re_yO_{12-\delta}$ ($0 \le y \le 0.2$)

5.2.1 Composition studies

In Table 5.5, a resume of the samples investigated in this chapter, along with the preparation methods, nominal and refined compositions, eventual secondary phases, techniques and sample labels, is presented. Specimens LWO52 and LWO56 introduced in chapter 5.1 are also referred to in this chapter and therefore they are reported in Table 5.5 for completeness. The overall composition presented in Table 5.5 includes the correction due to secondary phases already mentioned in chapter 5.1.2. More details on their calculation will follow.

Table 5.5. Preparation method, nominal and experimental composition, single phase status, techniques used and sample labels used throughout this chapter.

Sample series, preparation method nominal composition	***Experimental (EPMA+XRD) overall composition***	***Secondary phases***	***Techniques used***	***Label of referred samples in this chapter***
$La_{6-x}WO_{12-\delta}$ ($0.4 \le x \le 0.8$) Solid State Reaction			XRD, TG	LWO series
$La_{5.6}WO_{12-\delta}$	$La_{5.78(4)}WO_{12-\delta}$	La_2O_3 (< 1 wt. %)		LWO56
$La_{5.2}WO_{12-\delta}$	$La_{5.34(4)}WO_{12-\delta}$	$La_6W_2O_{15}$ (< 1 wt. %)		LWO52
$La_{5.4}W_{1-y}Re_yO_{12-\delta}$ ($0 \le y \le 0.2$) Pechini method			EPMA, XRD, TG,	LW(Re)O
$La_{5.4}WO_{12-\delta}$	$La_{5.56(3)}WO_{12-\delta}$	No	ND, HRXRD	LWO_**P**
$La_{5.4}W_{0.998}Re_{0.002}O_{12-\delta}$	$La_{5.67(3)}W_{0.997(1)}Re_{0.003(1)}O_{12-\delta}$	No	ND	Re02
$La_{5.4}W_{0.995}Re_{0.005}O_{12-\delta}$	$La_{5.66(3)}W_{0.994(1)}Re_{0.006(1)}O_{12-\delta}$	No	ND	Re05
$La_{5.4}W_{0.99}Re_{0.01}O_{12-\delta}$	$La_{5.61(3)}W_{0.990(2)}Re_{0.010(2)}O_{12-\delta}$	No	ND	Re1
$La_{5.4}W_{0.95}Re_{0.05}O_{12-\delta}$	$La_{5.61(3)}W_{0.951(2)}Re_{0.049(2)}O_{12-\delta}$	No	ND	Re5
$La_{5.4}W_{0.90}Re_{0.1}O_{12-\delta}$	$La_{5.65(6)}W_{0.899(5)}Re_{0.101(5)}O_{12-\delta}$	No	ND	Re10
$La_{5.4}W_{0.85}Re_{0.15}O_{12-\delta}$	$La_{5.67(5)}W_{0.858(5)}Re_{0.142(5)}O_{12-\delta}$	No	ND	Re15
$La_{5.4}W_{0.8}Re_{0.2}O_{12-\delta}$	$La_{5.66(7)}W_{0.845(7)}Re_{0.155(7)}O_{12-\delta}$	$La_6W_2O_{15}$ (< 3 wt. %), Re- rich phase		Re20_IMP*
$La_{5.4}W_{0.8}Re_{0.2}O_{12-\delta}$	$La_{5.86(7)}W_{0.826(7)}Re_{0.174(7)}O_{12-\delta}$	No	ND, HRXRD	Re20

Fig. 5.20 shows the La/(W+Re) ratios of the investigated specimens (Table 5.5) as a function of Re/(W+Re). The compositions of the LW(Re)O series measured with EPMA are indicated by green squares. The composition of the LWO series (open green squares) was determined through Vegard's law[99] and scaled to the composition of LWO_**P** measured with EPMA (see section 5.1.1). Open red squares describe the calculated La/(W+Re) ratios which take into account the contribution of secondary phases found by XRD (values reported in Table 5.5). An estimation of the single-phase region of LW(Re)O is reported in Fig. 5.20 (white region, delimited by green dotted lines). On the left side of Fig. 5.20, the single-phase region includes all the open green squares, beginning at La/W = 5.36(4) (LWO52

* The suffix '_IMP' stays for impure: it was added to the labelling in order to distinguish the phase-impure Re20 specimen (Re20_IMP) from the phase-pure one (Re20), due to the same nominal composition.

open green square) and ending at La/W = 5.76(4) (LWO56 open green square). On the right side of Fig. 5.20, due to the lack of experimental data points, the single phase region boundaries – green dotted lines – should reduce to a point at Re/(W+Re) ≈ 0.20, where a limit for Re solubility in LWO has been found[31,32] (grey region). Secondary phases were found in some samples (Re20_IMP, LWO52, LWO56) by XRD and their composition corrected (red squares in Fig. 5.20) accordingly as explained in the phase analysis section below. These phases were determined to be $La_6W_2O_{15}$ for data points within the orange region and to La_2O_3 for data points within the blue region[32,46,59], respectively, below and above the single-phase region in Fig. 5.20.

A BSE image of sample Re20_IMP is shown in Fig. 5.21. Large (diameter ≈ 5 µm to ≈ 20 µm) and small (< 2 µm) grains are observed. The difference in grain colour (whitish to dark grey) is due to different grain orientations and elemental contrast. The EPMA measurements taken in the (5-20) µm sized grains yield a composition of $La_{5.74(7)}W_{0.85(1)}Re_{0.15(1)}O_{12-\delta}$, which is ascribed to the main phase present in the specimen, while the EPMA measurements in smaller grains (< 2 µm) indicate a La/(W+Re) ratio of 3.5(4), which is referred to the secondary phase. Comparable results are reported from SEM/EDX measurements for samples of similar composition[32].

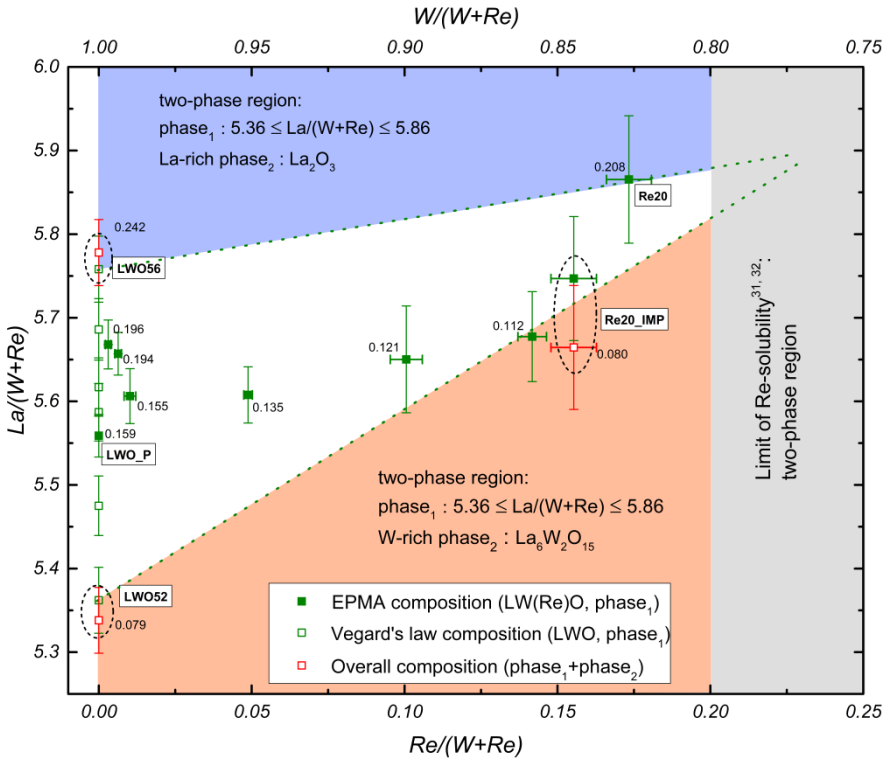

*Fig. 5.20. La/(W+Re) ratio as a function of W substitution by Re (Re/(W+Re)). The La/(W+Re) ratios described by green squares were determined by EPMA, the open green squares were determined through Vegard's law and comparison to LWO_**P** (cf. section 5.1.1), while the open red squares describe the La/W ratios modified according to secondary phase contributions indexed and quantified by XRD simulations. The white region between the green dotted lines represents the single-phase region of LW(Re)O specimens. The grey region represents the limit of Re solubility in LWO reported in the literature[31,32]. The mass loss (Δm in wt. %, reported next to the squares) has been measured by TG on humidified (D_2O(Ar)) samples with an error of about 0.005 wt. % (95 % C.L.). The samples LWO52, LWO56, LWO_**P**, Re20_IMP and Re20 are labelled in the figure.*

Discussion: according to the simulations of beam penetration depth, the measured compositions of the biggest grains shown in Fig. 5.21 are reliable, while for the grains of the secondary phase (< 2 µm) the composition measured yields a mixture of different phase compositions. For the Re20_IMP sample, the La/(W+Re) ratio of 3.5(4) corresponds to the $La_6W_2O_{15}$ phase. However, some of a highly Re-enriched

phase was also found by EPMA, which gives rise to a Re/(W+Re) ratio of ≈ 0.3. As only $La_6W_2O_{15}$ has been indexed in the available XRD-data base, it seems that the highly Re-enriched phase is present in small amounts and/or its crystallite size is appreciably below the coherence length of X-rays.

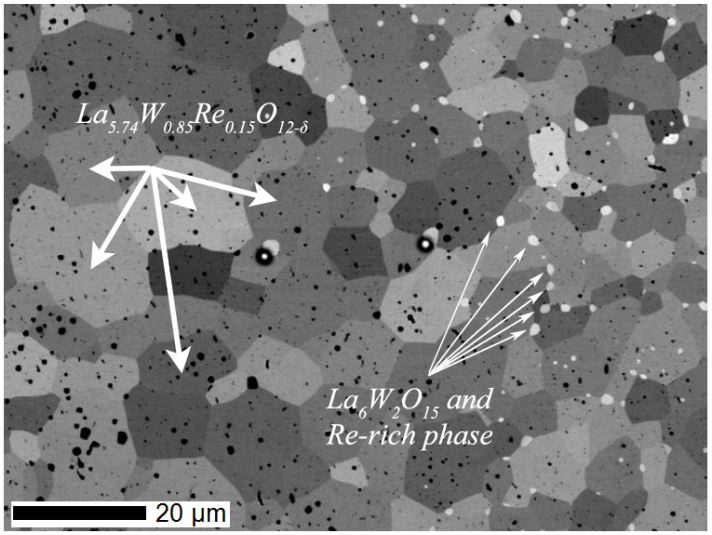

Fig. 5.21. Electron back-scattered image of sample Re20_IMP. Different grain sizes can be identified in the figure, where larger grains (between 5 µm and 20 µm, some of them indicated by thick white arrows) correspond to the main phase $La_{5.74}W_{0.85}Re_{0.15}O_{12-\delta}$ and smaller grains (< 2 µm, some of them indicated by thin white arrows) correspond to the secondary phase $La_6W_2O_{15}$ plus an unidentified Re-rich phase (cf. text). Bright points surrounded by black rings (sputtered carbon built-up) are the electron beam marks (Ø ≈ 500 nm) caused by the EPMA measurements.

Another possibility could be that the highly Re-enriched and the $La_6W_2O_{15}$ phases are the same phase in the form of $La_6W_{2-x}Re_xO_{15}$ and cannot be distinguished from $La_6W_2O_{15}$ by XRD. As at present neither the composition nor the amount of this highly Re-enriched phase can be estimated, only $La_6W_2O_{15}$ is mentioned in Fig. 5.20. DFT calculations[51] have shown that oxygen vacancies in LWO have a slightly lower energy when occupying the 32*f* Wyckoff site of the $Fm\bar{3}m$ space group and are bonded to the La_1 (4*b* Wyckoff) and La_2/W_2 (24d or 48h Wyckoff) sites. A higher concentration of La compared with W, therefore, results in a higher concentration of oxygen vacancies, which allows for a higher uptake of OD molecules into the lattice. This conclusion has been proven experimentally by Hancke *et al.*[108,109] and with TG in section 5.1.3, where it is shown that a higher La/W ratio corresponds to a higher mass loss caused by incorporated OD groups (see Fig. 5.5), i.e., to a higher concentration of oxygen vacancies. EPMA in combination with TG measurements, as reported in Fig. 5.20 suggest the same behaviour for LWO and LW(Re)O specimens, where a higher OD incorporation has been found with increasing La/(W+Re) content at a fixed Re/(W+Re). Furthermore, in order to obtain the same mass loss with increasing Re content, a shift to higher La/(W+Re) ratio can be noticed. This fact might be due to a possible slight decrease of the ionic conductivity with higher Re-concentration, which could be caused by the higher Re oxidation state (Re^{7+}) than that of the replaced W (W^{6+}). Having Re^{7+} instead of W^{6+}, according to the charge compensation given by Eq. (5.6), decreases the number of vacancies available to be filled (more on this in the final chapter). Even if this result cannot be directly compared with the literature, a lower hydration effect on conductivity is observed for the highest Re-substituted specimen (nominal LWO-Re20) when compared to the parent compound (see Seeger *et al.*[32] and Fig. 2.1). Such lower hydration effect can be ascertained by comparing the conductivities of the same compound in dry and wet(Ar/H_2).

5.2.2 Phase analysis

In Fig. 5.22, the XRD patterns of the LW(Re)O-dry(Ar) system are shown as a function of the scattering angle 2Θ.

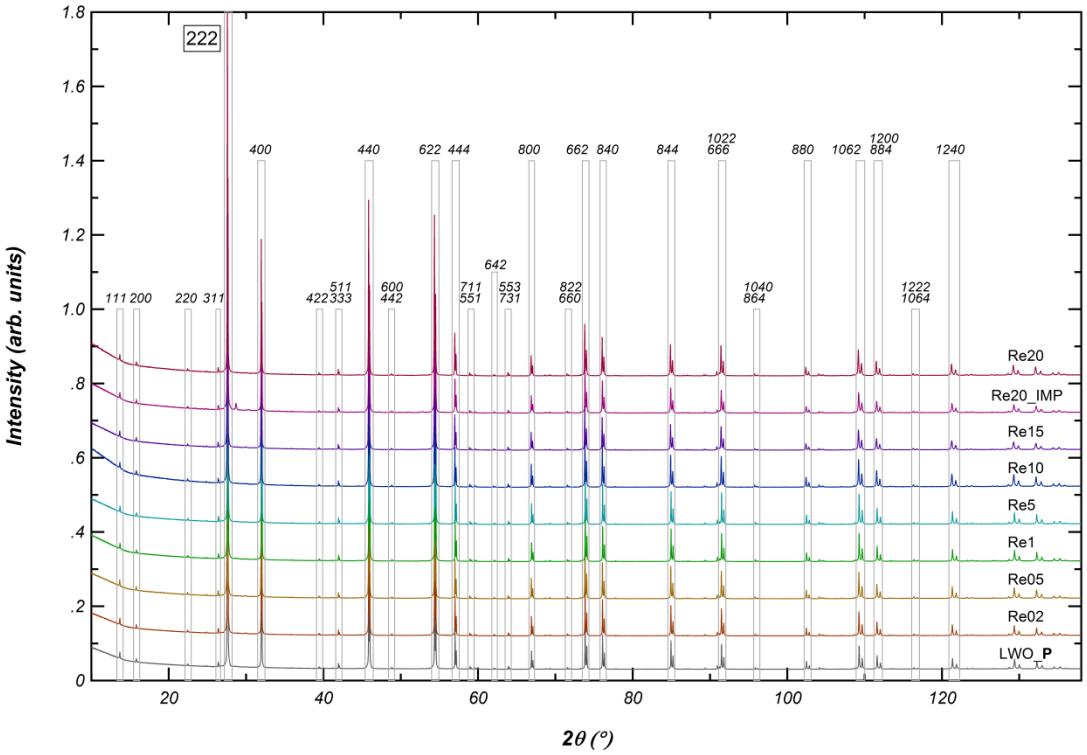

*Fig. 5.22. XRD patterns of the LW(Re)O-dry(Ar) specimens as a function of the scattering angle 2Θ (10° ≤ 2Θ ≤ 138°). The patterns are presented from the non-substituted LWO_**P** (black pattern) to the highest nominal Re/(W+Re) ratio (Re20, in red), from bottom to top, respectively. The hkl indices of the main reflections below 2Θ = 130° are also shown ($Fm\bar{3}m$ space group), and the patterns are normalized to the peak of highest intensity (hkl = 222 reflection). Peak splitting is due to the CuKα_1/Kα_2 doublet.*

All XRD peaks were indexed with the primary phase of the LWO series ($Fm\bar{3}m$ cubic) and a secondary phase $La_6W_2O_{15}$ ($C222_1$ orthorhombic[59,110]) in the case of Re20_IMP, visible in Fig. 5.22 between the (222) and the (400) reflections. One might notice that peak indexing implies no apparent change of the reflection conditions (*h*, *k*, *l* all odd or all even, i.e. *fcc* lattice) and of the superstructure reflections between the primary phase of LWO and that of LW(Re)O. Further structural details of LW(Re)O will be discussed in the following sections.

Discussion: Rietveld refinement is expected to provide the amount of different phases in Re20_IMP by using the integrated peak intensities of the diffraction patterns, from which the actual composition of the samples containing secondary phases can be inferred. However, as for LWO52 and LWO56, the XRD data fits on Re20_IMP failed when the crystal structure of the secondary phase given by the literature[59,110,111] was used. It is therefore concluded that the amount of the secondary phase(s) is too low to be refined as the peaks of the $La_6W_2O_{15}$ secondary phases of Re20_IMP are mostly hidden in the background. Nevertheless, single peak fitting and pattern simulations (using software CMPR) resulted in a maximum amount of $La_6W_2O_{15}$ of 3 wt. % for Re20_IMP. Considering the estimated amount of $La_6W_2O_{15}$, the La/(W+Re) ratio of sample Re20_IMP decreases from 5.74(7) to 5.66(7) (open red square Re20_IMP on the right hand side in Fig. 5.20). For completeness, the change in La/W ratio for sample LWO52 and LWO56 is also reported in Fig. 5.20, where the former decreases from La/W = 5.36(4) to La/W = 5.34(4) (open red square LWO52, bottom left of Fig. 5.20), and the latter increases from La/W = 5.76(4) to La/W = 5.78(4) (open red square LWO56, top left of Fig. 5.20).

5.2.3 Water uptake

In Fig. 5.23 the TG curves of the LW(Re)O-D_2O(Ar) specimens are presented.

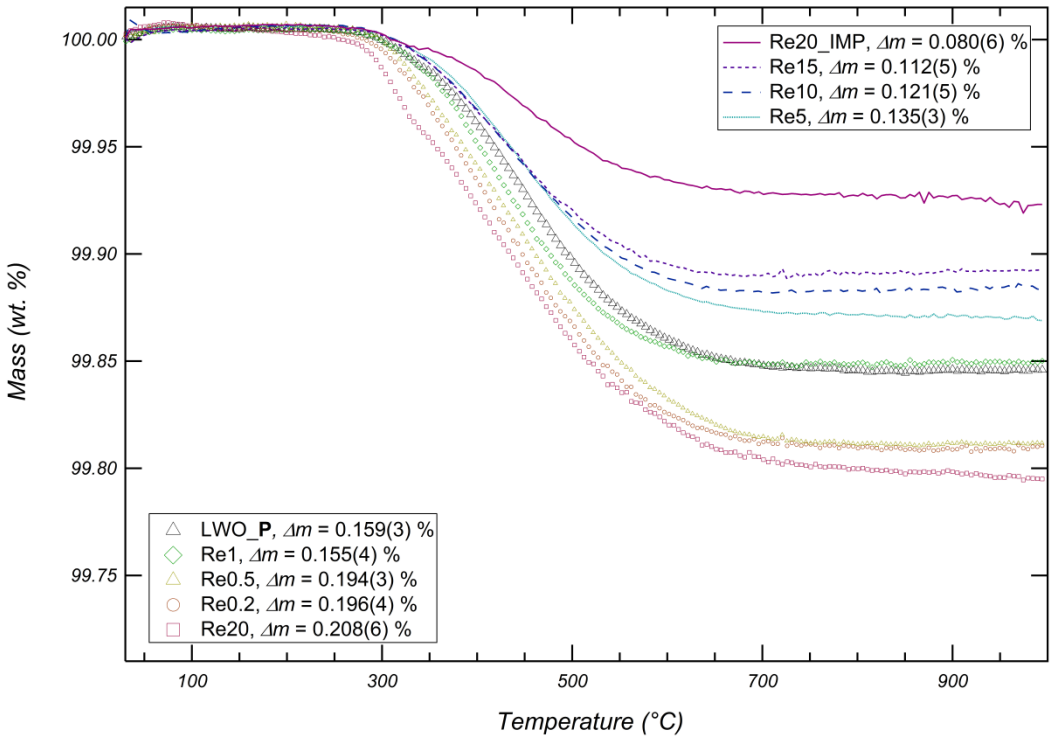

*Fig. 5.23. Thermogravimetric curves of LW(Re)O-D_2O(Ar) specimens measured under dry(Ar) gas, where the mass (wt. %) in dependence of temperature is shown. The colours used correspond to the colours used in Fig. 5.22. Δm values are resumed in the legend with a 95 % confidence level uncertainty. Lines and markers were used to distinguish the TG curves above and below the LWO_**P** TG curve (black plus markers).*

The values of *Δm* as well as the onset temperatures of mass loss T_i for LW(Re)O seem to be independent of the Re substitution. According to Fig. 5.20, the La/(W+Re) ratios need to be taken into account in order to understand the mass loss of LW(Re)O. The detailed explanation in terms of vacancy concentration will be reported in the final part of this work along with the comparison with the other systems investigated. However, particular attention to the curve at the top (Re20_IMP, line) and the curve at the bottom (Re20, squares) of Fig. 5.23 must be given. These TG curves are anomalous compared to the TG curves of the other LW(Re)O specimens, in the sense that they follow a multiple-stage decay.

Discussion: the Re20 specimen shows a similar behaviour to the LWO56 TG curve presented earlier (see Fig. 5.3, Fig. 5.4) hinting at a possible $La(OD)_3$ contribution, despite this specimen being supposed to be phase-pure (see Fig. 5.20). In contrast, the BSE image and the XRD patterns of the Re20_IMP specimen show only $La_6W_2O_{15}$ as a secondary phase (cf. Fig. 5.21, Fig. 5.22). It is expected that the $La_6W_2O_{15}$ secondary phase contributes neither to the mass loss nor to the TG curve of the main phase appreciably. This can be deduced from the TG and ion current measurements of the other $La_6W_2O_{15}$-containing specimen LWO52, where no anomalies were observed (cf. Fig. 5.3 and Fig. 5.5). These apparent inconsistencies, i.e. the unexpected contributions of La_2O_3 and $La_6W_2O_{15}$ phases to the Re20 and Re20_IMP TG curves, are discussed separately in section 5.2.5. It will be shown that in Re20 the TG anomaly is caused by segregation of La_2O_3 occurred over time, proved by XRD analysis. The TG anomaly in Re20_IMP will be ascribed to $La_6W_2O_{15}$ according to the TG curve of the pure $La_6W_2O_{15}$ specimen (same sample used by Ivanova *et al.*[59]) measured in the present work. The TG curve of $La_6W_2O_{15}$

presents a much lower onset temperature T_i than that of Re20_IMP. In addition, the amount of $La_6W_2O_{15}$ in Re20_IMP (< 3 wt. %) is sufficient to discriminate $La_6W_2O_{15}$ in the ion current measurements.

5.2.4 Crystal structure of Re20 ($La_{5.86}W_{0.83}Re_{0.17}O_{12-\delta}$)

5.2.4.1 Method of the average neutron scattering length

The final structure for the non-substituted LWO_**P** shown in Fig. 5.8 was adopted as a starting point to characterise the structure of Re-substituted specimens. Three possible models for Re substitution on W positions within the $Fm\bar{3}m$ space group are considered: (i) Re occupies exclusively the 4*a* Wyckoff site (Model A), (ii) Re occupies exclusively the 48*h* Wyckoff site (Model B), and (iii) Re statistically occupies 4*a* and 48*h* Wyckoff sites (Model C) (see Fig. 5.8). Due to the very different atomic radii of La ($R_i(La)_{3+}^{8fold}$= 1.16 Å) and Re ($R_i(Re)_{4+}^{6fold}$= 0.63 Å), Re substitution on the La_1 site was not considered. The first approach to determine the structure of Re20 was to refine the site occupancies with a single atom per site, a procedure known as average neutron scattering length[90,130], using the $Fm\bar{3}m$ space group (see section 4.4.3.2 for details). According to the refinement of the LWO_**P** sample, W atoms sit on 4*a* Wyckoff sites, whilst La occupies 4*b* and 48*h* Wyckoff sites. Vacancies on 4*a*, 4*b* and 48*h* Wyckoff sites are not considered. Refinements of occupancies within the average neutron scattering length approach have been done for each data set measured at the D2B beamline at ILL (*T* = 5 K) and at the HRPT beamline at the PSI (*T* = 1.5 K, *T* = 10 K) for dry(Ar) and D_2O(Ar/S.A.) humidified specimens. The results of the refinements are listed in Table 5.6. For comparison, the results of the refinements on LWO_**P** specimen through the neutron scattering length approach have also been added to Table 5.6.

*Table 5.6. Refined site occupancy factors of Re20 cation sites estimated through the average scattering approach for all low temperatures data sets acquired (first column). The weighted average site occupancy factors for the Re20 specimen and, for comparison, for the LWO_**P** specimen are reported in the bottom rows, and were calculated according to Eqs. (4.24) and (4.25). The asterisks (*) mean that it was not possible to refine simultaneously that SOF with all the other parameters (cf. text).*

Temp. - condition	SOF_{4a}^{W}	$SOF_{4b}^{La_1}$	$SOF_{48h}^{La_2}$
	Sample Re20		
10 K dry(Ar)^{HRPT}	1.162(22)	1.014(13)	0.489(2)
1.5 K D_2O(S.A.)^{HRPT}	1.093(21)	0.988(13)	0.495(3)
5 K dry(Ar)^{D2B}	1.174(23)*	0.983(15)	0.488(3)*
5 K D_2O(Ar)^{D2B}	1.133(24)	0.975(14)	0.492(3)
Average site occupancy	1.139(11)	0.988(7)	0.491(1)
	Sample LWO_P		
Average site occupancy	0.994(13)	0.989(8)	0.486(1)

From Table 5.6 it is clear that not only W atoms occupy the 4*a* Wyckoff site, as its occupancy values are much larger than one. The refined coherent scattering length of the 4*a* position is $\bar{b}_{4a}^{exp}$ = 5.42(5) fm and yields a Re concentration on the 4*a* site of 0.149(11). The same conclusion could be inferred for the 48*h* Wyckoff site after comparison between the average scattering occupancies of Re20 and LWO_**P** (Table 5.6) as the refined occupancy of the 48*h* site in LWO_**P** is 0.486(1) compared to 0.491(1) for Re20. However, due to the higher La/(W+Re) ratio of Re20 (La/(W+Re) = 5.86) compared to the LWO_**P** specimen (La/(W+Re) = 5.56), the 48*h* average occupancy for Re20 could also reflect a higher La contribution. Due to the fact that for each measured sample the 48*h* occupancies have in general La/(W+Re) ratio-dependent La contributions difficult to isolate, the 4*a* site (shared only by Re and W) average scattering length has been studied for the whole LW(Re)O series. Due to the low powder

amount, the LWO_**P** and Re1 specimens were prepared only in the D_2O(S.A.) condition for HRPT measurements. In addition, when the pre-treatments were performed under dry(Ar) conditions, such as the Re20-dry(Ar) pattern measured at D2B (see Table 5.6), the simultaneous refinement of all the occupancies gave inconsistent results. For the Re20-dry(Ar) D2B pattern, the refinement yielded a Re amount ≈35 % larger than that of EPMA ($\bar{b}_{4a}^{exp}$ = 5.9(1), Re/(W+Re) = 26(2) %). Therefore, only the results on LW(Re)O-D_2O(Ar) and LW(Re)O-D_2O(S.A.) specimens, for D2B and HRPT respectively, are compared in Fig. 5.24. A comparison of the average neutron scattering lengths considering the Re-concentration determined with EPMA (Fig. 5.20) is also presented in Fig. 5.24.

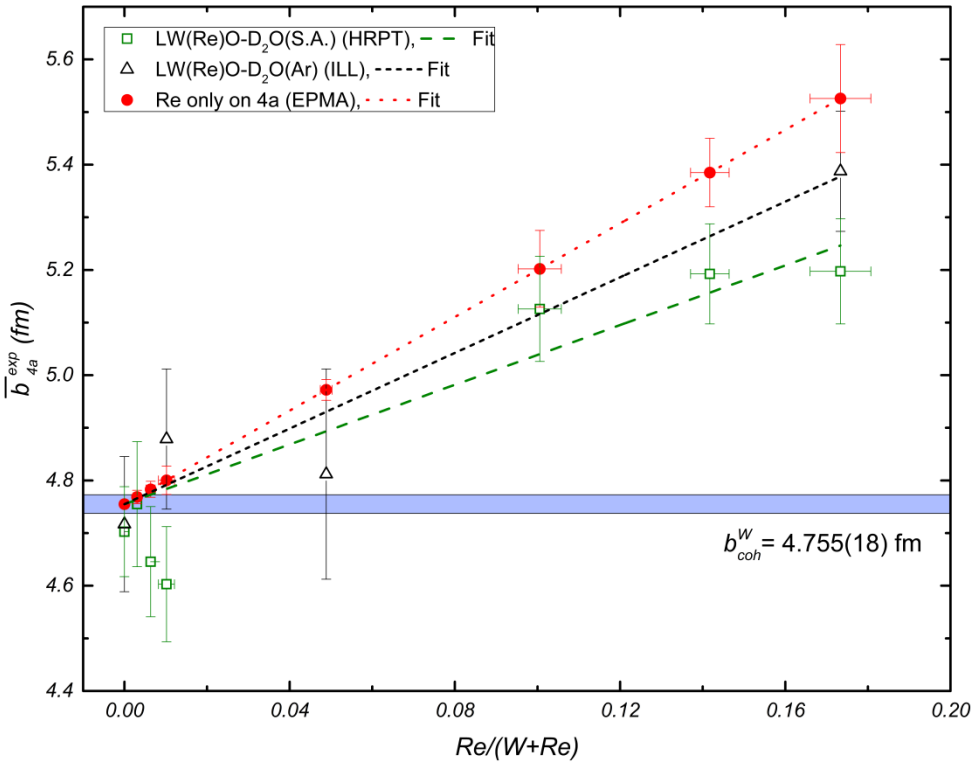

*Fig. 5.24. Average neutron scattering length of the 4a–W_1 Wyckoff site, $\bar{b}_{4a}^{exp}$, for the LW(Re)O series given as a function of W substitution by Re (Re/(W+Re)). Open green squares represent the $\bar{b}_{4a}^{exp}$ obtained from refinements performed on D_2O(S.A.) specimens measured at HRPT at 10 K (Re02, Re05, Re1, Re10, Re15, Re20) and at T = 1.5 K (LWO_**P**). Open black triangles represent the $\bar{b}_{4a}^{exp}$ obtained from refinements performed on D_2O(Ar) specimens measured at ILL at 5 K (LWO_**P**, Re20) and T = 298 K (Re1, Re5). Full red circles show the 4a site occupancy calculated under the assumption that the Re amount measured by EPMA entirely occupies the 4a site. Fits are straight lines performed with direct x-weighting (larger Re/(W+Re) weighs more) and with $\bar{b}_{4a}^{exp}$ (0) = 1 (4a fully occupied for the non-substituted LWO_**P**). The coherent scattering length of W is depicted in light blue.*

The 4*a* site occupancies obtained from the D2B data (open black triangles) and HRPT data (open green squares), deviate from the Re-content measured by EPMA assuming only Re on the 4*a* site (full red circles). This deviation increases with increasing Re concentration, suggesting that Re atoms do not occupy exclusively the 4*a* site. By combining EPMA and ND measurements, it is therefore possible to place the missing Re concentration on the 48*h* Wyckoff sites. According to these results it can be confidently concluded that Re is statistically substituting W. Re occupies the 4*a* position, shared with W, but also resides on the 48*h* position, shared by both W and La.

The above results from average scattering length refinements suggest that model (A) and model (B) can be excluded and model (C) is most appropriate to describe the structure of Re20, with Re occupying both 4*a* and 48*h* Wyckoff sites. Finally, the refinement strategy for the Re20 specimen can be

developed. As only two atoms (labelled W_1, Re_1) are sharing the 4*a* site, the starting occupancy values are set according to the average scattering length refinements, i.e. SOF_{4a}^{W1} = 0.851 and SOF_{4a}^{Re1}= 0.149, constrained to full site occupancy (SOF_{4a}^{W1} + SOF_{4a}^{Re1} = 1). In order to establish the starting values of the occupancies of the 48*h* Wyckoff site, another consideration has to be made. There are three atoms (labelled La_2, W_2, Re_2) that share the 48*h* Wyckoff site. From a computational point of view, only two equations (see below) are available to determine the three occupancies (SOF_{48h}^{La2}, SOF_{48h}^{W2} and SOF_{48h}^{Re2}): one equation that assumes half site occupancy of the 48*h* site,

$$SOF_{48h}^{La2} + SOF_{48h}^{W2} + SOF_{48h}^{Re2} = 0.5\,, \tag{5.15}$$

and a second equation that considers the average scattering length $\bar{b}_{48h}^{exp}$ calculated from Table 5.6,

$$\bar{b}_{48h}^{exp} = SOF_{48h}^{La2} b_{coh}^{La} + SOF_{48h}^{W2} b_{coh}^{W} + SOF_{48h}^{Re2} b_{coh}^{Re} = 0.491 \times b_{coh}^{La}\,, \tag{5.16}$$

where SOF_{48h}^{M2} and b_{coh}^{M} are, respectively, the occupancy of the 48*h* Wyckoff site and the neutron coherent scattering length of atom M.

The additional information for Rietveld refinement is provided by the EPMA measurements (La/(W+Re) = 5.86, cf. Fig. 5.20), which results in Eq. (5.17)

$$\frac{La_{TOT}}{W_{TOT} + Re_{TOT}} = \frac{48 \times SOF_{48h}^{La2} + 4 \times SOF_{4b}^{La1}}{48 \times (SOF_{48h}^{W2} + SOF_{48h}^{Re2}) + 4 \times (SOF_{4a}^{Re1} + SOF_{4a}^{W1})} = 5.86\,. \tag{5.17}$$

The preceding three equations were used to determine the starting refinement occupancies SOF_{48h}^{La2}, SOF_{48h}^{W2} and SOF_{48h}^{Re2} for the 48*h* Wyckoff site. The three unknown parameters are SOF_{48h}^{La2}, SOF_{48h}^{W2} and SOF_{48h}^{Re2}.The occupancy SOF_{4b}^{La1} and the constrained sum of the occupancies SOF_{4a}^{W1}+ SOF_{4a}^{Re1} are set to unity, according to the refinements of LWO_**P** ($\langle SOF_{4a}^{W1} \rangle$ = 0.994(13), $\langle SOF_{4b}^{La1} \rangle$ = 0.989(8), where ⟨ ⟩ denotes the weighted average, cf. Table 5.6) and to the results of Re20 ($\langle occ_{4b}^{La1} \rangle$ = 0.988(7), cf. Table 5.6). The numerical factors on the left hand side of Eq. (5.17) are the numbers of equivalent positions in the unit cell of the respective Wyckoff site (48 for the 48*h* and 4 for 4*a* and 4*b* sites). The site occupancies calculated from Eqs. (5.15)-(5.17) are SOF_{48h}^{La2} = 0.486(1) and therefore SOF_{48h}^{W2} + SOF_{48h}^{Re2} = 0.014(1). Due to the low remaining amount of W_2 and Re_2 the starting values have been set to SOF_{48h}^{W2} = SOF_{48h}^{Re2} = 0.07. In the refinements, the occupancy SOF_{48h}^{La2} was kept fixed to the value calculated (SOF_{48h}^{La2} = 0.486) until all other structural parameters (positions, ADPs, *SOFs*) had reached convergence. Finally, SOF_{48h}^{La2} was refined together with the other structural parameters and its value did not change. On the 48*h* site the parameters SOF_{48h}^{W2} and SOF_{48h}^{Re2} are constrained during the refinement by the condition SOF_{48h}^{W2}+ SOF_{48h}^{Re2} = 0.014. In this way, the ratio La/(W+Re) was fixed and a discrimination between W_2 and Re_2 was possible. Anisotropic displacement parameters were also constrained and set equal for atoms occupying the same Wyckoff site.

5.2.4.2 Neutron diffraction

As the Re20-wet(D_2O) specimens could be refined with all the structural parameters simultaneously, the Re20-D_2O(Ar) refinement results are shown as an example. In Fig. 5.25 and insets, the Re20-D_2O(Ar) ND pattern, along with the corresponding calculated and difference intensities (Rietveld method), is illustrated. The corresponding refined parameters are listed in Table 5.7.

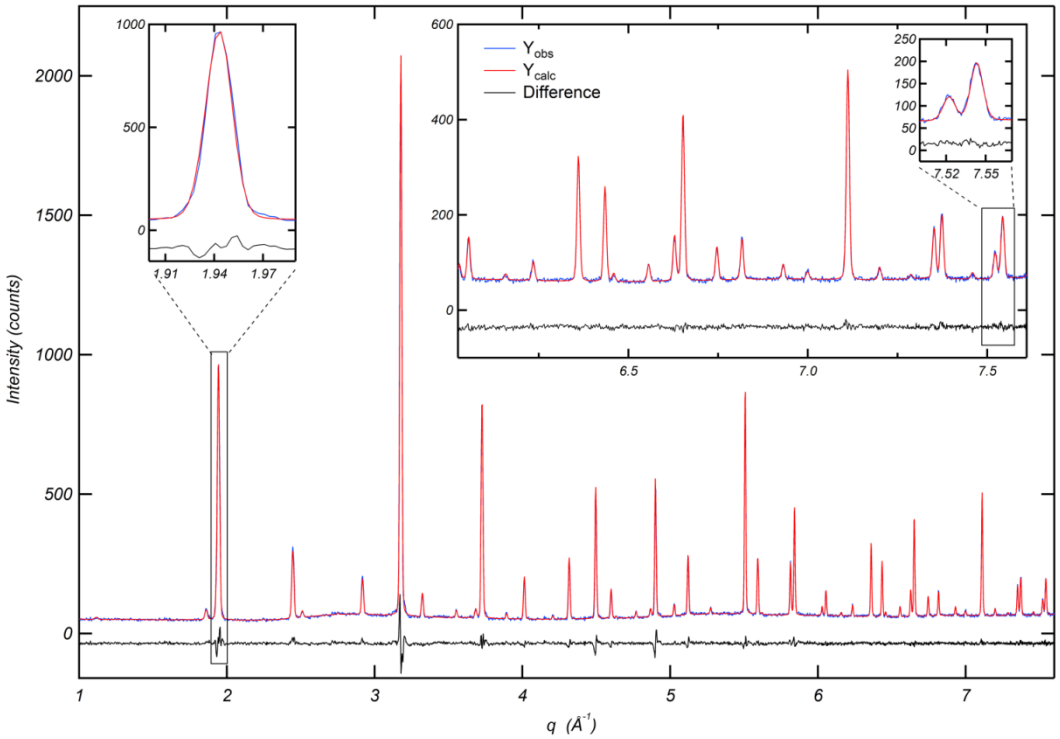

Fig. 5.25. Neutron diffraction intensity plots of Re20-D_2O(Ar) ($La_{5.86}W_{0.826}Re_{0.174}O_{12-\delta}$) data collected at T = 5 K at instrument D2B (ILL), as a function of the exchanged momentum q (blue line), calculated data (red line) and difference of the two (black line). In the inset the high q data (6 Å^{-1} < q < 7.6 Å^{-1}) is magnified, as well as three chosen diffraction peaks, one in the low q range and the last two in the high q range. In the insets, the difference line is shifted for better peak visualization.

Table 5.7. Fractional atomic coordinates, x, y, z, site occupancy factors, SOF, equivalent and anisotropic displacement parameters U_{eq}, U_{xy} of Re20-D_2O(Ar) ($La_{5.86}W_{0.83}Re_{0.17}O_{12-\delta}$) from ND at T = 5 K, refined with space group $Fm\bar{3}m$. All the displacement parameters (U_{eq}, U_{xx} and U_{xy}) are multiplied by a factor of 100. The lattice parameter and the residuals are also reported.

Atom	Site	x	y	z	U_{eq}(Å^2)	SOF
La_1	4*b*	0.5	0.5	0.5	0.82	0.990(14)
W_1	4*a*	0	0	0	0.36	0.854(24)
Re_1	4*a*	0	0	0	0.36	0.146(24)
La_2	48*h*	0	0.2355(2)	0.2355(2)	0.71	0.486(1)
W_2	48*h*	0	0.2355(2)	0.2355(2)	0.71	0.008(5)
Re_2	48*h*	0	0.2355(2)	0.2355(2)	0.71	0.006(5)
O_1	96*k*	0.1122(2)	0.1122(2)	0.0649(3)	1.57	0.245(3)
O_2	32*f*	0.3665(1)	0.3665(1)	0.3665(1)	1.36	0.967(5)
	U_{11}(Å^2)	U_{22}(Å^2)	U_{33}(Å^2)	U_{12}(Å^2)	U_{13}(Å^2)	U_{23}(Å^2)
La_1	0.82(10)	0.82(10)	0.82(10)			
W_1	0.36(14)	0.36(14)	0.36(14)			
Re_1	0.36(14)	0.36(14)	0.36(14)			
La_2	0.67(11)	0.73(16)	0.73(16)			0.26(14)
W_2	0.67(11)	0.73(16)	0.73(16)			0.26(14)
Re_2	0.67(11)	0.73(16)	0.73(16)			0.26(14)
O_1	1.05(17)	1.05(17)	2.60(25)	-0.19(9)	-0.38(10)	-0.38(10)
O_2	1.36(4)	1.36(4)	1.36(4)	0.07(4)	0.07(4)	0.07(4)
Lattice parameter (Å)	T (K)	R_{exp} (%)	R_{wp} (%)	χ^2	R_F^2 (%)	
11.1770(1)	5	3.56	5.63	2.502	3.35	

In Fig. 5.25, the observed and calculated intensities show good agreement to each other, giving the satisfactory residuals of χ^2 = 2.5 and R_F^2 = 3.35 %. From the refined parameters presented in Table 5.7 it is possible to confirm that Re occupies both 48*h* and 4*a* sites, as inferred from the average neutron scattering length (cf. Fig. 5.24). Convergence was achieved with all structural parameters refined simultaneously. In addition, the refined Re amount on the W site, Re/(W+Re) = 0.19(6), and the ratio, La/(W+Re) = 5.8(4), did not vary appreciably within the refinement procedure, keeping comparable values to the initial values calculated according to EPMA and the average neutron scattering length results with Eqs. (5.15)-(5.17). However, due to the simultaneous refinement of all the structural parameters, the uncertainties of the refined site occupancy factors and therefore of the La/(W+Re) or Re/(W+Re) ratios are inevitably significant.

5.2.4.3 High-resolution X-ray diffraction

Due to the similar scattering power of Re (Z_{Re} = 75) and W (Z_W = 74), for the Re20-dry(Ar) specimen neither X-ray studies as a function of temperature nor average scattering power analysis were performed. Instead, as neither the theoretical atomic form factors of Re^{6+} ions are tabulated in the refinement program TOPAS nor in Mann[122], the final refinements were carried out only with W^{6+} ions occupying the 4*a* site and 48*h* site, i.e. without Re substitution. This is due to the low amount of Re and because Re and W are indistinguishable with X-rays. Finally, the measured, calculated and difference X-ray intensity plots of Re20-dry(Ar) specimen are presented in Fig. 5.26 and the refined parameters in Table 5.8.

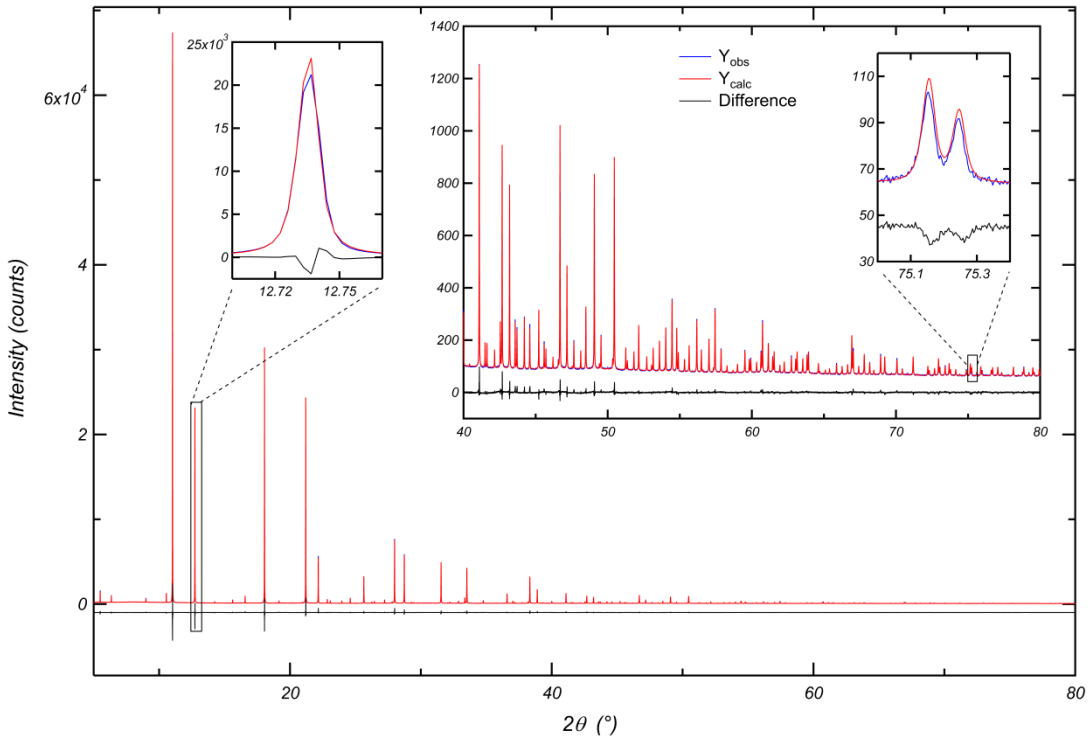

Fig. 5.26. High-resolution X-ray diffraction intensity plots of Re20-dry(Ar) ($La_{5.86}W_{0.826}Re_{0.174}O_{12-\delta}$) data collected at T = 295 K at the MS beamline (SLS) as a function of the scattering angle 2Θ (blue line), calculated data (red line) and difference of the two (black line). In the inset, the high-angle data (40° ≤ 2Θ ≤ 80°) is magnified as well as three chosen diffraction peaks, one at low scattering angles (2Θ ≈ 12.7°) and two at high scattering angles (2Θ ≈ 75.3°). In the insets, the difference line is shifted for better peak visualization.

Despite the approximation with W (W^{6+}) used instead of Re, good residuals were obtained for the refined pattern (χ^2 = 6.69, R_B = 2.05 %). Slight misfits in intensities compared to LWO_**P**, however, were

noticed at high scattering angles (insets Fig. 5.26).

Table 5.8. Fractional atomic coordinates, x, y, z, site occupancy factors, SOF, and anisotropic displacement parameters U_{xy} of Re20-dry(Ar) ($La_{5.86}W_{0.83}Re_{0.17}O_{12-\delta}$) from HRXRD data at T = 295 K, refined with space group $Fm\bar{3}m$. All the displacement parameters (U_{eq}, U_{xx} and U_{xy}) are multiplied by a factor of 100. The lattice parameter and the residuals are also reported. The SOFs in (+) were fixed.

Atom	Site	x	y	z	U_{eq}(Å^2)	SOF
La_1	4*b*	0.5	0.5	0.5	1.06(1)	0.995(1)
W_1	4*a*	0	0	0	0.35(1)	1.011(1)
La_2	48*h*	0	0.23632(2)	0.23632(2)	0.55(1)	0.486$^+$
W_2	48*h*	0	0.23632(2)	0.23632(2)	0.55(1)	0.014$^+$
O_1	96*k*	0.1127(3)	0.1127(3)	0.0673(6)	4.9(3)	0.253(2)
O_2	32*f*	0.3664(2)	0.3664(2)	0.3664(2)	0.99(4)	0.941(6)
	U_{11}(Å^2)	U_{22}(Å^2)	U_{33}(Å^2)	U_{12}(Å^2)	U_{13}(Å^2)	U_{23}(Å^2)
La_1	1.06(1)	1.06(1)	1.06(1)			
W_1	0.35(1)	0.35(1)	0.35(1)			
La_2	0.36(1)	0.65(1)	0.65(1)			0.18(1)
W_2	0.36(1)	0.65(1)	0.65(1)			0.18(1)
O_1	4.9(3)	4.9(3)	4.9(3)			
O_2	0.99(4)	0.99(4)	0.99(4)			
Lattice parameter (Å)	T (K)	R_{exp} (%)	R_{wp} (%)	χ^2	R_B (%)	
11.22472(1)	295	0.921	2.38	6.69	2.05	

5.2.5 Comparison and discussion

The anomalous mass loss behaviour of Re20_IMP and Re20 specimens observed in Fig. 5.23 is explained considering Fig. 5.27 and the following discussion.

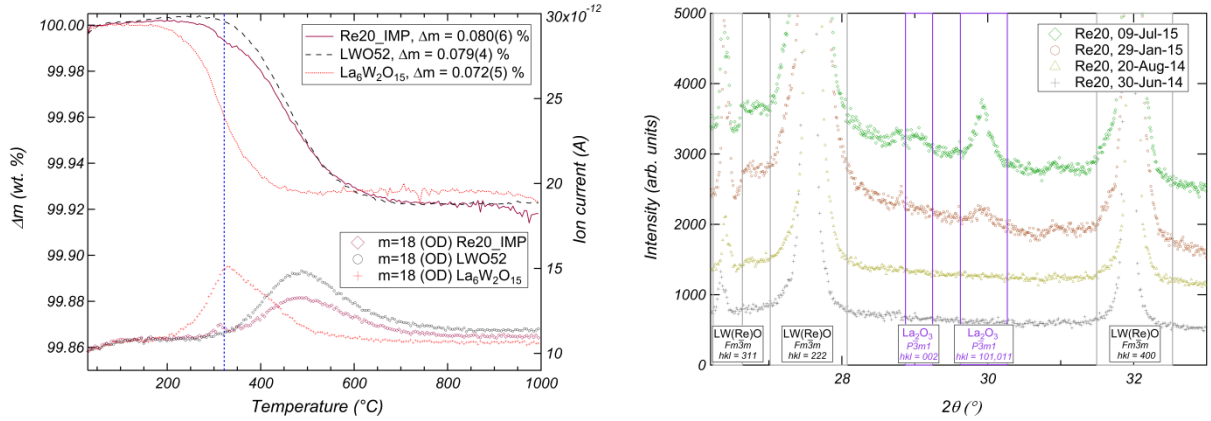

a) ***b)***

*Fig. 5.27. **a)** Thermogravimetric curves and corresponding ion currents (m = 18, OD groups) of Re20_IMP, LWO52 and $La_6W_2O_{15}$-D_2O(Ar) specimens, measured under dry(Ar) gas, as a function of temperature. Lines represent the mass loss Δm (left y-axis), while markers represent the ion currents (right y-axis), where the data referred to the same specimen are presented in the same colour. Δm values are resumed in the legend with a 95 % confidence level uncertainty. The vertical blue dashed line shows the inflection point temperature of the $La_6W_2O_{15}$ TG curve (T ≈ 319 °C), corresponding to the peak and small hump of the $La_6W_2O_{15}$ and Re20_IMP ion current signals, respectively. **b)** Re20 XRD patterns, collected in different time periods, as a function of the scattering angle 2Θ (26.2° ≤ 2Θ ≤ 33°).*

In Fig. 5.27a, the mass losses and the corresponding ion currents for *m* = 18 (OD groups) of LWO52 and $La_6W_2O_{15}$ are shown and compared with those of Re20_IMP. In Fig. 5.27b the magnification of the Re20 XRD diffraction patterns in the range 26.2° ≤ 2Θ ≤ 33° is represented. XRD data have been collected at

different time periods after the arrival of the Re20 specimen (June 2014). The importance of this will be discussed below.In Fig. 5.27a the LWO52, $La_6W_2O_{15}$ and Re20_IMP specimens exhibit comparable mass losses (Δm = 0.07-0.08 wt. %). In contrast, the T_i of $La_6W_2O_{15}$ ($T_i^{La_6W_2O_{15}}$= 274(3) °C) is much lower compared to the T_i of LWO52 (T_i^{LWO52} = 401(3) °C) and ($T_i^{Re20\_IMP}$= 378(3) °C). This difference allows for assigning the small hump in the Re20_IMP TG curve and ion current signal at $T \approx 319$ °C (blue dashed line in Fig. 5.27a) to the contribution of the < 3 wt. % $La_6W_2O_{15}$ phase in Re20_IMP. This hump at $T \approx 319$ °C was expected to appear also in the TG curve and ion current signal of LWO52 as this specimen also contains small amounts of $La_6W_2O_{15}$. However, no anomalies in the LWO52 curves were observed (Fig. 5.27a). This finding is ascribed to the insufficient amount of $La_6W_2O_{15}$ phase in LWO52 compared to Re20_IMP (< 1 wt. % to < 3 wt. %).

In Fig. 5.27b, a clear change in the Re20 XRD patterns with increasing time after specimen arrival can be ascertained. The main reflections of the La_2O_3 phase (e.g. *hkl* = 101, *hkl* = 111, $2\Theta \approx 30°$) increase in intensity with increasing time passed after sample arrival. Although Re20 is reported to be single phase according to the black and yellow XRD patterns in Fig. 5.27b, such results show that this specimen is not stable under reducing conditions at high temperatures (drying procedures in the present case). The repeated annealing performed as specimen pre-treatment (prior to humidification, pre-characterisation and ND and HRXRD measurements) led to some La_2O_3 segregation. This finding is observed for LWO specimens with high La/W ratio (nominal La/W = 5.6 and La/W = 5.7)[52], which is comparative to the high La/(W+Re) ratio determined for Re20 (La/(W+Re) = 5.86). This interpretation could not be proven systematically for the Re20 specimen, where, for instance, the two lower patterns in Fig. 5.27b (black and dark yellow) were not collected after dehydration as it was done for the upper two patterns (brown and green). However, it is supported by results from high-resolution X-ray diffraction (Aug. 2014) where no sign of La_2O_3 segregation in the Re20 specimen could be detected. The TG curves reported in Fig. 5.23 were, instead, performed long after specimen arrival (March – Aug. 2015) because of an interruption due to instrument maintenance. The Re20-dry(Ar) XRD pattern before hydration (in Fig. 5.22 and the brown pattern in Fig. 5.27b) and subsequent Re20-D_2O(Ar) TG measurement is compatible with small (< 1 wt. %) La_2O_3 segregation, responsible of the first shoulder at T_i = 290(3) °C of the Re20-D_2O(Ar) TG curve of Fig. 5.23. The T_i found for Re20 is close to the T_i reported for LWO56 (T_i = 272(3) °C). The slight temperature discrepancy is due to the different amount of La_2O_3 inside LWO56 and Re20 at the time of the measurement. In Fig. 5.28, the anisotropic displacement parameters as a function of temperature for cations of Re20-dry(Ar) (full symbols) and Re20-D_2O(Ar) (open symbols) are depicted. Only the ILL data (T = 5 K, 30 K, 60 K, 150 K, 200 K, 298 K) are shown in order to avoid any influence caused by differences between two different instruments (D2B, HRPT) and two different pre-treatments (D_2O(Ar), D_2O(S.A.)). On 4*a* (W_1, green diamonds) and 4*b* (La_1, black squares) sites, ADPs of the Re20-dry(Ar) specimen (full symbols) seem to have slightly higher values than the ADPs of the Re20-D_2O(Ar) specimen (open symbols), see Fig. 5.28. Although the refinement of the neutron pattern at T = 5 K with all free structural parameters was possible only for the wet specimens, it can be deduced from Fig. 5.28 that disorder in the dry(Ar) specimen is slightly higher than in the wet specimen. This feature is ascribed to a higher vacancy concentration in the dry(Ar) specimen in addition to Re reduction (see section 5.4.1 for details). This might also be the reason why the refinement of Re20 dry(Ar) patterns could not be finalized with coordinates, displacement parameters and occupancies refined at the same time. Finally, the only refined occupancies were SOF_{96k}^{O1}, SOF_{32f}^{O2} and $SOF_{4a}^{W1,Re1}$. The other occupancies were fixed to the corresponding values refined for the Re20-D_2O(Ar) pattern (Table 5.7). The ellipsoid orientation coefficient around the x axis of the 48*h* site U_{23} (blue reversed triangles) is not discussed. As reported by

Hill and Cranswick[87], the ellipsoid orientation coefficients U_{xy} (x, y = 1, 2, 3; $x \neq y$) are the most refinement-sensitive of any of the structural parameters.

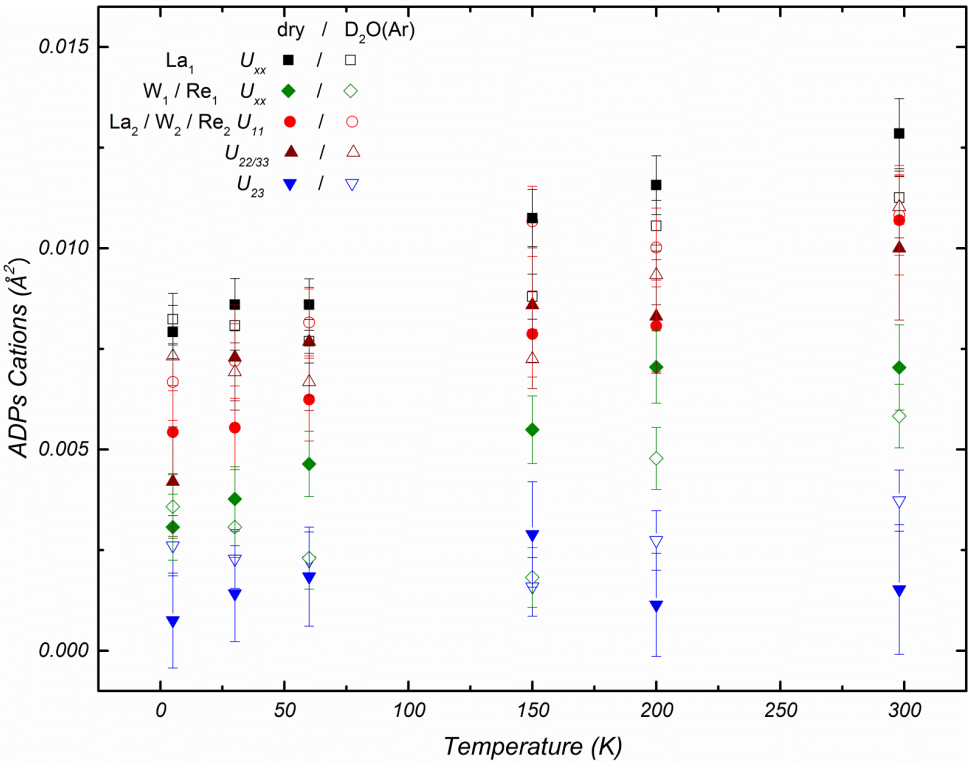

Fig. 5.28. Anisotropic displacement parameters (ADPs) as a function of temperature for cations of Re20-dry(Ar) (full symbols) and Re20-D_2O(Ar) (open symbols) obtained from ND data measured at D2B (ILL).

Through the anion occupancies (Table 5.9), information concerning the vacancy positions can be deduced. The occupancies have been taken from the refinement of the average neutron scattering length approach applied to the cations (see Table 5.6). As the anion sites are occupied only by oxygen atoms, the refined occupancy obtained by applying the average neutron scattering length approach is representative for the occupancy values refined with the appropriate structural model. In fact, the oxygen occupancy values between the final refinements (see for instance Table 5.7) and the average neutron scattering length approach (Table 5.9) are comparable to each other.
In Table 5.9, the refined occupancies of the anion sites are shown for Re20 and LWO_**P** specimens.

*Table 5.9. Refined anion site occupancy factors, SOF, of Re20 and LWO_**P** determined from the average neutron scattering approach for all low temperatures data sets acquired.*

Temp. - condition	SOF_{96k}^{O1}	SOF_{32f}^{O2}	SOF_{96k}^{O1}	SOF_{32f}^{O2}
	Sample Re20		Sample LWO_P	
10 K dry(Ar)^{HRPT}	0.252(3)	0.960(6)	--	--
1.5 K D_2O(S.A.)^{HRPT}	0.253(3)	0.985(5)	0.246(3)	0.964(4)
5 K dry(Ar)^{D2B}	0.241(4)	0.946(8)	0.234(4)	0.924(6)
5 K D_2O(Ar)^{D2B}	0.241(4)	0.957(6)	0.243(3)	0.967(6)

From Table 5.9, through the difference between dry(Ar) and wet(D_2O(Ar/S.A.)) specimens measured at the same instrument, it is possible to infer where the vacancies might be located. Sample Re20 shows that at both experimental stations the refined occupancy of the 96*k* site of dry(Ar) and wet specimen is the same within the error and in the HRPT case is also comparable with the expected oxygen occupancy for the W–O octahedron (SOF_{96k}^{O1} = 0.25 for octahedral W^{6+}). It can therefore be concluded that the O_2

(32*f*) site accommodates the vacancies. A difference is noticed between the occupancies of the 32*f* Wyckoff site, 0.025(11) and 0.011(14) for HRPT and D2B, respectively. Higher oxygen occupancies in the LWO_**P** specimen are also found in the 32*f* Wyckoff site. However, the oxygen occupancies of the Re20 and LWO_**P**-dry(Ar) specimens give an overall oxygen amount in the unit cell below the theoretical value. This inconsistency is ascribed to sample overdrying which might create vacancies also on the 96*k* site and give an average coordination of *N* = 5.69(9) of W instead of *N* = 6. Overdrying, or oxygen understoichiometry, could derive from repeated dehydrations in reducing conditions which may alter the structure and eventually create vacancies also in the 96*k* Wyckoff site in addition to La_2O_3 segregation (see Fig. 5.27b). Nevertheless, from Table 5.9 it can be confidently stated that most of the vacancies in the specimens investigated are located on the 32*f* Wyckoff site. This statement is confirmed by DFT calculations[49] for LWO. Such DFT calculations suggest that vacancies on O-sites (96*k*–O_1) neighbouring W (4*a*–W_1) are slightly higher in energy compared to vacancies on O-sites (32*f*–O_2) neighbouring La (4*b*–La_1). However, the 32*f* Wyckoff site is not found fully occupied upon hydration neither in LWO nor in Re20 specimens. A detailed discussion of this point will be presented in the final part of this work (section 5.4.1).

5.3 $La_{5.4}W_{1-y}Mo_yO_{12-\delta}$ ($0 \leq y \leq 0.2$)

5.3.1 Composition studies

In Table 5.10, a resume of the Mo-substituted LWO samples (LW(Mo)O) investigated in this chapter, along with the preparation methods, nominal and experimental (EPMA/XRD) compositions, possible secondary phases, techniques and sample labels, is presented.

Table 5.10. Preparation method, nominal and experimental composition, single phase status, techniques used and sample labels as used throughout this chapter.

Sample series, preparation method nominal composition	***Experimental (EPMA+XRD) overall composition***	***Secondary phases***	***Techniques used***	***Label of referred samples in the present work***
$La_{5.4}W_{1-y}Mo_yO_{12-\delta}$ ($0 \leq y \leq 0.2$) Pechini method			EPMA, XRD, TG, ND, HRXRD	LW(Mo)O
$La_{5.4}WO_{12-\delta}$	$La_{5.56(3)}WO_{12-\delta}$	No		LWO_**P**
$La_{5.4}W_{0.99}Mo_{0.01}O_{12-\delta}$	$La_{5.62(3)}W_{0.992(1)}Mo_{0.008(1)}O_{12-\delta}$	No		Mo1
$La_{5.4}W_{0.95}Mo_{0.05}O_{12-\delta}$	$La_{5.64(3)}W_{0.953(2)}Mo_{0.047(2)}O_{12-\delta}$	No		Mo5
$La_{5.4}W_{0.90}Mo_{0.1}O_{12-\delta}$	$La_{5.8(5)}W_{0.89(2)}Mo_{0.11(2)}O_{12-\delta}$	$La_6W_2O_{15}$ (< 1 wt. %) La_2O_3 (< 2 wt. %)		Mo10
$La_{5.4}W_{0.85}Mo_{0.15}O_{12-\delta}$	$La_{5.8(2)}W_{0.85(1)}Mo_{0.15(1)}O_{12-\delta}$	$La_6W_2O_{15}$ (< 1 wt. %) La_2O_3 (< 1 wt. %)		Mo15
$La_{5.4}W_{0.8}Mo_{0.2}O_{12-\delta}$	$La_{5.64(4)}W_{0.809(2)}Mo_{0.191(2)}O_{12-\delta}$	No		Mo20(1)
$La_{5.4}W_{0.8}Mo_{0.2}O_{12-\delta}$	$La_{5.64(7)}W_{0.803(7)}Mo_{0.197(7)}O_{12-\delta}$	$La_6W_2O_{15}$ (< 1 wt. %) La_2O_3 (< 1 wt. %)		Mo20(2)

Fig. 5.29 shows the La/(W+Mo) ratios of the LW(Mo)O investigated specimens (Table 5.10) as a function of the Mo-substitution on W site, Mo/(W+Mo), in the same fashion as the LW(Re)O specimens (see section 5.2.1). The compositions of the LW(Mo)O specimens measured by EPMA are indicated by blue

squares. It is recalled that the composition of the LWO series (open green squares) was determined through Vegard's law considering the lattice parameters of the dry(Ar) states according to Eq. (5.1) explained in section 5.1.1 and corrected (open red squares) according to the estimated contribution of secondary phases found by XRD. Due to the large uncertainties of Mo10 and Mo15 specimens, the correction on the composition values was neglected.

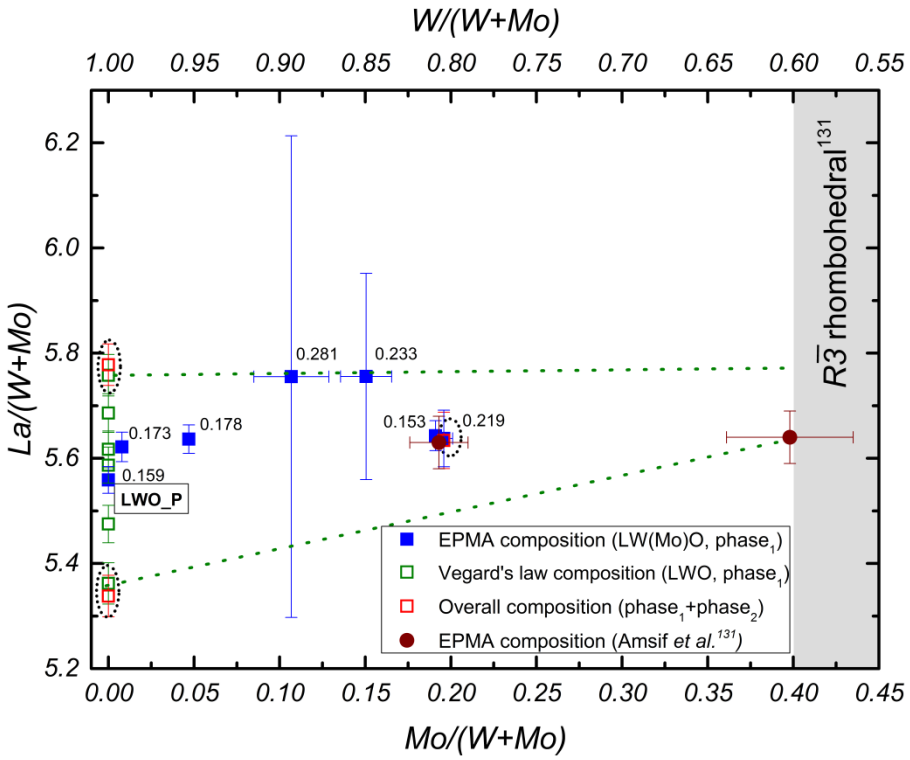

*Fig. 5.29. La/(W+Mo) ratio as a function of W substitution by Mo (Mo/(W+Mo)). The La/(W+Mo) ratios described by blue squares were determined by EPMA, the open green squares were determined through the Vegard's law and comparison to LWO_**P** (cf. section 5.1.1), while the open red squares describe the La/W ratios modified according to secondary phase contributions indexed and quantified by XRD simulations. The filled circles are data points taken from Amsif et al.[131], reported to be single phase. The region between the green dotted lines represents a guide to the eye for the presumed single-phase region of LW(Mo)O specimens. The grey region represents where the LW(Mo)O system presents a phase transition from cubic ($Fm\bar{3}m$) to rhombohedral ($R\bar{3}$), reported in literature[131]. The mass loss (Δm in wt. %, reported next to the squares) has been measured by TG on humidified (D_2O(Ar)) samples with an error of about 0.005 wt. % (95 % C.L.). The sample LWO_**P** is labelled in the figure.*

Discussion: in Fig. 5.29 the most likely reason for the large uncertainties on La/(W+Mo) ratios and Mo-substitution on W on samples Mo10 and Mo15 is the incomplete diffusion of the reactants to form the main LW(Mo)O phase. In addition, non-negligible amount of both secondary phases have been found in Mo10, Mo15 and Mo20(2) by XRD peak indexing. This fact could mean that the respective uncertainties in the La/(W+Mo) ratios might extend beyond the single phase region. Thus, the single phase region is represented roughly in between the dashed green lines. The represented boundaries of the LW(Mo)O single-phase region in Fig. 5.29 could not be established as precisely as for the LW(Re)O system due to the lack of data points. For this reason, two more data points taken from Amsif *et al.*[131] are added in the graph (brown dots). It is supposed that the specimens reported by Amsif *et al.*[131] are phase pure. From the XRD pattern they report, however, it is impossible to verify. Amsif *et al.*[131] observe a phase transition from cubic $Fm\bar{3}m$ to rhombohedral $R\bar{3}$ space group above Mo/(W+Mo) ≈ 0.40, which is shown in the phase diagram of Fig. 5.29 as a grey region. It might be also assumed that the single-phase region reduces with increasing Mo substitution, as is the case for the LW(Re)O system. This would also explain

the difficulties in preparing single-phase LW(Mo)O specimens in the region 0.2 < Mo/(W+Mo)) < 0.4. In addition, the mass loss as a function of the Mo/(W+Mo) ratio seems to behave similarly as LW(Re)O specimens; *Δm* at constant La/(W+Mo) ratio decreases with increasing Mo/(W+Mo) but in a less pronounced way than the LW(Re)O specimens.

As at present, the LW(Mo)O system has not been investigated in the region 0.2 < Mo/(W+Mo)) < 0.4, a final conclusion on the LW(Mo)O phase diagram cannot yet be drawn.

5.3.2 Phase analysis

In Fig. 5.30 the XRD patterns collected for all the LW(Mo)O specimens (CuKα_1/Kα_2 radiation) are plotted as a function of the scattering angle 2Θ (10° ≤ 2Θ ≤ 138°).

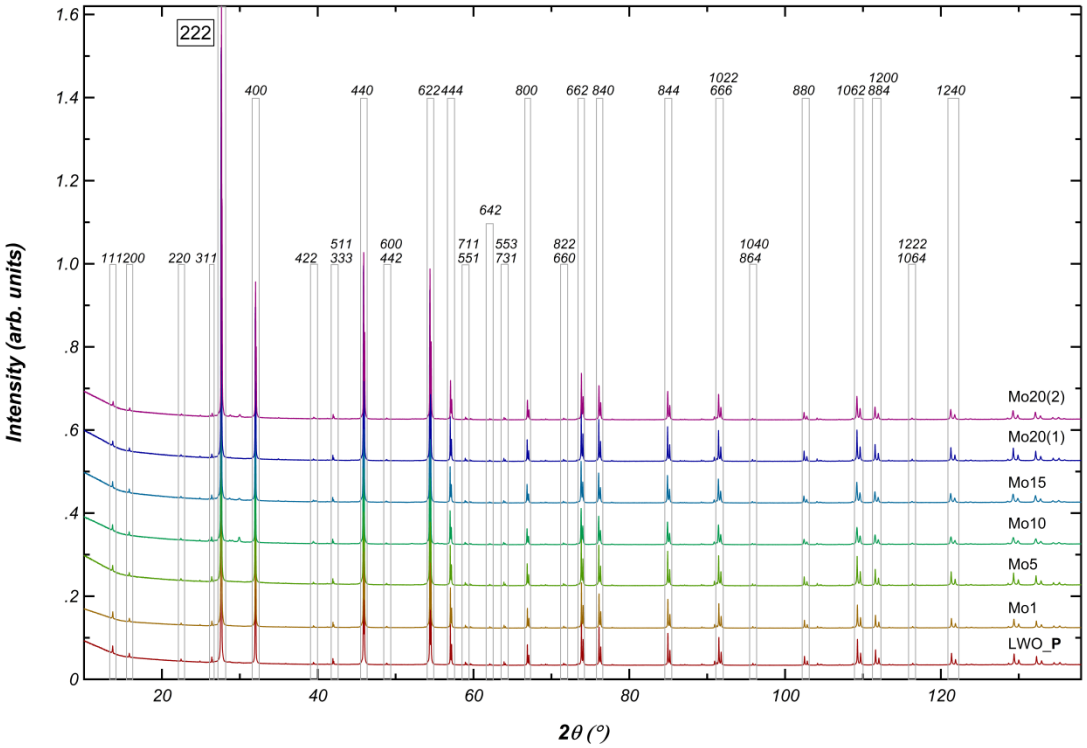

*Fig. 5.30. XRD patterns of the LW(Mo)O-dry(Ar) specimens as a function of the scattering angle 2Θ (10° ≤ 2Θ ≤ 138°). The patterns are presented from the non-substituted LWO_**P** (red pattern) to the highest nominal Mo/(W+Mo) ratio (Mo20(2), purple pattern), from bottom to top, respectively. The hkl indices of the main reflections below 2Θ = 130° are also shown ($Fm\bar{3}m$ space group), and the patterns are normalized to the peak of highest intensity (hkl = 222 reflection). Peak splitting is due to CuKα$_1$/Kα$_2$ doublet.*

As for the LW(Re)O system, no change of the reflection conditions in LW(Mo)O compared to the non-substituted LWO_**P** specimen is observed. All the *hkl* reflections were indexed according to the $Fm\bar{3}m$ space group used for LWO_**P** and reported in Fig. 5.30. The patterns were normalized to the (222) reflection and increasingly shifted in the y-axis with increasing degree of Mo-substitution on W (Mo/(W+Mo)) for better visualization. Secondary phase peaks at 2Θ ≈ 30° can be seen in Fig. 5.30 for Mo10, Mo15 and Mo20(2) specimens where the amount of $La_6W_2O_{15}$ and La_2O_3 was estimated to be less than 2 wt. %. More information about identification and quantification of those phases is presented in section 5.3.5.

5.3.3 Water uptake

In Fig. 5.31, the TG curves of the LW(Mo)O-D_2O(Ar) specimens are depicted.

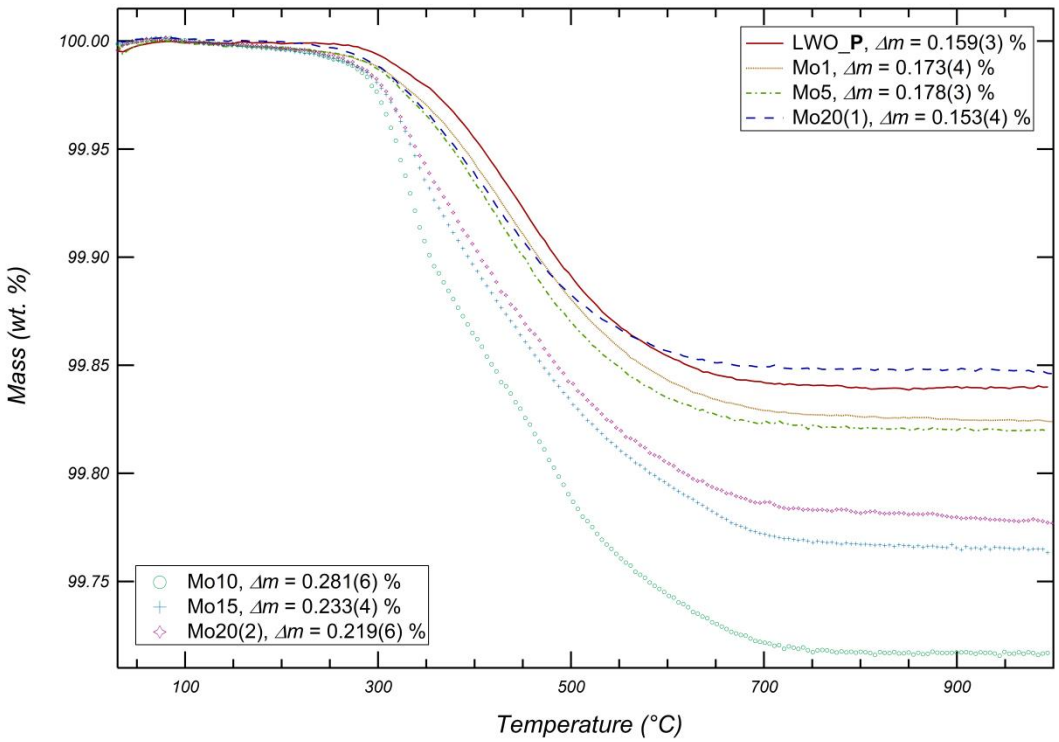

Fig. 5.31. Thermogravimetric curves of LW(Mo)O-D_2O(Ar) specimens measured under dry(Ar) gas, where the mass loss Δm in dependence of temperature is shown. The colours used correspond to the colours used in Fig. 5.30. Δm values are resumed in the legend with a 95 % confidence level uncertainty. Markers and lines were used for the specimens containing small amounts of secondary phases and phase-pure specimens, respectively.

In Fig. 5.31 two sample groups can be distinguished, the La_2O_3-containing specimens Mo10, Mo15 and Mo20(2) and the phase-pure specimens LWO_**P**, Mo1, Mo5 and Mo20(1). The La_2O_3-containing specimens Mo10, Mo15 and Mo20(2) reveal higher mass loss compared to the phase-pure specimens LWO_**P**, Mo1, Mo5 and Mo20(1). Among the LW(Mo)O phase-pure specimens, the lowest *Δm* has been measured for Mo20(1), $\Delta m^{Mo20(1)}$ = 0.153(4) wt. %.

Discussion: in Fig. 5.31, a decrease in mass loss with increasing Mo substitution can be ascertained. The finding that Δm^{Mo5} is slightly higher than Δm^{Mo1} is rationalised by the not equivalent La/(W+Mo) ratio (see Fig. 5.29). However, the mass loss decrease seen for LW(Mo)O with increasing Mo substitution is much lower than that measured for LW(Re)O with increasing Re substitution. While the mass loss of Mo20(1) ($\Delta m^{Mo20(1)}$ = 0.153(4) wt. %) is similar to the mass loss of LWO_**P** (Δm^{LWO_P} = 0.159(3) wt. %), the mass loss for the sample Re20_IMP (Δm^{Re20_IMP} = 0.080(6) wt. %) is about half the value. Mo20(1) and Re20_IMP have been compared due to their similar stoichiometry and substitution level on W site. These results yield that the oxidation state of Mo, in oxidized conditions, is similar to that of W (W^{6+}) and lower than Re (Re^{7+}), where Eq. (5.6) has been considered with Mo and Re donors on La_2 site ($Mo_{La2}^{\bullet\bullet\bullet}$ and $Re_{La2}^{\bullet\bullet\bullet\bullet}$ in K-V, respectively). No useful information, instead, can be extracted from the La_2O_3 containing specimens (Mo10, Mo15, Mo20(2)). As explained in detail in section 5.1.3, even a small amount of the $La(OD)_3$ secondary phase alters both the onset temperatures T_i and the mass loss *Δm* of the LWO specimens appreciably (about a factor two for Mo10).

5.3.4 Crystal structure of LaWMoO

5.3.4.1 Method of the average neutron scattering length

From the results on the LW(Re)O series, it has been concluded that Re atoms substitute W in both its Wyckoff sites, 4*a* and 48*h*. This result is a consequence of the different neutron scattering lengths of Re (b_{coh}^{Re} = 9.2(2) fm) and W (b_{coh}^{W}= 4.755(18) fm). Their relative difference $(b_{coh}^{Re} - b_{coh}^{W})/b_{coh}^{Re}$ ≈ 48 % allows for a sufficiently high contrast to distinguish Re and W through neutron diffraction. This feature is not as evident in LW(Mo)O specimens, due to the smaller difference between the neutron scattering length of Mo (b_{coh}^{Mo} = 6.715(20) fm), compared to W (b_{coh}^{W} = 4.755(18) fm), which results in a relative difference $(b_{coh}^{Mo} - b_{coh}^{W})$ / b_{coh}^{Mo} ≈ 29 %. However, the contrast between W and Mo seems also sufficiently high to apply the method of the average neutron scattering length in the same fashion as for LW(Re)O. The two LW(Mo)O specimens with the highest Mo-substitution, Mo20(1) ($La_{5.64(4)}W_{0.809(7)}Mo_{0.191(2)}O_{12-\delta}$) and Mo20(2) ($La_{5.64(7)}W_{0.803(7)}Mo_{0.197(7)}O_{12-\delta}$, see Table 5.10), were selected to be refined through the average scattering length approach, and the occupancy of the cation Wyckoff sites (4*a*, 4*b*, 48*h*) compared with the results of the LWO_**P** specimen. As shown in Fig. 5.30 and in the following discussion part in detail, specimen Mo20(2) shows a tiny amount of secondary phases (< 1 wt. % La_2O_3, < 1 wt. % $La_6W_2O_{15}$) but the composition of the main phase is very close to that of Mo20(1) specimen which is single-phase within the resolution of XRD measurements. However, the amount of powder available for Mo20(2) is about 10 g compared to < 2 g of the purer Mo20(1) specimen, which makes the first one Mo20(2) more suitable for temperature dependent neutron diffraction measurements, performed in the temperature range *T* = 10 K – 298 K. The latter specimen (Mo20(1)) was, however, also analysed with neutrons at *T* = 298 K at the ILL due to the high flux available at D2B. Nevertheless, no visible difference neither in the neutron patterns of Mo20(1) and Mo20(2) nor in the refinement results was ascertained. The average scattering length results of Mo20(1) and Mo20(2) specimens, the measuring temperature and the average site occupancies are reported in Table 5.11.

*Table 5.11. Refined site occupancy factors, SOF, of the cation sites 4a, 4b and 48h of specimens Mo20(1) and Mo20(2), obtained through the average neutron scattering length approach. Results of all data sets collected at low temperatures for Mo20(2) (T = 10 K, 30 K) and at T = 298 K for Mo20(1), and the different conditions dry(Ar), D2O(Ar/S.A.), are shown. For comparison, the average site occupancies factors of the LWO_**P** specimen and the calculated weighted average occupancies (see Eqs. (4.24), (4.25)) of Mo20(1) and Mo20(2) are also reported.*

Temp. - condition	SOF_{4a}^{W}	SOF_{4b}^{La1}	SOF_{48h}^{La2}
	Sample Mo20(2)		
10 K dry(Ar)^{HRPT}	1.070(21)	0.999(13)	0.488(2)
10 K D_2O(S.A.)^{HRPT}	1.031(20)	0.974(12)	0.499(2)
30 K dry(Ar)^{D2B}	1.042(25)	0.956(14)	0.493(3)
30 K D_2O(Ar)^{D2B}	1.045(29)	0.973(17)	0.498(3)
Average site occupancy	1.05(1)	0.98(1)	0.494(1)
	Sample Mo20 (1)		
298 K dry(Ar)^{D2B}	1.068(36)	0.997(21)	0.494(4)
298 K D_2O(Ar)^{D2B}	1.067(49)	1.004(30)	0.496(5)
Average site occupancy	1.07(3)	1.00(2)	0.495(3)
	Sample LWO_P		
Average site occupancy	0.994(13)	0.989(8)	0.486(1)

Neutron diffraction resulted in a 4*a* site occupancy of 1.05(1) for Mo20(2) and 1.07(3) for Mo20(1), resulting in Mo-amount on 4*a* site of 12(3) % and 17(7) % for Mo20(2) and Mo20(1), respectively. The latter value is less precise due to larger measuring temperature (*T* = 298 K) and the low amount of

powder available (< 1 g per specimen for each condition, dry(Ar) / D_2O(Ar)). A plot of the average scattering length $\bar{b}_{4a}^{exp}$ for the LW(Mo)O series as a function of the amount of W substitution by Mo along with the composition results from EPMA is presented in Fig. 5.32. From the refined 4*a* occupancies listed in Table 5.11 the experimental neutron scattering length for Wyckoff site 4*a*, $\bar{b}_{4a}^{exp}$, can be calculated using Eq. (4.15). The blue points in Fig. 5.32 were calculated under the assumption that the Mo amount measured by EPMA entirely occupies the 4*a* site (SOF_{4a}^{Mo} = Mo/(W+Mo) in Eq. (4.15)).

The two data points determined by EPMA corresponding to Mo10 and Mo15 specimens are reported in brackets because the refinements performed on Mo10 and Mo15 neutron patterns at *T* = 298 K for such specimens gave inconsistent results, which are not reported in Fig. 5.32. The reason is ascribed to the incomplete diffusion of the reactants, which will be discussed in section 5.3.5.

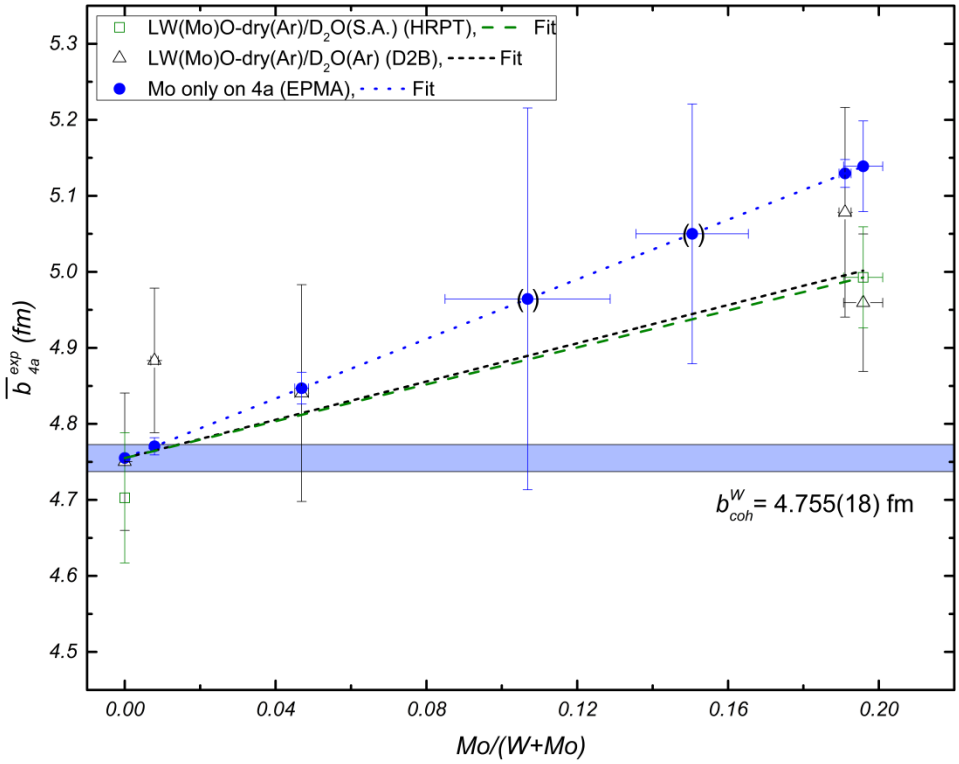

*Fig. 5.32. Average neutron scattering length of the 4a–W_1 Wyckoff site, $\bar{b}_{4a}^{exp}$, for the LW(Mo)O series, as a function of W substitution by Mo (Mo/(W+Mo)). Open green squares represent the $\bar{b}_{4a}^{exp}$ obtained from refinements performed on specimens measured at HRPT at 1.5 K (LWO_**P**-D_2O(S.A.)) and 10 K (Mo20(2)-dry(Ar)/ D_2O(S.A.)). Open black triangles represent the $\bar{b}_{4a}^{exp}$ obtained from refinements performed on dry(Ar)/D_2O(Ar) specimens measured at ILL at 5 K (LWO_**P**), at 30 K (Mo20(2)) and T = 298 K (Mo1, Mo5, Mo20(1)). Full blue circles show the 4a site occupancy calculated under the assumption that the Mo amount measured by EPMA entirely occupies the 4a site. The Mo10 and Mo15 data points are added in brackets (cf. text). Fits are straight lines performed with direct x-weighting (larger Mo/(W+Mo) weighs more) and with $\bar{b}_{4a}^{exp}$ (0) = 1 (4a fully occupied for the non-substituted LWO_**P**). The coherent scattering length of W is depicted in light blue.*

From all the data values represented by green open squares and black open triangles, the ones relating to the LWO_**P** specimen (Mo/(W+Mo) = 0) and to the Mo20(2) specimen (Mo/(W+Mo) = 0.197(7)) are the most reliable for the following reasons:

i. Low temperature acquisitions. The measurements were collected at low temperatures, *T* = 10 K (HRPT) and *T* = 30 K (D2B) for Mo20(1), and *T* = 1.5 K (HRPT) and *T* = 5 K (ILL) for LWO_**P**, which decrease the thermal vibrations and their correlation to the occupancy values.

ii. Reasonable measuring time. The amount of powder *m* (≈2.5 g < *m* < ≈5 g per specimen for each condition, dry(Ar)/D_2O(Ar/S.A.)) allows getting good signal to noise ratio, which is proportional to exposure time due to the incoherent scattering hitting the detector.

iii. Statistics. The cation occupancy values obtained from the refinements on D_2O(Ar/S.A.) and dry(Ar) specimens at the same experimental station and at the same temperature were averaged (except for the non-substituted LWO_**P**-D_2O(S.A.), measured at HRPT), reducing the uncertainties associated (see Eqs. (4.24), (4.25)).

Despite being single phase specimens, Mo1 and Mo5 reveal large errors in the occupancies because points (i) and (ii) were not fulfilled (data collection at *T* = 298 K and low amount of material, < 1 g per dry(Ar)/D_2O(Ar) state). However, point (ii) does not apply for high-resolution X-ray diffraction due to the high photon flux available at synchrotrons, for which a sample amount of the order of mg is sufficient. Moreover, Mo (Z_{Mo} = 42) has an electronic density substantially different from that of W (Z_W = 74), resulting in a higher relative contrast $(Re(f)^W - Re(f)^{Mo}) \,/\, Re(f)^W$ ≈ 47 %, calculated for the +6 ions, than that of neutron diffraction, $(b_{coh}^W - b_{coh}^{Mo}) \,/\, b_{coh}^W$ ≈ 29 %. Therefore, the LW(Mo)O series is particularly suitable for average X-ray scattering power studies, presented in the following.

5.3.4.2 Method of the average X-ray scattering power

In order to enhance even further the contrast between Mo and W, measurements were collected below the Mo K-edge at 19.9 keV, which increases the relative contrast from 47 % to about 54 %. The measurements were performed in a cryostat down to *T* = 10 K to reduce thermal vibration and also outside the cryostat, at *T* = 100 K using a cryo-jet and at *T* = 295 K, to reduce capillary wobbling, sample environment noise and thus enhancing the refinement precision. The resulting X-ray average scattering power of the cation positions 4*a* and 48*h*, refined for the phase-pure LW(Mo)O specimens LWO_**P**, Mo1, Mo5 and Mo20(1), are summarized in Table 5.12. The SOF of the 4*b* site was fixed to $SOF_{4b}^{La_1}$ = 1 (see discussion below) Moreover, the corresponding La/(W+Mo) ratio from EPMA (Table 5.10), the theoretical amount of anti-site disorder calculated according to $La_{28-x}(WMo)_{4+x}O_{54+\delta}$ and the theoretical electron number corresponding to the amount of anti-site disorder on 48*h* position are also presented (W_2 + Mo_2 on La_2, in at. % and e^-/atom) and separated in its atomic contributions (W_2, Mo_2 on La_2, in e^-/atom).

*Table 5.12. Refined site occupancies factors, SOF, of the cation sites 4a and 48h of the non-substituted LWO_**P** and the single-phase LW(Mo)O-D_2O(S.A.) specimens, obtained through the average X-ray scattering power approach. Also, the corresponding EPMA ratio, La/(W+Mo), the amount of anti-site disorder, W_2 + Mo_2 on La_2 (at. % and e^-/atom), and the two contributions of W_2 and Mo_2 on La_2 (e^-/atom) according to EPMA, are depicted.*

Samples in D_2O(S.A.) state, temperature	SOF_{4a}^W	$SOF_{48h}^{La_2}$	La/(W+Mo) EPMA	W_2 + Mo_2 on La_2 (EPMA) at. %	W_2 + Mo_2 on La_2 (EPMA) e^-/atom	W_2, Mo_2 on La_2 (EPMA) e^-/atom
LWO_P (295 K)	1.044(2)	0.5076(6)	5.56(3)	3.66(7)	2.46	2.46, 0
Mo1 (100 K)	1.027(2)	0.5053(7)	5.62(3)	3.43(7)	2.293	2.29, 0.003
Mo5 (100 K)	1.003(2)	0.5037(6)	5.64(3)	3.42(8)	2.28	2.23, 0.05
Mo20(1) (100 K)	0.927(4)	0.5030(13)	5.64(3)	3.40(9)	2.06	1.85, 0.21
Mo20(2) (295 K)	0.923(2)	0.5028(6)	5.64(5)	3.42(17)	2.06	1.85, 0.21

The 4*a* site occupancy shown in Table 5.12 decreases with increasing Mo concentration, due to the lower number of electrons per atom of Mo ($Re(f)_{19.9\,keV}^{Mo6+}$ ≈ 31.4 e^-/atom) than for W ($Re(f)_{19.9\,keV}^{W6+}$ ≈ 67.3 e^-/atom), comparatively with the neutron occupancies shown in Table 5.11 and Fig. 5.32. Again, this result provides an independent proof that Mo substitutes W on the 4*a* Wyckoff site. In

LWO_**P**, Mo1 and Mo5 specimens, moreover, the 4*a* site seems to be slightly overestimated. This has been found for both LWO_**P**-dry(Ar) and LWO_**P**-D_2O(S.A.) specimens (see Table 5.2). The 4*b* site, occupied by La_1 atom, has been assumed fully occupied and independent of Mo concentration due to the very different ionic radii between La ($R_i(La)_{3+}^{8fold}$ = 1.16 Å) and Mo($R_i(Mo)_{3+}^{6fold}$ = 0.69 Å). A decreasing trend is seen also for the refined 48*h* occupancy as a function of Mo-concentration. However, in order to understand and discuss correctly the 48*h* average X-ray scattering power, four columns were added in Table 5.12. The occupancy of the 48*h* position is delicate, in a sense that it depends on the La/(W+Mo) ratio and is also correlated to the other occupancies, especially to SOF_{4b}^{La1}. To reduce this correlation, La_1, O_1 and O_2 occupancies for all the specimens were fixed to SOF_{4b}^{La1} = 1, SOF_{96k}^{O1} = 0.25 and SOF_{32f}^{O2} = 0.96, respectively. The minor differences in the oxygen content for all specimens have been assumed invisible with X-rays, such as the vacancy concentration on O_2 position. In Table 5.12 The amount of anti-site disorder calculated (W_2 + Mo_2, on La_2, Table 5.12) shows that for each LW(Mo)O specimens, about 3.5 at. % of the 48*h* site is available to locate W (W_2) and/or Mo (Mo_2), and the remaining 96.5 at. % is occupied by La (La_2). If the 3.5 at. % anti-site disorder would be statistically occupied by W and Mo, it would result in a difference of about 0.4 e^-/atom for LWO_**P** and the Mo20 specimens (see last two columns in Table 5.12). Moreover, the reported values of electron/atom in the last column of Table 5.12 have to be divided by a factor of two to account for the 48*h* site half occupancy. Such small contributions to the scattering by a mixture of W (67.3 e^-) and Mo (31.4 e^-) are expected to be difficult to be separated from the main scatterer of the 48*h* site, La_2 (96.5 at. %, 53.5 e^-, see Table 5.12) even with synchrotron X-ray diffraction. However, combined experimental and theoretical results on the five measured samples and the refined occupancies for the 4*a* site hint that Mo atoms substitute W on both its 48*h* and 4*a* sites, which is explained as following. Theoretical calculations to estimate *Re(f)* were performed considering the 48*h* anti-site concentration fully occupied by W and also supposing the Mo substitution entirely going on the 4*a* Wyckoff site, similar to what has been shown for neutrons (see Fig. 5.32). Theoretical calculations (open symbols) and refinement results (full symbols), converted in *Re(f)*, are presented in Fig. 5.28. From the refined occupancies (shown in Table 5.12) the experimental amount of *Re(f)* according to Eq. (4.22) was calculated. The theoretical values take into consideration the *Re(f)* atomic form factor tabulation after Chantler[93] (see section 4.4.3.3). As explained in Chantler[93] and in the NIST documentation[94], the uncertainty was taken as 1 % of the calculated value. Considered that the X-ray energy used (*E* = 19.9 keV) is far away from any La edge, the uncertainty of 0.1 % on the calculated *Re(f)* for the 48*h* site is also presented.

In Fig. 5.33, the decreasing trend of *Re(f)* for the 4*a* Wyckoff site with increasing Mo-concentration is clearly visible (black dotted line), comparably with neutron diffraction results (see Fig. 5.32). However, the refined value of *Re(f)* for the 4*a* site is higher than the expected values, if Mo is occupying only the 4*a* Wyckoff site (open wine reversed triangles), for all specimens. This shift to higher values of the *Re(f)* must be clarified. A possible explanation could be that the correlation between the *SOF*s and the thermal vibrations is still too high, possibly due to the W thermal vibrations and librations in the disordered W–O octahedra. As *Re(f)* accounts for the average electronic density, the thermal vibrations and librations in the distorted octahedra may be reflected in an inaccurate form factor parametrization of the 4*a* Wyckoff site charge density with the W^{6+} ion. The *Re(f)* on the 48*h* Wyckoff site instead, seems to be consistent with the experimental values: the *Re(f)* corresponding to twice the 48*h* occupancies (full blue triangles) is comparable with the value expected, if W is occupying solely the 48*h* site (open green diamonds), only for the LWO_**P** and Mo1 specimens. The discrepancy with the theoretical values calculated considering only W antisite on the 48*h* site (green diamonds and dashed line) increases with increasing Mo substitution. If the uncertainty of 0.1 % is considered, from Fig. 5.33 it can be inferred

that the refined *Re(f)* value of 48*h* site changes from above to below the theoretical full La occupancy on 48*h* (53.47 e^-) with increasing Mo-concentration. This can be only rationalised by W_2 (67.3 e^-) anti-site disorder on La_2 (53.47 e^-) for the non-substituted compound, and by increasing Mo anti-site disorder with increasing W substitution by Mo (31.4 e^-). Moreover, if the 48*h* site were only occupied by La and W, its occupancy would be independent of Mo-concentration and the refined values would scatter above and below the values represented by the open green diamonds in a statistical fashion, considering the similar specimen La/(W+Mo) ratios for the LW(Mo)O series.

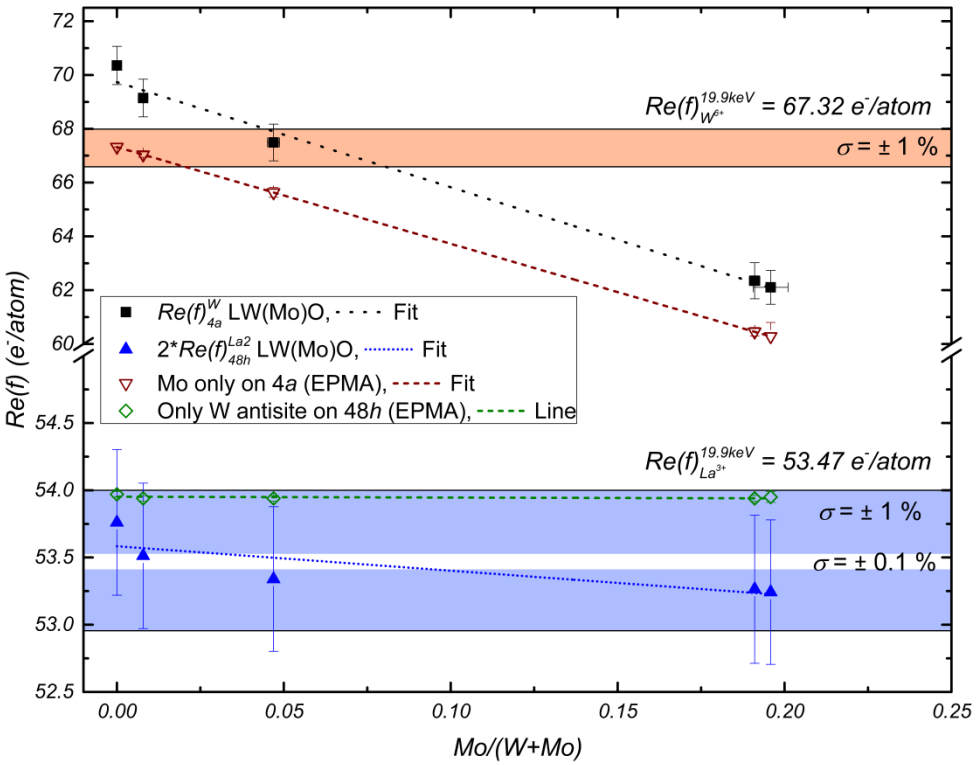

*Fig. 5.33. Average electron number per Wyckoff site, Re(f), for phase pure Mo-substituted specimens and LWO_**P**. Open wine triangles show the Re(f) for the 4a Wyckoff site calculated under the assumption that the Mo amount measured by EPMA entirely occupies the 4a site (comparably to ND data, see Fig. 5.32). Open green diamonds show the Re(f) for the 48h Wyckoff site calculated under the assumption that the anti-site disorder on 48h site (≈ 3.5 at. %, Table 5.12) is given only by W, where the green dashed line reported is a guide to the eye. The refined cation site occupancies (full symbols) were obtained through the method of the average X-ray scattering power (Table 5.12). The multiplication factor of 2 applied to the 48h refined Re(f) accounts for the split 48h Wyckoff site. In light orange and light blue the calculated electron numbers for W^{6+} and La^{3+} ions at 19.9 keV (see section 5.3.4.2) are depicted, respectively, with a 1 % associated uncertainties. Moreover, the 0.1 % uncertainty associated to the calculated Re(f) of La^{3+} (19.9 keV) is also depicted in white within the light blue region. Fits are straight lines.*

As for both the 4*a* and the 48*h* Wyckoff sites, the refined occupancies decrease with increasing Mo substitution and lie all above (full black squares) and below (full blue triangles) the calculated values (open triangles and open diamonds), it can be concluded that Mo, like Re, substitutes W on the 4*a* site and La and W on the and 48*h* Wyckoff site. Therefore, the 4*a* site is shared between W and Mo, and the 48*h* site is shared between La, W and Mo in a statistical way.

5.3.4.3 Neutron and high-resolution X-ray diffraction

At first, a combined neutron – X-ray refinement with Mo on 48*h* and 4*a* positions on Mo20(2) diffraction patterns (*T* = 295 K) was performed. The combined refinement succeeded only partially due to the medium resolution of the HRPT diffractometer and the difference of refined displacement parameters and site occupancies, which resulted only in slightly more precise atomic positions when the lattice

parameters were refined separately. The results of the separated fits are thus shown in Table 5.13, along with the obtained lattice parameters and residuals. In both neutron and X-ray diffraction refinements, SOF_{48h}^{La2} was fixed at the beginning of the refinements to the value obtained applying Eqs. (5.15), (5.16) and (5.17) already used for Re20 specimen, according to the EPMA composition (SOF_{48h}^{La2} = 0.483). As it was not possible to refine simultaneously all the parameters due to the low scattering power of oxygen atoms, the final steps used are described as following. In a cycling fashion, firstly the oxygen occupancies were refined with all ADPs and oxygen IDP fixing the cation occupancies (SOF_{48h}^{La2} fixed) and then, the oxygen occupancies were fixed and all ADPs and oxygen IDPs were refined along with the cation occupancies (SOF_{48h}^{La2} fixed), until no change was observed. In the last cycles, it was possible to let SOF_{48h}^{La2} free fixing SOF_{48h}^{W2} in a cycling fashion, and both occupancies did not change. Using neutrons, instead, when SOF_{48h}^{La2} was left free the errors of each occupancy increased substantially. Therefore, SOF_{48h}^{La2} was kept fixed to SOF_{48h}^{La2} = 0.483 and marked with an asterisk in Table 5.13.

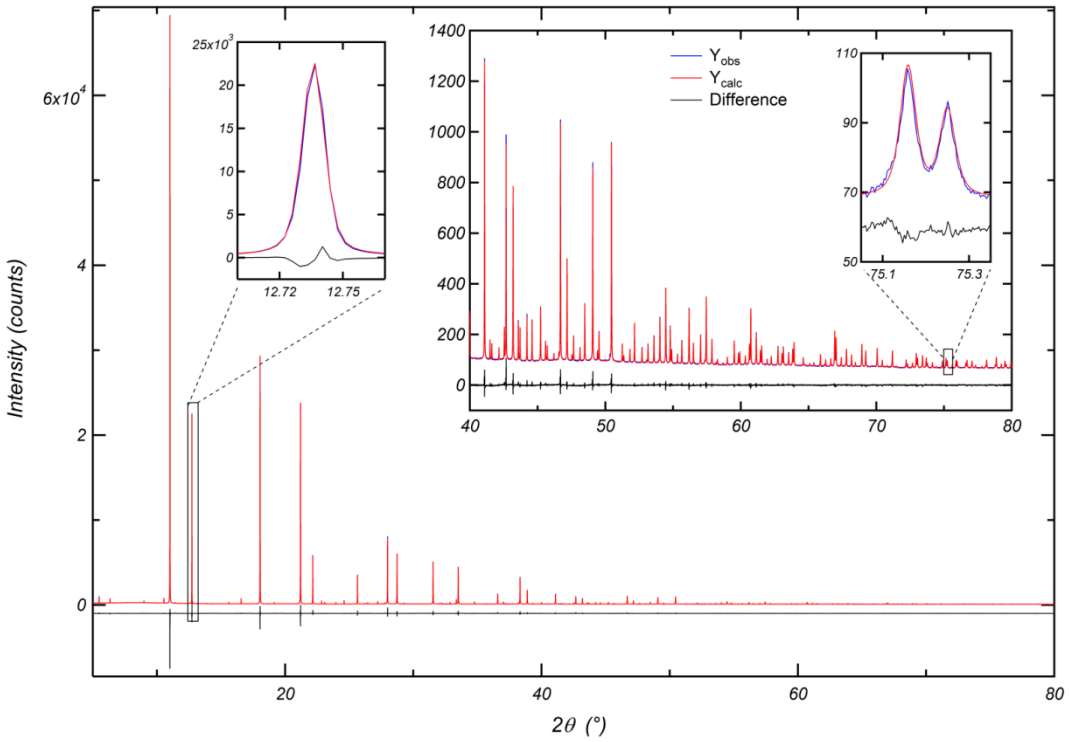

Fig. 5.34. High-resolution X-ray diffraction intensity plots of Mo20(2)-dry(Ar) ($La_{5.64}W_{0.803}Mo_{0.197}O_{12-\delta}$) data collected at T = 295 K at the MS beamline (SLS), as a function of the scattering angle 2Θ (blue line), calculated data (red line) and difference of the two (black line). In the inset, the high-angle data (40° ≤ 2Θ ≤ 80°) is magnified, as well as three chosen diffraction peaks, one at low scattering angles (2Θ ≈ 12.7°) and two at high scattering angles (2Θ ≈ 75.2°). In the insets, the difference line is shifted for better peak visualization.

As the combined refinement did not succeed, the two best refinements with Mo included in 48*h* and 4*a* Wyckoff sites are shown in the following, one for the HRXRD data (SLS(MS) at *T* = 295 K, Fig. 5.34 and Table 5.13) and one for the ND data (ILL(D2B) at *T* = 30 K, Fig. 5.35). In Fig. 5.34 the experimental intensities (Y_{obs}, blue line), the calculated intensities (Y_{calc}, red line) and the difference (Difference, black line) between experimental and calculated intensity are plotted as a function of the scattering angle 2Θ in the refined region, i.e. 5° ≤ 2Θ ≤ 80° (0.9 $Å^{-1}$ < *q* < 13 $Å^{-1}$). In the inset, the high-angle data with lower intensities is magnified (40° ≤ 2Θ ≤ 80°). Additionally, one peak at low scattering angles (*hkl* = 400) and two close peaks at high scattering angles are reported as examples to present the fit reliability.

Table 5.13. Fractional atomic coordinates, x, y, z, site occupancy factors, SOF, anisotropic displacement parameters, U_{xy}, and their equivalent, U_{eq}, for Mo20(2) ($La_{5.64}W_{0.803}Mo_{0.197}O_{12-\delta}$) dry(Ar) from neutron diffraction (HRPT at SINQ, T = 295 K), high-resolution X-ray diffraction (MS at SLS, T = 295 K). All the displacement parameters (U_{eq}, U_{xx} and U_{xy}) are multiplied by a factor of 100. The refinements were performed with space group $Fm\bar{3}m$. The lattice parameters and the residuals are also reported. With (*) and ($^+$) are denoted the parameters not refined, and not refined simultaneously with the others in the last cycles, respectively.

Atom Technique	Site	x	y	z	U_{eq}(Å^2)	SOF	U_{11}(Å^2)	U_{22}(Å^2)	U_{33}(Å^2)	U_{12}(Å^2)	U_{13}(Å^2)	U_{23}(Å^2)
La_1	4*b*	0.5	0.5	0.5								
Neutrons					1.29	0.99(1)	1.29(7)	1.29(7)	1.29(7)			
X-rays					0.73	0.995(1)	0.73(1)	0.73(1)	0.73(1)			
W_1	4*a*	0	0	0								
Neutrons					0.83	0.89(4)	0.83(10)	0.83(10)	0.83(10)			
X-rays					0.38	0.844(3)	0.38(1)	0.38(1)	0.38(1)			
Mo_1	4*a*	0	0	0								
Neutrons					0.83	0.11(4)	0.83(10)	0.83(10)	0.83(10)			
X-rays					0.38	0.156(3)	0.38(1)	0.38(1)	0.38(1)			
La_2	48*h*	0										
Neutrons			0.2352(1)	0.2352(1)	0.48	0.483*	0.74(9)	0.35(7)	0.35(7)			-0.27(7)
X-rays			0.23618(1)	0.23618(1)	0.49	0.483(1)	0.33(1)	0.57(1)	0.57(1)			0.33(1)
W_2	48*h*	0										
Neutrons			0.2352(1)	0.2352(1)	0.48	0.009(10)	0.74(9)	0.35(7)	0.35(7)			-0.27(7)
X-rays			0.23618(1)	0.23618(1)	0.49	0.013(1)$^+$	0.33(1)	0.57(1)	0.57(1)			0.33(1)
Mo_2	48*h*	0										
Neutrons			0.2352(1)	0.2352(1)	0.48	0.008(10)	0.74(9)	0.35(7)	0.35(7)			-0.27(7)
X-rays			0.23618(1)	0.23618(1)	0.49	0.004(1)	0.33(1)	0.57(1)	0.57(1)			0.33(1)
O_1	96*k*											
Neutrons		0.1119(1)	0.1119(1)	0.0663(3)	3.06	0.257(3)	2.05(1)	2.05(1)	5.08(3)	-0.32(10)	-0.84(12)	-0.84(12)
X-rays		0.1119(2)	0.1119(2)	0.0652(3)	1.87	0.251(1)$^+$	1.87(9)	1.87(9)	1.87(9)	--	--	--
O_2	32*f*											
Neutrons		0.3662(1)	0.3662(1)	0.3662(1)	1.92	0.979(5)	1.92(3)	1.92(3)	1.92(3)	0.08(4)	0.08(4)	0.08(4)
X-rays		0.3660(1)	0.3660(1)	0.3660(1)	1.03	0.968(4)$^+$	1.03(3)	1.03(3)	1.03(3)	--	--	--
	Lattice parameter (Å)		T(K)	R_{exp}(%)	R_{wp}(%)	χ^2	R_B(%)					
Neutrons	11.1837(1)		295	4.36	5.20	1.42	1.37					
X-rays	11.22501(1)		295	0.882	2.09	5.62	3.03					

The refinement of HRXRD data succeeded at T = 295 K with all cation ADPs, oxygen IDPs, La_1, W_1/Mo_1 and La_2 or W_2/Mo_2 cation occupancies and all atomic positions as free parameters. The significant outcome is that the refined composition, $La_{27.16(6)}W_{3.97(12)}Mo_{0.85(12)}O_{55.1(2)}$ (La/(W+Mo) = 5.63(3), Mo/(W+Mo) = 0.18(2)) agrees with EPMA and that the 48*h* Wyckoff site is shown to be occupied by La_2 (SOF_{48h}^{La2} = 0.483(1)), W_2 (SOF_{48h}^{W2} = 0.013(1)) and Mo_2 (SOF_{48h}^{Mo2} = 0.004(1)), confirming the expectations deduced from the average neutron scattering length (Fig. 5.32) and average X-ray scattering power (Fig. 5.33).

In Fig. 5.35 the observed neutron diffraction intensities (Y_{obs}, blue line), the calculated intensities (Y_{calc}, red line) and their difference (Difference, black line) are plotted as a function of 2Θ in the refined region, i.e., 10° ≤ 2Θ ≤ 150° (≈ 0.7 Å^{-1} < q < ≈ 7.6 Å^{-1}). In the inset the high-angle data is magnified (100° ≤ 2Θ ≤ 150°). Also, the first peak at low scattering angles (*hkl* = 222) and two close peaks at high scattering angles (*hkl* = 977; 11, 7, 3; 13, 3, 1 and *hkl* = 10, 8, 4; 12, 6, 0) are reported as examples to present the fit reliability.

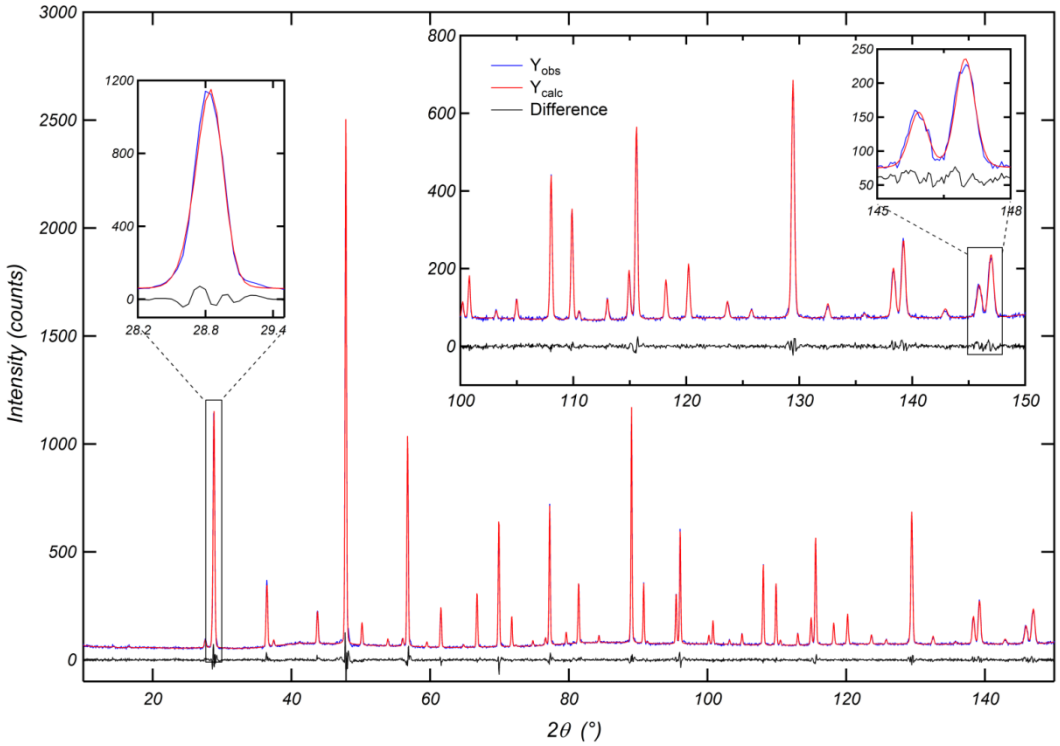

Fig. 5.35. Neutron diffraction intensity plots of Mo20(2)-D_2O(Ar) ($La_{5.64}W_{0.803}Mo_{0.197}O_{12-\delta}$) data collected at T = 30 K at instrument D2B (ILL), as a function of the scattering angle (blue line), calculated data (red line) and difference of the two (black line). In the inset the high-angle data (100° ≤ 2Θ ≤ 150°) is magnified, as well as three chosen diffraction peaks, one at low scattering angles (2Θ ≈ 28.8°) and the last two at high scattering angles (2Θ ≈ 145-148°). In the insets, the difference line is shifted for better peak visualization.

Despite the good fit result on neutron diffraction data (χ^2 = 2.3, R_B = 1.11 %) and the compatibility of the refined composition $La_{27.12(8)}W_{3.9(5)}Mo_{0.9(5)}O_{53.1(3)}$ (La/(W+Mo) = 5.65(2)) with results of EPMA, the occupancies of W and Mo on both 4*a* and 48*h* Wyckoff site are assigned with high uncertainties. Specifically, the occupancies $SOF_{4a}^{W} = 0.83(3)$ and $SOF_{48h}^{W} = 0.12(13)$ and, therefore, $SOF_{4a}^{Mo} = 0.17(3)$, $SOF_{48h}^{Mo} = 0.05(13)$ present for the 48*h* site uncertainties larger than the refined values. This yields a Mo concentration of Mo/(W+Mo) = 0.2(1). Contrary to X-ray diffraction data, neutron diffraction data even collected at T = 30 K, are less precise to distinguish between Mo and W. This result is due to the large difference in scattering powers between W and Mo for X-rays compared

with neutrons. To prove it, a direct comparison for the 4*a* site can be made on neutron diffraction data collected on Re20 specimen in the same conditions (*T* = 30 K at D2B). In the Re20 pattern, all the structural parameters were possible to be refined together, yielding $SOF_{4a}^{W} = 0.83(2)$ and $SOF_{48h}^{W} = 0.08(5)$ and, therefore, $SOF_{4a}^{Re} = 0.17(2)$, $SOF_{48h}^{Re} = 0.06(5)$. For the Re20 specimen, the uncertainties associated to the 48*h* Wyckoff site are half those found for the Mo20(2) specimen. As a result, the uncertainty associated to the refinements carried out on LW(Mo)O data is confidently ascribed to the insufficiently high difference in relative scattering lengths between Mo and W ($(b_{coh}^{Mo} - b_{coh}^{W})/\ b_{coh}^{Mo}$ ≈ 29 %), compared to that of Re and W ($(b_{coh}^{Re} - b_{coh}^{W})\ /\ b_{coh}^{Re}$ ≈ 48 %).

As a final point, the temperature dependence of some of the LW(Mo)O-dry(S.A.) specimens (Mo5, Mo20(1)) measured in the temperature range *T* = 10 K – 295 K by high-resolution X-ray diffraction, is presented. In addition, the temperature dependence of the Mo20(2)-dry(Ar) specimen measured in the range *T* = 10 K – 295 K through neutron diffraction is shown along with some selected bond lengths. In Fig. 5.36 all the Mo20(1) diffraction patterns collected as a function of the scattering angle 2*Θ* and temperature *T*, are depicted. The black diffraction patterns were recorded continuously during cooling whilst the red diffraction patterns were recorded upon re-heating and constant temperatures at *T* = 10 K, 30 K, 60 K, 100 K, 150 K, 200 K, 240 K, 270 K). The *T* = 295 K pattern was collected before cooling in a steady state (*T* = 294.99(5) K) and it was used for calibration, according to the lattice parameter of the diluted Si640d NIST. Therefore, it is considered as a pattern collected in a steady state and marked in red in Fig. 5.36. The temperature variation *ΔT* acting during cooling in most of the cases lies between *ΔT* = 5 K and *ΔT* = 7 K, except at the beginning (*ΔT* ≈ 12 K) and at the end of the cooling (below *T* = 60 K, ΔT^{MAX} ≈ 22 K). The maximum variation ΔT^{MAX} ≈ 22 K in one pattern collected in the low temperature region (*T* < 60 K) is because the contribution of the phonons to the heat capacity can be neglected in this temperature range. In Fig. 5.36, the decrease in diffraction intensity for both red and black XRD-patterns is due to two factors, namely capillary wobbling *w* (in both cases) and the temperature variation *ΔT* during data collection. If the capillary describes a circular trajectory around the capillary spinning axis (simplest case), such cylindrical wobbling is severe for *w* ≥ 0.25*D*, where *D* is the capillary diameter. In this case, the wobbling can change significantly the peak shape, eventually causing peak splitting[69]. In Fig. 5.36, notice the intensity decrease with decreasing temperature of the first high intensity reflection, (222), at about 2*Θ* ≈ 10°. Generally, the peak shape of the measured reflections broadened to some extent only below *T* = 100 K but remained reasonably approximated by the Gaussian profile parameters, as capillary wobbling produces Gaussian peak broadening[69]. Such wobbling was mainly caused by glue instability with decreasing temperature. The second reason for the decrease in diffraction intensity is given by temperature variation during data collection. Due to thermal expansion/contraction of the unit cell, a temperature variation results in a set of lattice parameters proportional to the time the specimen spent at that particular temperature. The subsequent lattice parameter variation, in addition to specimen wobbling, gave in some case slightly asymmetric peak shapes which were possible to fit through the asymmetry parameter described by Finger *et al.*[132]. Though this asymmetry parameter was developed to correct for axial beam divergence and is normally kept fixed to instrumental values during the refinement, it improved the profile shape parametrization during cooling. The X-ray diffraction pattern background was partly fitted manually through the *fit_object* equations reported in TOPAS wiki[79] (see also Scardi and Dinnebier[133]) due to not negligible cryostat contributions. In order to have the background free from specimen environment contributions, more measurements were taken without cryostat at room temperature and at *T* = 100 K using a cryo-jet device, without diluting the specimen and hence using a smaller capillary (Ø = 0.1 mm).

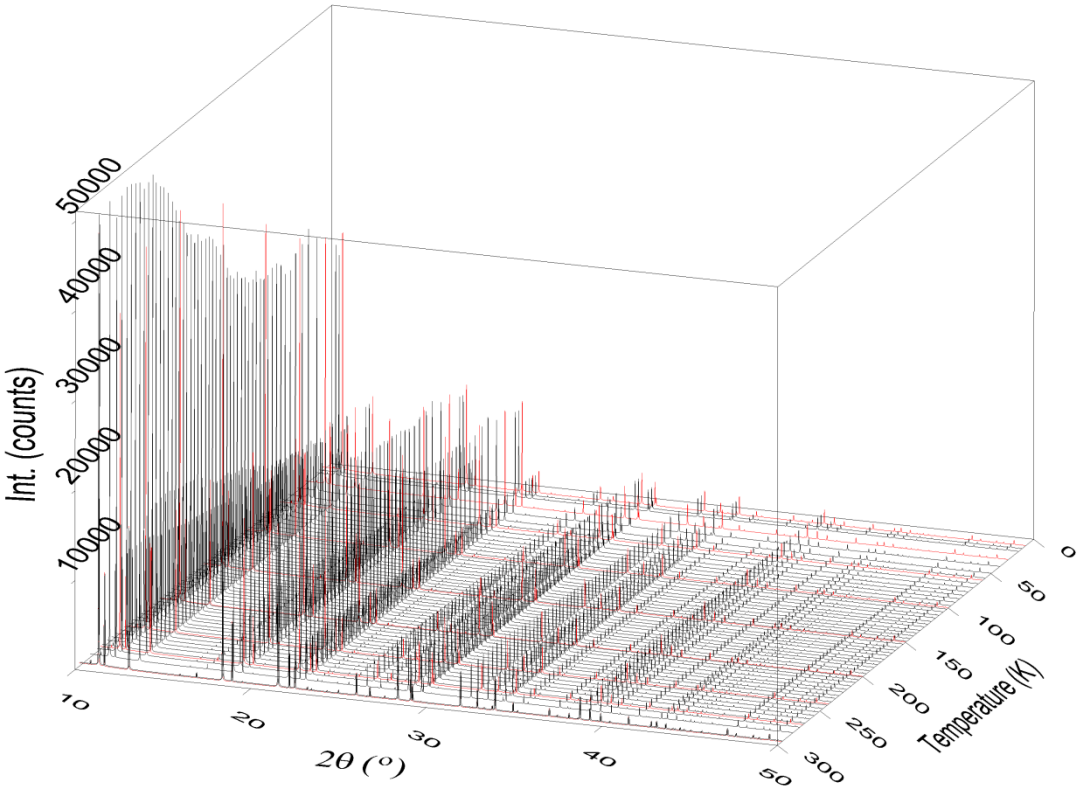

Fig. 5.36. Measured X-ray diffraction intensity of Mo20(1)-dry(S.A.) as a function of 2Θ between T = 10 K and T = 295 K. The diffraction patterns taken continuously during cooling are depicted in black lines whilst the diffraction patterns taken during heating at constant temperatures (T = 10 K, 30 K, 60 K, 100 K, 150 K, 200 K, 240 K, 270 K) are shown in red lines. The measurement at T = 295 K was collected before starting the cooling ramp (T = 294.99(5) K) and used in the cooling and the re-heating (steady state) data sets. The decrease in intensity for the patterns in red is due to some capillary wobbling in the cryostat while for the patterns in black it is also due to the temperature variation during each measurement (between ΔT = 5 K and ΔT = 22 K).

In order to enhance the measurements collected with different capillaries and the peak broadening, one diffraction peak (*hkl* = 222) for the measured specimen Mo20(1) is magnified in Fig. 5.37a. Notice that the correspondent peaks at *T* = 295 K and at *T* = 100 K (blue peaks in Fig. 5.37a) have less intensity and smaller *FWHM* than the other peaks (due to the smaller capillary diameter), negligible temperature dependent wobbling (due to the different glue used and a better alignment), in addition to the smoother background (not visible in Fig. 5.37a). Finally, the lattice parameters of Mo20(1) and Mo5 specimens in dependence of temperature (during cooling, heating, using the cryo-jet at *T* = 100 K and without sample environment at *T* = 295 *K*) obtained from the refinements are shown in Fig. 5.37b. In addition, the refined lattice parameters of Si640d NIST powder were added to Fig. 5.37b. The Si640d NIST powder was used to dilute Mo20(1) and Mo5 in order to avoid specimen absorption while using larger capillaries (Ø = 0.2 mm), necessary for better alignments in the cryostat.

In Fig. 5.37b, open diamonds and filled circles represent the refinements on Mo5-dry(S.A.) and Mo20(1)-dry(S.A.), respectively. In Fig. 5.37b the part above the break describes the lattice parameters of the Mo20(1) and Mo5 during cooling (black symbols), at fixed temperatures (red symbols) and without cryostat using a cryo-jet at *T* = 100 K and at room temperature (blue symbols). Additionally, the lattice parameters of the reference Si640d NIST used as diluent are shown for the same measurements in Fig. 5.37b (below the break). Same notation in Fig. 5.37b was used for Mo5/Mo20 specimens and the Si

reference, except that no dilution was necessary for the measurements without the cryostat due to the smaller capillary diameter used.

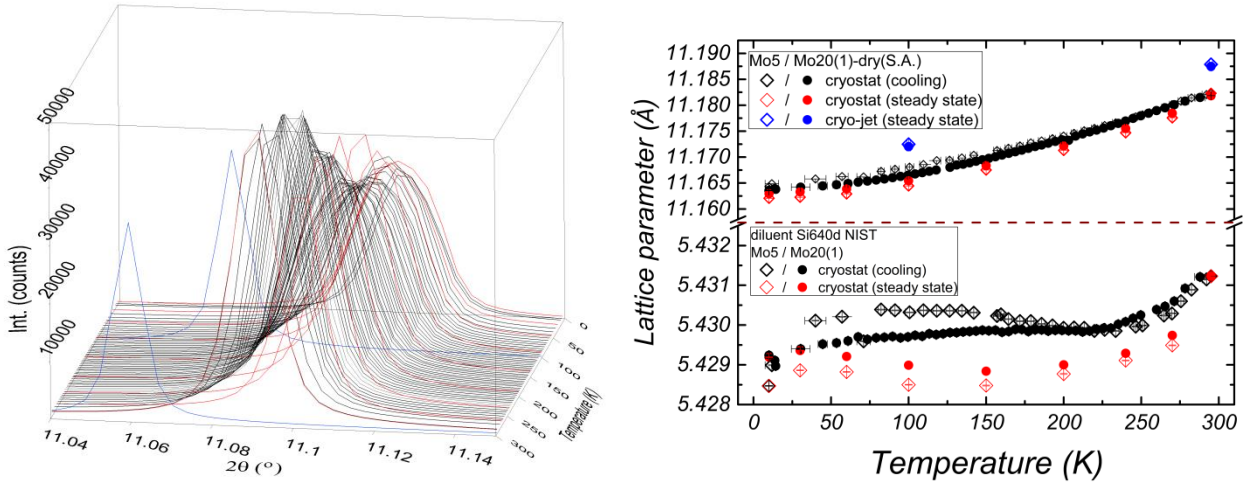

a) ***b)***

Fig. 5.37. ***a)*** *Measured X-ray diffraction intensity of Mo20(1)-dry(S.A.) as a function of 2Θ and temperature (T = 10 K – 295 K), where a magnification of the (222) reflection in the low 2Θ region (11.04° ≤ 2Θ ≤ 11.15°) is presented. Patterns collected in the cryostat during cooling (black lines) and during heating at constant temperature (red lines). The pattern at T = 295 K taken before cooling is also shown in red colour. Additionally, the two patterns collected outside the cryostat (blue lines) at T = 295 K and at T = 100 K (cryo-jet) are shown. The decrease in intensity is due to some capillary wobbling and temperature variation (cf. text).* ***b)*** *Lattice parameter of Si640d NIST and Mo5/Mo20(1)-dry(S.A.) specimens as a function of temperature. Open diamonds and full circles represent the lattice parameters of Mo5 and Mo20(1) and of the corresponding diluent Si640d NIST, respectively.*

All the LeBail fits performed for both Mo5 and Mo20(1) specimens yield 0.5 % ≤ R_{exp} ≤ 0.7 % and 1.3 % ≤ R_{wp} ≤ 1.9 % resulting in average χ^2 between 2 and 4, proving the good reliability of the fits. Concerning the Si lattice parameter, the same reasoning as for Fig. 5.12 applies. The decrease in lattice parameter with increasing temperature in the region 18 K < *T* < 125 K[124] cannot be ascertained from the refined values when data was collected during cooling, but its evidence comes clear when the temperature was kept fixed. The lattice parameters of Mo5 and Mo20(1)-dry(S.A.) decrease with decreasing temperature and seem to level off in the low temperature region, similarly as LWO (see Fig. 5.12). Due to the not equivalent capillary positions in the cryostat, the absolute lattice parameter values cannot be compared. This can be justified by comparing the lattice parameters of the diluted Si640d NIST, not equivalent for Mo5 and Mo20(1), especially for low temperatures (*T* < 100 K). However, the measurements without cryostat (blue symbols) allow for a quantitative comparison. The difference in lattice parameter averaged for *T* = 100 K and *T* = 295 K (blue data points in Fig. 5.37b) is $\overline{a_{Mo5} - a_{Mo20}}$ = 4.3(4)x10^{-4} Å. Such a comparison is only possible because of the similar La/(W+Mo) ratio between the Mo5 (La/(W+Mo) = 5.64(3)) and Mo20(1) (La/(W+Mo) = 5.64(4), see Fig. 5.29 and Table 5.10), in addition to the identic data collection and refinement procedure. Such tiny decrease of lattice parameters found upon increasing the Mo content proves that Mo does not reduce in dry(S.A.) atmosphere. This is rationalised by the ionic radius of Mo ($R_i(Mo)_{6+}^{6fold}$ = 0.59 Å), only slightly smaller compared to that of W ($R_i(W)_{6+}^{6fold}$= 0.60 Å) if 6-fold coordination and +6 oxidation state for both elements are considered. In Fig. 5.38a the neutron diffraction patterns of Mo20(2)-dry(Ar) specimen are presented as a function of the exchanged momentum *q* and temperatures between *T* = 10 K and *T* = 298 K. The representation in *q*, needed because of the different wavelengths used at D2B

(λ^{D2B} = 1.594 Å) and HRPT (λ^{HRPT} = 1.494 Å) gives for HRPT measurements in Fig. 5.38a (blue patterns) a higher q range, up to $q \approx 8.3$ Å^{-1}, compared to the D2B measurements, where $q \approx 7.7$ Å^{-1} (black patterns).

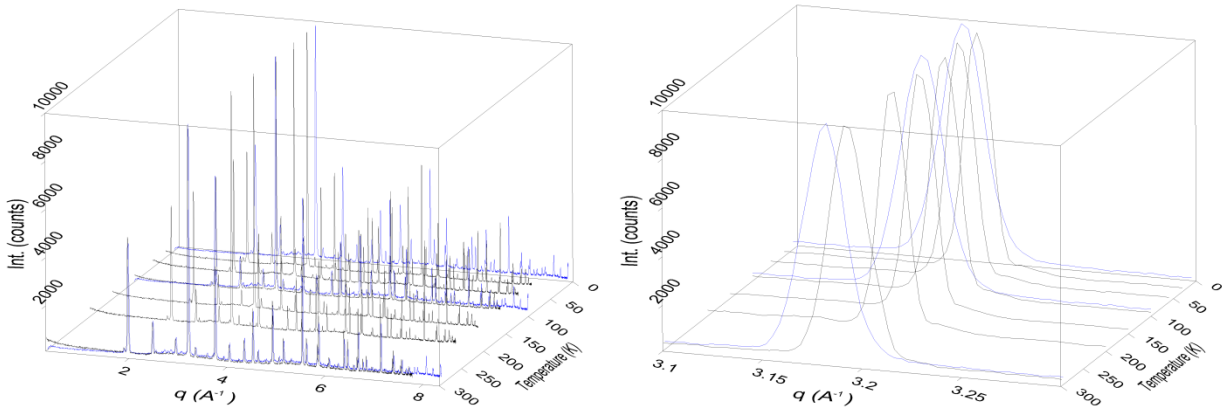

a) ***b)***

Fig. 5.38. ***a)*** *Neutron diffraction intensity as a function of q of Mo20(2)-dry(Ar) and for different temperatures between T = 10 K and T = 298 K. The black and blue lines represent the diffraction patterns taken at D2B (T = 30 K, 60 K, 100 K, 150 K, 200 K, 298 K) and at HRPT (T = 10 K, 100 K, 295 K), respectively. The patterns are normalized to 10000 counts.* ***b)*** *Magnification of Fig. 5.38a where the highest reflection (hkl = 440, q ≈ 3.17 Å^{-1}) is presented. The representation in q is required due to the different wavelengths used at D2B (λ^{D2B}=1.594 Å, black patterns) and at HRPT (λ^{HRPT}=1.494 Å, blue patterns).*

In Fig. 5.38b a magnification of the (440) reflection is shown. Notice the smaller peak width on D2B patterns, where smaller slit sizes were used compared to HRPT for $T \neq 298$ K. Due to the high uncertainties of the refined occupancies for Mo20(2) (T = 30 K pattern) shown above, all the refinements for D2B and HRPT patterns were performed fixing the cations occupancies as obtained from HRXRD refinements (see Table 5.13, 'X-rays' rows), i.e., La_1 site fully occupied (SOF_{4b}^{La1} = 1), SOF_{4a}^{W1} = 0.844, SOF_{4a}^{Mo1} =0.156, SOF_{48h}^{La2} = 0.483, SOF_{48h}^{W2} = 0.013, SOF_{48h}^{Mo2} = 0.004. The other structural parameters such as coordinates, displacement parameters and oxygen occupancies were refined. As the neutron technique is particularly suitable for getting the atomic positions due to scattering of the nuclei, a discussion of some of the bond lengths as a function of temperature and dry(Ar)/D_2O(Ar) state is presented in the next section.

5.3.5 Comparison and discussion

In Fig. 5.39a, a magnification of the XRD patterns in between the *hkl* = 222 and *hkl* = 400 reflection is shown in order to better visualize the contribution of secondary phases. In Fig. 5.39a, it can be seen that the most intense peaks of the La_2O_3 and $La_6W_2O_{15}$ phases exist in the Mo10, Mo15 and Mo20(2) specimens. A rough estimation of these peaks could be deduced from intensity comparison reported in Fig. 5.39b, where the XRD patterns of the dried references La_2O_3 and $La_6W_2O_{15}$ are plotted in addition to the XRD patterns of Mo10, Mo15 and Mo20(2). In Fig. 5.39b, the LW(Mo)O patterns are normalized to 1 count. La_2O_3 and $La_6W_2O_{15}$, instead, are normalized to 0.02 counts (2 % of the scale) for comparison. The data shown in Fig. 5.39b have been collected using the same parameters and instrumental setup. Comparing the intensity of the diffractograms, the amount of $La_6W_2O_{15}$ in Mo10, Mo15 and Mo20(2) is estimated to lie in between 1 % and 3 %. In Mo10, the amount of La_2O_3 seems to be slightly larger than 2 % while in Mo15 and Mo20(2) the La_2O_3 amount lies between 1 % and 2 %. These results agree with the TG curves shown in Fig. 5.31, where the highest mass loss has been found for the highest La_2O_3 contamination, i.e., in the Mo10 specimen (Δm^{Mo10} = 0.281(6) wt. %). Single peak-fitting and pattern

simulations allowed to estimate more accurately the amount of secondary phases in Mo10, Mo15 and Mo20(2). Such procedure has been performed in the following way. Firstly, the $La_6W_2O_{15}$ / La_2O_3-dry(Ar) patterns were merged with a single-phase LW(Mo)O specimen (e.g., Mo5, see Table 5.10) in different ratios *r* (*r* : 1-*r*, e.g., 0.01 : 0.99). Then, the areas of the main reflections indexed for La_2O_3 (*hkl* = 101, *hkl* = 011) or $La_6W_2O_{15}$ (*hkl* = 221, see Fig. 5.39b) were computed as a function of the relative merging and compared to Mo10, Mo15 and Mo20(2) patterns.

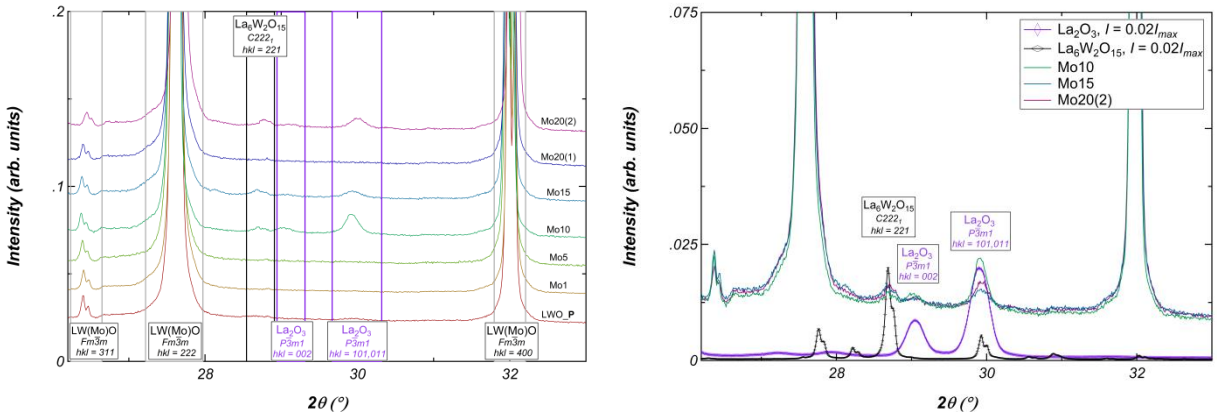

a) ***b)***

Fig. 5.39. ***a)*** *XRD patterns of the LW(Mo)O-dry(Ar) series as a function of the scattering angle 2Θ (26.2° ≤ 2Θ ≤ 33°). The patterns are presented from the non-substituted LWO_**P** (red pattern) to the highest nominal Mo/(W+Mo) ratio (Mo20(2), purple pattern), from bottom to top, respectively.* ***b)*** *XRD patterns of Mo10 (green line), Mo15 (blue line), Mo20(2) (red line)-dry(Ar) specimens as a function of the scattering angle 2Θ in the region 26.2° ≤ 2Θ ≤ 33°, in addition to the La_2O_3 (purple line) and $La_6W_2O_{15}$ (black line) dry(Ar) reference patterns. The intensities of the Mo10, Mo15 and Mo20(2)-dry(Ar) patterns are normalized to 1 count (I_{max} = 1) while the La_2O_3 and $La_6W_2O_{15}$ patterns are normalized to 0.02I_{max} (2 % of the scale), for comparison.*

A rough estimation of La_2O_3 amount has been inferred also according to the TG results of Fig. 5.31 and Fig. 5.4 as following. It is assumed that the mass losses reported for LW(Mo)O in Fig. 5.31 are the weighted sum of the mass losses of $La(OD)_3$, $\Delta m^{La(OD)_3}$ = 9.72 wt. %, and the mass loss of the main LW(Mo)O phase of Mo10, Mo15 and Mo20(2). The weight is the ratio *r* : *1-r* of the secondary phase to the main phase. The mass losses of Mo10, Mo15 and Mo20(2) main phases (MP) are assumed to be equal and to lay in between the mass loss values recorded for the phase-pure specimens, thus $\Delta m^{Mo10MP} = \Delta m^{Mo15MP} = \Delta m^{Mo20(2)MP}$ = 0.16 wt. %. Finally, the results are listed in Table 5.14.

Table 5.14. Quantitative estimation of secondary phases in Mo10, Mo15 and Mo20(2) specimens according to intensity comparison (Fig. 5.39b), pattern simulations (single peak fitting) and water uptake.

Sample	Phase	Intensity comparison (Fig. 5.39b), wt. %	Pattern simulations, wt. %	Water uptake (only La_2O_3), wt. %
Mo10	$La_6W_2O_{15}$	< 2	≈ 0.6	--
	La_2O_3	≈ 2	≈ 1.1	≈ 1.3
Mo15	$La_6W_2O_{15}$	< 2	≈ 0.7	--
	La_2O_3	< 2	≈ 0.4	≈ 0.8
Mo20(2)	$La_6W_2O_{15}$	< 2	≈ 0.5	--
	La_2O_3	< 2	≈ 0.5	≈ 0.6

In Table 5.14 it can be seen how the intensity comparison between the LW(Mo)O specimens and the references gives an overestimation of the amount of secondary phases compared to the quantitative analyses. When single peak fitting on simulated patterns was performed, or the La_2O_3 concentration in

LW(Mo)O was estimated from the mass loss in TG measurements, lower values were determined and better agreement between the TG and the XRD quantitative estimations was achieved. Though such low amounts of La_2O_3 and $La_6W_2O_{15}$ have only minor influence on the diffraction patterns, they may strongly alter the material performances leading for instance to membrane disintegration. This could be caused either by the volume change induced by the high water uptake of segregated La_2O_3 in the membrane[37], or by the asymmetrical thermal expansion of the $La_6W_2O_{15}$ orthorhombic unit cell[59].

In addition to the secondary phases, the main phases of Mo10, Mo15 and Mo20(2) show prominent peak broadening in the diffraction patterns, where the greatest peak widths are observed in the Mo10 specimen. A selected reflection (*hkl* = 12, 4, 0) in the high-2Θ range (120° ≤ 2Θ ≤ 124°) is presented in Fig. 5.40 in order to enhance the peak shapes of the LW(Mo)O-dry(Ar) specimens. Such a high 2Θ range was chosen due to the resolved splitting of $CuK\alpha_1/K\alpha_2$ lines. The prominent peak broadening observed for Mo10, Mo15 and Mo20(2) is rationalised by incomplete reactant diffusion and demonstrated in the following.

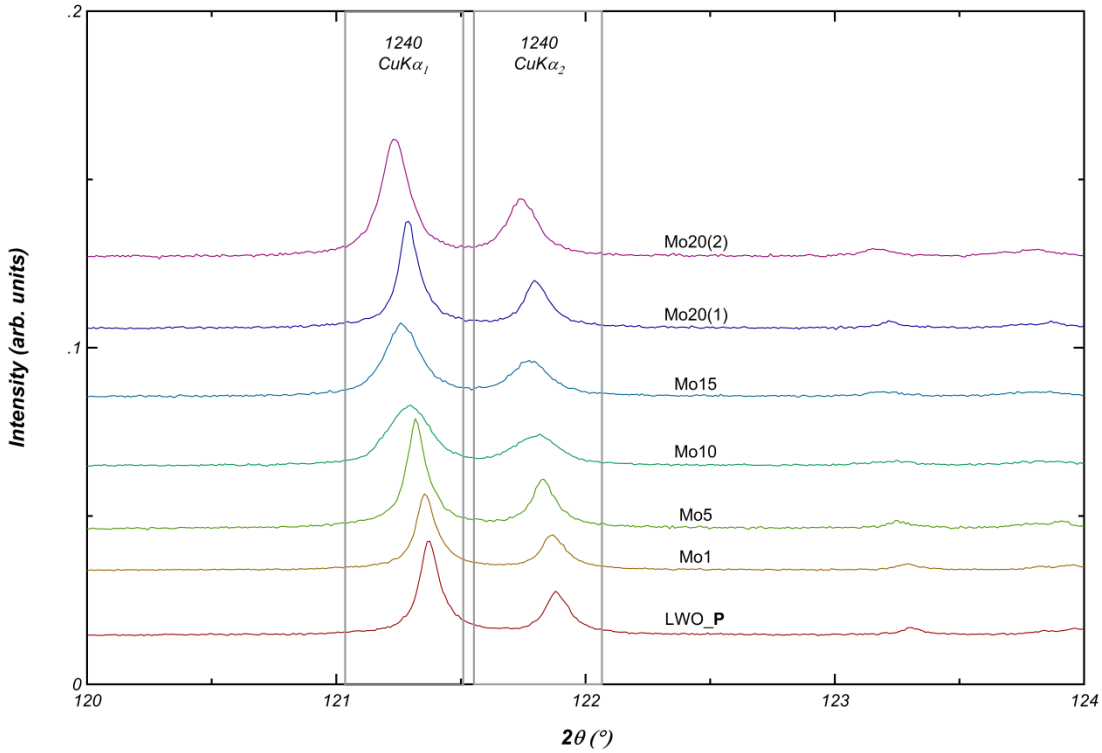

*Fig. 5.40. XRD patterns of the LW(Mo)O-dry(Ar) specimens as a function of the scattering angle 2Θ (120° ≤ 2Θ ≤ 124°). The patterns are presented from the non-substituted LWO_**P** (red pattern) to the highest nominal Mo/(W+Mo) ratio (Mo20(2), purple pattern), from bottom to top, respectively. The reflection shown is the (12, 4, 0), according to the $Fm\bar{3}m$ space group, and the patterns are normalized to the peak of highest intensity (hkl = 222 reflection). The resolved peak splitting of the $CuK\alpha_1/K\alpha_2$ doublet is also labelled.*

In order to obtain a quantitative approach, the analysis of the peak width as a function of the composition uncertainties is performed for a high-2Θ reflection. However, in order to avoid the increasing instrumental broadening coming from the satellite Cu lines, it has been chosen not to go beyond 2Θ = 80°.This was the reason why the selected reflection for LW(Mo)O for peak analysis studies lies at 2Θ = 73.8° (662 reflection). A reference specimen ($LaB_6$660a NIST) was also used to determine the instrumental contribution to the peak width, where the diffraction peak at 2Θ ≈ 67.6° (two superimposing reflections, *hkl* = 221/300) has been chosen because its proximity to the (662) reflection of LW(Mo)O, allowing to compare consistently the peak broadening. A common X-ray diffractometer as

the one used (D8 Advance) gives mainly Lorentzian peak shapes, where the Lorentzian contribution increases with increasing scattering angle due to wavelength dispersion[134]. In fact, when the pseudo-Voigt (*pV(x)*) of Eq. (5.13) was employed for single peak fitting, the Lorentzian contribution to *pV(x)* was 82(2) % for the (221/300) peak of $LaB_6$660a NIST. In a first approximation, it is assumed that the specimen induced broadening ($\Delta FWHM_{LW(Mo)O}$) has also a Lorentzian peak shape. Hence, the peak deconvolution to isolate the specimen broadening can be made just by subtraction of instrument broadening ($FWHM_{LaB6}$) from the measured broadening ($FWHM_{measured}$) such that

$$\Delta FWHM_{LW(Mo)O}^{2\theta \cong 73.8} \sim FWHM_{measured}^{2\theta \cong 73.8} - FWHM_{LaB6}^{2\theta \cong 67.6^\circ}. \quad (5.18)$$

The results are presented in Fig. 5.41. $\Delta FWHM_{LW(Mo)O}^{2\theta \cong 73.8}$ from Eq. (5.18) is represented as a function of the Mo/(W+Mo) uncertainties of LW(Mo)O specimens (ΔMo/(W+Mo)) measured with EPMA (Fig. 5.29 blue horizontal error bars). In Fig. 5.41, negative broadening values are beyond the resolution of the instrument, assumed to be correctly estimated by the LaB_6 reference peak widths.

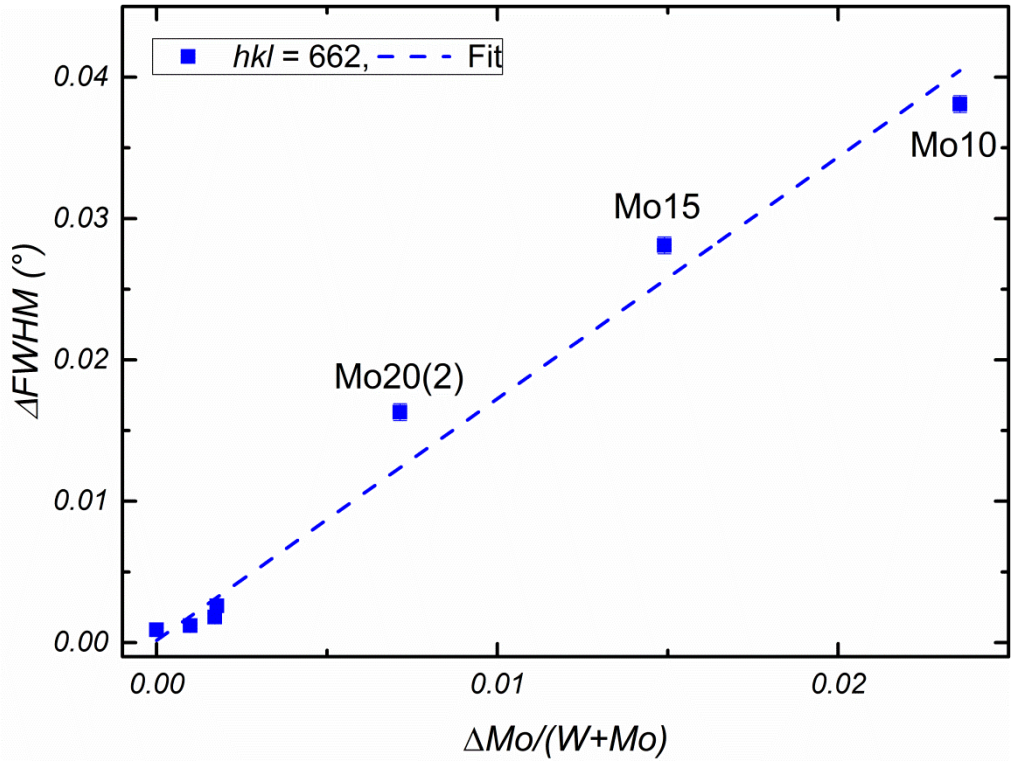

Fig. 5.41. LW(Mo)O-dry(Ar) peak broadening of the (622) reflection, after subtraction of the instrumental contribution of LaB_6, as a function of the Mo/(W+Mo) uncertainty measured by EPMA. The dashed straight line represents a linear fit (R^2 = 0.981) to the data.

From Fig. 5.41, it can be deduced that the *FWHM* of the (662) reflection of LW(Mo)O is directly proportional to the composition uncertainty (linear fit, blue dashed line). Also, it can be noticed how the peak broadening of well-prepared samples (bottom left of Fig. 5.41) is close to the instrument resolution, comparably to Fig. 5.15, hinting negligible specimen contribution to the broadening such as small crystallite sizes. Fig. 5.41 clarifies why the Mo10 and Mo15 specimens gave inconsistent refinements and also rationalise why Mo10 and Mo15 were excluded from studies in dependence of temperature.

In Fig. 5.42, selected metal-oxygen bond lengths obtained from neutron refinements are presented as a function of temperature, i.e. the 4*a*–96*k* (W_1/Mo_1–O_1), 4*b*–32*f* (La_1–O_2) and 48*h*–32*f* (La_2/W_2/Mo_2–O_2). The bond lengths between the 48*h* and 96*k* Wyckoff sites are not treated due to the

high disorder of both the 48*h* and 96*k* Wyckoff sites, explained for LWO in section 5.1.5. In addition, the 48*h*–96*k* bonds in LW(Mo)O are even more difficult to discuss because of the additional Mo atoms in both 48*h* and 4*a* Wyckoff sites.

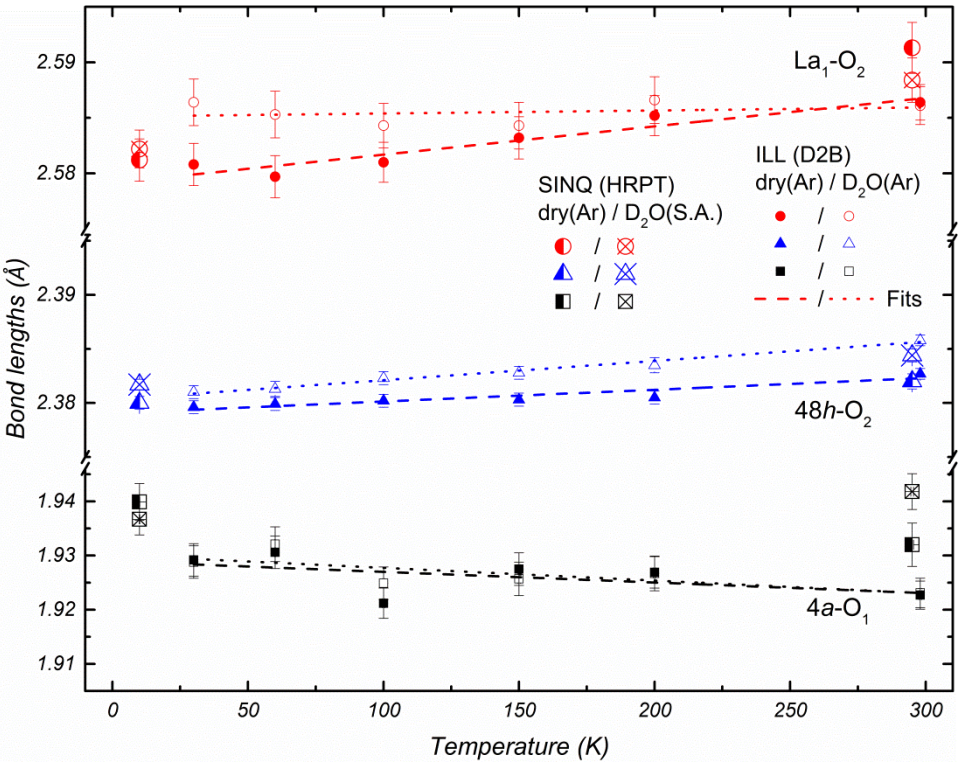

Fig. 5.42. Selected bond lengths from refinements of ND data of Mo20(2) specimen at HRPT, dry(Ar)/D_2O(S.A.), and D2B, dry(Ar)/D_2O(Ar), experimental stations as a function of temperature. Fits are straight lines and were performed including only ILL data, due to the higher number of data points and the higher resolution of D2B compared to HRPT. Dashed lines represent Mo20(2)-dry(Ar) while dotted lines represent Mo20(2)-D_2O(Ar).

In Fig. 5.42, the bond lengths of La_1–O_2 and 48*h*–O_2 increase with increasing temperature, as expected. The interpolations on data points in Fig. 5.42 were performed only on results from ILL, because of the higher resolution achieved with D2B and the larger number of patterns measured, compared with SINQ (HRPT). The latter values are, however, reported in Fig. 5.42 for completeness. As shown in section 5.1.5 for LWO, the angular oscillations of O_1 around W_1 creates an apparent bond shortening with increasing temperature, visible also for the 4*a*–O_1 bond lengths of the Mo20(2) specimen in Fig. 5.42. No change upon deuteration is noticed in the 4*a*–O_1 bond lengths for any temperature, so that deuteration does not change the first shell of the 4*a* Wyckoff site (W_1/Mo_1), octahedrally coordinated with oxygen atoms (O_1). Contrary to the 4*a*–O_1 bonds, the distance between La_1–O_2 and 48*h*–O_2 increases upon deuteration, as it can be seen in Fig. 5.42 and from the corresponding linear fits, where the dashed and dotted lines represent the dry(Ar) and D_2O(Ar) bond length trend with temperature. It is recalled that in the $Fm\bar{3}m$ model used, O_2 (32*f* site - *x*, *x*, *x*) can move along the [111] direction towards or away from the La_1-4*b* site. As the La_1–O_2 bond length depends on the ionic radii and the coordination of La, an 8-fold coordinated La has theoretical higher bond length compared to a 7-fold coordinated La. In general, due to geometrical restrictions, higher coordination yields higher bond lengths. This fact could be addressed considering the concept of bond strength firstly defined by Pauling to predict and rationalise the crystal structures of ionic compounds[135]. The second of his rules states that if *z* is the electronic charge of the cation and *N* its coordination number, the bond strength *S* is defined as $S = z / N$. As the

charge of lanthanum in ionic compounds is z_{La}=+3 [98], it follows that *S* increases with decreasing *N*. It also follows that the bond length, inversely proportional to the bond strength, increases with the coordination number *N*. Even if the O_2 atoms are constrained to move in the (*x*, *x*, *x*) direction and thus are not free to rearrange, a vacancy at the 32*f* site should induce a decrease in the bond length 4*b*–32*f* of dry(Ar) specimens, visible in Fig. 5.42 below *T* = 150 K (full red circles). The decrease of the 4*b*–32*f* bond length difference between dry(Ar) and D_2O(Ar) conditions seen at *T* > 150 K may be explained considering the increasing thermal vibration effects and/or the repulsion between the 32*f* and the 48*h* site. The understanding of the 48*h* (La_2/W_2/Mo_2)–O_2 bonding is more difficult because of the many atoms involved and the free refineable positions of 48*h* (0, *y*, *y*) and 32*f* (*x*, *x*, *x*) which give a relative displacement of one atom with respect to the other one. However, the same reasoning as for La_1–O_2 bond can be applied for (La_2/W_2/Mo_2)–O_2. It is considered only La_2 on 48*h* site, as from average X-ray scattering power refinements (see Table 5.11) it was estimated that about 96.5 at. % of the 48*h* site is occupied by La_2. La_2 is 7-fold coordinated when no vacancies in the 32*f* position are present and 6-fold coordinated when one vacancy occupies the 32*f* site. According to the Pauling bond strength definition, a decrease in coordination from 7-fold to 6-fold of La (z_{La} = +3) would induce a bond length shortening with the surrounding oxygens. For a detailed comparison of the bond lengths in dependence of Mo/Re-substitution in LWO, temperature and state (dry(Ar), D_2O(Ar)) the reader is referred to the next chapter.

5.4 Comparison between LWO and LW*M*O (*M* = Mo, Re)

5.4.1 Composition studies, phase analysis and water uptake

In this chapter, a comparison between the three investigated systems LWO and LW*M*O (*M* = Mo, Re) is outlined. In Fig. 5.43, the amount of vacancies obtained from TG and calculated using the charge compensation model reported for LWO[48,52,109] are presented as a function of the La/(W+*M*) ratio (integration of Fig. 5.14 with LW*M*O data). Likewise for the LWO system, a difference between the number of calculated and experimentally determined oxygen vacancies in the LW*M*O unit cell can be noticed. It is recalled that the humidification treatments were performed under wet(D_2O) argon gas whilst the TG measurements were performed in dry argon gas (reducing atmosphere). For LW(Re)O specimens, the deviation of the vacancy concentration from theory (red dotted line in Fig. 5.43) is even larger than for the LWO system and shows a systematic trend to lower vacancy concentrations with increasing Re substitution at constant La/(W+Re) ratio. Instead, the vacancy concentration in LW(Mo)O specimens seems to be only slightly dependent on the Mo substitution and lies at about the same value of vacancy concentration as that of the LWO system with the same La/(W+Mo) ratio.

Before the changes in vacancy concentration in the LW*M*O (*M* = Mo, Re) specimens will be discussed, the charge compensation model for LWO according to the literature[48,52,109] is recalled. The reaction upon deuteration is given by Eqs. (5.7) and (5.8), where the substitution on a La_2 site by a W_2 donor (x_W) carries a +3 charge ($W_{La2}^{\bullet\bullet\bullet}$ in K-V notation) and is compensated by δ_W = 3/2x_W oxygen atoms. According to Eqs. (5.7) and (5.8), *v* = 2 - δ_W = 2 - 3/2x_W vacancies (y-axis of Fig. 5.43). The situation for Mo substitution in LWO is as following. As the vacancy concentration in LW(Mo)O specimens obtained from TG measurements agrees with that for LWO and only slightly depends on Mo substitution, the excess charge of Mo should be equal to that of W ($Mo_{La2}^{\bullet\bullet\bullet}$ in K-V). Thus, in its oxidized state, the oxidation state of Mo is +6 (Mo^{6+}). After the TG measurement, Mo might have been reduced to Mo^{5+} or Mo^{4+} as reported in temperature-programmed reduction (TPR) studies for dry H_2 (10 % in Ar) atmosphere[31].

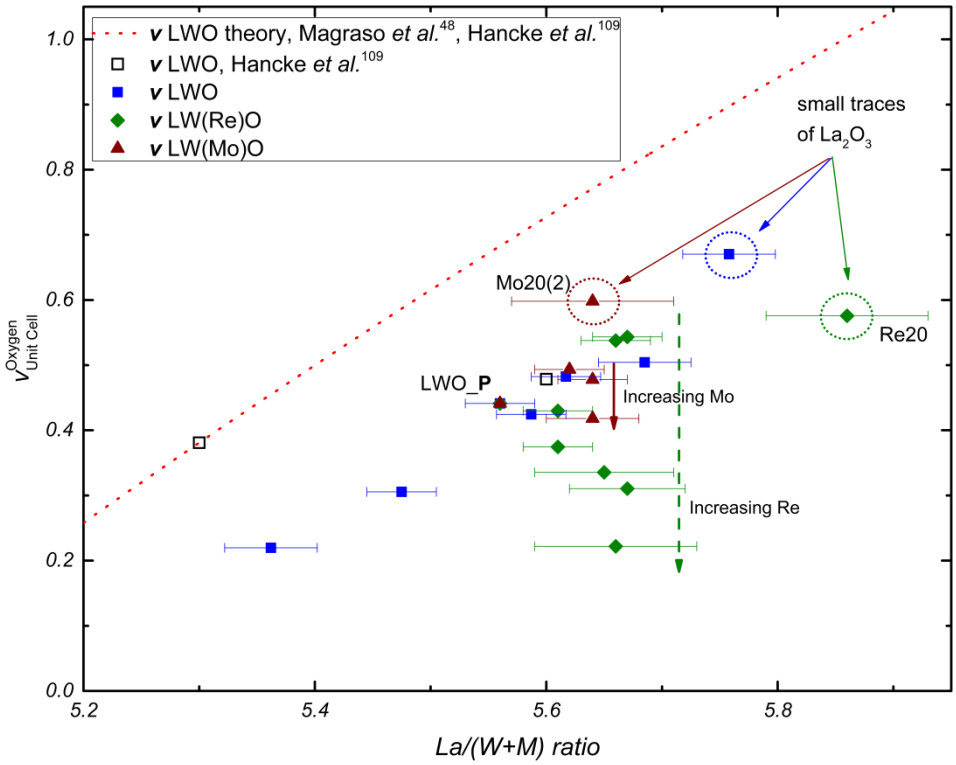

Fig. 5.43. Oxygen vacancies obtained from TG (full symbols) as a function of the La/(W+M) ratio, where LWO, LW(Mo)O and LW(Re)O results are depicted in blue squares, brown triangles and green diamonds, respectively. The theoretical amount of oxygen vacancies in LWO (red dotted line) was calculated according to the charge compensation equation derived from formulation (5.6)[48,109], while Eq. (5.10) was employed to calculate the oxygen vacancy concentration from TG measurements. In open black squares the two values for LWO from Hancke et al.[109] are shown. The data points inside the circles denote the specimens with some $La(OD)_3$ phase, which thus are not representative because of the not negligible contribution to mass loss of $La(OD)_3$ (see Fig. 5.4). This figure is the integration of Fig. 5.14 with LWMO data extracted from Fig. 5.23 (LW(Re)O) and Fig. 5.31 (LW(Mo)O).

In contrast, for the LW(Re)O system a clear trend of decreasing vacancy concentration with increasing Re substitution was found. This is in line with the higher oxidation state of Re than W when Re is oxidized, i.e., as-sintered or oxidized LW(Re)O could contain Re^{7+} and Re^{6+} cations. If the TG measurement is carried out under reducing conditions, the higher reducibility of Re compared to W and Mo[31] should change the Re oxidation state from $Re^{7+/6+}$ to $Re^{5+/4+}$. From the results of the diffraction measurements shown in the previous chapters, it was concluded that the O_1 site bonded to the 4*a* site (W_1/Mo_1 or W_1/Re_1) does not exhibit vacancies in any of the LW*M*O (*M* = Mo, Re) systems. Therefore, substitution on a W_1 site by Mo_1 or Re_1 does not change the octahedral coordination, giving for W_1, Mo_1 and Re_1 a coordination number of *N* = 6. However, nothing can be deduced for the oxidation state of the substituted Mo/Re, as, in principle, octahedral coordination is possible for all the allowed oxidation states (+3 to +6 for Mo, +4 to +7 for Re)[98]. Nevertheless, as the vacancies contributing to the measured mass change sit only on the 32*f* Wyckoff site, it is expected that Re^{7+} occupies at least the 48*h* site ($Re^{\bullet\bullet\bullet\bullet}_{La2}$ in K-V). This results in $\delta_{Re} = 4/2x_{Re}$ and $v_{Re} = 2 - 4/2x_{Re}$ (cf. Eqs. (5.7) and (5.8)), where x_{Re} is the Re amount on 48*h* site. This means, Re^{7+} in the structure replacing W^{6+} on the 48*h* site results theoretically ($v_{Re} < v_w$) in a lower vacancy concentration, which explains Fig. 5.43.

The discussion above concerns TG results on oxidized specimens with the mass loss obtained under reducing conditions. The oxidation states of Re and Mo in the oxidized specimen are supposed to be $Re^{7+/6+}$ and Mo^{6+}, respectively, before the TG measurements are carried out. It is expected that Re and Mo reduce to $Re^{5+/4+}$ and $Mo^{5+/4+}$, respectively, after the TG measurements have been performed.

However, whether Mo/Re reduction during the TG measurements influences the experimental and/or theoretical vacancy concentration and plays a role in the deviation between model and results is not yet clear even for W in the parent compound LWO. Nevertheless, it is possible to infer more information on oxidation and reduction of *M* = Mo, Re metals in LW*M*O specimens by evaluating and comparing the lattice parameters of dry(Ar) and D_2O(Ar) specimens, as presented in Fig. 5.44 and inset, respectively.

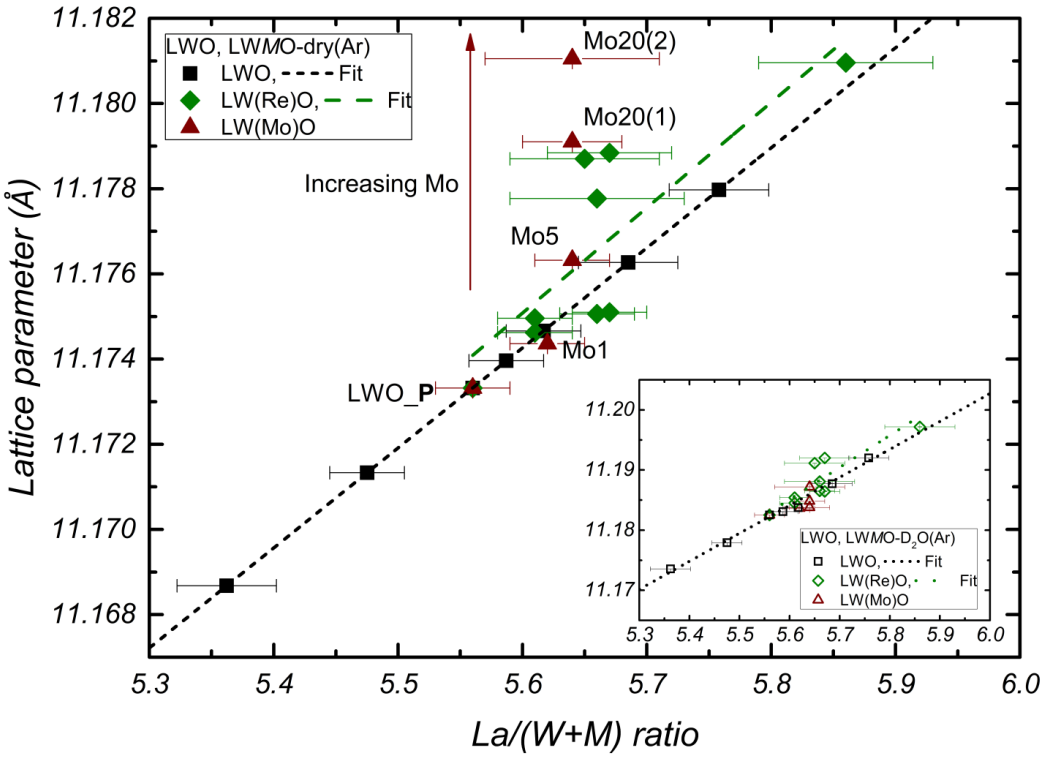

Fig. 5.44. Lattice parameters of LWO and LWMO in the dry(Ar) (full symbols) and in the D_2O(Ar) (inset, open symbols) conditions, as a function of the La/(W+M) ratio. The LWO specimens are represented by squares, while the LWMO series with M = Mo and M = Re is depicted in triangles and diamonds, respectively. The lattice parameters in dry(Ar) conditions of the LWMO specimens are extracted from the patterns represented in Fig. 5.22 (M = Re) and Fig. 5.30 (M = Mo). The lattice parameters of LWO-dry(Ar)/D_2O(Ar) are those represented in Fig. 5.13. Fits are straight lines.

Fig. 5.44 shows the lattice parameter in the dry(Ar) state and in the D_2O(Ar) state of the LWO and LW*M*O series (*M* = Mo, Re), as a function of the La/(W+*M*) ratio. For La/(W+Mo) ratios between 5.56 and 5.63, the lattice parameter of the dry(Ar) specimens increases with increasing La concentration. At La/(W+Mo) ≈ 5.65 the lattice parameter increases with increasing Mo concentration at constant La/(W+Mo) ratio. From this result it can be inferred that the average size of the substituting Mo is higher than that of the substituted W. Thus, after the drying procedure, Mo can be reduced to Mo^{5+} ($R_i(Mo)_{5+}^{6fold}$ = 0.63 Å) and/or Mo^{4+} ($R_i(Mo)_{4+}^{6fold}$ = 0.65 Å), larger than W, ($R_i(W)_{6+}^{6fold}$ = 0.60 Å). It is assumed that Mo^{4+} does not reduce further according to the TPR studies performed under more reducing conditions than in the present work[31]. The lattice parameters reported in Fig. 5.44 are a consequence of specimen drying at oxygen concentrations of about 10^{-12} (this value is measured at *T* = 25 °C) for longer times (4 h) compared to a normal TG measurement (< 2 h at 10 K/min heating rate) and at *T* = 900 °C. Moreover, the oxygen concentration in TG measuring conditions under dry argon gas was estimated to lie in the 10^{-5}-10^{-4} range at *T* = 22 °C. Therefore, reduction during the drying procedure is expected (Fig. 5.44) that is higher than during TG measurements (Fig. 5.43). Such an argument could also be applied for Re-substitution in LWO. Re cations are more reducible than Mo and may exist in

many different oxidation states upon reduction ($Re^{7+/6+} \rightarrow Re^{5+/4+}$). At *T* = 900 °C, following the TPR studies reported[31], most of Re cations should have an oxidation state of Re^{4+}, ($R_i(Re)_{4+}^{6fold}$ = 0.63 Å), with a possible contribution of the Re^{5+} oxidation state ($R_i(Re)_{5+}^{6fold}$= 0.58 Å). As $R_i(Re)_{4+}^{6fold}$ = 0.63 Å > 0.60 Å = $R_i(W)_{6+}^{6fold}$, but also $R_i(Re)_{5+}^{6fold}$ = 0.58 Å < 0.60 Å = $R_i(W)_{6+}^{6fold}$, this could explain the slight increase in the dry(Ar) lattice parameters upon Re substitution and for the same La/(W+Re) ratio.

Regarding the lattice parameters of the deuterated specimens (Fig. 5.44 inset) and by comparison of these lattice parameters with the TG results shown in Fig. 5.43, the oxidized Re and Mo are expected to have $Re^{7+/6+}$ and Mo^{6+} oxidation states, respectively, and, therefore, smaller ionic radii than W. This would result in smaller lattice parameters for LW*M*O-D_2O(Ar) compared to LWO-D_2O(Ar) specimens, which should increase as lattice(LW(Re)O) < lattice(LW(Mo)O) < lattice(LWO) or $R_i(Re)_{7+,6+}^{6fold}$ < $R_i(Mo)_{6+}^{6fold}$ < $R_i(W)_{6+}^{6fold}$. However, the oxygen atoms / OD groups filling the vacant oxygen sites also contribute to the unit cell size due to anion-anion repulsion and cation rearrangements, which results in an increasing unit cell size with increasing number of filled vacancies (see Fig. 5.13). As inferred from TG studies at constant La/(W+*M*), the amount of vacant sites filled by charge compensation (δ in Eqs. (5.6)-(5.8)) goes in the opposite direction than the lattice parameters, being δ(LWO) ≈ δ(LW(Mo)O) < δ(LW(Re)O), or δ(W^{6+}) ≈ δ(Mo^{6+}) < δ($Re^{7+/6+}$) and compensate the decrease due to changes in ionic radii.

The above discussion is the present understanding of such systems as many free parameters have to be properly evaluated to provide a complete comprehension of the LWO and LW*M*O (*M* = Mo, Re) systems, such as the different La/(W+*M*) ratio, substitution degree, reducing/oxidizing atmospheres, time and temperature. It can be concluded, however, that an answer to the discrepancies observed between the defect chemistry calculations and the vacancy concentration established with the TG data in LWO and LW*M*O (*M* = Mo, Re) is, at present, still missing. Besides, it has been noticed that in many publications on LWO and LW*M*O that report composition studies with the EPMA method, as in the present work, the measured La/(W+*M*) ratios for most of the specimens are slightly shifted from the nominal to higher values[46,52-54,131]. Notice that if this shift of the composition is neglected, the LWO/LW*M*O properties in terms e.g. of oxygen vacancy prediction (see Fig. 5.43) or conductivity may lead to biased interpretations of the results. The reasons for the minor differences in La/(W+*M*) ratio are ascribed to evaporation of W during LWO / LW*M*O synthesis[131,136] and/or due to segregation of W-rich phases at the specimen surface.

Moreover, for some specimens (e.g. Re20, but to a minor extent also LWO_**P** and others) segregation of La_2O_3 occurs over annealing time (see section 5.2.5 and literature for LWO[52]). This is another variable to take into account as La_2O_3 segregation may alter substantially the specimen's water uptake (see section 5.2.3). Information on this feature may be ascertained by comparing the elemental maps of LWO_**P**, Re20 and Mo20(2), measured by EPMA and shown in Fig. 5.45. Here, the elemental maps were collected from pieces of the sintered pellets after polishing. Hence, these maps represent the specimen conditions as-sintered. The relative intensity scale used by each detector is also represented and can be used for comparison within a single elemental image.

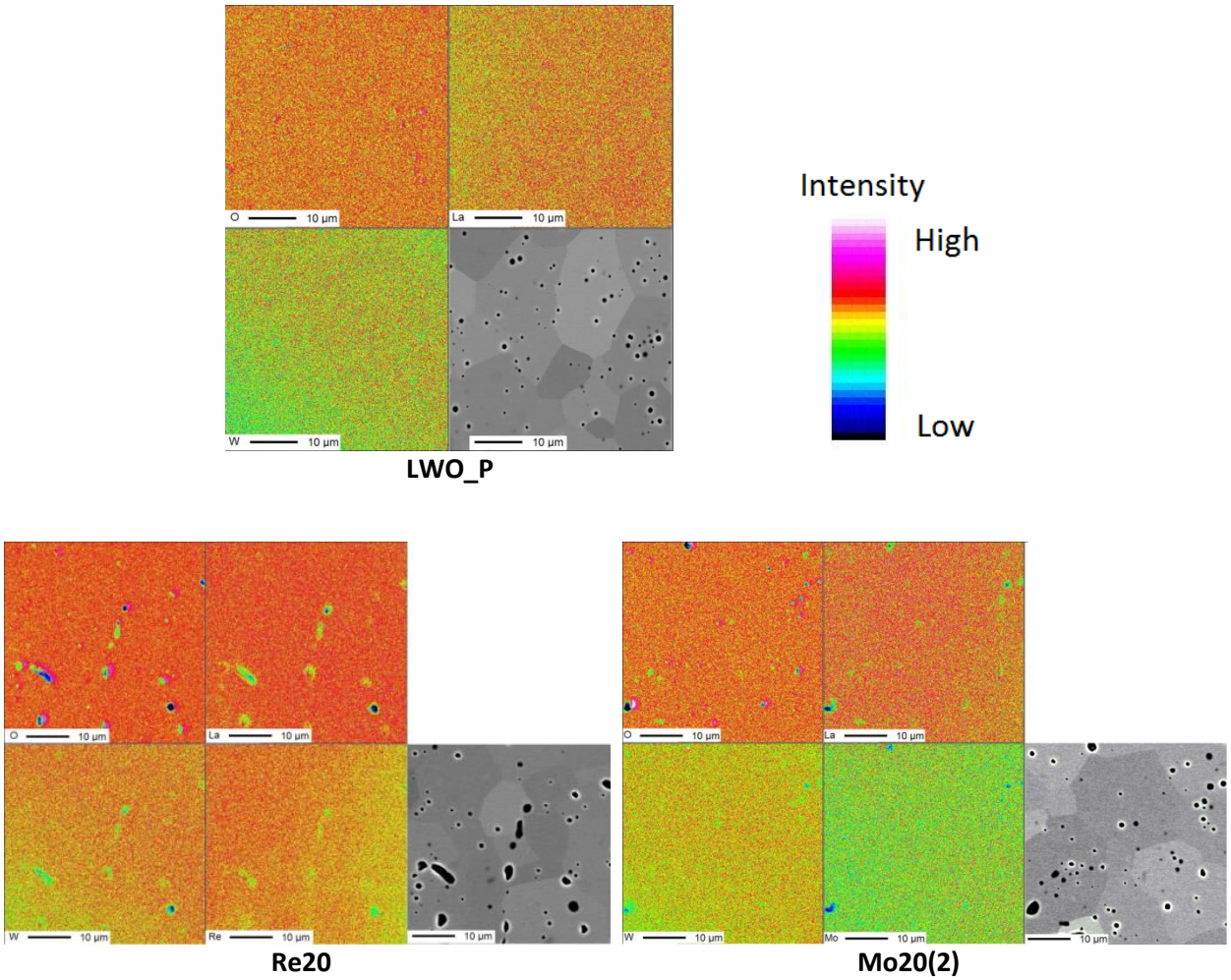

*Fig. 5.45. EPMA maps of the constituting elements of LWO_**P** ($La_{5.56(3)}WO_{12-\delta}$, top), Re20 ($La_{5.86(7)}W_{0.826(7)}Re_{0.174(7)}O_{12-\delta}$, bottom left), Mo20(2) ($La_{5.64(7)}W_{0.803(7)}Mo_{0.197(7)}O_{12-\delta}$, bottom right) along with their corresponding backscattered electron images. The relative intensity scale used by each detector is also reported.*

In all the maps and for all the different elements, the islands with colour towards green and blue (lower intensities) correspond to pores, whose presence as black areas can be confirmed in the corresponding back-scattered electron images. At the bottom-left and top-right corners of the W images, for each specimen, and in the right side of the Re image, for the Re20 specimen, a slight decrease of measured intensity is observed. This feature is ascribed to a slight shift of the calibrated energy during the measurement time (≈ 2 h). Nevertheless, as neither La-rich regions (fingerprint of La_2O_3), nor W(Mo/Re)-rich regions are visible in the elemental maps of the LWO_**P**, Re20 and Mo20(2) constituting elements, the specimen's homogeneity is confirmed in the as-sintered state on the micrometer scale. This finding suggests that the secondary phases observed in XRD/TG measurements in these specimens (e.g. Re20, see Fig. 5.27b) could have been induced by annealing only.

5.4.2 Temperature dependence of lattice parameters

In Fig. 5.46, the temperature dependence of lattice parameters obtained from ND (Fig. 5.46a) and HRXRD (Fig. 5.46b) refinements is shown. In Fig. 5.46a, the results on dry(Ar) and wet LWO_**P**, Re20 and Mo20(2) specimens are represented. In Fig. 5.46b the results on LWO_**P**-dry(S.A.), Mo20(1)-dry(S.A.) and on the reference NIST Si640d used as diluent are depicted above and below the break, respectively (brown dashed line).

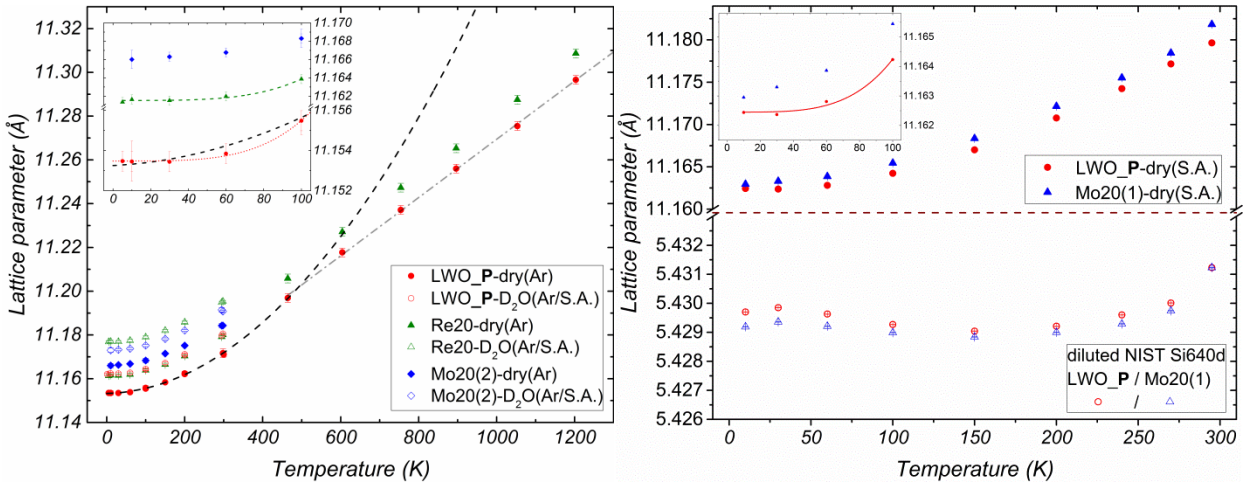

a) ***b)***

Fig. 5.46. ***a)*** *Temperature dependence of lattice parameters in dry(Ar) (full symbols) and wet(D_2O(Ar/S.A.)) (open symbols) conditions of LWO_**P** (red circles), Re20 (green triangles), Mo20(2) (blue diamonds), obtained from ND data (BERII, ILL, PSI). Due to small instrumental offsets, the lattice parameters have been scaled to values measured at ILL. The fit interpolations denote the temperature variation of LWO_**P**-dry(Ar) according to a quadratic fit (black dashed line) and a linear fit (grey dash-dotted line), respectively, below and above 470 K. In the inset, a magnification of the low temperature region (0 K < T < 105 K) of the LWO_**P**, Re20 and Mo20(2)-dry(Ar) lattice parameters is presented along with the magnification of the quadratic fit (black dashed line). Additionally, the best fits of the lattice parameter shown in the inset (0 < T < 105 K), according to the Debye model ($a(T) = A + BT^4$, cf. text) are shown by the red dotted (LWO_**P**) and green dashed (Re20) lines.* ***b)*** *Temperature dependence of lattice parameters of LWO_**P** (from Fig. 5.13) and Mo20(1) (from Fig. 5.37b) in dry(S.A.) conditions, obtained from HRXRD data, along with the lattice parameters of the diluent Si reference. In the inset, the fit (red line) according to the Debye model ($a(T) = A + BT^4$, cf. text) is shown for LWO_**P**-dry(S.A.).*

In Fig. 5.46a, the lattice parameters of Re20 and Mo20(2)-dry(Ar) at any temperature are larger compared to those of the LWO_**P** specimen. This finding confirms the XRD results shown in Fig. 5.44, where the lattice parameters in the dry(Ar) condition at T = 298 K order as lattice(LWO_**P**) < lattice(Re20) < lattice(Mo20(2)), or, in other words, as $R_i(W)_{6+}^{6fold} < R_i(Re)_{4+}^{6fold} < R_i(Mo)_{4+,5+}^{6fold}$. The absolute values of the lattice parameters in the dry(Ar) conditions, however, are predominantly determined by the La/(W+*M*) ratios, namely La/(W+Re) = 5.86 for Re20, La/(W+Mo) = 5.64 for Mo20(2), Mo20(1) and La/W = 5.56 for LWO_**P**. Lanthanum in 7-fold coordination has an ionic radius of $R_i(La)_{3+}^{7fold}$ = 1.10 Å, which is about two times the value of W ($R_i(W)_{6+}^{6fold}$ = 0.60 Å) or Mo/Re ions, irrespective of their oxidation states. Therefore, a higher La/(W+*M*) ratio results in a larger lattice parameter. In the D_2O(Ar) conditions, however, the larger expansion for Re20 upon deuteration compared to Mo20(2) and LWO_**P** can only be explained by a larger vacancy concentration in Re20 as Mo/Re-oxidation upon deuteration to $Re^{7+/6+}$ and Mo^{6+} would induce only a slight decrease of unit cell size. Once more, using the information of EPMA (Fig. 5.20, Fig. 5.29) and of the dry(Ar)/D_2O(Ar) lattice parameters represented in Fig. 5.44, it can be inferred that most of the contribution to the D_2O(Ar) lattice parameter discrepancies is due to slight differences in the La/(W+*M*) ratios. A higher lanthanum content also leads to a larger lattice expansion upon deuteration, especially visible for Re20, where the comparison to LWO_**P** yields a difference by a factor of two at T = 298 K. A second confirmation that Re20 has a higher La/(W+Re) content than LWO_**P** arises from the comparison between the lattice parameters shown in Fig. 5.44. The Re20 lattice parameter (a = 11.1914(1) Å) lies on the lattice parameter fit (black dashed line) of the LWO series in both dry(Ar) and D_2O(Ar) conditions, indicating that the effect of Re compared to La to the unit cell size is negligible.

In Fig. 5.46b, the results of LeBail refinements on the HRXRD patterns of specimens LWO_**P** and Mo20(1)-dry(S.A.) are shown. It is not excluded that the absolute values of the lattice parameter of LWO_**P**-dry(S.A.) and Mo20(1)-dry(S.A.) may not be exact, as small shifts due to capillary displacements and increasing wobbling when cooling to low temperatures are likely to be present. However, it can be expected that the Mo20(1)-dry(S.A.) values lie above the LWO_**P**-dry(S.A.) values as can be seen from XRD data (Fig. 5.44), from neutron data of Mo20(2) (Fig. 5.46a) and accounting for the larger La/(W+*M*) ratios of Mo20(1) (La/(W+*M*)=5.64)) compared to LWO_**P** (La/W = 5.56). Moreover, if the lattice parameter values of the diluent Si640d NIST are compared, the lattice parameter of Mo20(1)-dry(S.A.) seems to be slightly underestimated (≈ $5x10^{-4}$ Å at T = 10 K). Even supposing that the lattice parameter difference between LWO_**P** and Mo20(1)-dry(S.A.) is slightly underestimated, it remains an order of magnitude lower in the dry(S.A.) conditions compared to the dry(Ar) conditions. This is rationalised because Mo does not reduce in dry(S.A.) conditions, keeping a +6 oxidation state (Mo^{6+}). Summarizing these results, the lattice parameters as a function of temperature deduced by ND patterns could be interpreted and compared to those obtained from HRXRD patterns.

In Fig. 5.46a, for the Re20-dry(Ar) and LWO_**P**-dry(Ar) specimens, the temperature dependence below T = 470 K follows well a second order polynomial (R^2 = 0.999, $a(T) = A + BT + CT^2$), given by the black dashed line on the LWO_**P** dry specimen taken as representative example in Fig. 5.46. The second order polynomial interpolation yields equally good residuals (R^2 = 0.999) also on Mo20(2)-dry(Ar) and LWO_**P**, Re20, Mo20(2)-wet(D_2O) specimens below T = 298 K. Above T = 470 K, linear regression fits on LWO_**P**-dry(Ar) and Re20-dry(Ar) describe the data well. The grey dash-dotted line represents the fit to the data of LWO_**P** dry. This is in line with most compounds where in the high-temperature region $T > T_D$ (T_D: Debye temperature) the lattice parameter expansion is linear in temperature, thus fulfilling the Dulong-Petit law (constant heat capacity at high T, see Eq. (5.21) below). On the other hand, as shown in the inset, in the low temperature region (Fig. 5.46a inset) the quadratic fit (black dashed line) does not describe the behaviour of the lattice parameter adequately. According to Debye theory, the specific heat capacity at constant volume, c_v, is proportional to T^3 for low temperatures. This follows from approximations made for some parameters used in the Grüneisen relation, from which it follows that the temperature dependence of the lattice parameter $a(T)$ is given by a simple integration of c_v (see below). Hence, in the temperature region shown in the inset (0 K < T < 105 K), $a(T)$ should be approximately proportional to T^4, provided that LWO does not behave as a metal at such temperatures. According to Debye theory, the T^4 interpolation $a(T) = A + BT^4$, where A and B are constant (see red dotted line in the inset) gives better residuals (R^2 = 0.995) for LWO_**P** than a T^2 interpolation (R^2 = 0.969) performed in the same temperature range (results not shown here). The same low-temperature dependence as for LWO_**P** has been inferred for Re20 where the T^4 interpolation gives R^2 = 0.986 (green dashed line in Fig. 5.46a) compared to the T^2 interpolation where R^2 = 0.966. This result is confirmed also by HRXRD data for LWO_**P**, where the residual R^2 = 0.989 for the T^4 interpolation is higher than the residual for the T^2 one (R^2 = 0.976). For Mo-substituted specimens Mo20(1) and Mo20(2), in contrast, the T^2 interpolation yields better residuals for both ND (R^2 = 0.995 compared to R^2 = 0.976) and HRXRD data (R^2 = 0.996 compared to R^2 = 0.946). However, due to the different specimens considered, the different treatment and the small number of data points measured for Mo20(2) in the low temperature range (T < 60 K) at the same neutron source, it is not possible at present to give an exhaustive interpretation. It is expected that the low-temperature dependence of the lattice parameters upon Mo/Re substitution should not differ substantially from the parent compound, especially for such low concentrations (< 3 wt. %) of the substituted elements. Synchrotron data provide, in general, more precise lattice parameters and the anomaly seen at low temperatures of the Mo20(1) specimen might be interpreted considering a possible electronic contribution to heat capacity at low temperatures for

Mo-substituted specimens. This finding may indicate that LW(Mo)O behaves as a metal at low temperatures. In the literature it is mentioned that a class of materials, amongst them oxides containing transition metal ions (Mo, W, Re in the present case) may be generalized as reduction- and oxidation-type semiconductors, that change their insulating/conducting properties upon reduction or oxidation[137]. It is reported that these materials are generally light coloured when semiconductors and black when insulators. This feature is visible in Mo/Re-substituted LWO specimens while in the mother compound LWO no colour change upon different treatment is observed, see Appendix. However, very little is known about this issue at present. Whether Mo/Re substitution could make LW*M*O (*M* = Mo, Re; *M*/(W+*M*) ≠ 0) semiconducting even at low temperatures, such that LW*M*O systems (*M* = Mo, Re; *M*/(W+*M*) ≠ 0) belong to the reduction-type semiconductors remains unclear. A comparison with synchrotron HRXRD data for Re20 at low temperatures is needed to achieve a better understanding of thermal expansion at low temperatures. Despite the reasonable fits obtained for Re20 ND data the lattice parameter uncertainties could mask electronic contributions to heat capacity.

Even though the low-temperature data upon substitution seem to carry conflicting information, the linear thermal expansion coefficient $\alpha_L = \frac{1}{L_0}\frac{dL}{dT}$ could be plotted as a function of *T* if the data set is considered as a whole in the temperature range 5 K ≤ T ≤ 1200 K. In the general equation $\alpha_L = \frac{1}{L_0}\frac{dL}{dT}$, *L* and L_0 are calculated according to the refined lattice parameters a of Fig. 5.46, with $L = a$. The calculated α_L were fitted with the Debye model according to the following equation:

$$\alpha_L = \alpha_0 \left(\frac{T}{T_D}\right)^3 \int_0^{T_D/T} \frac{y^4 e^y}{(e^y - 1)^2}\, dy\,, \tag{5.19}$$

where α_0 is a temperature-independent fitting parameter.

Approximations were made for some parameters used in the Grüneisen relation $c_v\gamma = k\alpha_V$, where c_v, γ, k and α_V are, respectively, the specific heat capacity, Grüneisen parameter, bulk modulus and volumetric expansion. As k and γ are usually weakly dependent on temperature, the thermal expansion coefficient α_V and the specific heat capacity c_v reveal about the same temperature dependence. For any cubic structure, the volumetric expansion then becomes $\alpha_V = 3\alpha_L$. The Debye model can hence be applied to the present ND and HRXRD data to deduce the thermal expansion. Furthermore, from a simple integration in *dT* of the first and the last term of the following equations*

$$\frac{1}{a_0}\frac{da}{dT} = \alpha_L \cong c_v \propto T^3 \; and \qquad (T \ll \theta_D) \tag{5.20}$$

$$\frac{1}{a_0}\frac{da}{dT} = \alpha_L \cong c_v = constant\,, \qquad (T > \theta_D) \tag{5.21}$$

it can be inferred that the behaviour of the lattice parameter as a function of temperature *a(T)* can be described as $a(T) = A + BT^4$ and $a(T) = CT$ (with *A*, *B* and *C* constants) for $T \ll \theta_D$ and $T > \theta_D$, respectively, as shown in Fig. 5.46 for LWO_**P**-dry(Ar) and Re20-dry(Ar) specimens. However, if electrons significantly contributed to heat capacity, a term linear in *T* should be added in Eq. (5.20) and give a non-negligible T^2

* The right part of Eq. (5.21), $c_v = constant$, is the high temperature limit ($T > \theta_D$) of the Debye model for the specific heat capacity $c_v(T)$, also known as the Dulong-Petit law.

contribution to the temperature dependence of the lattice parameter at low temperatures, where the electronic heat capacity dominates[138,139].

The linear thermal expansion coefficient α_L is in the following referred to as thermal expansion coefficient (TEC). The TECs determined using the ND and XRD data of LWO_**P**, Re20 and Mo20 are shown in Fig. 5.47. In addition, TECs from dilatometry measurements (Seeger *et al.*[32]) were added to Fig. 5.47 for LWO_**P**, LWO-Re20 and LWO-Mo20 as red stars, green pluses and blue crosses, respectively.

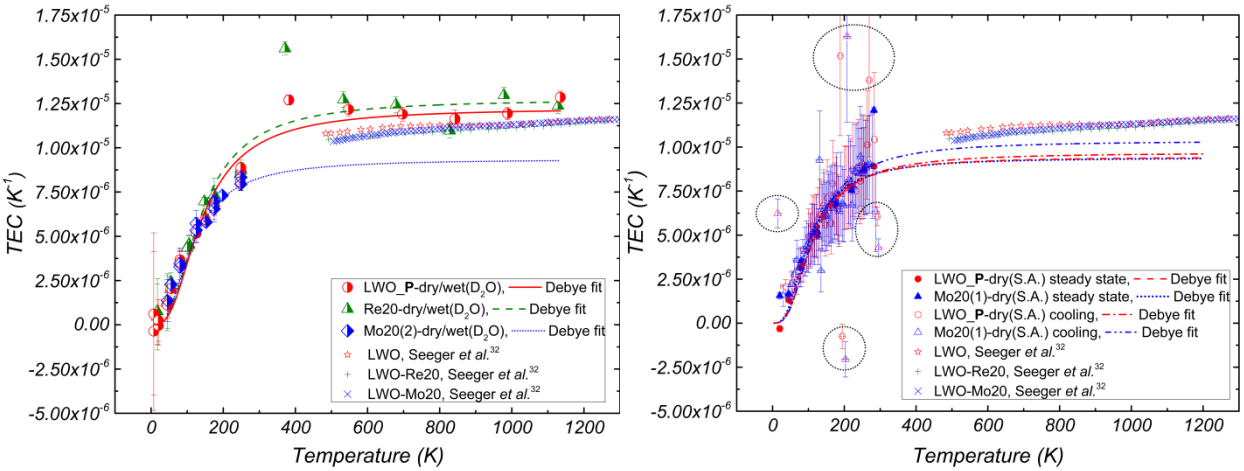

a) ***b)***

Fig. 5.47. Linear thermal expansion coefficient (TEC) as a function of the temperature, ***a)*** *from the ND data of samples LWO_**P**, Re20 and Mo20(2) with all different pre-treatments contained in the same data set, and* ***b)*** *from HRXRD for LWO_**P** and Mo20(1) in their dry(S.A.) state. The fit of the TEC was performed with Eq. (5.19). Results of the fits are given in Table 5.15. Red stars, green pluses and blue crosses represent dilatometry data for LWO, LWO-Re20 and LWO-Mo20, respectively, taken from Seeger et al.[32].*

More importance is given to the Debye fits (Eq. (5.19)) performed in the widest temperature range (5 K ≤ T ≤ 1200 K) for LWO_**P** and Re20 ND data (Fig. 5.47a) by the increased amount of data points available also at high temperatures. The lack of ND data for Mo20(2) and HRXRD data for LWO_**P** and Mo20(1) at high temperatures results in a shift of the corresponding Debye fits to lower values compared to either the dilatometry measurements, or to the LWO_**P** and Re20 Debye interpolations (see Fig. 5.47a, Fig. 5.47b). To improve the statistics, in the left figure all measurements of thermal expansion for one and the same specimen were combined, irrespective of their specific treatment, i.e., it was assumed that the TEC is independent of the specific treatment[32]. The obtained values for the Debye temperatures in the T range of 5 K ≤ T ≤ 1200 K are T_D = 580(33) K and T_D = 571(45) K for LWO_**P** and Re20, respectively. TEC values for Re20 and LWO_**P** at high temperatures are close to but not identical to those obtained by dilatometry measurements as reported in the literature (Fig. 5.47 green pluses and red stars, respectively)[32]. This discrepancy could be due to differences in sample stoichiometry, to small temperature differences between the recorded temperature and the specimen temperature in the high temperature furnace during the experiment at the FIREPOD instrument, or to the creation of thermal vacancies[140]. The latter, however, is not expected as the specimens were investigated in a temperature range still far away from the melting temperature of La_6WO_{12} (2050(20) °C) reported in the literature[57]. In Fig. 5.47b, TEC data extracted from the synchrotron measurements for the specimens LWO_**P**-dry(S.A.) and Mo20(1)-dry(S.A.) are presented. The data obtained by measuring during the cooling procedure and also at constant temperature are depicted in Fig. 5.47b and were fitted with Eq. (5.19), despite the absence of data in the high-temperature (T > 295 K) region. The data points included in the dotted circles were not considered in the fit procedure. The Debye temperatures obtained with Eq. (5.19) are reported in Table 5.15.

Table 5.15. Debye temperatures T_D (K) obtained from the fits according to Eq. (5.19) on ND data (Fig. 5.47a) and HRXRD (Fig. 5.47b). The term 'steady state' stands for data collection performed at constant temperature.

Sample	T_D (K) ND data (all T)	T_D (K) ND data (T ≤ 298 K)	T_D (K) HRXRD data Cooling (T ≤ 295 K)	T_D (K) HRXRD data Steady state (T ≤ 295 K)
LWO_P	580(33)	462(26)	431(56)	467(32)
Re20	571(45)	438(19)	--	--
Mo20(1)	--	--	415(25)	481(83)
Mo20(2)	--	473(41)	--	--

From Table 5.15, a comparison can only be made between the fit performed in the same temperature range, i.e., for $T \leq 298/295$ K or the entire T range. Nevertheless, good agreement between the Debye temperature is reached, either for the same specimen independently of the technique used, or for the same technique independently of the substitution, if the HRXRD data during cooling is not considered. In spite of the low accuracy due to the collection upon cooling, such data yields acceptable T_D estimations and comparable results for LWO_**P** and Mo20(1)-dry(S.A.).

5.4.3 Static and dynamic disorder

A different approach based on thermal vibrations (after Willis and Pryor[141]) permits to establish the Debye temperature T_D of the compounds and, in addition, the remaining static disorder of the analysed specimens. A reliable estimation of the remaining static disorder could help finding possible structural inconsistencies for the LW*M*O specimens. The Willis and Pryor[141] approach applied in the following is similar to the Housley and Hess[116] approach described in section 5.1.4.1 for LWO_**P** (see Fig. 5.7).
The Willis and Pryor[141] approach has been used to calculate T_D and the minimum static disorder for Re20 and Mo20(2) and has been applied also to the LWO_**P** specimen for comparison. ND data have been used because of the more accurate determination of atomic vibrations. The unit cell mass-weighted average displacement parameter B_M^{exp} has been estimated. B_M^{exp} represents the sum of two displacement parameters, mass-weighted over the unit cell: a temperature-dependent ($B_M^{thermal}$) and a temperature-independent (B_M^{static}) term. Willis and Pryor[141] adapted the Debye model to the temperature-dependent term, $B_M^{thermal}$, in a way that

$$B_M^{thermal} = \frac{6gh^2}{Mk_BT_D}\left[\frac{\varphi(x)}{x} + \frac{1}{4}\right], \qquad x = \frac{T_D}{T}, \tag{5.22}$$

where

$$B_M = \frac{1}{M}\sum_k m_k B_k \tag{5.23}$$

and the summation is done over the unit cell. h and k_B are Planck and Boltzmann constants, respectively, M and g are the mass and the number of atoms in the unit cell, respectively, and $\varphi(x)$ is the Debye function, given by

$$\varphi(x) = \frac{1}{x}\int_0^x \frac{y}{e^y - 1} dy \,. \tag{5.24}$$

In summary, the refined anisotropic displacement parameters mass-weighted over the unit cell, B_M^{exp}, determined according to Eq. (5.23), comply with the following expression[120,121]:

$$B_M^{exp} = B_M^{thermal} + B_M^{static} = \frac{6gh^2}{MK_BT_D}\left[\frac{\varphi(x)}{x} + \frac{1}{4}\right] + B_M^{static} \,. \tag{5.25}$$

Eq. (5.25) has two free parameters, B_M^{static} and T_D.

The cell-weighted displacement parameter B_M^{exp} calculated from refinements of samples LWO_**P**, Re20 and Mo20(2) is represented in Fig. 5.48 along with the fits performed with Eq. (5.25). The values of B_M^{static} obtained by Eq. (5.25) are then compared to those obtained from the model of Housley and Hess[116], whose values of B_k^{static} have been calculated as explained in the section 5.1.4.1 (see Fig. 5.7) and are then averaged over the unit cell with Eq. (5.23). All the parameters determined in this way are listed in Table 5.16.

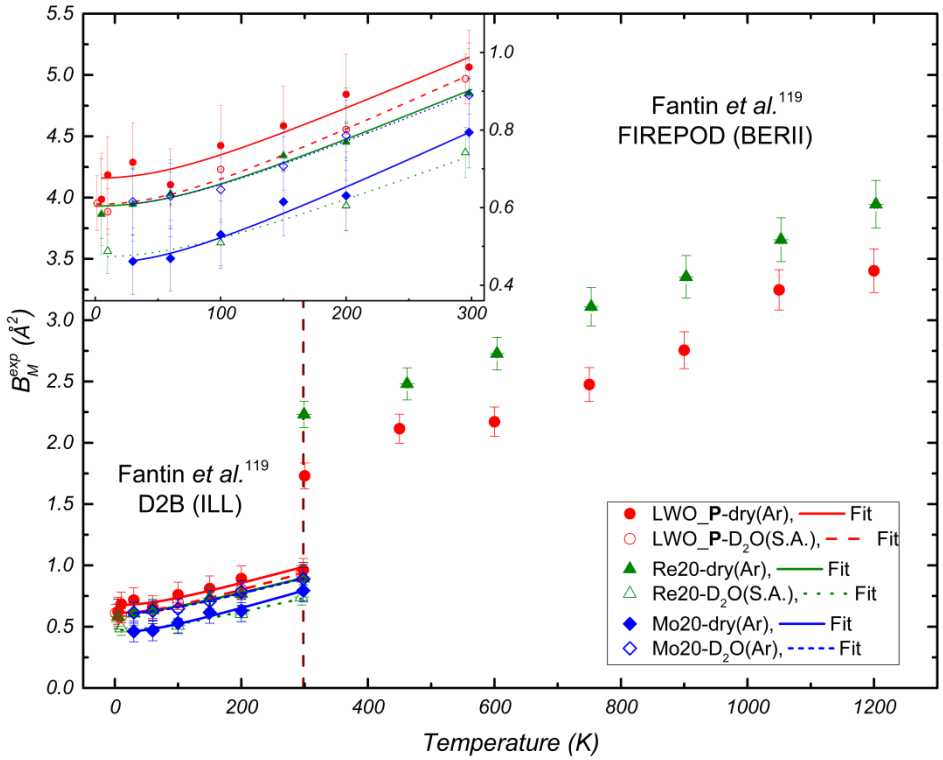

*Fig. 5.48. Unit cell mass-weighted displacement parameter B_M^{exp} from ND data as a function of temperature for sample LWO_**P**-dry(Ar)/D_2O(S.A.), Re20-dry(Ar)/D_2O(S.A.) and Mo20-dry(Ar)/D_2O(Ar), fitted with Eq. (5.25) for T ≤ 298 K (see inset). Below and above T = 298 K (brown dashed line) the results from D2B(ILL) and FIREPOD(BERII) ND data are reported, respectively.*

All the fits using the Willis and Pryor[141] approach partly shown in the inset of Fig. 5.48 represent the experimental data satisfactorily and intercept *T* = 0 K ($B_M^{static}(T = 0\,K)$) at about the same value. In general, a comparison between the absolute values of $B_M^{static}(T = 0\,K)$ is difficult due to the dependence of the ADPs on the background and the site occupancies. Nevertheless, slightly lower $B_M^{static}(T = 0\,K)$ absolute values have been found for Re20-wet(D_2O) and LWO_**P**-wet(D_2O), compared the Re20-dry(Ar) and LWO_**P**-dry(Ar) specimens, respectively. This is in agreement with Fig. 5.28 for

Re20-dry(Ar) and Re20-D_2O(Ar) anisotropic displacement parameters and could be explained by a higher vacancy concentration, in addition to Re reduction, as mentioned above. A lower number of vacant sites in the unit cell in wet(D_2O) specimens compared to the dry(Ar) pre-treated specimens may be linked to higher structural stability. As different pre-treatments yield different oxidation states the reduced Re or Mo are expected to increase static disorder. Although it is expected that vacancies and a reduction of cations could contribute to higher disorder, this interpretation is not confirmed by the results on Mo20(2) specimens for which the trend is opposite. The measurements done at the optimum wavelength (λ = 1.798 Å) at the FIREPOD diffractometer at the BERII reactor allow one to refine consistently only the isotropic displacement parameters (IDPs) due to the lack of high-angle data and only medium resolution. Hence, a fit according to the Willis and Pryor[141] approach including all data points shown in Fig. 5.48 for LWO_**P** and Re20 could not be performed.
Good agreement is achieved between the two approaches of Willis and Pryor[141] and Housley and Hess[116] for $T \leq 298$ K (see Table 5.16).

*Table 5.16. Unit cell mass-weighted minimum static disorder parameters ($B_M^{static}(T = 0K)$) obtained from the two different approaches of Housley and Hess[116] and Willis and Pryor[141]. Values for the Debye temperature T_D are also listed, fitted with the Willis and Pryor[141] approach and derived from the TEC, respectively. For Re20, Mo20(2) and LWO_**P** specimens, all pre-treatments were used in the same TEC data set and hence only one T_D is derived. Averages were performed according to Eqs. (4.24) and (4.25).*

Sample condition	Housley and Hess B_M^{static} (Å^2) $T \leq 298$ K	Willis and Pryor B_M^{static} (Å^2) $T \leq 298$ K	Willis and Pryor T_D (K) $T \leq 298$ K	Willis and Pryor T_D (K) Average	TEC T_D (K) $T \leq 298$ K	TEC T_D (K) All T range
LWO_P-dry(Ar)^{ILL}	0.41(17) (Fig. 5.7)	0.55(2)	354(19)			
LWO_P-D_2O(Ar)^{ILL}	0.38(12)	0.51(2)	358(21)	348(9)	462(26)	580(33)
LWO_P-D_2O(S.A.)^{SINQ}	0.41(12)	0.48(1)	343(11)			
Re20-dry(Ar)^{ILL}	0.41(14)	0.48(1)	361(10)			
Re20-D_2O(Ar)^{ILL}	0.42(11)	0.47(2)	343(13)	359(7)	438(19)	571(45)
Re20-D_2O(S.A.)^{SINQ}	0.30(11)	0.36(2)	383(17)			
Mo20(2)-dry(Ar)^{ILL}	0.27(13)	0.33(2)	342(11)	358(6)	473(41)	--
Mo20(2)-D_2O(Ar)^{ILL}	0.47(13)	0.48(1)	366(8)			

Moreover, the values for $B_M^{static}(T = 0\ K)$ indicate that the structural model used to fit Re20 and Mo20(2) is as good as for fitting LWO_**P**. In order to estimate the average static disorder, the values obtained from the Willis and Pryor[141] approach were transformed into average root mean square displacements (r.m.s.), as calculated previously for LWO_**P**-dry(Ar) (0.07(4) Å, cf. Fig. 5.7). The Willis and Pryor[141] approach is more accurate than that of Housley and Hess[116] and gives average r.m.s. values of 0.08(2) Å for LWO_**P**-dry(Ar)/wet(D_2O) specimens. Likewise, average r.m.s. values of 0.07 - 0.08(2) Å for Re20 and Mo20(2) specimens were determined. Hence, as for sample LWO_**P**, calculated r.m.s. values for Re20 and Mo20(2) are too low to further improve the structural model. In other words, for such disordered samples, the remaining static disorder cannot at present be accounted for. This conclusion, however, excludes the detailed modelling of anion librations (see section 5.1.5) or anharmonicity (see below), which requires a deeper understanding of recent software, theoretical simulations and implementation in refinement programs rather than general crystallography.
The comparison of the T_D obtained from the TEC (Fig. 5.47, Table 5.15) and those extracted from the Willis and Pryor[141] approach are also presented in Table 5.16. The average values of T_D derived from the thermal expansion coefficients (Eq. (5.19)) for LWO_**P**, Re20 and Mo20(2) in the temperature region $T \leq 298$ K are comparable with each other. However, they do not match with the ones extracted from the Willis and Pryor[141] approach (Table 5.16) for the same temperature range, being in average larger by

about 22 %. The reason for the large variation in T_D might be related to the restricted temperature range of ADP data points in the high-temperature region ($T > T_D$) and/or data which cannot be used to fit T_D through the Willis and Pryor[141] approach. As a rule of thumb, the Debye temperature values established with Eq. (5.25) in Fig. 5.48 depends on the slope of the interpolation curve for high temperatures: the steeper the slope, the lower is T_D. A comparable discrepancy has been reported for yttria-stabilized cubic zirconia (YSZ), which has a structure (fluorite $Fm\bar{3}m$) similar to the LWO and LW*M*O (*M* = Mo, Re) treated here. Argyriou[121] reported for YSZ a Debye temperature T_D = 533(20) K, fitted with Eq. (5.25) in a temperature range of 5 K ≤ T ≤ 1323 K. In contrast, the best fit of T_D in YSZ of Erich and Ma[142] yielded T_D = 963 K in the range 4 K ≤ T ≤ 1923 K. The latter authors, however, add an anharmonic term to Eq. (5.25) suggesting that the harmonic approximation applied to thermal displacement parameters (from which Eq.(5.25) is derived) does not hold for disordered structures with anionic defects as in YSZ. As the LWO structure is related to YSZ, being also disordered and containing oxygen vacancies, it can be inferred that LWO could also undergo cubic anharmonic vibration of the anions as reported for perfect fluorite structures in the work of Willis and Pryor[141]. Following the YSZ example, anharmonic and harmonic interpolations of W_1, O_1 and O_2 equivalent displacement parameter values (B_{eq}) for LWO have been performed. The B_{eq} values are taken from Fig. 5.6, including the two data sets of the present work (LWO_**P** specimen) and of Magraso *et al.*[50]. B_{eq} data were interpolated with the harmonic approximation according to the Willis and Pryor[141] model (Eq. (5.25)) and the quasi-harmonic approximation used in Erich and Ma[142]

$$B_{eq}^{An}(i) = B_{eq}^{static}(i) + B_{eq}^{thermal}(i)(1 + AT)\,, \tag{5.26}$$

where $B_{eq}(i)$ is the atomic equivalent thermal vibration parameter B_{eq} of atom i and the quasi-harmonic correction A is a constant dependent on the atomic potential force constants, the Grüneisen parameter and the volume coefficient of thermal expansion (see Erich and Ma[142] for details). Notice that Eq. (5.26) reduces to the harmonic approximation of Willis and Pryor[141], applied to a single atom, when A = 0.
The B_{eq} parameters of O_1, O_2 and W_1 atoms obtained from LWO_**P** data (T ≤ 298 K, Fantin *et al.*[119]) and from the LWO data reported in literature (T ≥ 298 K, Magraso et al.[50]) are depicted in Fig. 5.49, along with the interpolations performed according to Eq. (5.26) with A = 0 (harmonic approximation) and $A \neq 0$ (quasi-harmonic approximation).

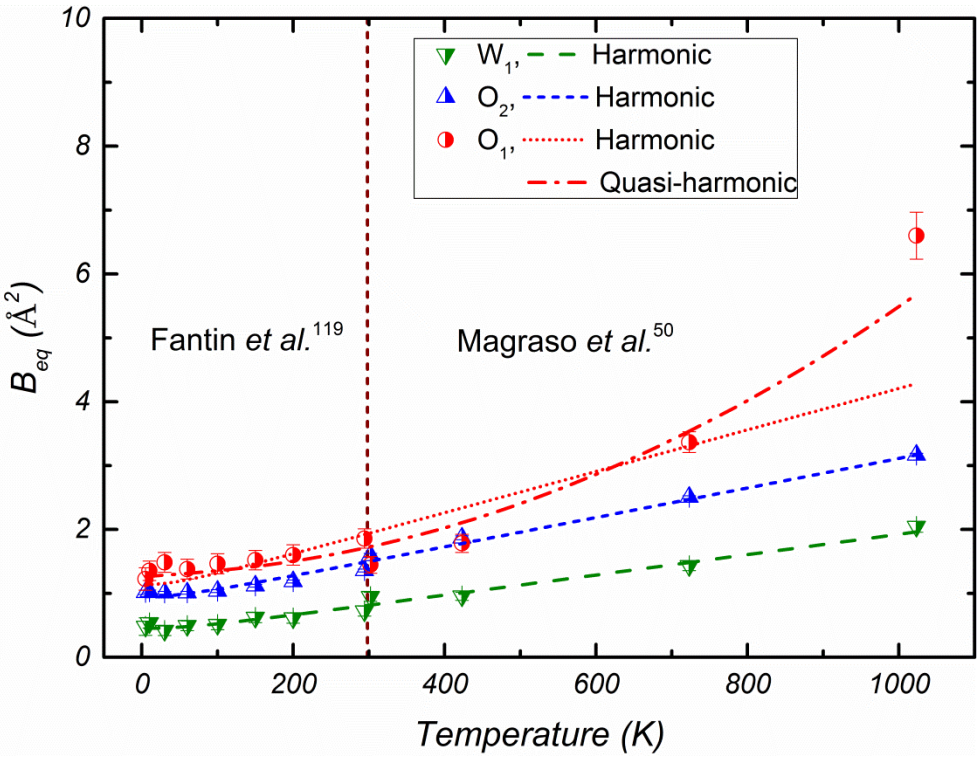

Fig. 5.49. Equivalent displacement parameter B_{eq} for O_1, O_2 and W_1 atoms in LWO as a function of the temperature. The data from the present work (Fantin et al.[119]) and the data of Magraso et al.[50] are shown in the temperature regions T ≤ 298 K and T ≥ 298 K, respectively, as in Fig. 5.6, where the red dashed line is drawn at T = 298 K. The data point at T = 298 K from the present work is shifted to T = 294 K, while the data point at T = 298 K taken from Magraso et al.[50] is shifted to T = 302 K, for better visualization. Fits with the harmonic approximation (Eq. (5.26), A = 0) were performed for O_1 (red dotted line), O_2 (blue short dashed line) and W_1 (green dashed line) atoms. For the O_1 atom, the fit using the quasi-harmonic approximation (Eq. (5.26), A ≠ 0) is also reported in red dash-dotted line.

For the W_1 and O_2 atoms, the harmonic approximation yields good residuals, with R^2 = 0.99 and R^2 = 0.97, respectively. For the O_1 atom, in contrast, the residual obtained is poor (R^2 = 0.72, cf. red short-dotted line in Fig. 5.49). When the quasi-harmonic approximation is used, the improvement of the fit is substantial, with a residual R^2 = 0.93. Applying Eqs. (5.25) and (5.26) to W_1, O_1 and O_2 allows one to estimate a Debye temperature for each of these atoms. Such Debye temperatures for the individual ions do not have much physical significance: in order to obtain physical values, Eq. (5.26) should be instead applied to the unit cell-weighted displacement parameter B_M^{An} in the same fashion as shown in Fig. 5.48 for low temperatures. As shown in Fig. 5.48, a lack of precise data at high temperature does, however, not allow this procedure. The harmonic (Eq. (5.25)) and anharmonic (Eq. (5.26)) interpolations give two values of T_D for the O_1 atom, where $T_D(O_1)$ = 233(21) K and $T_D{}^{An}(O_1)$= 841(37) K, respectively. From these estimations, it follows that an implementation of an anharmonic correction in O_1 would increase substantially the T_D(LWO_**P**) established by the Willis and Pryor[141] approach. To conclude, there is indeed a non-negligible anharmonic vibration of the anions occupying the 96*k* Wyckoff sites that is not present for the O_2 and W_1 atoms. In general, anharmonic vibrations are not likely to exist for heavy cations, as discussed for the YSZ system in Erich and Ma[142]. At present, it is not clear whether the discrepancy between the two estimates of T_D reported in Table 5.16 is mainly due to anharmonic parameters not included in Eq. (5.25) or due to the lack of high-temperature data. In addition, the non-modelled O_1 librations around W_1 (see section 5.1.5) could also contribute to an apparent anion anharmonicity. However, it is reasonable to conclude that the three terms may have contributed to the underestimation of the Debye temperature determined with the harmonic approach of Willis and

Pryor[141]. Therefore, it is assumed that the Debye temperatures in the present case are better estimated through the thermal expansion coefficients, resulting in Debye temperatures of T_D = 580(33) K and T_D = 571(45) K for LWO_**P** and Re20 specimens, respectively. For Mo20, it is expected that T_D lies also close to the values of LWO_**P** and Re20 as demonstrated to be the case for the $T \leq 298$ K range (see Table 5.15). However, in order to understand how much the anionic/cationic vibrations in the LWO system deviate from the harmonic oscillator approximation and, consequently, how to determine the Debye temperatures of LWO based systems within independent approaches such as that of Willis and Pryor[141], further insights are needed. For instance, an improved structural model that allows for anharmonic vibrations should be tested for diffraction patterns and more data should be collected in the $T > T_D$ region, where the anharmonic displacement terms become more relevant[141,142].

5.4.4 Temperature dependence of bond distances

In Fig. 5.50, selected metal-ion bond lengths are represented as a function of temperature for dry(Ar)/D_2O(Ar) states of LWO_**P**, Re20 and Mo20(2). Refinement with isotropic parameters was performed for all the specimens in both dry(Ar)/D_2O(Ar) conditions in order to obtain increasing W_1–O_1 distances with increasing temperature and a better comparison between the different substitutions and conditions.

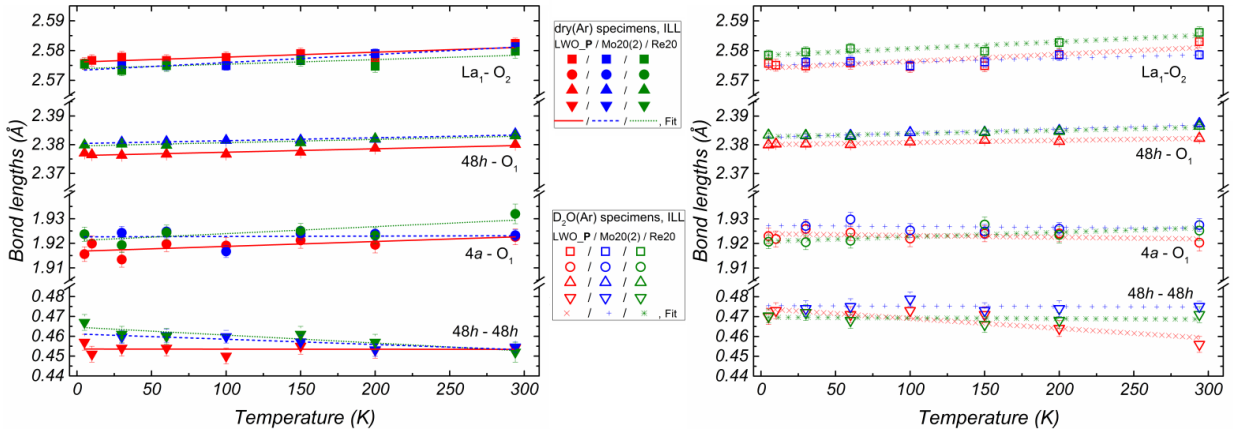

a) dry(Ar) ***b) D_2O(Ar)***

*Fig. 5.50. Selected bond lengths from ND data of LWO_**P**, Re20 and Mo20(2) in **a)** dry(Ar) and **b)** D_2O(Ar) as a function of temperature. The ND data reported were collected at the D2B experimental station. Linear fits are added as a guide to the eyes.*

It is not surprising that the 48*h*–48*h* bond gives the largest discrepancy between the three specimens in the dry(Ar) condition, in D_2O(Ar) conditions, and also between dry(Ar) and D_2O(Ar) conditions: the metal-metal distances are in general poorly estimated by neutron diffraction (see Fig. 5.18). The 48*h* site remains split at any temperature and condition investigated and in all the specimens treated in the present work the 48*h*–48*h* distances lie between 0.44 and 0.48 Å. The 4*a*–O_1 bond length seems to slightly increase upon Mo/Re substitution in the dry(Ar) state (Fig. 5.50a). This fact may be explained considering the results of Fig. 5.46 and Fig. 5.47, and recalling the Pauling bond strength concept $S = z / N$. A bond strength lower than the W_1–O_1 bond may hint at an oxidation state z, which may be smaller than the +6 oxidation state of W (W^{6+}) due to the reduction of the substituted elements Mo or Re, when equal coordination N is assumed. In fact, 4*a* site coordination was established to be N = 6 independently of the substitution. This has been inferred from the occupancy values of the O_1 site in LW*M*O obtained from Rietveld refinements. This reasoning may be also applied to the 48*h*–O_2 bond length, which presents in the dry state larger values for the substituted specimens than for the LWO_**P**. However, another explanation might be simply the cell expansion due to a higher La/(W+*M*) or, in other

words, to a higher amount of the largest La atom ($R_i(La)_{3+}^{7fold}$ = 1.10 Å) on the 48*h* site. Higher cell expansion due to higher La/(W+*M*) ratio, however, cannot explain the La_1–O_2 bond values, which seem to be shortened in LW*M*O-dry(Ar) specimens. As this bond reflects the vacancy number on the O_2 position, lower bond lengths are related to higher number of vacancies, which is proven to increase with increasing La content in the unit cell. Considering the bond strength concept, for z_{La} = +3 and the bond strength increasing with increasing La/(W+*M*) ratio, the coordination number *N* must decrease as shown for the dry specimens in Fig. 5.50a. This aspect is confirmed in Fig. 5.50b, where the bond lengths as a function of temperature for the deuterated specimens are shown. In Fig. 5.50b, the La_1–O_2 distance for Re20 exceeds the La_1–O_2 bond length for LWO_**P** and Mo20(2) due to the larger number of vacant sites occupied upon deuteration. By comparison of Fig. 5.50a and Fig. 5.50b, upon deuteration the 4*a*–O_1 bond length of Re20 exhibits a trend opposite to the La_1–O_2 bond length. Despite the expansion of the unit cell upon deuteration, the 4*a*–O_1 bond length of Re20 changes from above (Fig. 5.50a) to below (Fig. 5.50b) the 4*a*–O_1 bond length of LWO_**P**. This can be rationalised by Re oxidation, hinting that Re^{7+} may be present also in the 4*a* site. No clear information for the Mo20(2) specimen in addition to the behaviour of the La_1–O_2 bond lengths can be extrapolated from Fig. 5.50. A final statement on the relation between bond lengths, oxidation states and Wyckoff site occupied by Mo/Re atoms is very difficult to derive univocally from diffraction techniques due to the highly disordered LWO/LW*M*O crystal structures. However, probing the local structure with X-ray absorption spectroscopy (XAS) in the near edge (NEXAFS: near edge X-ray absorption fine structure) or extended (EXAFS: extended X-ray absorption fine structure) region could improve the understanding of the role played by Mo/Re substitution in LWO, especially on the 48*h* position which is responsible for charge compensation and vacancy concentration. However, the XAS technique is very demanding due to the low concentration of the substituted elements in addition to the strong absorption of the heavy metals.

6 Summary

6.1 $La_{6-x}WO_{12-\delta}$ ($0.4 \leq x \leq 0.8$)

The systematic study and a comparison of EPMA and XRD carried out on the specimen series $La_{6-x}WO_{12-\delta}$ ($0.4 \leq x \leq 0.8$) reveals a shift of the La/W nominal ratio to higher values. Phase analysis on LWO confirmed the existence of three regimes of La/W ratio postulated in the literature. There, less than 1 wt. % of secondary phases $La_6W_2O_{15}$ and La_2O_3 was estimated for specimens at the single phase boundaries, LWO52 and LWO56, respectively.

Thermogravimetry shows a systematic increase of mass loss with increasing La/W ratio, which is in accordance with the available theory based on the charge compensation equation for LWO. In addition, the onset temperature T_i for mass loss decreases with increasing La/W ratio. Despite its low amount (< 1 wt. %), the hygroscopic La_2O_3 phase alters significantly the mass loss and T_i value measured for LWO56. At this point, the ion current signal measured with the mass spectrometer gives clear La_2O_3 fingerprints. The vacancy concentration in LWO obtained from TG measurements shows a systematic deviation from theory, since less than 65 % of the theoretically predicted vacancies are found to be filled. The reason for this is at present not understood.

In addition, the peak widths of the XRD patterns in dry(Ar) and D_2O(Ar) conditions increase with increasing La/W ratio, suggesting lattice parameter variations between different unit cells. This finding is ascribed to W substitution on the La site and a varying vacancy concentration for different unit cells, caused by local lattice distortions. Such local lattice distortions would also explain the very broad ion current peaks (*FWHM* ≈ 220 °C for *m* = 18), ascribed to the different activation energies of the filled vacant sites. Neutron diffraction was performed on the LWO_**P** specimen for varying temperatures (1.5 K ≤ *T* ≤ 1200 K) and dry(Ar)/D_2O(Ar/S.A.) conditions. Comparison between the structural models of Scherb[53] and Magraso *et al.*[50] was performed by studying the atomic vibrations in the crystal structure and thus retrieving the remaining static disorder according to the model of Housley and Hess[116]. The model of Scherb[53] results in a remaining static disorder in the unit cell which is about 4 times lower than that found with the model of Magraso *et al.*[50]. This is ascribed to the split position of La_2/W_2 atoms also observed in electron density maps. A study of the LWO_**P** bond lengths as a function of temperature (1.5 K ≤ *T* ≤ 1200 K) was performed while allowing only for either isotropic or anisotropic displacement parameters. In the latter case, a slight bond shortening with increasing temperature is observed for the W–O distances (4*a*–96*k* Wyckoff sites). This result changed by constraining the atomic vibrations to be only isotropic. When isotropic displacements were allowed, the W–O bond distances increased with increasing temperature. This is caused by libration movements of the oxygen atoms bonded to tungsten and can be verified by nuclear density maps. However, libration movements are not correctly modelled neither by isotropic, nor by anisotropic oxygen vibrations. Rigid body/TLS refinements of diffraction data must be attempted. High-resolution X-ray diffraction data was refined based on the $Fm\bar{3}m$ space group and do not show the tetragonal distortions reported by Magraso *et al.*[48]. HRXRD data shows that the apparent bond length 48*h*–48*h* decreases with increasing temperature, which is not in accordance with

neutron data. This underlines how the 48*h* site is split and how at lower temperatures the splitting increases and the 48*h* site gets closer to the nearest W–O octahedra.

6.2 $La_{5.4}W_{1-y}Re_yO_{12-\delta}$ ($0 \leq y \leq 0.2$)

Composition studies by EPMA on the LW(Re)O system allowed one to estimate the position of the single-phase region in the phase diagram. Moreover, EPMA reveals a shift of the single phase region to higher values of La/(W+Re) ratio with increasing Re substitution on the W site (Re/(W+Re). The secondary phases seem to have the same composition as that established for the LWO series, being $La_6W_2O_{15}$ and La_2O_3, respectively, located below and above the single phase region. The reflection conditions according to the measured XRD patterns were not changed for Re-substituted specimens in dry(Ar)/D_2O(Ar) conditions, where the indexed reflections were the same as those of LWO_**P**.

By combination of composition studies and thermogravimetry, a decrease of water uptake with increasing Re substitution is revealed, hinting at a higher oxidation state of Re (Re^{7+}) compared to the substituted W (W^{6+}). Moreover, an anomaly in the TG curve of Re20_IMP specimen can be explained if the ion current signals of the $La_6W_2O_{15}$ are considered. For the Re20 specimen, an increase of the amount of the La_2O_3 phase with time is noticed. The lower stability for La-rich LWO specimens (higher La/W ratio) reported in the literature, which results in increased La_2O_3 segregation over the time, applies also to the LW(Re)O system.

By combining the average neutron scattering length approach and composition studies, Re has been found to substitute W on both of its Wyckoff sites, namely the 48*h* and the 4*a* sites. In addition, similar results as for LWO_**P** established that the oxygen vacancies sit on the 32*f* Wyckoff sites and that the coordination of the 4*a* sites remains the same as in the non-substituted compound (*N* = 6). This finding allows for concluding that in LW(Re)O the 48*h* is also bonded to the vacancies in 32*f*, and that Re^{7+} sitting in the position 48*h* could be the only responsible for the lower hydration of LW(Re)O with increasing Re concentration.

6.3 $La_{5.4}W_{1-y}Mo_yO_{12-\delta}$ ($0 \leq y \leq 0.2$)

Composition studies by EPMA on the LW(Mo)O system provide only a rough estimate of the location of the single phase region in the phase diagram, due to the lack of data points even when considering two data points given by Amsif *et al.*[131]. As for the LW(Re)O system, the reflection conditions in the LW(Mo)O XRD patterns did not change upon Mo substitution and for dry(Ar)/D_2O(Ar) conditions. By combining the composition studies and thermogravimetry, a slight decrease of water uptake with increasing Mo substitution is noticed. However, as the values established are similar to the LWO series, it can be deduced that the oxidation state of Mo in oxidizing conditions has to be the same as that of W (Mo^{6+}, W^{6+}). Secondary phases for three out of seven LW(Mo)O specimens were identified as $La_6W_2O_{15}$ and La_2O_3. Two amongst the three phase-impure specimens (Mo10, Mo15) revealed prominent peak broadening. This was demonstrated to be due to incomplete reactant diffusion.

By combining the composition studies with average neutron scattering length and with the average X-ray scattering power approach, it has been demonstrated how Mo substitutes W on both its 48*h* and 4*a* Wyckoff sites. Moreover, high-resolution X-ray diffraction studies on Mo5-dry(S.A.) and Mo20(1)-dry(S.A.) specimens were performed as a function of temperature. The lattice parameters of Mo5-dry(S.A.) and Mo20(1)-dry(S.A.) decrease with decreasing temperature and seem to level off in the low temperature region (T < 30 K). It has been found that the lattice parameter of Mo5-dry(S.A.) is slightly larger than that of Mo20-dry(S.A.), hinting that in dry(S.A.) Mo has a +6 oxidation state (Mo^{6+}), thus confirming TG results. The bond lengths from ND measurements of the Mo20(2) specimen in

dependence of condition (dry(Ar) vs D_2O(Ar/S.A.) and increasing temperature show a shortening of the W–O distances similar to what has been observed for LWO_**P**. No difference is seen in the absolute values of the bond lengths in both dry(Ar)/D_2O(Ar/S.A.) conditions, hinting that there is no change in coordination of both W and Mo sitting on the 4*a* sites (*N* = 6). Therefore, the vacancies in the LW(Mo)O system also sit on the 32*f* Wyckoff site.

6.4 Comparison between LWO and LW*M*O (*M* = Mo, Re)

Comparison of the TG measurements of LWO and LW*M*O (*M* = Mo, Re) shows that the deviation between the experimental results and theory observed for the LWO series is slightly larger for the LW(Mo)O system and much larger for the LW(Re)O system and increases with increasing Mo/Re substitution. This seems to confirm the Re^{7+} oxidation state when the specimens are oxidized. In addition, it can be inferred that Re^{7+} occupies the 48*h* site, as the 48*h* site plays a role in the charge compensation equation and, thus, in the vacancy concentration. A comparison between the lattice parameter in dry(Ar)/D_2O(Ar) conditions and the ionic radii suggests that the oxidation states of the metals Mo/Re strongly depend on the atmospheres used. In dry(Ar) conditions, the Re oxidation state is mainly Re^{4+} (ionic radius of Re^{4+} larger than W^{6+}), while in D_2O(Ar) conditions it is mainly $Re^{7+/6+}$ (ionic radius of $Re^{7+/6+}$ smaller than W^{6+}). Larger differences between the lattice parameters in the dry(Ar) and D_2O(Ar) conditions are observed for LW(Mo)O. After comparison between the ionic radii, Mo in the reduced state (dry(Ar)) is supposed to be $Mo^{4+/5+}$ (ionic radius of $Mo^{4+/5+}$ larger than W^{6+}), while in D_2O(Ar) conditions the Mo oxidation state is mainly Mo^{6+} (similar ionic radii of Mo^{6+} and W^{6+}). These conclusions have been inferred supposing that the oxidation state of W is W^{6+} and that W does not reduce, as described in the literature[31,49]. The comparison between the lattice parameters of LWO_**P** and Re20 as a function of temperature yields a Debye trend for low ($T \le 100$ K) and high ($T \ge 470$ K) temperatures which for Mo20(1) and Mo20(2) is not observed. The corresponding thermal expansion coefficients extracted from the lattice parameters yield comparable results for Mo20(1), Mo20(2), Re20 and LWO_**P** specimens, where the Debye temperatures for Re20 and LWO_**P** are found to be T_D = 580(33) K and T_D = 571(45) K, respectively. These Debye temperatures were estimated considering the whole temperature range data (1.5 K ≤ *T* ≤ 1200 K), which was not possible for Mo20 specimens due to lack of high-temperature data. The minimum static disorder found for the three specimens LWO_**P**, Re20 and Mo20(2), as established from ND data according to the model of Willis and Pryor[141], is similar in size with unit cell r.m.s. values of 0.07-0.08(2) Å. This finding provides a final proof that the models employed to refine the structure of Mo- and Re-substituted specimens are as valid as for the non-substituted LWO_**P**. This finding gives an ulterior proof that Mo and Re statistically substitute W on both its Wyckoff sites. The Debye temperatures extracted from the model of Willis and Pryor[141], along with the minimum static disorder, do not match those obtained from the thermal expansion coefficients in any of the LWO or LW*M*O system. This is due to the anharmonic vibrations of the O_1 atom around W_1. This interpretation is proven by adding a quasi-harmonic term to the model of Willis and Pryor[141] and by comparison between the harmonic and quasi-harmonic interpolations in LWO. This result, anharmonic vibration of the O_1 atom, is comparable to observations on yttria-stabilized zirconia as reported by Erich and Ma[142].

Finally, the comparison of bond lengths between Re20, Mo20(2) and LWO_**P** obtained from neutron data as a function of temperature and the specimen condition (dry(Ar)/D_2O(Ar)) confirms that the vacancies sit on the 32*f* site. Additionally, the comparison of bond lengths of Re20 and LWO_**P** hints at a change of the oxidation state of the 4*a* Wyckoff site in Re20 between pre-treated dry(Ar) and D_2O(Ar) specimens. The relation between bond length variation and Re oxidation states could be explained by the Pauling bond strength concept[135].

7 Conclusions

In this work, a systematic study of the composition, water uptake and structural studies of three different systems was performed: the predominantly protonic conducting material LaWO and the mixed ionic/electronic conductors LaW(Re)O and LaW(Mo)O. The *M*-substitution (*M* = Mo, Re) on W sites allows these compounds to be used as filters for CO_2/H_2 in gas separation membranes due to the substantially improved electronic conductivity and thus improved hydrogen permeation. It can be concluded that:

(1) The La/(W+*M*) ratios govern many properties of such systems:
   a. The actual composition for all specimens deviates from the nominal composition to higher La/(W+*M*) ratios. Small W evaporation must be considered when weighing the educts, in addition to polishing the surfaces to remove W-rich phases.
   b. The single phase region for the LaW(Re)O system is shifted to higher La/(W+Re) ratios with increasing Re/(W+Re) ratios. Synthesis and stoichiometry of LaW(Re)O specimens must agree to the single phase region determined in the present work.
   c. The vacancy concentration in the unit cell for all specimens increases with increasing La/(W+*M*) ratio for constant *M*/(W+*M*) ratio.
      - For the LaWO system, a systematic decrease of the onset temperature T_i in the TG curves with increasing La/W is observed. The vacancy concentration in specimens with higher La/W ratio is thus larger, but at the same time vacant sites are produced more easily.
      - For LaW*M*O specimens, the vacancy concentration in the unit cell decreases with increasing *M* (*M* = Mo, Re) concentration at constant La/(W+*M*) ratio, thus decreasing the specimen hydration with increasing substitution. Hence, Mo/Re-substitution for W decreases the specimen hydration. This decrease of specimen hydration is more pronounced for Re substitution than for Mo substitution.

(2) The experimental results on vacancy concentration are not explained by the available charge compensation equation in LaWO, where a clear discrepancy between theory and results is observed. The lowest deviation from full hydration is about 35 %.
   a. Upon increasing Re-substitution, the deviation from the charge compensation equation predictions in LaWO increases. This is caused by the higher oxidation state of Re (Re^{7+}) compared to W (W^{6+}) in oxidizing condition.
   b. Upon increasing Mo-substitution, the deviation from the charge compensation equation in LaWO is only slightly larger than that of LaWO. Therefore, the oxidation state of W (expected W^{6+}) and Mo (supposed Mo^{6+}) in oxidizing conditions is concluded to be the same.

(3) Secondary phases may influence the thermogravimetry curves. Multiple stage decays were observed when ≈ 3 wt. % or less than 1 wt. % of $La_6W_2O_{15}$ and La_2O_3, respectively, was present.

(4) The thermogravimetry technique is more sensitive than laboratory X-ray diffraction to small amounts of La_2O_3 (point (3)).

(5) In the $La_{5.86}W_{0.83}Re_{0.17}O_{12-\delta}$ (Re20) and to a minor extent also in the $La_{5.56}WO_{12-\delta}$ (LWO_**P**) specimens, segregation of La_2O_3 is observed with increasing number of dehydration cycles. The higher the La/(W+*M*) ratio, the more unstable the crystal structure is upon annealing in reducing conditions.

(6) The structure of LaWO is described by the model of Scherb[53,54] ($Fm\bar{3}m$ space group). Moreover:
   a. Unexpected W_1–O_1 bond shortening with increasing temperature is observed. Anisotropic vibrations do not model accurately the O_1 anion due to libration movements around W_1. Rigid body/translation-libration-screw refinements might help improving the present model.
   b. The La_2/W_2–La_2/W_2 apparent distance decreases with increasing cell size. This apparent distance mainly accounts for La atoms (≈ 94(4) %). The La_2/W_2 split Wyckoff site (48*h*) moves towards an un-split Wyckoff site (24*d*) with increasing temperature. If a linear dependence is assumed, however, a structural model with an un-split site is not applicable until beyond the melting temperature of LaWO.

(7) From a structural point of view, Mo/Re-substituted LaWO are similar to the parent compound:
   a. Mo and Re atoms substitute W on both its Wyckoff sites, 4*a* and the shared (La_2/W_2) and split 48*h*. The $Fm\bar{3}m$ space group used for the parent compound LaWO describes accurately also the substituted specimens in the region investigated, i.e. up to *M*/(W+*M*) = 0.20.
   b. No tetragonal distortions were found for any of the substituted specimens. It follows that the $Fm\bar{3}m$ space group describes well LaWO and LaW*M*O crystal structures up to *M*/(W+*M*) = 0.20 and for any La/(W+*M*) ratios.
   c. Similar remaining static disorder in the unit cells of $La_{5.56}WO_{12-\delta}$, $La_{5.86}W_{0.80}Mo_{0.20}O_{12-\delta}$ and $La_{5.86}W_{0.83}Re_{0.17}O_{12-\delta}$ was observed within the $Fm\bar{3}m$ model used.
   d. Similar Debye temperatures for $La_{5.56}WO_{12-\delta}$, $La_{5.86}W_{0.80}Mo_{0.20}O_{12-\delta}$ and $La_{5.86}W_{0.83}Re_{0.17}O_{12-\delta}$ in the same temperature range were deduced.
      - In the temperature range 1.5 K ≤ *T* ≤ 1200 K, T_D(Re20) = 580(33) K, T_D(LWO_**P**) = 571(45) K.
      - Low/high temperatures Debye behaviour for LWO_**P** and Re20 specimens was observed.
   e. Substitution of W by Mo and Re atoms on a 4*a* site does not change the octahedral coordination in dry(Ar) and D_2O(Ar) condition.
      - The vacancies in LaWO and LaW*M*O sit on the 32*f* Wyckoff site, bonded to the shared 48*h* (La_2/W_2) and to the 4*b* (La_1) Wyckoff sites. Nothing could be inferred from the coordination of Mo and Re in the 48*h* site. However, from conclusions (2a, 2b), in oxidized specimens, Re and Mo oxidation states in the 48*h* site are supposed Re^{7+} and Mo^{6+}, respectively. In dry(Ar) condition, from XRD patterns it can be concluded that the supposed oxidation state of Mo ($Mo^{4+/5+}$) is lower than the expected oxidation of W (W^{6+}), assuming that all Mo reduces. It can also be concluded that the supposed oxidation state of Re (Re^{4+} or $Re^{4+/5+}$) is lower than the expected oxidation state of W (W^{6+}).
   f. On the 4*a* site, hints of a change in the oxidation state of Re from $Re^{4+/5+}$ to Re^{7+} upon deuteration have been observed.
   g. Even if Mo and Re occupy the same Wyckoff sites of W, their oxidation state is strongly dependent on the pre-treatment used and possibly on the Wyckoff site occupied (point 7e).
   h. O_1 atoms in LaWO show anharmonic vibrations. The origin of these anharmonic vibrations is at present unknown but they are possibly related to O_1 librations around W_1 (point 6a). Refinements considering anharmonic contributions to the O_1 atomic potential and/or crystal structure simulations must be performed and compared to rigid body/translation-libration-screw refinements.

8 Outlook

In this work, the main technique used to unravel the structure of LaWO and LaW*M*O (*M* = Mo, Re) systems was diffraction of X-rays and neutrons. Detailed information about the structure has been retrieved through these techniques exploiting the different sensitivity to light and heavy elements of neutrons and X-rays. Still, the structural model of LaWO could be slightly improved if the role of anharmonic O_1 vibrations and/or librations around W_1 was clarified. Also, the available theoretical model describing the vacancy concentration in the unit cell and/or the hydration of LaWO presents some inconsistencies and deserves more attention.

Possibly, different techniques such as X-ray absorption spectroscopy (XAS) and measuring the pair distribution functions (PDF) would allow for a broader understanding of the local surroundings of selected atoms and bond lengths, respectively. The local surroundings of the 48*h* site shared by La, W and Mo or Re are the most interesting surroundings to investigate, being bonded to the vacant Wyckoff sites and thus responsible for charge compensation. This may also help to solve the deviation from full hydration observed for LaWO and LaW*M*O. Especially near-edge X-ray absorption spectroscopy could clarify the oxidation states of W, Re and Mo in dependence of the pre-treatments used, where more reducing (dry Ar/H_2, dry Ar, dry S.A.) conditions as well as more oxidizing conditions (wet Ar/H_2, wet Ar, wet S.A.) may be employed for systematic studies. X-ray photoelectron spectroscopy (XPS) and TPR studies have already been performed on LaWO and LaW*M*O in order to determine the oxidation states of W, Re and Mo. However, XAS in the absorption mode is expected to provide bulk information, in contrast to XPS where only information from surface near regions (1-10 nm) could be deduced. In TPR studies shown in literature[31] the role of the not negligible secondary phases and the prominent peak asymmetry observed in the reported diffraction patterns is not discussed. The detailed knowledge of the crystal structure given by the present work provides the basis for the understanding of proton diffusion in LW*M*O which is presently investigated by our collaboration partners through quasi-elastic neutron scattering.

Literature

1. U. Nations, Conference of Parties 21st - Paris agreement. Retrieved: Feb. 18, 2016; from: http://unfccc.int/resource/docs/2015/cop21/eng/l09r01.pdf
2. *Nature*, 2012, **491**, 7491
3. D. J. C. MacKay, P. Cramton, A. Ockentels and S. Stoft, *Nature*, 2015, **526**, 315-316
4. D. J. C. MacKay, P. Cramton, A. Ockentels and S. Stoft, Global carbon pricing - We will if you will. Retrieved: Dec. 26, 2015; from: http://carbon-price.com/wp-content/uploads/Global-Carbon-Pricing-cramton-mackay-okenfels-stoft.pdf
5. IPCC, Climate change 2014 - Synthesis report. Retrieved: Feb. 18, 2016; from: http://www.ipcc.ch/pdf/assessment-report/ar5/syr/SYR_AR5_FINAL_full.pdf
6. U. Nations, Synthesis report on the aggregate effect of the intended nationally determined contributions. Retrieved: Feb. 18, 2016; from: http://unfccc.int/resource/docs/2015/cop21/eng/07.pdf
7. IEA, World Energy Outlook, special briefing for COP21. Retrieved: Feb. 18, 2016; from: https://www.iea.org/media/news/WEO_INDC_Paper_Final_WEB.PDF
8. IEA, World Energy Outlook special report. Retrieved: Feb. 18, 2016; from: https://www.iea.org/publications/freepublications/publication/WEO2015SpecialReportonEnergyandClimateChange.pdf
9. IEA, Key trends in CO2 emissions. Retrieved: Feb. 18, 2016; from: https://www.iea.org/publications/freepublications/publication/CO2EmissionsTrends.pdf
10. IEA, Energy technology Perspectives 2012. Retrieved: Feb. 18, 2016; from: https://www.iea.org/publications/freepublications/publication/ETP2012_free.pdf
11. J. D. Figueroa, T. Fout, S. Plasynski, H. McIlvried and R. D. Srivastava, *International Journal of Greenhouse Gas Control*, 2008, **2**, 9-20
12. J.-R. Li, Y. Ma, M. C. McCarthy, J. Sculley, J. Yu, H.-K. Jeong, P. B. Balbuena and H.-C. Zhou, *Coordination Chemistry Reviews*, 2011, **255**, 1791-1823
13. S. Choi, J. H. Drese and C. W. Jones, *ChemSusChem*, 2009, **2**, 796-854
14. B. Sorensen, *Int. J. Hydrogen Energy*, 2007, **32**, 1597-1604
15. T. Ho and V. Karri, *Int. J. Hydrogen Energy*, 2011, **36**, 10065-10079
16. A. Genovese, N. Contrisciani, F. Ortenzi and V. Cazzola, *Int. J. Hydrogen Energy*, 2011, **36**, 1775-1783
17. M. Kim, Y.-J. Sohn, C.-W. Cho, W.-Y. Lee and C.-S. Kim, *Journal of Power Sources*, 2008, **176**, 529-533
18. T. Niknam, M. Bornapour and A. Gheisari, *Energy Conversion and Management*, 2013, **66**, 11-25
19. D. Wang, S. Chen, C. Xu and W. Xiang, *Int. J. Hydrogen Energy*, 2013, **38**, 5389-5400
20. T. Norby, *Solid State Ionics*, 1999, **125**, 1-11
21. H. Iwahara, T. Esaka, H. Uchida and N. Maeda, *Solid State Ionics*, 1981, **3-4**, 359-363
22. H. Iwahara, H. Uchida, K. Ono and K. Ogaki, *J. Electrochem. Soc.*, 1988, **135**, 529-533
23. R. Haugsrud, Y. Larring and T. Norby, *Solid State Ionics*, 2005, **176**, 2957-2961
24. T. Shimura, M. Komori and H. Iwahara, *Solid State Ionics*, 1996, **86-8**, 685-689
25. R. Haugsrud and T. Norby, *Nat. Mater.*, 2006, **5**, 193-196
26. M. E. Ivanova, W. A. Meulenberg, J. Palisaitis, D. Sebold, C. Solis, M. Ziegner, J. M. Serra, J. Mayer, M. Hansel and O. Guillon, *J Eur Ceram Soc*, 2015, **35**, 1239-1253
27. M. Ivanova, S. Ricote, W. A. Meulenberg, R. Haugsrud and M. Ziegner, *Solid State Ionics*, 2012, **213**, 45-52
28. J. Palisaitis, M. E. Ivanova, W. A. Meulenberg, O. Guillon and J. Mayer, *J Eur Ceram Soc*, 2015, **35**, 1517-1525
29. Z. Tao, L. Yan, J. Qiao, B. Wang, L. Zhang and J. Zhang, *Progress in Materials Science*, 2015, **74**, 1-50
30. *Germany Pat.,* DE 102010027645 A1, 2013
31. S. Escolastico, J. Seeger, S. Roitsch, M. Ivanova, W. A. Meulenberg and J. M. Serra, *ChemSusChem*, 2013, **6**, 1523-1532
32. J. Seeger, M. E. Ivanova, W. A. Meulenberg, D. Sebold, D. Stover, T. Scherb, G. Schumacher, S. Escolastico, C. Solis and J. M. Serra, *Inorg Chem*, 2013, **52**, 10375-10386
33. S. Escolastico, C. Solis and J. M. Serra, *Solid State Ionics*, 2012, **216**, 31-35
34. S. Escolastico, C. Solis, T. Scherb, G. Schumacher and J. M. Serra, *Journal of Membrane Science*, 2013, **444**, 276-284
35. D. van Holt, E. Forster, M. E. Ivanova, W. A. Meulenberg, M. Mueller, S. Baumann and R. Vassen, *J Eur Ceram Soc*, 2014, **34**, 2381-2389
36. R. Hancke, Z. A. Li and R. Haugsrud, *Journal of Membrane Science*, 2013, **439**, 68-77
37. J. Seeger, PhD Thesis, Ruhr-Universität Bochum, 2013
38. Y. Liu, X. Tan and K. Li, *Catalysis Reviews*, 2006, **48**, 145-198

39. T. Schober, W. Schilling and H. Wenzl, *Solid State Ionics*, 1996, **86–88, Part 1**, 653-658
40. K. D. Kreuer, *Annu. Rev. Mater. Res.*, 2003, **33**, 333-359
41. T. Norby and R. Haugsrud, in *Nonporous Inorganic Membranes*, Wiley-VCH Verlag GmbH & Co. KGaA, 2006, DOI: 10.1002/3527608796.ch1, pp. 1-48
42. M. Fontaine, T. Norby, Y. Larring, T. Grande, R. Bredesen, M. Reyes and M. Miguel, in *Membrane Science and Technology*, Elsevier, 2008, vol. Volume 13, pp. 401-458
43. F. A. Kroger and H. J. Vink, *Solid State Phys*, 1956, **3**, 307-435
44. F. A. Kröger, *The chemistry of imperfect crystals*, North-Holland Pub. Co.; Interscience Publishers, Amsterdam; New York, 1964
45. T. Norby and R. Haugsrud, in *Membranes for Energy Conversion*, Wiley-VCH Verlag GmbH & Co. KGaA, 2008, DOI: 10.1002/9783527622146.ch6, pp. 169-216
46. A. Magraso, C. Frontera, D. Marrero-Lopez and P. Nunez, *Dalton Trans*, 2009, DOI: 10.1039/b916981b, 10273-10283
47. R. Haugsrud, *Solid State Ionics*, 2007, **178**, 555-560
48. A. Magraso, J. M. Polfus, C. Frontera, J. Canales-Vazquez, L. E. Kalland, C. H. Hervoches, S. Erdal, R. Hancke, M. S. Islam, T. Norby and R. Haugsrud, *J. Mater. Chem.*, 2012, **22**, 1762-1764
49. S. Erdal, L. E. Kalland, R. Hancke, J. Polfus, R. Haugsrud, T. Norby and A. Magraso, *Int. J. Hydrogen Energy*, 2012, **37**, 8051-8055
50. A. Magraso, C. H. Hervoches, I. Ahmed, S. Hull, J. Nordstrom, A. W. B. Skilbred and R. Haugsrud, *Journal of Materials Chemistry A*, 2013
51. L.-E. Kalland, A. Magraso, A. Mancini, C. Tealdi and L. Malavasi, *Chem. Mater.*, 2013, **25**, 2378-2384
52. A. Magraso and R. Haugsrud, *Journal of Materials Chemistry A*, 2014, **2**, 12630-12641
53. T. Scherb, DOI: http://dx.doi.org/10.5442/d0014, PhD, Technische Universität Berlin, 2011
54. T. Scherb, S. A. J. Kimber, C. Stephan, P. F. Henry, G. Schumacher, S. Escolástico, J. M. Serra, J. Seeger, J. Just, A. H. Hill and J. Banhart, *Journal of Applied Crystallography*, 2016, **49**, 997-1008
55. M. Yoshimura and A. Rouanet, *Materials Research Bulletin*, 1976, **11**, 151-158
56. L. L. Y. Chang, M. G. Scroger and B. Phillips, *J Inorg Nucl Chem*, 1966, **28**, 1179-&
57. L. L. Y. Chang and B. Phillips, *Inorg. Chem.*, 1964, **3**, 1792-1794
58. *United States Pat.,* 3 330 697, 1967
59. M. E. Ivanova, J. Seeger, J. M. Serra, C. Solis, W. A. Meulenberg, W. Fischer, S. Roitsch and H. P. Buchkremer, *Chemistry and Materials research*, 2012, **2**, 56-81
60. W. H. Bragg and W. L. Bragg, *Proceedings of the Royal Society of London A: Mathematical, Physical and Engineering Sciences*, 1913, **88**, 428-438
61. R. A. Young, *The Rietveld Method*, Oxford University Press, 1995
62. Argonne, X-ray absorption correction. Retrieved: Dec. 28, 2015; from: http://11bm.xray.aps.anl.gov/absorb/absorb.php
63. A. W. Hewat and S. Heathman, *Acta Crystallogr A*, 1984, **40**, C364-C364
64. D2B instrument Website. Retrieved: Dec. 24, 2015; from: http://www.ill.eu/instruments-support/instruments-groups/instruments/d2b
65. P. Fischer, G. Frey, M. Koch, M. Konnecke, V. Pomjakushin, J. Schefer, R. Thut, N. Schlumpf, R. Burge, U. Greuter, S. Bondt and E. Berruyer, *Physica B*, 2000, **276**, 146-147
66. V. Pomjakushin, HRPT instrument Website. Retrieved: Feb. 18, 2016; from: http://sinq.web.psi.ch/sinq/instr/hrpt/index.html
67. P. R. Willmott, D. Meister, S. J. Leake, M. Lange, A. Bergamaschi, M. Boege, M. Calvi, C. Cancellieri, N. Casati, A. Cervellino, Q. Chen, C. David, U. Flechsig, F. Gozzo, B. Henrich, S. Jaeggi-Spielmann, B. Jakob, I. Kalichava, P. Karvinen, J. Krempasky, A. Luedeke, R. Luescher, S. Maag, C. Quitmann, M. L. Reinle-Schmitt, T. Schmidt, B. Schmitt, A. Streun, I. Vartiainen, M. Vitins, X. Wang and R. Wullschleger, *Journal of Synchrotron Radiation*, 2013, **20**, 667-682
68. A. Bergamaschi, A. Cervellino, R. Dinapoli, F. Gozzo, B. Henrich, I. Johnson, P. Kraft, A. Mozzanica, B. Schmitt and X. Shi, *Journal of Synchrotron Radiation*, 2010, **17**, 653-668
69. F. Gozzo, A. Cervellino, M. Leoni, P. Scardi, A. Bergamaschi and B. Schmitt, *Z Kristallogr*, 2010, **225**, 616-624
70. N. Casati, MS beamline Website. Retrieved: Dec. 24, 2015; from: https://www.psi.ch/sls/ms/ms
71. D. M. Tobbens, N. Stusser, K. Knorr, H. M. Mayer and G. Lampert, in *Epdic 7: European Powder Diffraction, Pts 1 and 2*, eds. R. Delhez and E. J. Mittemeijer, 2001, vol. 378-3, pp. 288-293
72. FIREPOD instrument Website. Retrieved: Dec. 24, 2015; from: https://www.helmholtz-berlin.de/pubbin/igama_output?modus=einzel&sprache=de&gid=1702&typoid=50722
73. B. H. Toby, *Powder Diffraction*, 2006, **21**, 67-70
74. W. I. F. David, *J Res Natl Inst Stan*, 2004, **109**, 107-123

75. E. Prince, *Mathematical techniques in crystallography and materials science*, Springer-Verlag, 1994
76. A. C. Larson and R. B. V. Dreele, *Los Alamos National Laboratory Report*, 2004, LAUR 86-748
77. B. H. Toby, *Journal of Applied Crystallography*, 2001, **34**, 210-213
78. J. Rodriguez-Carvajal and T. Roisnel, FULLPROF Website. Retrieved: Feb. 18, 2016; from: www.ill.eu/sites/fullprof/
79. J. S. O. Evans, *Materials Science Forum*, 2010, **651**, 1-9
80. H. M. Rietveld, *Journal of Applied Crystallography*, 1969, **2**, 65-&
81. G. Pawley, *Journal of Applied Crystallography*, 1981, **14**, 357-361
82. A. Le Bail, H. Duroy and J. L. Fourquet, *Materials Research Bulletin*, 1988, **23**, 447-452
83. A. Le Bail, *Powder Diffraction*, 2005, **20**, 316-326
84. H. M. Rietveld, *Acta Crystallogr*, 1967, **22**, 151-&
85. L. B. McCusker, R. B. Von Dreele, D. E. Cox, D. Louer and P. Scardi, *Journal of Applied Crystallography*, 1999, **32**, 36-50
86. R. J. Hill, *Journal of Applied Crystallography*, 1992, **25**, 589-610
87. R. J. Hill and L. M. D. Cranswick, *Journal of Applied Crystallography*, 1994, **27**, 802-844
88. A. Belsky, M. Hellenbrandt, V. L. Karen and P. Luksch, *Acta Crystallographica Section B*, 2002, **58**, 364-369
89. NIST, Neutron absorption correction. Retrieved: Dec. 28, 2015; from: https://www.ncnr.nist.gov/instruments/bt1/neutron.html
90. A. Furrer, J. Mesot and T. Strässle, *Neutron Scattering in Condensed Matter Physics*, World Scientific, London, 2009
91. C. Stephan, T. Scherb, C. A. Kaufmann, S. Schorr and H. W. Schock, *Applied Physics Letters*, 2012, **101**
92. ILL, Neutron data booklet. Retrieved: 26.12, 2015; from: https://www.ill.eu/quick-links/publications/
93. C. Chantler, *Journal of Physical and Chemical Reference Data*, 1995, **24**, 71-643
94. NIST, Atomic form factor. Retrieved: Dec. 26, 2015; from: http://physics.nist.gov/PhysRefData/FFast/Text2000/sec02.html
95. E. Prince and IUCR, *International Tables for Crystallography, Mathematical, Physical and Chemical Tables*, Wiley, 2004
96. P. Macchi, J.-M. Gillet, F. Taulelle, J. Campo, N. Claiser and C. Lecomte, *IUCrJ*, 2015, **2**, 441-451
97. G. Taylor, *Acta Crystallographica Section D*, 2003, **59**, 1881-1890
98. R. D. Shannon, *Acta Crystallogr A*, 1976, **32**, 751-767
99. L. Vegard, *Z Phys*, 1921, **5**, 17-26
100. K. T. Jacob, S. Raj and L. Rannesh, *International Journal of Materials Research*, 2007, **98**, 776-779
101. A. V. G. Chizmeshya, M. R. Bauer and J. Kouvetakis, *Chem. Mater.*, 2003, **15**, 2511-2519
102. S. T. Murphy, A. Chroneos, C. Jiang, U. Schwingenschlogl and R. W. Grimes, *Phys. Rev. B*, 2010, **82**
103. S.-J. Su, B.-W. Cheng, C.-L. Xue, D.-L. Zhang, G.-Z. Zhang and Q.-M. Wang, *Acta Physica Sinica*, 2012, **61**
104. P. Ganguly, N. Shah, M. Phadke, V. Ramaswamy and I. S. Mulla, *Phys Rev B Condens Matter*, 1993, **47**, 991-995
105. W. Li, M. Pessa and J. Likonen, *Applied Physics Letters*, 2001, **78**, 2864-2866
106. J. F. Q. Rey and E. N. S. Muccillo, *J Eur Ceram Soc*, 2004, **24**, 1287-1290
107. F. Schulze-Kueppers, S. F. P. ten Donkelaar, S. Baumann, P. Prigorodov, Y. J. Sohn, H. J. M. Bouwmeester, W. A. Meulenberg and O. Guillon, *Separation and Purification Technology*, 2015, **147**, 414-421
108. R. Hancke, Z. Li and R. Haugsrud, *Int. J. Hydrogen Energy*, 2012, **37**, 8043-8050
109. R. Hancke, A. Magrasó, T. Norby and R. Haugsrud, *Solid State Ionics*, 2013, **231**, 25-29
110. M. H. Chambrier, R. M. Ibberson and F. Goutenoire, *J. Solid State Chem.*, 2010, **183**, 1297-1302
111. G. Schiller, PhD Thesis, Drei-Eck-Verl. Löchner, 1986
112. M. P. Rosynek and D. T. Magnuson, *J Catal*, 1977, **46**, 402-413
113. M. Ozawa, R. Onoe and H. Kato, *Journal of Alloys and Compounds*, 2006, **408–412**, 556-559
114. X. Zhang, P. Yang, D. Wang, J. Xu, C. Li, S. Gai and J. Lin, *Crystal Growth & Design*, 2012, **12**, 306-312
115. O. Yamamoto, Y. Takeda, R. Kanno and M. Fushimi, *Solid State Ionics*, 1985, **17**, 107-114
116. R. M. Housley and F. Hess, *Phys Rev*, 1966, **146**, 517-&
117. W. Massa, *Crystal Structure Determination*, Springer-Verlag, Berlin Heidelberg, 2004
118. R. X. Fischer and E. Tillmanns, *Acta Crystallographica Section C-Crystal Structure Communications*, 1988, **44**, 775-776
119. A. Fantin, T. Scherb, G. Schumacher, J. Seeger, M. E. Ivanova, U. Gerhards, W. A. Meulenberg, R. Dittmeyer and J. Banhart, *Journal of Applied Crystallography*, 2016, **49**, 1544-1560
120. R. W. Cheary, *Acta Crystallogr. Sect. B-Struct. Commun.*, 1991, **47**, 325-333
121. D. Argyriou, *Journal of Applied Crystallography*, 1994, **27**, 155-158

122. J. B. Mann, *Atomic Structure Calculations. 2.Hartree-Fock Wave Functions and Radial Expectation Values: Hydrogen to Lawrencium*, 1968
123. NIST, NIST SRM Certificates. Retrieved: Dec. 27, 2015; from: https://wiki-ext.aps.anl.gov/ug11bm/index.php/NIST_SRM_Certificates
124. K. G. Lyon, G. L. Salinger, C. A. Swenson and G. K. White, *Journal of Applied Physics*, 1977, **48**, 865-868
125. T. Schober and J. Friedrich, *Solid State Ionics*, 1998, **113–115**, 369-375
126. G. Caglioti, A. Paoletti and F. P. Ricci, *Nuclear Instruments*, 1958, **3**, 223-228
127. R. T. Downs, G. V. Gibbs, K. L. Bartelmehs and M. B. Boisen, *American Mineralogist*, 1992, **77**, 751-757
128. L. N. Becka and D. W. J. Cruickshank, *Acta Crystallogr*, 1961, **14**, 1092
129. A. Urzhumtsev, P. V. Afonine and P. D. Adams, *Crystallography Reviews*, 2013, **19**, 230-270
130. C. Stephan, S. Schorr, M. Tovar and H. W. Schock, *Applied Physics Letters*, 2011, **98**, -
131. M. Amsif, A. Magraso, D. Marrero-Lopez, J. C. Ruiz-Morales, J. Canales-Vazquez and P. Nunez, *Chem. Mater.*, 2012, **24**, 3868-3877
132. L. W. Finger, D. E. Cox and A. P. Jephcoat, *Journal of Applied Crystallography*, 1994, **27**, 892-900
133. P. Scardi and R. E. Dinnebier, *Extending the Reach of Powder Diffraction Modelling by User Defined Macros: Special Topic Volume with Invited Peer Reviewed Papers Only*, Trans Tech, 2010
134. H. P. Klug and L. E. Alexander, *X-Ray Diffraction Procedures: For Polycrystalline and Amorphous Materials*, Wiley, 1974
135. L. Pauling, *J Am Chem Soc*, 1929, **51**, 1010-1026
136. S. Escolastico, S. Somacescu and J. M. Serra, *Chem. Mater.*, 2014, **26**, 982-992
137. J. W. McCauley and V. Weiss, *Materials Characterization for Systems Performance and Reliability*, Springer US, 2013
138. N. W. Ashcroft and N. D. Mermin, *Solid State Physics*, Holt, Rinehart and Winston, 1976
139. C. Kittel, *Introduction to solid state physics*, Wiley, 1986
140. R. O. Simmons and R. W. Balluffi, *Phys Rev*, 1960, **117**, 52-61
141. B. T. M. Willis and A. W. Pryor, *Thermal vibrations in crystallography*, Cambridge University Press, Cambridge, 1975
142. K. Erich and Y. Ma, *J. Phys. Condens. Matter*, 1998, **10**, 3823

Acknowledgements

To conclude, I would like to thank all the people who have contributed to this dissertation:

- Professor Dr. John Banhart, for the possibility he gave me to pursue this research in his department.
- Professor Dr. Lorenz Singheiser, for his willingness to review this dissertation.
- Professor Dr. Gerhard Schumacher, for the supervision of this work, useful discussions and support.
- Dr. Tobias Scherb, for the knowledge he shared with me from the beginning, the support, the discussions and help before, during and after the experiments.
- Dr. Janka Seeger, for the preparation of all the specimens discussed in this dissertation, the permission to use her conductivity and permeation measurements reported in this work, the help during beamtime and during my stay in Jülich.
- Dr. W. A. Meulenberg and Dr. M.E. Ivanova, for specimen preparation, help and useful discussions.
- Professor Dr. Roland Dittmeyer and Uta Gerhards, for the electron microprobe measurements at KIT.
- Claudia Leistner, for the help in thermogravimetric and laboratory X-ray diffraction measurements, as well as for the different specimen pre-treatments performed. I thank Claudia also for the food supply during my PhD period.
- Christiane Förster, for her help in specimen preparation for electron microprobe measurements.
- Dr. Mirko Boin, Dr. Jatinkumar Rana and Zhou Dong for their help during beamtimes and discussion.
- Jörg Bajorat, for all the IT-related help he provided.
- All colleagues and friends who helped to improve the form of this dissertation, by including remarks, grammar corrections and any type of suggestions.
- ILL, PSI and HZB for allocation of beamtimes and the responsible instrument scientists for their help and discussions before, during and after the measurements.

Finally, I gratefully thank my parents, Mauro and Pierina, who supported me at any time and with any help they could provide me. Also, special thanks to my uncles, my grandmother and my life-long friends Mattia and Massimo. Last, but not least, I would like to thank Joanna for the moral support, the food support and the patience she had with me especially during the final months of my PhD period.

Erklärung

Ich erkläre hiermit, dass ich die vorliegende Dissertation selbst verfasst und keine anderen als die angegebenen Quellen und Hilfsmittel verwendet habe,

Berlin, 22. February 2016

_____

Andrea Fantin

Appendix

Re20 Re20_IMP Re02 LWO_**P** Mo20(1)

Fig. #S1. Specimens dried under dry(Ar) atmosphere, 900 °C, 4 h.

Re20 Re20_IMP Re02 LWO_**P** Mo20(1)

Fig. #S2. Specimens humidified under D_2O(Ar) atmosphere, 350 °C, 5 h.

LWO_P Tables

LWO_P-dry(Ar) T = 5 K ILL 'Scherb model'

Lattice constants are

a = 11.15354(6) Å, b = a, c = a

Cell volume = 1387.518(12) *Å^3*

Name	*X*	*Y*	*Z*	*Ui/Ue*100*	*Site sym*	*Mult*	*Type*	*Seq*	*Fractn*
La1	0.500000	0.500000	0.500000	0.68(11)	M3M	4	LA	1	1.000(16)
La2	0.000000	0.23601(28)	0.23601(28)	0.69*	MM2(011)	48	LA	2	0.484(7)
W1	0.000000	0.000000	0.000000	0.61(17)	M3M	4	W	3	1.021(28)
O1	0.11201(22)	0.11201(22)	0.06539(34)	1.55*	M(+-0)	96	O	4	0.237(4)
O2	0.36615(12)	0.36615(12)	0.36615(12)	1.29*	3M(111)	32	O	5	0.938(6)
W2	0.000000	0.23601(28)	0.23601(28)	0.69*	MM2(011)	48	W	6	0.016(7)

Thermal parameters multiplied by 100.0 are

Name	*U11*	*U22*	*U33*	*U12*	*U13*	*U23*
La1	0.68(11)	0.68	0.68	0.00	0.00	0.00
La2	0.64(11)	0.72(18)	0.72(18)	0.00	0.00	0.28(16)
W1	0.61(17)	0.61	0.61	0.00	0.00	0.00
O1	0.63(18)	0.63(18)	3.40(30)	-0.14(10)	-0.69(11)	-0.69(11)
O2	1.29(5)	1.29(5)	1.29(5)	-0.03(4)	-0.03(4)	-0.03(4)
W2	0.64(11)	0.72(18)	0.72(18)	0.00	0.00	0.28(16)

LWO_P-dry(Ar) T = 5 K ILL 'Magraso model'

Lattice constants are

a = 11.15354(6) Å, b = a, c = a

Alpha = 90° Beta = 90° Gamma = 90°

Cell volume = 1387.518(12) Å^3

Name	*X*	*Y*	*Z*	*Ui/Ue*100*	*Site sym*	*Mult*	*Type*	*Seq*	*Fractn*
La1	0.500000	0.500000	0.500000	0.66(11)	M3M	4	LA	1	0.982(16)
La2	0.000000	0.250000	0.250000	2.84*	MMM(100)	24	LA	2	0.967(14)
W1	0.000000	0.000000	0.000000	0.64(18)	M3M	4	W	3	1.001(28)
O1	0.11148(19)	0.11148(19)	0.06567(34)	---	M(+-0)	96	O	4	0.226(4)
O2	0.36586(10)	0.36586(10)	0.36586(10)	1.21*	3M(111)	32	O	5	0.915(6)
W2	0.000000	0.250000	0.250000	2.84*	MMM(100)	24	W	6	0.034(14)

Thermal parameters multiplied by 100.0 are

Name	*U11*	*U22*	*U33*	*U12*	*U13*	*U23*
La1	0.66(11)	0.66	0.66	0.00	0.00	0.00
La2	0.66(10)	3.93(7)	3.93(7)	0.00	0.00	3.21(8)
W1	0.64(18)	0.64	0.64	0.00	0.00	0.00
O1	0.10(16)	0.10(16)	3.61(32)	-0.41(9)	-0.51(10)	-0.51(10)
O2	1.21(4)	1.21(4)	1.21(4)	-0.04(4)	-0.04(4)	-0.04(4)
W2	0.66(10)	3.93(7)	3.93(7)	0.00	0.00	3.21(8)

LWO_P-dry(Ar) T = 10 K ILL 'Scherb model'

Lattice constants are

a = 11.153450(32) Å, b = a, c = a

Alpha = 90° Beta = 90° Gamma = 90°

Cell volume = 1387.483(7) Å^3

Name	*X*	*Y*	*Z*	*Ui/Ue*100*	*Site sym*	*Mult*	*Type*	*Seq*	*Fractn*
La1	0.500000	0.500000	0.500000	0.78(6)	M3M	4	LA	1	1.0005
La2	0.000000	0.23627(28)	0.23627(28)	0.77*	MM2(011)	48	LA	2	0.4838
W1	0.000000	0.000000	0.000000	0.68(10)	M3M	4	W	3	1.0215
O1	0.11226(22)	0.11226(22)	0.06557(32)	1.71*	M(+-0)	96	O	4	0.2373
O2	0.36617(11)	0.36617(11)	0.36617(11)	1.30*	3M(111)	32	O	5	0.9379
W2	0.000000	0.23627(28)	0.23627(28)	0.77*	MM2(011)	48	W	6	0.0162

Thermal parameters multiplied by 100.0 are

Name	*U11*	*U22*	*U33*	*U12*	*U13*	*U23*
La1	0.78(6)	0.78	0.78	0.00	0.00	0.00
La2	0.64(10)	0.83(17)	0.83(17)	0.00	0.00	0.32(15)
W1	0.68(10)	0.68	0.68	0.00	0.00	0.00
O1	0.874(148)	0.874(148)	3.395(284)	-0.14(10)	-0.75(12)	-0.75(12)
O2	1.304(28)	1.304(28)	1.304(28)	0.03(5)	0.03(5)	0.03(5)
W2	0.64(10)	0.83(17)	0.83(17)	0.00	0.00	0.32(15)

LWO_P-dry(Ar) T = 10 K ILL 'Magraso model'

Lattice constants are

a = 11.153457(32) Å, b = a, c = a

Alpha = 90° Beta = 90° Gamma = 90°

Cell volume = 1387.485(7) Å^3

Name	*X*	*Y*	*Z*	*Ui/Ue*100*	*Site sym*	*Mult*	*Type*	*Seq*	*Fractn*
La1	0.500000	0.500000	0.500000	0.76(6)	M3M	4	LA	1	0.9823
La2	0.000000	0.250000	0.250000	2.82*	MMM(100)	24	LA	2	0.9666
W1	0.000000	0.000000	0.000000	0.69(10)	M3M	4	W	3	1.0008
O1	0.11175(20)	0.11175(20)	0.06584(32)	---	M(+-0)	96	O	4	0.2257
O2	0.36588(10)	0.36588(10)	0.36588(10)	1.23*	3M(111)	32	O	5	0.9146
W2	0.000000	0.250000	0.250000	2.82*	MMM(100)	24	W	6	0.0345

Thermal parameters multiplied by 100.0 are

Name	*U11*	*U22*	*U33*	*U12*	*U13*	*U23*
La1	0.76(6)	0.76	0.76	0.00	0.00	0.00
La2	0.67(10)	3.90(7)	3.90(7)	0.00	0.00	3.14(8)
W1	0.69(10)	0.69	0.69	0.00	0.00	0.00
O1	0.364(128)	0.364(128)	3.599(292)	-0.39(10)	-0.59(11)	-0.59(11)
O2	1.228(28)	1.228(28)	1.228(28)	0.02(5)	0.02(5)	0.02(5)
W2	0.67(10)	3.90(7)	3.90(7)	0.00	0.00	3.14(8)

LWO_P-dry(Ar) T = 30 K ILL 'Scherb model'

Lattice constants are

a = 11.153437(31) Å, b = a, c = a

Alpha = 90° Beta = 90° Gamma = 90°

Cell volume = 1387.478(7) Å^3

Name	*X*	*Y*	*Z*	*Ui/Ue*100*	*Site sym*	*Mult*	*Type*	*Seq*	*Fractn*
La1	0.500000	0.500000	0.500000	0.76(6)	M3M	4	LA	1	1.0005
La2	0.000000	0.23641(30)	0.23641(30)	0.87*	MM2(011)	48	LA	2	0.4838
W1	0.000000	0.000000	0.000000	0.53(10)	M3M	4	W	3	1.0215
O1	0.11202(23)	0.11202(23)	0.06521(32)	1.88*	M(+-0)	96	O	4	0.2373
O2	0.36617(11)	0.36617(11)	0.36617(11)	1.28*	3M(111)	32	O	5	0.9379
W2	0.000000	0.23641(30)	0.23641(30)	0.87*	MM2(011)	48	W	6	0.0162

Thermal parameters multiplied by 100.0 are

Name	*U11*	*U22*	*U33*	*U12*	*U13*	*U23*
La1	0.76(6)	0.76	0.76	0.00	0.00	0.00
La2	0.74(10)	0.93(18)	0.93(18)	0.00	0.00	0.51(16)
W1	0.53(10)	0.53	0.53	0.00	0.00	0.00
O1	1.119(156)	1.119(156)	3.406(282)	-0.17(11)	-0.88(12)	-0.88(12)
O2	1.279(28)	1.279(28)	1.279(28)	0.05(4)	0.05(4)	0.05(4)
W2	0.74(10)	0.93(18)	0.93(18)	0.00	0.00	0.51(16)

LWO_P-dry(Ar) T = 30 K ILL 'Magraso model'

Lattice constants are

a = 11.153450(31) Å, b = a, c = a

Alpha = 90° Beta = 90° Gamma = 90°

Cell volume = 1387.483(7) Å^3

Name	*X*	*Y*	*Z*	*Ui/Ue*100*	*Site sym*	*Mult*	*Type*	*Seq*	*Fractn*
La1	0.500000	0.500000	0.500000	0.75(6)	M3M	4	LA	1	0.9823
La2	0.000000	0.250000	0.250000	2.86*	MMM(100)	24	LA	2	0.9666
W1	0.000000	0.000000	0.000000	0.55(9)	M3M	4	W	3	1.0008
O1	0.11156(21)	0.11156(21)	0.06547(32)	---	M(+-0)	96	O	4	0.2257
O2	0.36591(10)	0.36591(10)	0.36591(10)	1.20*	3M(111)	32	O	5	0.9146
W2	0.000000	0.250000	0.250000	2.86*	MMM(100)	24	W	6	0.0345

Thermal parameters multiplied by 100.0 are

Name	*U11*	*U22*	*U33*	*U12*	*U13*	*U23*
La1	0.75(6)	0.75	0.75	0.00	0.00	0.00
La2	0.74(10)	3.92(7)	3.92(7)	0.00	0.00	3.27(8)
W1	0.55(9)	0.55	0.55	0.00	0.00	0.00
O1	0.615(136)	0.615(136)	3.556(290)	-0.39(10)	-0.71(11)	-0.71(11)
O2	1.202(27)	1.202(27)	1.202(27)	0.05(4)	0.05(4)	0.05(4)
W2	0.74(10)	3.92(7)	3.92(7)	0.00	0.00	3.27(8)

LWO_P-dry(Ar) T = 60 K ILL 'Scherb model'

Lattice constants are

a = 11.153840(32) Å, b = a, c = a

Alpha = 90° Beta = 90° Gamma = 90°

Cell volume = 1387.629(7) Å^3

Name	*X*	*Y*	*Z*	*Ui/Ue*100*	*Site sym*	*Mult*	*Type*	*Seq*	*Fractn*
La1	0.500000	0.500000	0.500000	0.78*	M3M	4	LA	1	1.0005
La2	0.000000	0.23617(27)	0.23617(27)	0.74*	MM2(011)	48	LA	2	0.4838
W1	0.000000	0.000000	0.000000	0.63*	M3M	4	W	3	1.0215
O1	0.11201(22)	0.11201(22)	0.06569(32)	1.75*	M(+-0)	96	O	4	0.2373
O2	0.36615(12)	0.36615(12)	0.36615(12)	1.29*	3M(111)	32	O	5	0.9379
W2	0.000000	0.23617(27)	0.23617(27)	0.74*	MM2(011)	48	W	6	0.0162

Thermal parameters multiplied by 100.0 are

Name	*U11*	*U22*	*U33*	*U12*	*U13*	*U23*
La1	0.78(6)	0.78(6)	0.78(6)	0.00	0.00	0.00
La2	0.77(10)	0.73(16)	0.73(16)	0.00	0.00	0.31(15)
W1	0.63(10)	0.63(10)	0.63(10)	0.00	0.00	0.00
O1	0.869(151)	0.869(151)	3.503(292)	-0.13(10)	-0.77(12)	-0.77(12)
O2	1.290(28)	1.290(28)	1.290(28)	0.09(5)	0.09(5)	0.09(5)
W2	0.77(10)	0.73(16)	0.73(16)	0.00	0.00	0.31(15)

LWO_P-dry(Ar) T = 60 K ILL 'Magraso model'

Lattice constants are

a = 11.153853(32) Å, b = a, c = a

Alpha = 90° Beta = 90° Gamma = 90°

Cell volume = 1387.634(7) Å^3

Name	*X*	*Y*	*Z*	*Ui/Ue*100*	*Site sym*	*Mult*	*Type*	*Seq*	*Fractn*
La1	0.500000	0.500000	0.500000	0.76(6)	M3M	4	LA	1	0.9823
La2	0.000000	0.250000	0.250000	2.82*	MMM(100)	24	LA	2	0.9666
W1	0.000000	0.000000	0.000000	0.65(10)	M3M	4	W	3	1.0008
O1	0.11150(20)	0.11150(20)	0.06600(33)	---	M(+-0)	96	O	4	0.2257
O2	0.36584(10)	0.36584(10)	0.36584(10)	1.20*	3M(111)	32	O	5	0.9146
W2	0.000000	0.250000	0.250000	2.82*	MMM(100)	24	W	6	0.0365

Thermal parameters multiplied by 100.0 are

Name	*U11*	*U22*	*U33*	*U12*	*U13*	*U23*
La1	0.76(6)	0.76	0.76	0.00	0.00	0.00
La2	0.75(10)	3.85(7)	3.85(7)	0.00	0.00	3.18(8)
W1	0.65(10)	0.65	0.65	0.00	0.00	0.00
O1	0.333(129)	0.333(129)	3.769(300)	-0.40(10)	-0.60(11)	-0.60(11)
O2	1.200(28)	1.200(28)	1.200(28)	0.07(4)	0.07(4)	0.07(4)
W2	0.75(10)	3.85(7)	3.85(7)	0.00	0.00	3.18(8)

LWO_P-dry(Ar) T = 100 K ILL 'Scherb model'

Lattice constants are

a = 11.155488(32) Å, b = a, c = a

Alpha = 90° Beta = 90° Gamma = 90°

Cell volume = 1388.244(7) Å^3

Name	*X*	*Y*	*Z*	*Ui/Ue*100*	*Site sym*	*Mult*	*Type*	*Seq*	*Fractn*
La1	0.500000	0.500000	0.500000	0.83(7)	M3M	4	LA	1	1.0005
La2	0.000000	0.23644(31)	0.23644(31)	0.91*	MM2(011)	48	LA	2	0.4838
W1	0.000000	0.000000	0.000000	0.64(10)	M3M	4	W	3	1.0215
O1	0.11230(23)	0.11230(23)	0.06537(32)	1.85*	M(+-0)	96	O	4	0.2373
O2	0.36619(12)	0.36619(12)	0.36619(12)	1.31*	3M(111)	32	O	5	0.9379
W2	0.000000	0.23644(31)	0.23644(31)	0.91*	MM2(011)	48	W	6	0.0162

Thermal parameters multiplied by 100.0 are

Name	*U11*	*U22*	*U33*	*U12*	*U13*	*U23*
La1	0.83(7)	0.83	0.83	0.00	0.00	0.00
La2	0.71(10)	1.01(18)	1.01(18)	0.00	0.00	0.41(16)
W1	0.64(10)	0.64	0.64	0.00	0.00	0.00
O1	1.108(156)	1.108(156)	3.346(287)	-0.08(11)	-0.72(12)	-0.72(12)
O2	1.314(28)	1.314(28)	1.314(28)	0.05(5)	0.05(5)	0.05(5)
W2	0.71(10)	1.01(18)	1.01(18)	0.00	0.00	0.41(16)

LWO_P-dry(Ar) T = 100 K ILL 'Magraso model'

Lattice constants are

a = 11.155488(32) Å, b = a, c = a

Alpha = 90° Beta = 90° Gamma = 90°

Cell volume = 1388.244(7) Å^3

Name	*X*	*Y*	*Z*	*Ui/Ue*100*	*Site sym*	*Mult*	*Type*	*Seq*	*Fractn*
La1	0.500000	0.500000	0.500000	0.82(6)	M3M	4	LA	1	0.9823
La2	0.000000	0.250000	0.250000	2.90*	MMM(100)	24	LA	2	0.9666
W1	0.000000	0.000000	0.000000	0.65(10)	M3M	4	W	3	1.0008
O1	0.11185(21)	0.11185(21)	0.06565(33)	---	M(+-0)	96	O	4	0.2257
O2	0.36593(11)	0.36593(11)	0.36593(11)	1.23*	3M(111)	32	O	5	0.9146
W2	0.000000	0.250000	0.250000	2.90*	MMM(100)	24	W	6	0.0365

Thermal parameters multiplied by 100.0 are

Name	*U11*	*U22*	*U33*	*U12*	*U13*	*U23*
La1	0.82(6)	0.82	0.82	0.00	0.00	0.00
La2	0.73(10)	3.98(7)	3.98(7)	0.00	0.00	3.15(8)
W1	0.65(10)	0.65	0.65	0.00	0.00	0.00
O1	0.618(137)	0.618(137)	3.499(295)	-0.31(10)	-0.58(11)	-0.58(11)
O2	1.235(28)	1.235(28)	1.235(28)	0.05(5)	0.05(5)	0.05(5)
W2	0.73(10)	3.98(7)	3.98(7)	0.00	0.00	3.15(8)

LWO_P-dry(Ar) T = 150 K ILL 'Scherb model'

Lattice constants are

a = 11.158355(32) Å, b = a, c = a

Alpha = 90° Beta = 90° Gamma = 90°

Cell volume = 1389.314(7) Å^3

Name	*X*	*Y*	*Z*	*Ui/Ue*100*	*Site sym*	*Mult*	*Type*	*Seq*	*Fractn*
La1	0.500000	0.500000	0.500000	0.89(7)	M3M	4	LA	1	1.0005
La2	0.000000	0.23639(31)	0.23639(31)	0.95*	MM2(011)	48	LA	2	0.4838
W1	0.000000	0.000000	0.000000	0.79(10)	M3M	4	W	3	1.0215
O1	0.11220(22)	0.11220(22)	0.06533(32)	1.93*	M(+-0)	96	O	4	0.2373
O2	0.36601(11)	0.36601(11)	0.36601(11)	1.42*	3M(111)	32	O	5	0.9379
W2	0.000000	0.23639(31)	0.23639(31)	0.95*	MM2(011)	48	W	6	0.0162

Thermal parameters multiplied by 100.0 are

Name	*U11*	*U22*	*U33*	*U12*	*U13*	*U23*
La1	0.89(7)	0.89	0.89	0.00	0.00	0.00
La2	0.74(10)	1.05(18)	1.05(18)	0.00	0.00	0.47(16)
W1	0.79(10)	0.79	0.79	0.00	0.00	0.00
O1	0.961(147)	0.961(147)	3.859(290)	-0.28(10)	-0.71(12)	-0.71(12)
O2	1.420(29)	1.420(29)	1.420(29)	0.00(5)	0.00(5)	0.00(5)
W2	0.74(10)	1.05(18)	1.05(18)	0.00	0.00	0.47(16)

LWO_P-dry(Ar) T = 150 K ILL 'Magraso model'

Lattice constants are

a = 11.158355(32) Å, b = a, c = a

Alpha = 90° Beta = 90° Gamma = 90°

Cell volume = 1389.314(7) Å^3

Name	*X*	*Y*	*Z*	*Ui/Ue*100*	*Site sym*	*Mult*	*Type*	*Seq*	*Fractn*
La1	0.500000	0.500000	0.500000	0.87(6)	M3M	4	LA	1	0.9823
La2	0.000000	0.250000	0.250000	2.95*	MMM(100)	24	LA	2	0.9666
W1	0.000000	0.000000	0.000000	0.80(10)	M3M	4	W	3	1.0008
O1	0.11175(20)	0.11175(20)	0.06562(33)	---	M(+-0)	96	O	4	0.2257
O2	0.36576(10)	0.36576(10)	0.36576(10)	1.34*	3M(111)	32	O	5	0.9146
W2	0.000000	0.250000	0.250000	2.95*	MMM(100)	24	W	6	0.0365

Thermal parameters multiplied by 100.0 are

Name	*U11*	*U22*	*U33*	*U12*	*U13*	*U23*
La1	0.87(6)	0.87	0.87	0.00	0.00	0.00
La2	0.76(10)	4.05(7)	4.05(7)	0.00	0.00	3.21(8)
W1	0.80(10)	0.80	0.80	0.00	0.00	0.00
O1	0.474(128)	0.474(128)	4.065(298)	-0.50(10)	-0.59(11)	-0.59(11)
O2	1.340(28)	1.340(28)	1.340(28)	-0.01(5)	-0.01(5)	-0.01(5)
W2	0.76(10)	4.05(7)	4.05(7)	0.00	0.00	3.21(8)

LWO_P-dry(Ar) T = 200 K ILL 'Scherb model'

Lattice constants are

a = 11.162082(33) Å, b = a, c = a

Alpha = 90° Beta = 90° Gamma = 90°

Cell volume = 1390.707(7) Å^3

Name	*X*	*Y*	*Z*	*Ui/Ue*100*	*Site sym*	*Mult*	*Type*	*Seq*	*Fractn*
La1	0.500000	0.500000	0.500000	1.00(7)	M3M	4	LA	1	1.0005
La2	0.000000	0.23645(32)	0.23645(32)	1.08*	MM2(011)	48	LA	2	0.4838
W1	0.000000	0.000000	0.000000	0.78(10)	M3M	4	W	3	1.0215
O1	0.11221(23)	0.11221(23)	0.06488(33)	2.03*	M(+-0)	96	O	4	0.2373
O2	0.36622(12)	0.36622(12)	0.36622(12)	1.50*	3M(111)	32	O	5	0.9379
W2	0.000000	0.23645(32)	0.23645(32)	1.08*	MM2(011)	48	W	6	0.0162

Thermal parameters multiplied by 100.0 are

Name	*U11*	*U22*	*U33*	*U12*	*U13*	*U23*
La1	1.00(7)	1.00	1.00	0.00	0.00	0.00
La2	0.91(11)	1.16(19)	1.16(19)	0.00	0.00	0.47(17)
W1	0.78(10)	0.78	0.78	0.00	0.00	0.00
O1	1.137(156)	1.137(156)	3.812(293)	-0.22(11)	-0.81(12)	-0.81(12)
O2	1.503(29)	1.503(29)	1.503(29)	0.07(5)	0.07(5)	0.07(5)
W2	0.91(11)	1.16(19)	1.16(19)	0.00	0.00	0.47(17)

LWO_P-dry(Ar) T = 200 K ILL 'Magraso model'

Lattice constants are

a = 11.162082(33) Å, b = a, c = a

Alpha = 90° Beta = 90° Gamma = 90°

Cell volume = 1390.707(7) Å^3

Name	*X*	*Y*	*Z*	*Ui/Ue*100*	*Site sym*	*Mult*	*Type*	*Seq*	*Fractn*
La1	0.500000	0.500000	0.500000	0.98(7)	M3M	4	LA	1	0.9823
La2	0.000000	0.250000	0.250000	3.06*	MMM(100)	24	LA	2	0.9666
W1	0.000000	0.000000	0.000000	0.90(10)	M3M	4	W	3	1.0215
O1	0.11178(21)	0.11178(21)	0.06511(33)	---	M(+-0)	96	O	4	0.2257
O2	0.36597(11)	0.36597(11)	0.36597(11)	1.42*	3M(111)	32	O	5	0.9146
W2	0.000000	0.250000	0.250000	3.06*	MMM(100)	24	W	6	0.0365

Thermal parameters multiplied by 100.0 are

Name	*U11*	*U22*	*U33*	*U12*	*U13*	*U23*
La1	0.98(7)	0.98	0.98	0.00	0.00	0.00
La2	0.92(10)	4.13(7)	4.13(7)	0.00	0.00	3.22(8)
W1	0.90(10)	0.90	0.90	0.00	0.00	0.00
O1	0.654(137)	0.654(137)	4.004(302)	-0.45(10)	-0.69(11)	-0.69(11)
O2	1.417(29)	1.417(29)	1.417(29)	0.07(5)	0.07(5)	0.07(5)
W2	0.92(10)	4.13(7)	4.13(7)	0.00	0.00	3.22(8)

LWO_P-dry(Ar) T = 298 K ILL 'Scherb model'

Lattice constants are

a = 11.171657(31) Å, b = a, c = a

Alpha = 90° Beta = 90° Gamma = 90°

Cell volume = 1394.289(7) Å^3

Name	*X*	*Y*	*Z*	*Ui/Ue*100*	*Site sym*	*Mult*	*Type*	*Seq*	*Fractn*
La1	0.500000	0.500000	0.500000	1.17(6)	M3M	4	LA	1	1.0005
La2	0.000000	0.23634(27)	0.23634(27)	1.10*	MM2(011)	48	LA	2	0.4838
W1	0.000000	0.000000	0.000000	0.92(10)	M3M	4	W	3	1.0215
O1	0.11181(22)	0.11181(22)	0.06529(32)	2.36*	M(+-0)	96	O	4	0.2373
O2	0.36608(11)	0.36608(11)	0.36608(11)	1.72*	3M(111)	32	O	5	0.9379
W2	0.000000	0.23634(27)	0.23634(27)	1.10*	MM2(011)	48	W	6	0.0162

Thermal parameters multiplied by 100.0 are

Name	*U11*	*U22*	*U33*	*U12*	*U13*	*U23*
La1	1.17(6)	1.17	1.17	0.00	0.00	0.00
La2	0.83(9)	1.23(16)	1.23(16)	0.00	0.00	0.46(15)
W1	0.92(10)	0.92	0.92	0.00	0.00	0.00
O1	1.349(153)	1.349(153)	4.370(271)	-0.54(10)	-0.77(12)	-0.77(12)
O2	1.722(28)	1.722(28)	1.722(28)	0.18(4)	0.18(4)	0.18(4)
W2	0.83(9)	1.23(16)	1.23(16)	0.00	0.00	0.46(15)

LWO_P-dry(Ar) T = 298 K ILL 'Magraso model'

Lattice constants are

a = 11.171657(32) Å, b = a, c = a

Alpha = 90° Beta = 90° Gamma = 90°

Cell volume = 1394.289(7) Å^3

Name	*X*	*Y*	*Z*	*Ui/Ue*100*	*Site sym*	*Mult*	*Type*	*Seq*	*Fractn*
La1	0.500000	0.500000	0.500000	1.16(6)	M3M	4	LA	1	0.9823
La2	0.000000	0.250000	0.250000	3.13*	MMM(100)	24	LA	2	0.9666
W1	0.000000	0.000000	0.000000	0.88(9)	M3M	4	W	3	1.0008
O1	0.11143(20)	0.11143(20)	0.06544(31)	---	M(+-0)	96	O	4	0.2257
O2	0.36590(10)	0.36590(10)	0.36590(10)	1.64*	3M(111)	32	O	5	0.9146
W2	0.000000	0.250000	0.250000	3.13*	MMM(100)	24	W	6	0.0345

Thermal parameters multiplied by 100.0 are

Name	*U11*	*U22*	*U33*	*U12*	*U13*	*U23*
La1	1.16(6)	1.16	1.16	0.00	0.00	0.00
La2	0.87(9)	4.26(6)	4.26(6)	0.00	0.00	3.30(8)
W1	0.88(9)	0.88	0.88	0.00	0.00	0.00
O1	0.871(134)	0.871(134)	4.206(273)	-0.71(9)	-0.59(11)	-0.59(11)
O2	1.636(28)	1.636(28)	1.636(28)	0.22(4)	0.22(4)	0.22(4)
W2	0.87(9)	4.26(6)	4.26(6)	0.00	0.00	3.30(8)